Université de Montréal

Sur les origines photosphériques des structures dans les vents des étoiles chaudes et lumineuses

par

Tahina Ramiaramanantsoa

Département de physique

Faculté des arts et des sciences

Thèse présentée à la Faculté des études supérieures

en vue de l'obtention du grade de

Philosophiæ Doctor (Ph.D.)

en physique

Août, 2018

Université de Montréal

Faculté des études supérieures

Cette thèse intitulée:

Sur les origines photosphériques des structures dans les vents des étoiles chaudes et lumineuses

présentée par:

Tahina Ramiaramanantsoa

a été évaluée par un jury composé des personnes suivantes:

Patrick Dufour,	Président-rapporteur
Anthony F. J. Moffat,	Directeur de recherche
Björn Benneke,	Membre du jury
Matteo Cantiello,	Examinateur externe
Patrick Dufour,	Représentant du Doyen de la FES

Thèse acceptée le: 20 Août 2018

Sommaire

Des progrès majeurs dans la caractérisation des vents des étoiles chaudes et lumineuses de type spectral O ont été accomplis durant l'ère de la mission spatiale *IUE (International Ultraviolet Explorer)*. La détection des énigmatiques composantes discrètes en absorption ('discrete absorption components' – DACs) est d'un intérêt primordial: ces petites raies en absorption variables apparaissent et se propagent dans les parties en absorption des profils P Cygni des raies de résonance non saturées des étoiles O dans l'UV, et sont interprétées comme la manifestation spectroscopique de la présence de structures spiralées à grande échelle dans leurs vents, les régions d'interactions en corotation ('corotating interaction regions' – CIRs). En outre, plusieurs observations spectroscopiques menées à partir du sol ont révélé la nature grumelée des vents des étoiles O. De nombreux travaux théoriques sont apparus pendant les trois dernières décennies concernant les origines de ces deux catégories distinctes de structures. Notamment, certaines études théoriques ont trouvé que ces structures peuvent prendre source au niveau de la photosphère stellaire. Néanmoins, le dernier mot revient toujours aux observations, même si, dans ce cas-ci, beaucoup de travail reste encore à faire à cet égard.

Le projet de recherche mené dans le cadre de cette thèse, essentiellement de nature observationnelle, a pour objectif d'investiguer cette possibilité des origines photosphériques des structures dans les vents des étoiles massives de type spectral O, en sondant la variabilité photosphérique à faibles amplitudes de trois étoiles massives de type spectral O clés, ξ Persei [O7.5III(n)((f))], ζ Puppis [O4I(n)fp], et V973 Scorpii [O8Iaf], moyennant la photométrie à haute précision et résolue dans le temps avec le

microsatellite *MOST (Microvariabilité et Oscillations STellaires)* et les nanosatellites de la mission *BRIght Target Explorer (BRITE-Constellation)*. Pour ζ Pup, un suivi spectroscopique de la variabilité de la raie d'émission He II λ4686 émise dans son vent a aussi été réalisé simultanément avec les observations *BRITE* de l'étoile. Ces efforts ont permis la détection de taches claires photosphériques induisant les CIRs dans les vents des étoiles O, ainsi que la détection de structures générées stochastiquement à la photosphère et induisant le grumelage dès la base du vent. Le mécanisme à l'origine des taches claires (notamment la possibilité qu'elles soient d'origine magnétique), la vraie nature des structures photosphériques excitées aléatoirement (qu'elles soient la manifestation d'ondes de gravité internes ou de turbulences dans une zone de convection subsurfacique), ainsi que la question de l'universalité de ces deux catégories de structures photosphériques chez les étoiles O, feront l'objet des prochaines étapes de cette quête à long terme.

Mots clés: étoiles: étoiles massives – étoiles: taches stellaires – étoiles: vents stellaires – techniques: photométrie – spectroscopie – méthode: astérosismologie – étoiles: individuelles: ξ Per – ζ Pup – V973 Sco.

Abstract

Major advances in the characterization of hot star winds have been achieved during the era of the *International Ultraviolet Explorer (IUE)* space-based mission. Of paramount interest was the detection of the enigmatic discrete absorption components (DACs): time-variable discrete absorption features propagating in the P Cygni absorption troughs of unsaturated UV resonance lines of O stars, best interpreted as spectroscopic manifestations of the presence of large-scale spiral-like corotating interaction regions (CIRs) in the stellar wind. Additionally, ground-based optical spectroscopic observations have indicated the clumpy nature of the winds of O stars. Several theoretical investigations on the origins of these two distinct types of hot star wind structures have emerged over the past three decades. Particularly, some theoretical studies have found the possibility that both of these wind structures might have their origins at the level of the stellar photosphere. Nevertheless, the last words always belong to the observations, although in this particular case a lot of work still needs to be done in that regard.

The research project conducted in the context of this thesis, essentially observational in nature, aims towards the investigation of the potential photospheric sources of those structures in hot stellar winds, by probing the low-amplitude photospheric variability of three key massive O-type stars, ξ Persei [O7.5III(n)((f))], ζ Puppis [O4I(n)fp], and V973 Scorpii [O8Iaf], by means of high-precision time-dependent photometry with the *Microvariability and Oscillations of STars (MOST)* microsatellite, and the nanosatellites of the *BRIght Target Explorer (BRITE-Constellation)* mission. For ζ Pup, simultaneous ground-based intensive spectroscopic monitoring of the He II λ4686 wind emission line of the star was also performed. These efforts led to the detection of

observational evidence for the presence of bright photospheric spots driving CIRs in hot stellar winds, as well as some stochastically-triggered surface structures initiating clumping at the very base of the wind. The origins of the bright spots (particularly the possibility that they might be of magnetic origin), the true nature of the randomly-excited photospheric structures (whether they are the manifestations of internal gravity waves or turbulent convection in a subsurface convection zone), as well as the universality of both of these photospheric structures in O-type stars, will be the main subjects of the next steps in this long-term quest.

Keywords: stars: massive stars – stars: starspots – stars: stellar winds – techniques: photometry – spectroscopy – method: asteroseismology – stars: individual: ξ Per – ζ Pup – V973 Sco.

Table des matières

Liste des tables

Liste des figures

Liste des sigles et des abréviations

ACF Fonction d'autocorrélation, de l'anglais *Autocorrelation function*

BRITE *BRIght Target Explorer*

BEST *BRITE* Executive Science Team

CCD Dispositif à transfert de charges, de l'anglais *Charge-Coupled Device*

CFHT Canada–France–Hawaii Telescope

CIRs Régions d'Intéractions en corotation, de l'anglais *Corotating interaction regions*

CoRoT *Convection, Rotation et Transits planétaires*

CTIO Cerro Tololo Inter-American Observatory

CWT Transformée en ondelettes continue, de l'anglais *Continuous wavelet transform*

DAC Composante discrète en absorption, de l'anglais *discrete absorption component*

DFT Transformée de Fourier discrète, de l'anglais *discrete Fourier transform*

ESO European Southern Observatory

ESPaDOnS Echelle SpectroPolarimetric Device for the Observation of Stars

EW Largeur équivalente, de l'anglais *equivalent width*

FeCZ Zone de convection due au pic d'opacité associé à l'ionisation partielle du Fer à $T \simeq 170$ kK, de l'anglais *iron convection zone*

GIRAFFE Grating Instrument for Radiation Analysis with a Fibre Fed Échelle

HARPSpol High Accuracy Radial velocity Planet Searcher's polarimeter

HD Hydrodynamique

Hipparcos *High precision parallax collecting satellite*

HWHM Demi-largeur à mi-hauteur, de l'anglais *half width at half maximum*

IGWs Ondes de gravité internes, de l'anglais *internal gravity waves*

IMF Fonction de masse initiale, de l'anglais *initial mass function*

IRAF Image Reduction and Analysis Facility

ISIS Integrated Spectrographic Innovative Software

IUE *International Ultraviolet Explorer*

LBV Étoile lumineuse, bleue et variable

LER Région de formation de la raie, de l'anglais *line emission region*

LDI Instabilité des vents radiatifs poussés par les raies spectrales, de l'anglais *line-deshadowing instability*

LI Inversion de courbe de lumière, de l'anglais *light curve inversion*

LPV Variations de profil de raie, de l'anglais *line profile variation*

LTE Équilibre thermodynamique local, de l'anglais *local thermodynamic equilibrium*

MOST *Microvariabilité et Oscillations STellaires*

NAC Composante étroite en absorption, de l'anglais *narrow absorption component*

NLPCA Analyse en composantes principales non-linéaires, de l'anglais *non-linear principal component analysis*

NRPs Pulsations non-radiales, de l'anglais *non-radial pulsations*

PCA Analyse en composantes principales, de l'anglais *principal component analysis*

PIZ Zone d'ionisation partielle, de l'anglais *partial ionization zone*

PoWR Potsdam Wolf–Rayet

PSF Fonction d'étalement du point, de l'anglais *point spread function*

RLOF Débordement du lobe de Roche, de l'anglais *Roche lobe overflow*

RTS Bruits en créneaux, de l'anglais *random telegraph signal*

SAAO South-African Astronomical Observatory

SASER Southern Astro Spectroscopy Email Ring

SGR Supergéante rouge

SMARTS Small and Moderate Aperture Research Telescope System

SMEI *Solar Mass Ejection Imager*

SN Supernova

S/N Rapport signal sur bruit

SPB Étoile B à pulsations lentes, de l'anglais *Slowly Pulsating B star*

TAMS Fin de la séquence principale, de l'anglais *terminal-age main sequence*

TBL Telescope Bernard Lyot

TMT Télescope de Trente Mètres, de l'anglais *Thirty Meter Telescope*

UV Ultraviolet

WR Wolf–Rayet

WIRE *Wide Field Infrared Explorer*

ZAMS Début de la séquence principale, de l'anglais *zero-age main sequence*

Remerciements

Il y a six ans de ça, j'étais alors à mi-chemin dans mon projet de M.Sc. au NExScI quand j'ai commencé à jouer avec des courbes de lumière à haute précision et à cadence élevée d'étoiles, et à les apprécier petit à petit. C'est ainsi que j'ai été amené à postuler à des projets de doctorat dans le même thème. Quand j'ai reçu l'offre de Tony pour venir faire ma thèse à Montréal sur 'l'astérosismologie des étoiles massives avec la mission *BRITE*', j'avoue qu'à l'époque je ne connaissais quasiment rien de Montréal, mais j'étais, pour ainsi dire, aveuglément motivé par le sujet de recherche. Quand j'ai reçu l'offre de Tony pour venir faire ma thèse à Montréal, je n'avais pas suffisamment prévu que six ans après j'aurais accumulé Autant de connaissances sur les étoiles massives et leurs vents, et appris Énormément sur le Québec et le Canada. Je tiens donc vraiment à remercier mon directeur de thèse, Tony Moffat, de m'avoir recruté pour ce projet, et surtout d'avoir bien voulu me transmettre une partie de son savoir, de m'avoir partagé sa passion et son enthousiasme qui sont, à mon avis, exemplaires. Je le remercie également de m'avoir permis de découvrir et de vivre les subtilités de la culture Canadienne.

Je remercie aussi Nicole, Noel, Bert, Emily, Melissa, Danny, Sébastien, et Tomer pour les discussions intéressantes au Club, portant sur... à peu près tout! Je tiens à remercier particulièrement Sébastien de m'avoir transmis le savoir-faire sur la réduction et la normalisation homogène d'"un million" de spectres, savoir faire qui remonte à je ne sais plus qui, mais dont je suis sûr qu'il s'est transmis de génération en génération.

Un grand merci à Bert, James, Anna, Paul, Benoit, Deniz et Yan pour les après-midi

board games de fins de semaines et les soirées au Randolph – c'était le fun!

Je tiens aussi à remercier spécialement Caroline pour son soutien de tous les jours, sur tous les aspects...

Je voudrais aussi exprimer ma gratitude envers Elisabeth et Michel pour leur grande ouverture d'esprit et pour m'avoir accueilli chez eux comme si je faisais partie de leur famille. Sur cette occasion, je tiens à remercier Laura et Charles pour leurs enthousiasmes vraiment inégalés dès que l'appel à Exploding Kittens ou à Ticket to Ride s'annonce!

Ary mazava ho azy, misaotra betsaka ny fianakaviako aho amin'ny fanohanana izay asehony ahy amin'ny lafiny rehetra, na inon-kidona na inon-kihatra.

Finalement, je tiens à remercier Eva, Vincent, Saskia, et Léonard, à qui je dois tout simplement le fait que j'en suis arrivé jusque-là.

1

Introduction

Nos connaissances actuelles sur l'histoire de notre Univers sont au point où elles nous permettent de réaliser que les toutes premières étoiles étaient des étoiles très chaudes, très lumineuses et très massives qui ont contribué à la fin des âges sombres de l'Univers (Bromm & Larson 2004). Depuis l'aube cosmique, ces étoiles ont littéralement constitué les centres de recyclage chimique des galaxies, non seulement à cause des énormes quantités de matière qu'elles éjectent par leurs vents radiatifs très intenses tout au long de leurs vies, mais surtout par les explosions supernovae qu'elles subissent à la fin de leurs vies et qui permettent la formation de nouvelles étoiles et systèmes planétaires. Ironiquement, ce processus d'enrichissement du milieu interstellaire a été tellement efficace qu'il a graduellement transformé le mode de formation d'étoiles initialement dominé en masse par les étoiles chaudes et massives au mode

actuel dominé par les étoiles froides et de faible masse. Toujours est-il qu'aujourd'hui, les étoiles chaudes et lumineuses, malgré leur sous-nombre, demeurent les moteurs qui alimentent le cycle de vie des étoiles.

Le projet de recherche faisant l'objet de cette thèse se lance dans une aventure en quête des origines des structures dans les vents intenses des étoiles chaudes et lumineuses, ou plus précisément, des étoiles massives de type spectrale O[1]. Qu'est-ce donc formellement qu'une étoile massive de type spectrale O? Cela fera l'objet du Chapitre 2. Ensuite, le Chapitre 3 aura pour objectif d'évoquer les différentes structures dans les vents de ces étoiles. Après viendra le Chapitre 4 dont la mission sera de faire l'inventaire des structures qui pourraient être présentes à la surface des étoiles massives de type spectral O. Dans les Chapitres 5, 6, et 7 seront décrits les efforts observationnels entrepris dans ce projet de recherche en vue de déceler des signes de manifestations de structures à la surface de trois étoiles clés, ξ Persei, ζ Puppis, et V973 Scorpii – par photométrie à haute précision à partir de l'espace – et surtout de déterminer s'il y a des liens entre ces structures photosphériques et celles présentes dans les vents de ces étoiles. En particulier, la campagne d'observations menée sur ζ Pup – pour laquelle un suivi spectroscopique intensif sondant le vent de l'étoile a pu être mené à partir du sol simultanément avec la photométrie à haute précision fournie par la mission *BRIght Target Explorer (BRITE)* – nous a apporté des preuves claires sur les origines photosphériques des structures dans les vents des étoiles massives de type spectral O. Le Chapitre 8 mettra en exergue les conclusions les plus saillantes apportées par cette thèse, ainsi que les questions importantes dont les réponses restent à dévoiler dans les prochaines étapes de cette quête à long terme.

[1]Cela dit, contrairement aux premières étoiles chaudes et lumineuses qui étaient responsables de l'aube cosmique et qui seraient de Population III ($Z \simeq 0$ car il n'y avait quasiment pas d'éléments plus lourds que l'hélium à ces époques-là), les étoiles que nous considèrerons ici sont des étoiles de Population I.

2

Les étoiles massives de type spectral O

Il est quelquefois considéré qu'une étoile est massive dès qu'elle est un tant soit peu plus massive que le Soleil. Étant donné que tout est relatif, il faut être tolérant et ne pas donner complètement tort à cette considération. Cependant, il est important de noter que la définition formelle d'une étoile massive est fondée sur le comportement en fin de vie: la phase terminale en supernova à effondrement de coeur. Cela correspond aux étoiles commençant leur vie avec une masse initiale minimale aux alentours de huit fois la masse du Soleil (Vanbeveren *et al.* 1998a; Conti 2002). Dans le diagramme de Hertzsprung–Russell (diagramme H–R; Figure 2.1), cette limite correspond, pour une étoile débutant sa vie sur la séquence principale ('zero-age main sequence' – ZAMS), à une luminosité minimale de quelques $10^3 L_{\odot}$, une température effective minimale $T_{\rm eff} \simeq 20$ kK et un type spectral minimal aux alentours de B2V.

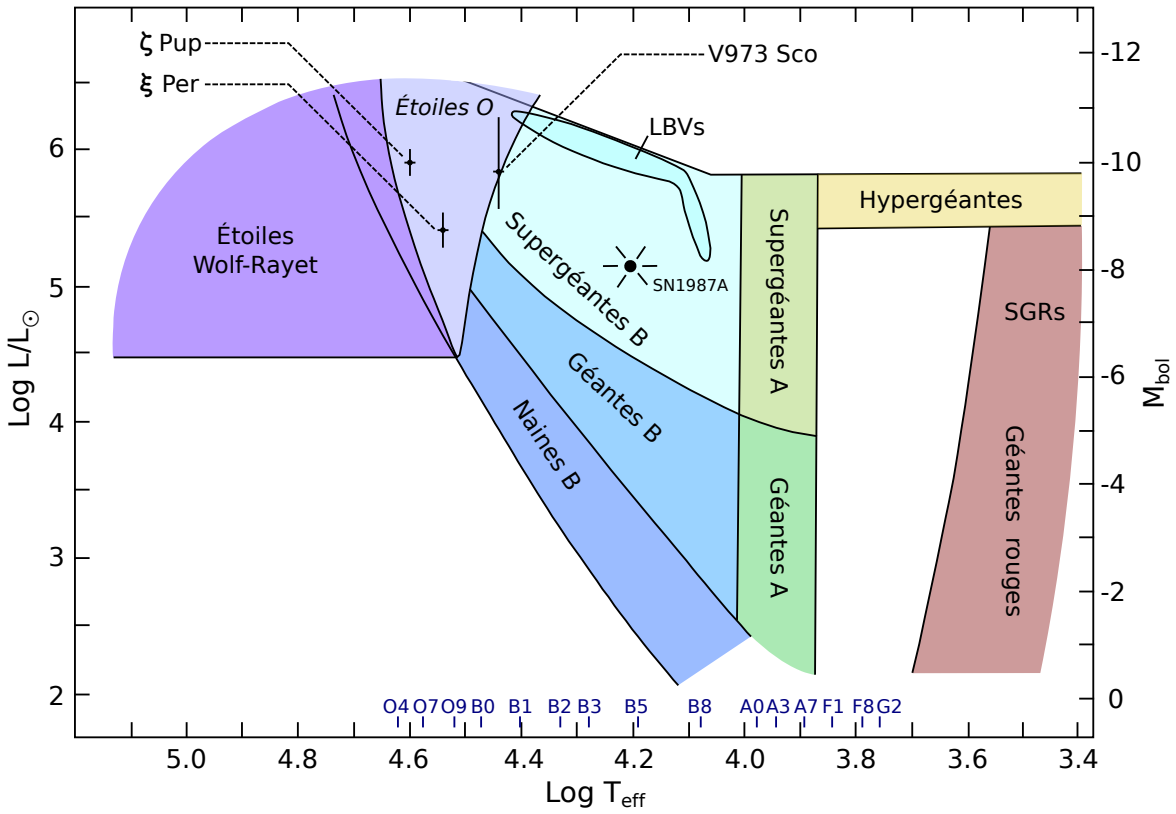

Figure 2.1: Localisation des étoiles massives de type spectral O dans la partie haute du diagramme de Hertzsprung–Russell. Les emplacements actuels des trois étoiles O clés considérées dans ce projet de recherche – ξ Per [O7.5III(n)((f))p], ζ Pup [O4I(n)fp], et V973 Sco [08Iaf] – y sont aussi indiqués. D'une manière générale, un diagramme de Hertzsprung–Russell montre la distribution d'un ensemble d'étoiles, avec en abscisse la température effective, le type spectral, ou la couleur, et en ordonnée la magnitude ou la luminosité. Ce genre de graphe a été produit pour la première fois par Russell en 1913 sur la base des travaux de Hertzsprung en 1911. Figure adaptée de Vanbeveren *et al.* (1998a).

Ainsi, cela ne concerne que les étoiles qui arrivent sur la séquence principale avec des types spectraux OV ou B0-2V. Particulièrement, les étoiles massives ZAMS de type spectral O se caractérisent généralement par le trio de conditions:

$$M_{\rm ZAMS} \gtrsim 15 M_\odot,\ L \gtrsim 4\times10^4 L_\odot \text{ et } T_{\rm eff} \gtrsim 30 \text{ kK}.$$

2.1 Sur la séquence principale

Les étoiles massives sont rares comparées aux étoiles de faible masse et de masse intermédiaire. Cela se traduit dans la décroissance de la loi de probabilité de la masse stellaire initiale – communément appelée 'fonction de masse initiale' – qui s'avère être universelle et suivre une loi de puissance $\phi(M_\star) \propto M_\star^{-2.35}$ pour $M_\star \sim 1.25 - 150 \mathrm{M}_\odot$ (Salpeter 1955; Bastian *et al.* 2010). Cela dit, la rareté des étoiles massives est surtout due à leurs durées de vie très courtes comparées à celles des étoiles de faible masse[1]: des naines de masses $M_{\rm ZAMS} = 120\mathrm{M}_\odot$ et $M_{\rm ZAMS} = 15\mathrm{M}_\odot$ vont passer typiquement $\sim 3\times10^6$ ans et $\sim 13\times10^6$ ans respectivement sur la séquence principale, comparé à $\sim 9\times10^9$ ans pour le Soleil et $\sim 22\times10^9$ ans pour une naine de $M_{\rm ZAMS} = 0.8\mathrm{M}_\odot$ (Ekström *et al.* 2012).

2.1.1 Structure interne globale

Une des particularités bien connues des étoiles massives est le fait de posséder un coeur convectif et une enveloppe radiative (Kippenhahn & Weigert 1990, page 212). La Figure 2.2 indique qu'en réalité, la structure coeur convectif–enveloppe radiative

[1]Une 'règle générale' pour estimer rapidement le temps de brûlage central de l'hydrogène d'une étoile est de considérer $\tau_{\rm H} \sim M^{1-\eta}$ avec $\eta \sim 3.5$ en moyenne (ultimement à cause de la relation masse-luminosité; Kippenhahn & Weigert 1990, pages 209 et 280). En réalité, il y a bien sûr plusieurs paramètres qui influent sur cette estimation (par exemple le taux de perte de masse par le vent stellaire, la métallicité et la rotation stellaire).

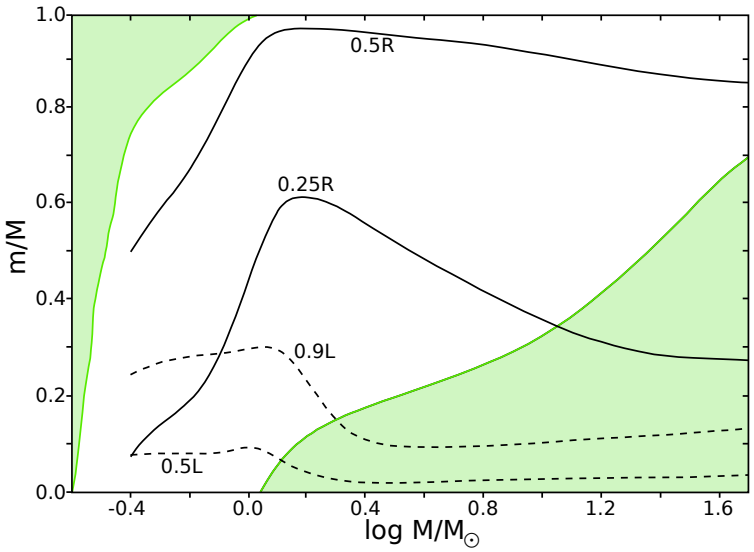

Figure 2.2: Extension de la zone de convection (région verte) en fonction de la masse stellaire. Figure adaptée de Kippenhahn & Weigert (1990).

apparaît dès $M_{\rm ZAMS} \simeq 1.5 {\rm M}_{\odot}$. Aussi, la limite supérieure de la zone convective augmente avec la masse stellaire et, arrivé à $50 {\rm M}_{\odot}$, le coeur couvre 70% de la masse stellaire. Le régime super-massif ($M_{\rm ZAMS} \gtrsim 120 {\rm M}_{\odot}$) serait probablement peuplé par des étoiles dont les intérieurs sont complètement convectives.

De surcroît, il faut noter que la frontière entre le coeur convectif et l'enveloppe radiative est théoriquement l'endroit de l'étoile où l'accélération du fluide due à la poussée d'Archimède est nulle. Cependant, les cellules convectives provenant du coeur n'ont pas une vitesse strictement nulle quand elles traversent cette frontière, et vont la dépasser sur une distance $d_{\rm ov}$ par inertie jusqu'à ce qu'elles soient complètement freinées. Ce phénomène de dépassement du coeur convectif est typiquement caractérisé par le paramètre $\alpha_{\rm ov}$ tel que $d_{\rm ov} = \alpha_{\rm ov} H_p$, où H_p est l'échelle de hauteur locale vis-à-vis de la pression du fluide.

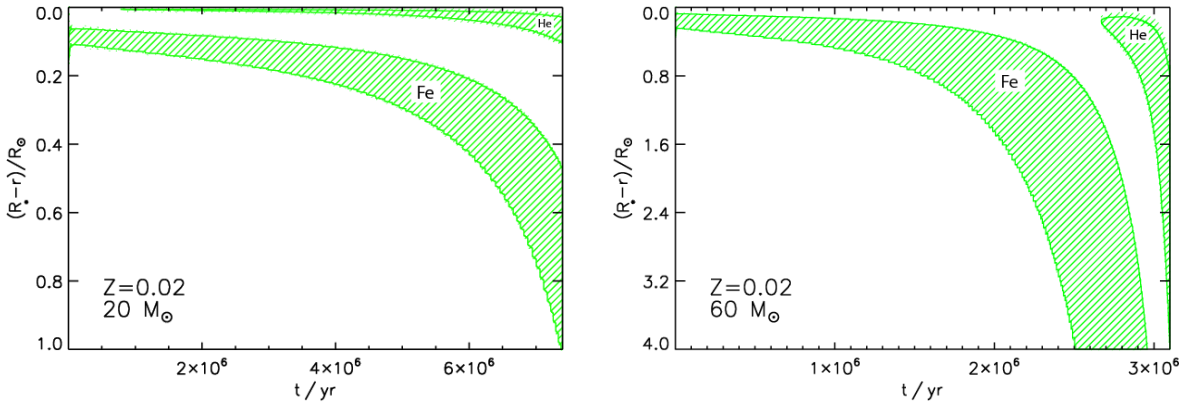

Figure 2.3: Évolution de l'extension des zones de convection sub-surfaciques dues aux pics d'opacité associés aux ionisations partielles du fer et de l'hélium, pour des étoiles de Population I telles que $M_{\rm ZAMS} = 20 M_\odot$ (*Gauche*) et $M_{\rm ZAMS} = 60 M_\odot$ (*Droite*). Figure tirée de Cantiello *et al.* (2009b).

2.1.2 Zones de convection sub-surfaciques

La structure globale coeur convectif–enveloppe radiative des étoiles massives est maintenant très bien établie. Il a longtemps été admis qu'au delà du coeur convectif des étoiles massives, le transport d'énergie ne peut se faire que de manière radiative tout au long de l'enveloppe, jusqu'à la photosphère stellaire. Cependant, vers le début des années 90, la découverte d'un pic d'opacité à des températures voisines de 170 kK, dû à l'ionisation partielle du fer (Iglesias *et al.* 1992), a commencé à remettre en cause cette vision. En effet, Stothers & Chin (1993) ont montré que ce pic d'opacité est capable de générer une zone de convection dans l'enveloppe radiative des étoiles massives. Plus tard, Cantiello *et al.* (2009b) effectuent des simulations confirmant ce comportement, et prédisent l'apparition de cette zone de convection tout près de la surface stellaire (Figure 2.3). Le terme 'zone de convection sub-surfacique due à l'ionisation partielle du Fer', raccourci en 'FeCZ', est né de cette découverte théorique.

Par ailleurs, les simulations de Cantiello *et al.* (2009b) trouvent aussi un autre pic d'opacité dû à la deuxième ionisation partielle de l'hélium à $T \simeq 50$ kK, et prédisent qu'une zone de convection associée à ce pic peut aussi se former tout près de la surface stellaire.

2.1.3 Vent stellaire radiatif

Toutes les étoiles éjectent de la matière par un vent stellaire d'une manière ou d'une autre. Par exemple le Soleil émet un vent qui est constitué de particules chargées (des électrons, des protons, et des particules alpha) poussées par la pression thermique du gaz constituant la couronne solaire. Les vents des étoiles massives, quant à eux, sont maintenus par la pression de radiation sur les particules de l'atmosphère extérieure. En effet, le transfert de quantité de mouvement entre la très forte radiation photosphérique (qui se fait essentiellement dans l'UV) et le gaz de l'atmosphère, par absorption ou diffusion dans les raies spectrales s'avère être efficace pour maintenir le vent stellaire des étoiles massives (Lamers & Cassinelli 1999). S'ajoute à cela le fait que les éléments susceptibles d'absorber ou de diffuser ce rayonnement UV se trouvent en quantité importante dans l'atmosphère de l'étoile.

Le taux de perte de masse ($\dot{M} = dM/dt$) par le vent stellaire des étoiles massives ZAMS de type spectral O est de l'ordre de $10^{-7}\mathrm{M}_\odot$ an^{-1} (Vink *et al.* 2001), c'est-à-dire environ sept ordres de grandeurs plus élevé que celui du vent solaire qui est d'environ $2 \times 10^{-14}\mathrm{M}_\odot$ an^{-1} (McComas *et al.* 2000). Une particule est dite éjectée par le vent quand elle commence à être découplée de la photosphère, ce qui arrive seulement quand le module de la composante radiale de sa vitesse atteint la vitesse du son locale, $v_{\mathrm{sonic}} = \sqrt{RT/\mu}$ (T étant la température, R la constante universelle du gaz parfait, et μ la masse moléculaire moyenne). Dans les étoiles massives de type spectral

O, $v_{\rm sonic} \simeq 20$ km s^{-1}. Ainsi, typiquement, une particule du vent d'une étoile massive de type spectral O s'échappe de la photosphère avec une vitesse de composante radiale $v_{\rm I} \sim 20$ km s^{-1} et est accélérée jusqu'à atteindre une vitesse asymptotique v_∞ de l'ordre de $2000 - 3000$ km s^{-1} l'amenant dans le milieu interstellaire. Il est maintenant bien connu que le comportement de la composante radiale de la vitesse d'une telle particule suit une loi β:

$$v_r(r) = v_{\rm I} + (v_\infty - v_{\rm I})\left(1 - \frac{r_{\rm I}}{r}\right)^\beta , \tag{2.1}$$

avec typiquement $\beta = 0.8 - 1$ pour les étoiles massives de type spectral O (Lamers & Cassinelli 1999).

Par ailleurs, le vent d'une étoile massive de type spectral OB peut présenter des raies en absorption, en émission ou une combinaison des deux. Dans le troisième cas, la raie a un profil dénommé 'profil P Cygni'. Bien que cette recherche ne se concentre pas sur les profils P Cygni, son objectif principal est basé entre autres sur une forme de variabilité du vent des étoiles O détectée auparavant dans ces catégories de raies (Chapitre 3, Section 3.2.1). Ainsi, il est intéressant d'évoquer brièvement le processus sous-jacent à la formation d'un profil P Cygni.

Une raie ayant un profil P Cygni est constituée d'une composante en absorption décalée vers le violet, adjacente à une composante en émission décalée vers le rouge (Figure 2.4). Le processus de base responsable de l'apparition des profils P Cygni est la diffusion résonante (excitation–désexcitation radiative) des photons émis par la photosphère par des ions du vent stellaire. Le décalage Doppler des composantes est dû au mouvement des particules entrainées par le vent en expansion.

La formation d'un profil P Cygni peut se décrire qualitativement comme montré à la Figure 2.4, en considérant un modèle simple d'une étoile dotée d'un vent en expansion

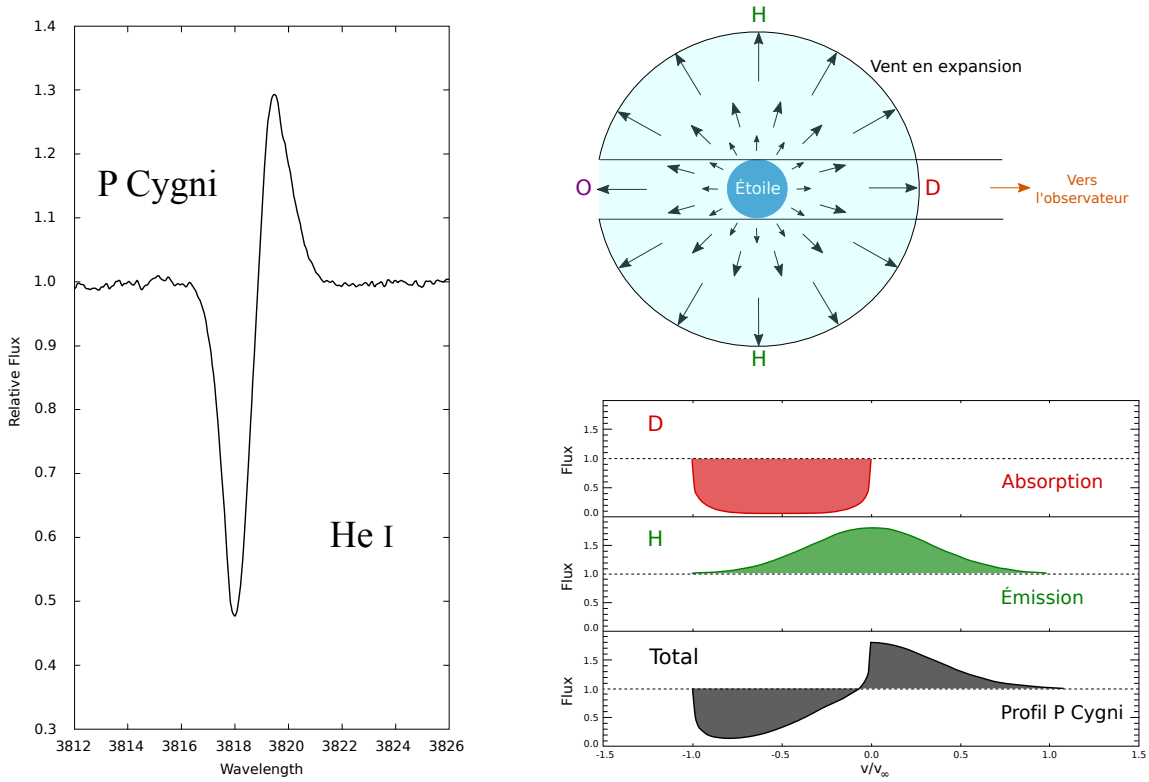

Figure 2.4: *Gauche*: Profil P Cygni de la raie He I de la supergéante P Cygni (Israelian & de Groot 1999). *Droite*: Modèle simple de vent en expansion à symétrie sphérique avec les différentes régions perçues par l'observateur ('D': tube de devant; 'H': halo; 'O': zone occultée) et contribution de ces régions dans la formation d'un profil P Cygni. Figure adaptée de Lamers & Cassinelli (1999).

à symétrie sphérique (Lamers & Cassinelli 1999). L'étoile émet un continu, éventuellement avec une raie d'absorption photosphérique à la longueur d'onde au repos de la raie. Les particules de la région D diffusent les photons émis par l'étoile en dehors de la ligne de visée, ce qui produit une composante en absorption. Cette composante est décalée vers le violet entre $-v_\infty$ et 0 puisque les particules sont en mouvement vers l'observateur. Le halo H diffuse la radiation provenant de la photosphère dans toutes les directions, avec une partie de la radiation envoyée vers l'observateur. Cela produit une composante en émission décalée entre $+v_\infty$ et $-v_\infty$. La somme de ces contributions donne le profil P Cygni.

Un des facteurs qui influent beaucoup sur la forme du profil P Cygni est la densité de colonne N des ions absorbants dans le vent stellaire. Notamment, le profil P Cygni n'apparait que si $N \gtrsim 10^5$ ions cm^{-2}. Dans les étoiles OB, les raies de résonance les plus courantes sont celles du C IV λ1548, N V λ1239, et Si IV λ1394, toutes dans l'UV.

2.2 Après la fin du brûlage de l'hydrogène central

Quand une étoile massive a fini le brûlage du réservoir d'hydrogène dans son coeur, elle entre dans une phase de brûlage central de l'helium. Dans le diagramme H–R, elle part de la séquence principale pour suivre un chemin évolutif qui dépend de sa composition chimique initiale, sa vitesse de rotation initiale et surtout sa masse initiale (Figure 2.5). Les différents scénarios d'évolution pour des étoiles massives simples de composition chimique de Population I sont résumés dans le Tableau 2.I.

2.2.1 Évolution vers une supergéante rouge

Les étoiles massives OB telles que $M_{\rm ZAMS} \lesssim 25 M_\odot$ évoluent en supergéantes rouges (SGR) une fois le brûlage de l'hydrogène central terminé. Les SGRs sont donc au stade

Table 2.I: Scénarios d'évolution d'une étoile massive simple de métallicité $Z = 0.02$ en fonction de la masse initiale. SGR: supergéante rouge; LBV: étoile lumineuse bleue et variable; WNE/L, WC, WO: étoiles Wolf–Rayet; SN: Supernova. Tableau adaptée de Crowther (2007).

M_{ZAMS}	Scénario d'évolution
$10M_\odot - 25M_\odot$	OB $\rightsquigarrow$ SGR $\rightsquigarrow$ SNII
$25M_\odot - 40M_\odot$	O $\rightsquigarrow$ SGR/LBV $\rightsquigarrow$ WNE $\rightsquigarrow$ SNIb
$40M_\odot - 75M_\odot$	O $\rightsquigarrow$ LBV $\rightsquigarrow$ WNE $\rightsquigarrow$ WC $\rightsquigarrow$ SNIc
$\gtrsim 75M_\odot$	O $\rightsquigarrow$ WNL $\rightsquigarrow$ LBV $\rightsquigarrow$ WNE $\rightsquigarrow$ WC $\rightsquigarrow$ SNIc

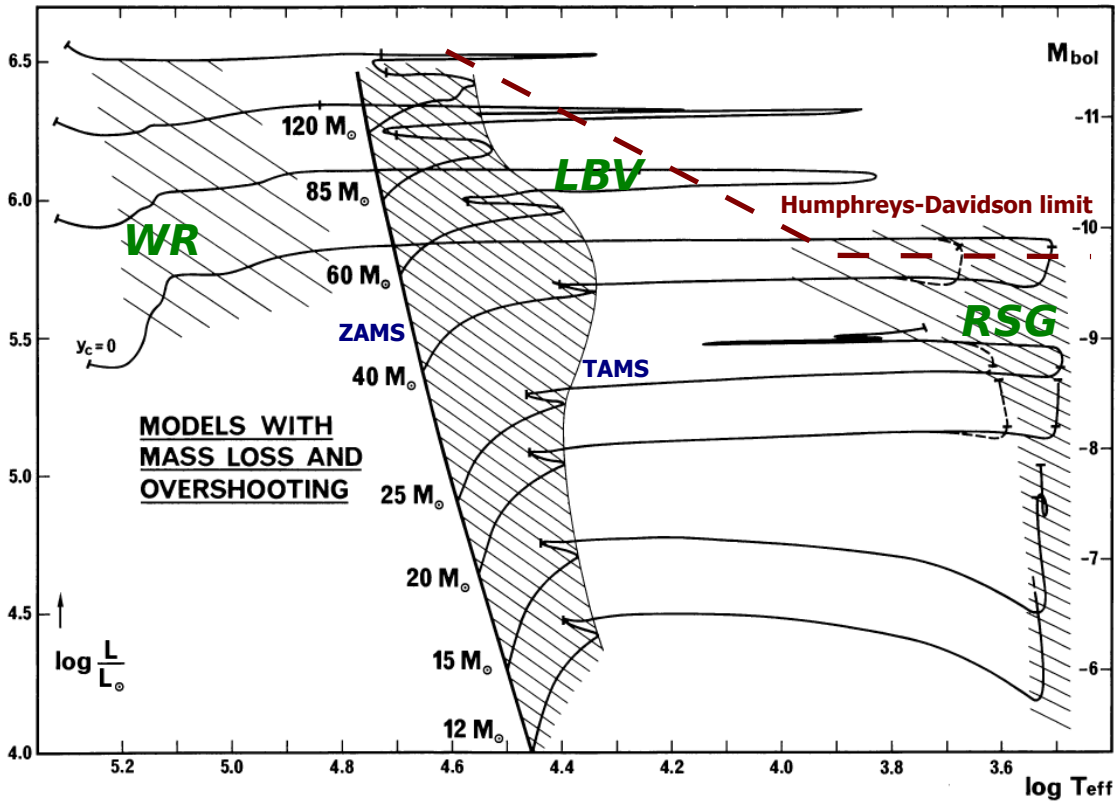

Figure 2.5: Chemins évolutifs théoriques d'étoiles massives de $M_{\mathrm{ZAMS}} = 12M_\odot$ à $M_{\mathrm{ZAMS}} = 120M_\odot$. Les phases Wolf–Rayet (WR), étoile lumineuse, bleue, variable (LBV) et supergéante rouge (SGR) ainsi que la limite de Humphreys–Davidson y sont indiquées. Figure adaptée de Maeder & Meynet (1987).

où elles brûlent de l'hélium dans leur coeur et possèdent des atmosphères très étendues, avec des rayons pouvant atteindre $1500 R_\odot$ et des gravités de surface $\log g \sim 0$. Les SGRs de la Voie Lactée ont des types spectraux aux alentours de M1–M2.

Une fois dans la phase SGR, deux possibilités se présentent: soit l'étoile reste dans cet état et explose en supernova à effondrement de coeur, soit elle revient vers la partie bleue du diagramme H–R. Le facteur principal qui va déterminer ce retour est la fraction de masse occupée par le coeur d'hélium $q_0 = M_{He}/M$ (Giannone 1967): tant que cette fraction de masse dépasse $60 - 70\%$, l'étoile revient vers la partie bleue du diagramme H–R.

2.2.2 Les étoiles près de la limite de Humphreys-Davidson

Vers la fin des années 70, une étude comparative des paramètres stellaires d'un grand nombre d'étoiles massives évoluées dans la Voie Lactée et dans le grand nuage de Magellan a permis à Humphreys & Davidson (1979) de déceler une limite sur la luminosité au-dessus de laquelle il n'y a pas de SGRs dans le diagramme H–R. Cette limite est aussi représentée sur la Figure 2.5, montrant qu'elle est plate pour $T_{\rm eff} \lesssim 10$ kK et augmente avec la température effective au-delà de cette valeur. La partie croissante de cette limite empirique de Humphreys–Davidson peut être interprétée qualitativement comme une limite d'Eddington 'modifiée'. À la base, la limite d'Eddington classique est la luminosité à partir de laquelle la pression de radiation devient plus importante que l'accélération gravitationnelle centripète, entraînant la rupture de l'équilibre hydrostatique et l'expulsion d'une quantité importante de matière stellaire:

$$L_{\rm Edd} = \frac{4\pi c \mathcal{G} M}{\kappa} \tag{2.2}$$

où κ est l'opacité de la photosphère. Cette limite d'Eddington classique correspond à une luminosité constante, car elle ne tient compte que de l'opacité due à la diffusion électronique qui est essentiellement constante. La limite d'Eddington modifiée tient compte de l'opacité due aux raies spectrales, qui est une fonction décroissante de la température au-dessus de ∼10 kK (Lamers & Fitzpatrick 1988; Lamers 1997). Le comportement de la limite de Humphreys–Davidson dans ce régime de températures effectives est généralement expliqué par cet effet.

Une étoile massive proche de la limite de Humphreys–Davidson est généralement très instable, subissant de larges déplacements dans le diagramme H–R et pouvant perdre plus de $10^{-3}M_{\odot}$ an^{-1}. Une telle étoile est soit dans la phase hypergéante jaune soit dans la phase lumineuse, bleue, variable.

2.2.2.1 La phase hypergéante jaune

La phase hypergéante jaune correspond à une étape très brève où une étoile ayant passé la phase SGR subit des allers-retours quasiment horizontaux dans le diagramme H–R, avec des températures effectives variant entre ∼ 4.8 kK et ∼ 7.5 kK. Le fait que les hypergéantes jaunes ont nécessairement été dans la phase SGR est généralement témoigné dans leurs spectres par des excès d'abondances de surface d'éléments relativement lourds tels que le sodium, résultant d'un brassage dû à la convection qui les a apporté jusqu'à la surface lors de la phase SGR (de Jager & Nieuwenhuijzen 1997; de Jager 1998; Stothers & Chin 2001). Pendant leurs allers-retours dans le diagramme H–R, les hypergéantes jaunes sont sujettes à des instabilités dynamiques qui entraînent occasionnellement des éruptions (Section 4.4.1) où le taux de perte de masse peut atteindre $10^{-3}M_{\odot}$ an^{-1}.

2.2.2.2 Les étoiles lumineuses, bleues, variables

Les étoiles lumineuses, bleues, variables (LBVs), appelées aussi variables de type S Dor, ont un rapport L/M élevé et sont sujettes à des variations de taux de perte de masse qui culminent occasionnellement par de grosses éjections d'une quantité de matière importante vers le milieu interstellaire.

Les étoiles LBVs sont généralement entourées d'une nébuleuse circumstellaire formée par les matériaux éjectés lors de la perte de masse. La nébuleuse est particulièrement riche en azote, indiquant que les couches stellaires où a lieu le cycle CNO sont éjectées. Dues à leur perte de masse importante, les étoiles LBVs ne peuvent pas passer par la phase SGR et deviennent plutôt des étoiles Wolf–Rayet qui vont ultimement exploser en supernova. Cependant, de plus en plus d'observations ont récemment montré que des étoiles LBVs pourraient éventuellement exploser directement en supernova par production de paires si l'étoile ne perd pas assez de masse (Gal-Yam & Leonard 2009; Mauerhan *et al.* 2013).

2.2.3 La phase Wolf–Rayet

Les étoiles arrivées dans la phase Wolf–Rayet (WR) sont particulièrement chaudes et très lumineuses ($\log T_{\rm eff} \gtrsim 4.6$ et $\log (L/L_\odot) \gtrsim 5.2$; Figures 2.1 et 2.5), et montrent de fortes raies d'émissions dans leurs spectres, indiquant la présence d'un vent stellaire intense et optiquement épais. Une étoile WR est le résultat de l'évolution d'une étoile O ayant subi une perte de masse importante par le vent stellaire, révélant d'abord les produits du cycle CNO à la surface, puis les produits du brûlage de l'hélium. Ainsi, sur la base des abondances en surface, les étoiles WR sont classées en trois catégories:

- **WN**: abondances élevées en He et N. Les WNL (WN tardif) ont encore de l'hydrogène en surface ($X_{\rm H} < 0.4$) tandis que les WNE (WN précoce) sont vrai-

ment dépourvues d'hydrogène ($X_{\mathrm{H}} \simeq 0$).

- **WC**: dépourvues d'hydrogène, ayant peu ou pas d'azote, et des abondances élevées en He, C et O (dû au brûlage partiel de l'hélium).
- **WO**: similaires aux étoiles WC mais avec plus d'oxygène en termes d'abondance (dû au brûlage complet de l'hélium).

Seules les étoiles ayant une masse initiale supérieure à une certaine limite peuvent perdre une masse suffisante pour les emmener vers la phase WR. De manière empirique, cette masse initiale minimale se trouve à $\sim 25\mathrm{M}_{\odot}$ pour les étoiles de Population I, ce qui correspond à peu près à la limite de Humphreys–Davidson. Ainsi, quelques étoiles WR sont des post-SGRs tandis que les étoiles de masse initiale plus élevée ont pour progéniteurs des étoiles LBVs (Tableau 2.I).

2.2.4 Explosion supernova

C'est la phase terminale pour la majorité des étoiles massives. Les supernovae sont classifiées comme Type I si elles ne présentent pas d'hydrogène dans leur spectre optique, et Type II dans le cas contraire. Les supernovae de Type I sont à leur tour subdivisées en Ia, Ib, Ic selon qu'il y a du silicium ou de l'hélium, tandis que les supernovae de Type II sont subdivisées selon la forme de leur courbe de lumière.

Les SNIa proviennent de l'explosion thermonucléaire d'une naine blanche, et seuls les autres types de supernovae résultent des effondrements de coeurs d'étoiles massives. Ainsi, dans le deuxième cas, l'effondrement se produit lorsque l'étoile arrive au stade où son coeur est constitué de $^{56}\mathrm{Fe}$, noyau stable dont la fusion ou la fission sont endothermiques. À ce stade, il n'y a plus de source d'énergie pour générer une pression de radiation suffisante pour soutenir les couches supérieures, qui écrasent alors le coeur. Cet effondrement s'effectue sur une échelle de temps de l'ordre de la milliseconde et

s'accompagne d'une émission de neutrinos. L'étoile massive meurt alors et donne naissance, soit à une étoile à neutrons, soit à un trou noir (Heger *et al.* 2003).

2.3 Pourquoi exclusivement les étoiles O?

À ce stade, il est naturel de se demander pourquoi ne considérer que les étoiles de type spectral O, alors que notamment les étoiles dans la phase WR ou les étoiles massives de type spectral B peuvent également être qualifiées de 'chaudes et lumineuses'.

En effet, il serait pertinent de considérer aussi ces deux autres catégories d'étoiles chaudes et lumineuses. Cependant, le problème fondamental avec les étoiles dans la phase WR réside dans leurs vents optiquement épais qui nous empêchent de voir directement leurs photosphères. Avant de se lancer dans le cas plus complexe des étoiles WR, il est judicieux de se pencher d'abord sur le cas 'plus simple' des étoiles O. La situation est renversée pour le cas des étoiles massives de type spectral B: les vents des étoiles B étant beaucoup plus faibles que ceux des étoiles O, il serait moins évident de déceler clairement des liens entre les structures photosphériques et les structures dans les vents des étoiles B. De plus, la recherche des structures photosphériques dans les étoiles O a été rarement faite comparé au cas des étoiles B souvent ciblées par les observations photométriques à haute précision à partir de l'espace (voir plus tard, au Chapitre 4). Bien entendu, le fait que les étoiles O soient plus rares influe aussi sur cette tendance inévitable. Ainsi, en considérant exclusivement les étoiles O ici, dans un certain sens nous nous lançons en territoire quasiment inconnu, rendant ainsi la quête plus intriguante.

3

Structures dans les vents des étoiles O

Comme l'objectif principal de cet effort est de déterminer les éventuelles origines photosphériques des structures dans les vents des étoiles massives de type spectral O, il est avant tout nécessaire de mettre au clair de quelles structures il s'agit et comment elles peuvent se manifester dans la variabilité du vent.

À ce propos, près de quarante ans se sont maintenant écoulés depuis la première découverte de la nature inhomogène des vents des étoiles O (Lucy & White 1980). Il est alors naturel d'imaginer naïvement que, si les inhomogénéités dans le vent ne restent pas statiques, elles pourraient se manifester par une variabilité détectable à travers les comportements temporels de certains profils de raies provenant du vent stellaire. Aussi naïve qu'elle puisse paraître, cette conjecture est loin d'être farfelue. En effet, à ce jour, deux types de structures sont connus comme pouvant contribuer à l'inhomogénéité

des vents des étoiles massives de type spectral O et pouvant se manifester dans la variabilité de leurs vents stellaires. Ces deux catégories de structures sont classées selon leurs étendues spatiales: les inhomogénéités à petite échelle et les structures à grande échelle.

3.1 Inhomogénéités à petite échelle

Il s'agit de petites régions de sur-densité dans le vent stellaire, qui se propagent vers l'extérieur avec le vent global environnant. Ces grumeaux et leur cinématique se manifestent notamment dans les profils des raies d'émission des vents des étoiles massives par la présence de petites bosses (i.e. excès d'émission de quelques % par rapport au profil moyen de la raie) qui se forment de manière aléatoire relativement proche des centres des raies et qui se propagent vers les ailes, avec des temps de vie de l'ordre de quelques heures, comme illustré à la Figure 3.1 (voir aussi Figures 6.20 et 6.21 à la Section 6.5.2.1 du Chapitre 6).

Il est à noter que, grâce au fait que les raies d'émission formées dans les vents des étoiles qui sont dans la phase WR sont beaucoup plus intenses que celles de leurs progéniteurs (essentiellement parce que les vents des étoiles WR sont d'un ordre de grandeur plus intenses que les vents des étoiles O), le grumelage du vent des étoiles massives est un phénomène qui a été détecté pour la première fois dans les vents des étoiles WR (Schumann & Seggewiss 1975, qui ont alors utilisé le terme 'nuages en mouvement' pour décrire les grumeaux en mouvement dans le vent ambiant), et reconnu comme universel pour la première fois dans ces types d'étoiles (Lépine & Moffat 1999). L'aspect grumelé des vents des étoiles O n'a été trouvé qu'un peu plus tard, commençant par l'évocation de la possibilité d'existence de 'blobs' dans le vent de ζ Pup pour expliquer sa luminosité dans le domaine des rayons X (Lucy & White 1980), suivis plus

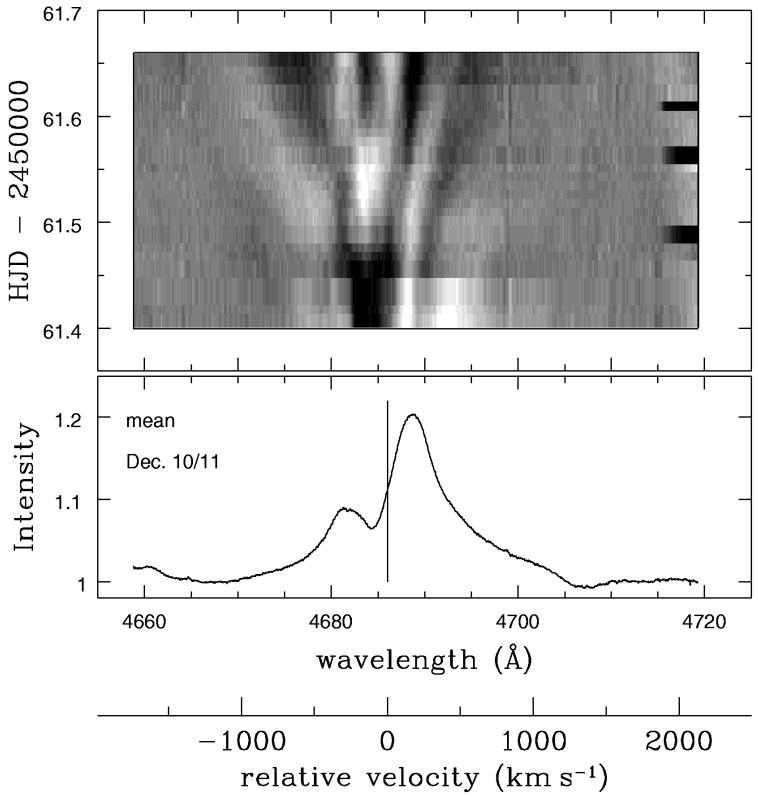

Figure 3.1: Signatures spectroscopiques de la présence de grumeaux dans le vent de l'étoile O clé ζ Puppis, telles que détéctées dans la raie d'émission He II λ4686 générée dans la partie intérieure de son vent. Figure tirée de Eversberg *et al.* (1998).

tard par la détection des signatures des grumeaux à travers le profil de la raie d'émission He II λ4686 de plusieurs étoiles O (Eversberg *et al.* 1998; Lépine & Moffat 2008).

La caractérisation des propriétés des grumeaux dans les vents des étoiles massives – par exemple leurs tailles, leurs formes, leur nombre et leur(s) mécanisme(s) de formation – demeure un sujet de recherche actif. En termes de tailles, formes et nombre, une possibilité que le phénomène de grumelage des vents des étoiles massives s'apparente à de la turbulence compressible a été proposée par Moffat (1994). Dans ce cas, le contraste d'intensité (soit A) des grumeaux et leurs densité de population (soit N) pourraient

suivre des lois de puissance de la taille σ des petites bosses qu'ils génèrent dans les raies d'émission du vent. Par exemple, dans le cas des grumeaux dans les vents des étoiles WR, Lépine *et al.* (1996) ont trouvé $A \sim \sigma^{\alpha}$ et $N \sim \sigma^{\beta}$ tels que $2\alpha + \beta = 2.7 \pm 0.5$ ou 3.4 ± 0.6 selon que les bosses sont modélisées par des petites Gaussiennes ou par des triangles. La discussion sur cette notion de turbulence compressible, notamment sur une idée pour la tester, est reprise à la fin de la Section 6.6 du Chapitre 6.

Quant au mécanisme de formation des grumeaux dans les vents des étoiles massives, deux scénarios prédominent à ce jour. Le premier naît de l'instabilité inhérente aux vents radiatifs, communément appelée 'line-deshadowing instability' (LDI; Lucy & Solomon 1970; MacGregor *et al.* 1979; Owocki & Rybicki 1984). En effet, les analyses numériques de stabilité linéaire des vents radiatifs des étoiles chaudes montrent que de petites perturbations de vitesses dans le vent peuvent générer des chocs inverses intenses qui compriment localement la matière du vent pour former des grumeaux denses et étroits baignant dans des régions inter-grumeaux larges et moins denses (Owocki *et al.* 1988; Dessart & Owocki 2003). Le panneau latéral gauche de la Figure 3.2 illustre la distribution de densité du vent ainsi engendrée dans le plan équatorial de l'étoile. Ce premier scénario à lui seul a permis d'expliquer la formation de grumeaux dans la partie extérieure du vent stellaire ($R \gtrsim 2R_{\star}$), mais ne permet pas d'expliquer le grumelage dès la base du vent stellaire tel que souvent observé chez les étoiles O.

Le deuxième scénario, apparu un peu plus récemment, serait lié à l'existence de la FeCZ (Cantiello *et al.* 2009b). Cette zone serait capable de générer des ondes de gravité et des ondes acoustiques qui pourraient à leur tour exciter aléatoirement la formation de grumeaux dans la partie du vent stellaire juste au-dessus de la photosphère (Figure 3.2, panneau latéral droit). Ce deuxième scénario, qui expliquerait la formation de grumeaux dans la région du vent proche de la photosphère ($R \lesssim 2R_{\star}$), pourrait être considéré comme complémentaire au premier paradigme. Dans ce contexte, Sundqvist &

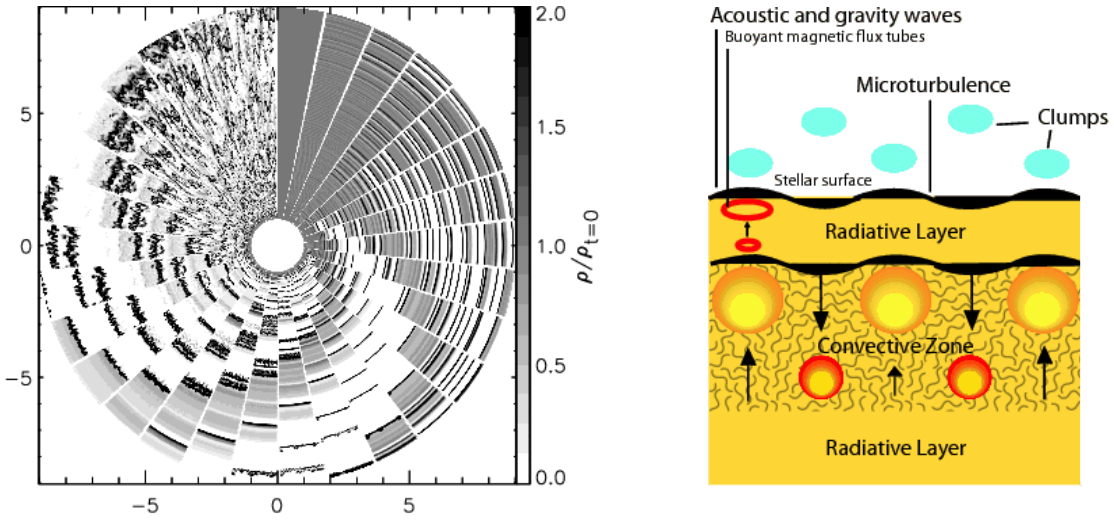

Figure 3.2: *Gauche:* Simulations 2D montrant la distribution de la densité du vent dans le plan équatorial sous l'effet des instabilités du vent radiatif (Figure tirée de Dessart & Owocki 2003). *Droite:* Schéma illustrant la possibilité de formation de grumeaux près de la partie inférieure du vent stellaire, ainsi que d'autres phénomènes, à cause de l'existence d'une zone de convection sub-surfacique dans les étoiles massives. Figure tirée de Cantiello *et al.* (2009b).

Owocki (2013) ont refait les calculs des simulations hydrodynamique du LDI mais cette fois-ci en tenant compte des perturbations photosphériques (qui pourraient provenir de la FeCZ), et ont pu retrouver la formation de grumeaux dès la base du vent stellaire.

Le grumelage des vents des étoiles massives est un phénomène non négligeable dans les études théoriques des phases évolutives des étoiles massives. Par exemple, l'inclusion de ce phénomène a permis de rendre compte que la supposition d'un vent stellaire homogène a pour effet de surestimer les taux de pertes de masse d'au-moins un facteur 3 (Moffat & Robert 1994).

La quantification du degré de grumelage du vent stellaire est donnée par le facteur de grumelage $f_{\rm cl} = <\rho^2>/<\rho>^2$ (ρ étant la densité du vent) ou, de manière équivalente, par le facteur de remplissage $f = f_{\rm cl}^{-1}$. Un vent non grumelé a un facteur $f_{\rm cl} = 1$ et le

grumelage devient considérable pour $f_{\rm cl} > 4$. La valeur de ce facteur de grumelage est encore controversée dans les étoiles O, les propositions allant de $f_{\rm cl} = 5$ (Repolust *et al.* 2004) à $f_{\rm cl} > 10$ (Fullerton *et al.* 2006).

3.2 Structures à grande échelle dans le vent stellaire

L'existence de structures spatialement cohérentes et à grande échelle dans les vents des étoiles O a été initialement proposé vers la moitié des années 80 (Mullan 1986) pour expliquer la formation de petites composantes discrètes et variables en absorption détectées dans les parties en absorption des profils P Cygni des raies de résonance et des raies subordonnées non saturées formant dans les vents des étoiles O.

3.2.1 Composantes discrètes en absorption (DACs)

Historiquement, les observations spectroscopiques d'étoiles OB effectuées dans l'UV avec le satellite *Copernicus* ont été les premières à révéler l'existence de 'composantes étroites en absorption' ('narrow absorption components' – NACs) dans les parties en absorption des profils P Cygni des raies de résonance (par ex.: Si IV, N V) et des raies subordonnées (par ex.: N IV) non-saturées provenant des vents stellaires de ces étoiles (Morton 1976; Snow & Morton 1976; Snow 1977). Ces observations initiales n'ont pas permis de discerner la variabilité de ces NACs. Mais, un peu plus tard, la spectroscopie UV plus intensive de ξ Per conduite par Prinja *et al.* (1987) avec le satellite *International Ultraviolet Explorer (IUE)* a indiqué l'aspect variable des NACs à travers la partie en absorption des profils P Cygni. Ensuite, Prinja (1988) a évoqué la possibilité que les NACs pourraient être des manifestations d'une modulation rotationnelle dans le vent, en se basant sur les observations *IUE* de quatre étoiles O (68 Cyg, ξ Per, 19 Cep, HD 162978), et en remarquant une corrélation entre l'échelle de temps de

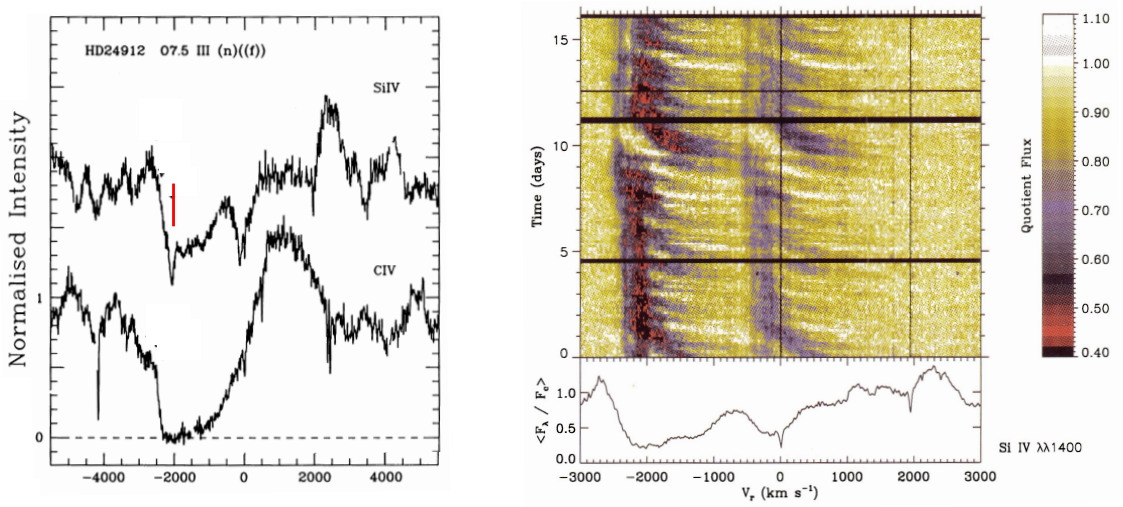

Figure 3.3: *Gauche:* Profils du doublet de la raie de résonance du Si IV $\lambda\lambda$1393, 1402 (non saturé) et de la raie de résonance du C IV λ1548 (saturé) de ξ Per, le trait rouge indiquant une DAC dans le profil P Cygni non saturé du Si IV (Figure tirée de Prinja *et al.* 1990). *Droite*: Évolution temporelle des DACs du doublet de la raie de résonance du Si IV $\lambda\lambda$1393, 1402 de ζ Pup. Figure tirée de Massa *et al.* (1995a).

récurrence des NACs et la vitesse de rotation projetée suivant la ligne de visée ($v \sin i$). Subséquemment, la spectroscopie UV de 203 étoiles O avec *IUE* a révélé la quasi-universalité de la présence des NACs chez les étoiles O (Howarth & Prinja 1989). Des campagnes d'observations de plus en plus intensives de quelques étoiles O clés avec *IUE* ont permis de mieux contraindre les propriétés de ces NACs, qui sont dorénavant dénommés 'composantes discrètes en absorption' ('discrete absorption components' – DACs; Howarth 1992a; Kaper *et al.* 1996; Howarth *et al.* 1995; Kaper *et al.* 1999). Il a ainsi été déduit de ces observations que les DACs:

[i] apparaissent à une vitesse faible près de l'extrémité rouge de la composante en absorption du profil P Cygni, et se propagent vers l'extrémité violette en approchant asymptotiquement la vitesse terminale v_∞ du vent stellaire. Ce mouvement de propagation est cyclique (Figure 3.3);

[ii] sont typiquement larges à leur naissance ($\mathbf{FWHM} \simeq 0.5 v_\infty$) et deviennent plus étroites ($\mathbf{FWHM} \simeq 0.1 v_\infty$) et plus profondes dans leur parcours vers le violet;

[iii] sont telles qu'en général il y en a en moyenne deux par cycle de rotation stellaire.

Ainsi, il est clair d'après ces caractéristiques que la détermination de la vitesse centrale finale d'une DAC peut être exploitée pour obtenir une estimation de la vitesse terminale du vent stellaire (Howarth & Prinja 1989; Prinja *et al.* 1990). Cependant, Prinja *et al.* (1990) ont même montré qu'il est aussi possible d'estimer la vitesse terminale du vent à partir d'un seul spectre UV si l'acquisition des spectres ne se fait pas avec une cadence suffisamment courte ou ne couvre pas assez de cycles de rotations de l'étoile. Dans ce cas, une bonne estimation de la vitesse terminale est:

$$v_\infty = \bar{v}_{\mathrm{DAC}} + \frac{1}{2}\overline{\mathrm{FWHM}}_{\mathrm{DAC}} \tag{3.1}$$

où $\bar{v}_{\mathrm{DAC}}$ et $\overline{\mathrm{FWHM}}_{\mathrm{DAC}}$ sont respectivement la moyenne des vitesses centrales et la moyenne de la largeur à mi-hauteur des DACs présents dans toutes les raies de résonances non saturées dans le spectre (si plusieurs composantes discrètes en absorption sont présents simultanément dans une raie, c'est la composante la plus proche du bord violet du profil P Cygni qui est considérée). Cette approche a été utilisée par Prinja *et al.* (1990) pour estimer v_∞ pour 133 étoiles O et 57 supergéantes de type spectral B0-3 où les DACs sont observables dans leurs profils P Cygni non saturés.

En outre, l'obtention de v_∞ permet aussi de déterminer la loi de vitesse dans le vent stellaire, généralement bien approximée par une loi β pour les étoiles massives (voir Chapitre 2, Équation 2.1).

Les propriétés des DACs telles qu'énoncées donnent déjà des indications concernant les structures physiques qui pourraient les engendrer: des structures cohérentes dans le vent, pouvant s'étendre loin jusqu'à la frontière entre le vent et le milieu interstellaire,

donnant lieu à des variations cycliques et probablement étroitement liées à la rotation stellaire. Ces informations semblent pointer vers une structure particulière: les régions d'interaction en co-rotation ('corotating interaction regions' – CIRs).

3.2.2 Régions d'interactions en corotation (CIRs)

À la base, les CIRs sont des structures à grande échelle observées et bien étudiées en détail depuis longtemps dans le vent solaire (Carovillano & Siscoe 1969; Hundhausen 1972; Pizzo 1978; Crooker *et al.* 1999; Gosling & Pizzo 1999; Broiles *et al.* 2012). En effet, dans la couronne solaire, des portions de plasma peuvent subir des accélérations sous l'influence d'un champ magnétique local. Cela fait apparaître des courants de vitesses différentes dans le vent. De ce fait, des courants rapides du vent solaire peuvent occasionnellement rattraper des courants de vitesses plus lentes devant eux, créant une région de compression dans héliosphère, qui, sous l'effet de la rotation du Soleil, résultent donc en des structures larges en forme de spirales en corotation avec le Soleil: les CIRs (voir figure 1 dans Pizzo 1978).

Mullan (1986) s'était inspiré des CIRs du vent solaire pour étendre ce paradigme aux vents des étoiles OB et notamment suggérer que les DACs émanants des vents de ces étoiles-là pourraient provenir des régions de compressions des CIRs.

Plus tard, Cranmer & Owocki (1996) ont effectué des simulations hydrodynamiques de la formation des CIRs dans les vents des étoiles O. Dans leurs modèles, une perturbation telle qu'une tache claire est appliquée à la surface stellaire. Cette perturbation photosphérique, en corotation avec la surface stellaire, a pour effet d'amplifier localement la force de radiation, et donc aussi la perte de masse, générant une portion de vent qui est plus dense et (donc) moins rapide que le vent environnant. Par conséquent, au fur et à mesure que la perturbation photosphérique est entrainée par la rotation stel-

laire, le courant lent associé dans le vent est vite rattrapé par le vent ambiant moins dense et plus rapide qui se situe juste derrière. Les interactions de ces courants génèrent des chocs et une région de compression de matière dans le vent. Comme dans le cas des CIRs du vent solaire, les bras de CIRs ainsi constitués s'organisent en forme de spirales, dans le fond à cause de la rotation stellaire. Cranmer & Owocki (1996) ont alors trouvé que les DACs sont produites non pas dans la région de compression du CIR comme envisagé par Mullan (1986), mais plutôt par des plateaux de vitesses qui apparaissent dans la région située devant la zone de compression du CIR.

Le panneau latéral gauche de la Figure 3.4 montre une vue dans le plan équatorial de la distribution de densité du vent obtenue dans le modèle de Cranmer & Owocki (1996) en appliquant deux taches claires diamétralement opposées comme perturbations photosphériques. Les taches claires créent donc des courants de densités élevées et de faibles vitesses dans la zone I qui s'étend jusqu'à $\sim 3R_\star$. La partie gauche de la Figure 3.4 montre la propagation des DACs ainsi générées dans la région V. Ce modèle avec des taches claires comme perturbations photosphériques produit des DACs dont les propriétés correspondent bien avec les caractéristiques des DACs déduites des observations. Cranmer & Owocki (1996) ont aussi testé des taches sombres comme perturbations photosphériques, mais les plateaux de vitesses ainsi générés sont trop élevés comparés aux observations. À cet égard, il est important de noter que ces simulations ne font aucune supposition quant à l'origine des perturbations photosphériques impliquées.

Suite aux travaux de Cranmer & Owocki (1996), les propagations et les récurrences des DACs dans les parties en absorption des profils P Cygni des raies de résonance et des raies subordonnées des étoiles O sont considérées comme les signatures spectroscopiques, dans l'UV, de la présence de CIRs au sein de leurs vents. Une demi-douzaine d'années plus tard, Dessart & Chesneau (2002) ont exploré la possibilité que les CIRs se

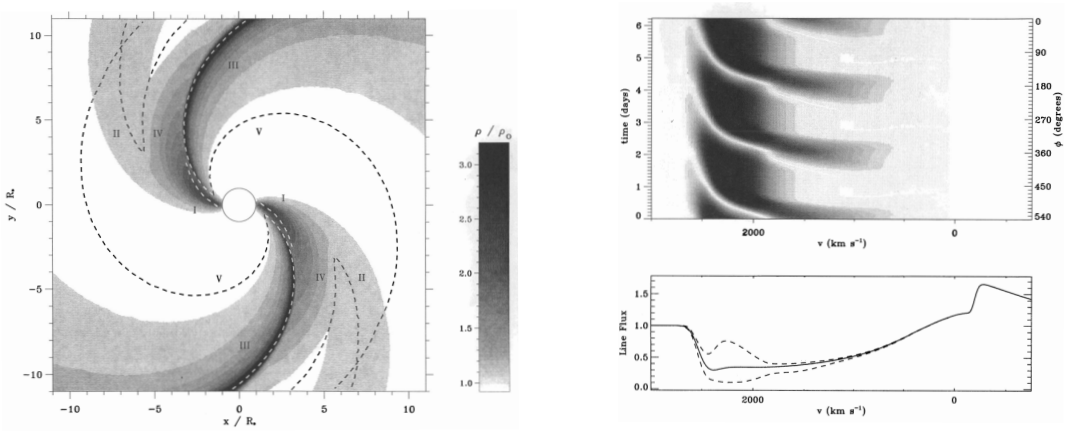

Figure 3.4: Modèles 2D de CIRs de Cranmer & Owocki (1996). *Gauche:* Distribution de densité de matière du vent, normalisée par sa densité à l'état non perturbé. Les différentes régions du vent sont délimitées par des lignes pointillées (voir texte). *Droite*: Propagation des DACs générées par les CIRs montrées sur la figure de gauche, pour un profil P Cygni non saturé. Le panneau du bas montre des exemples de profils instantanés (courbes discontinues) et le profil moyen (courbe continue). Figures tirées de Cranmer & Owocki (1996).

manifestent par des variations dans les raies d'émission du vent stellaire dans le visible. Les signatures spectroscopiques des CIRs y seraient comme celles qui sont illustrées sur la Figure 3.5: cette fois-ci, ce sont vraiment les régions de compressions des bras spiralés des CIRs qui se manifestent par des bosses (excès d'émission) dans la raie, et qui forment des patrons en forme de 'S' dans le spectre dynamique à cause de leur mouvement corotationnel. Une approche de modélisation analytique de telles variations de profils de raies ('line profile variations' – LPVs par la suite), est décrite de manière détaillée à la Section 6.5.1.2.2 du Chapitre 6.

3.3 Influence d'un champ magnétique global

À prime abord, le fait de parler de champ magnétique global pourrait sembler complètement déplacé dans le contexte de l'objectif de ce chapitre dédié au vent stellaire.

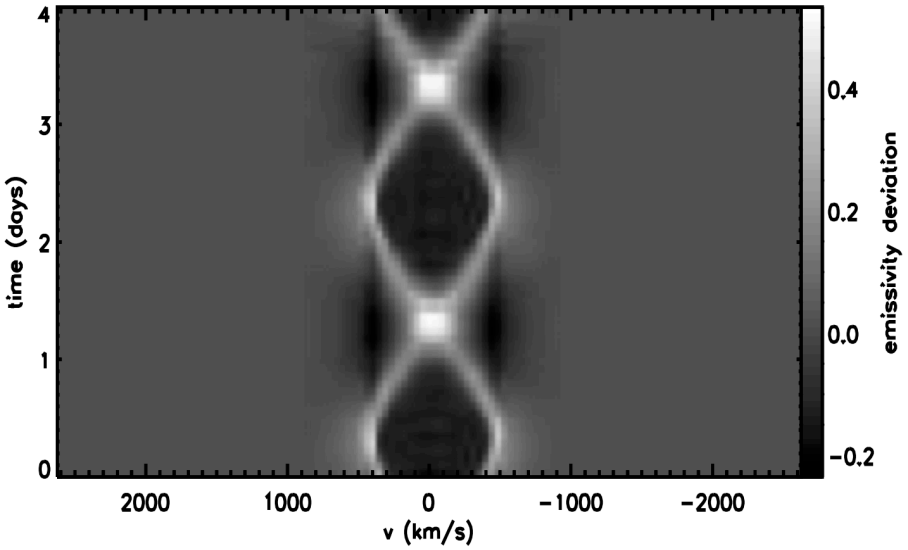

Figure 3.5: Variations du profil d'une raie d'émission d'une étoile O dues à la présence de deux bras de CIRs initialement induites par deux taches diamétralement opposées au niveau de l'équateur stellaire. L'inclinaison de l'étoile est de 20° et la raie est supposée former à $(3 \pm 1)R_\star$. Figure tirée de Dessart & Chesneau (2002).

Pourquoi parler de champ magnétique global ici? Pour deux raisons:

[i] la présence d'un champ magnétique global peut affecter le comportement du vent stellaire et peut même se manifester par des variations de lumière et des variations des profils des raies émises dans le vent;

[ii] il a été suggéré que des champs magnétiques globaux pourraient être à l'origine des DACs.

3.3.1 Champ magnétique global et variabilité du vent stellaire

Les étoiles dotées d'un champ magnétique global peuvent montrer des variations de leurs profils de raies émises dans leurs vents si les lignes de champ sont dans une configuration particulière. C'est en l'occurrence le cas d'un rotateur oblique (Figure 3.6). Initialement

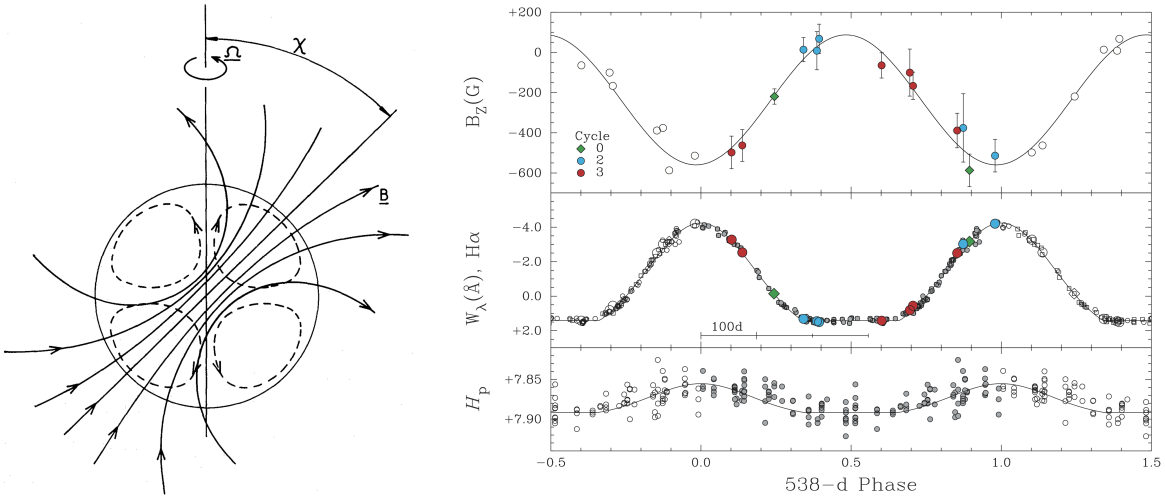

Figure 3.6: *Gauche:* Lignes de champ magnétique (lignes continues) et de circulation méridienne (lignes discontinues) dans le modèle du rotateur oblique (schéma tirée de Moss 1990). *Droite:* Effets de modulations rotationnelles dues à la configuration de rotateur oblique de l'étoile massive de type spectral Of?p HD 191612. Les variations de la composante longitudinale du champ magnétique de l'étoile sont illustrées (panneau du haut), ainsi que les variations de la largeur équivalente de sa raie d'émission Hα (panneau du milieu) et les variations de sa lumière (panneau du bas) telles qu'observées par la mission *Hipparcos (High precision parallax collecting satellite)*. Toutes ces variations sont remises en phase avec la période de rotation de l'étoile qui est de 538 jours (Figure tirée de Wade *et al.* 2011a).

introduit par Stibbs (1950), ce modèle propose que l'axe du champ magnétique soit incliné d'un angle d'obliquité χ par rapport à l'axe de rotation de l'étoile. Dans ce cas, le vent en co-rotation avec l'étoile est confiné dans le champ magnétique. Cela introduit des variations associées à de la modulation rotationnelle dans les raies émanant du vent stellaire. Le profil de raie au complet oscille verticalement à la période de rotation de l'étoile, avec une émission maximale lorsque le pôle magnétique pointe vers la ligne de visée.

Les informations que donnent les caractéristiques des variations de profils de raies

d'un rotateur oblique sont riches. L'information la plus facile à soutirer est la période de rotation de l'étoile, déterminable par l'analyse Fourier des variations de la largeur équivalente des raies émises du vent stellaire. De surcroît, la mesure des variations de la composante longitudinale B_l du champ magnétique permet aussi de déterminer l'angle d'obliquité χ et l'angle d'inclinaison i de l'axe de rotation de l'étoile par rapport à la ligne de visée, vérifiant les relations (Shore 1987):

$$\frac{B_l^{max}}{B_l^{min}} = \frac{\cos(i+\chi)}{\cos(i-\chi)} \tag{3.2}$$

et

$$\cos\frac{\Delta\Phi}{2} = \frac{1}{\tan i \tan\chi} \tag{3.3}$$

où B_l^{max} et B_l^{min} sont les extrema de B_l, tandis que $\Delta\Phi$ est le déphasage entre deux maxima dans les variations des largeurs équivalentes des raies.

Aussi, les variations des largeurs équivalentes des raies permettent de contraindre la symétrie du vent. Par exemple, la présence de minima de différents profondeurs dans les variations de la largeur équivalente implique un vent asymétrique (par exemple le cas de β Cephei; Henrichs *et al.* 2013).

Finalement, la connaissance du taux de perte de masse $\dot{M}$ et de la vitesse terminale du vent v_∞ permet d'estimer la compétition entre le vent stellaire en expansion et le champ magnétique global B. Cela se fait par l'intermédiaire du paramètre de confinement magnétique du vent, généralement noté $\eta_\star$, initialement introduit par ud-Doula & Owocki (2002) qui l'ont formulé comme suit:

$$\eta_\star = \frac{B_{\rm eq}^2 R_\star^2}{\dot{M} v_\infty}, \tag{3.4}$$

traduisant donc le rapport entre la densité d'énergie magnétique et la densité d'énergie

cinétique du vent. Quand $\eta_\star > 1$, le plasma du vent stellaire est canalisé suivant les lignes de champ fermées. Pour un champ global dipolaire, cette situation $\eta_\star > 1$ correspond à un vent stellaire complètement confiné dans une région de rayon caractéristique $R_{\rm Alf} \simeq \eta_\star^{1/4} R_\star$, appelé rayon d'Alfvén et définissant le magnétosphère de l'étoile. Cela dit, Ud-Doula *et al.* (2008) ont trouvé que même à $\eta_\star > 0.1$ le champ magnétique pourrait avoir une influence non négligeable sur le vent stellaire.

3.3.2 Champ magnétique global et DACs

Connaissant les effets potentiels d'un champ magnétique global sur la variabilité du vent et sachant que les DACs sont une forme de variabilité du vent, l'idée que des champs magnétiques globaux pourraient être à l'origine des DACs est loin d'être irréaliste. En effet, la configuration particulière d'un rotateur oblique doté d'un champ magnétique dipolaire global serait un candidat adéquat (Kaper & Henrichs 1994). Cette hypothèse est même renforcée par le fait que la plupart des étoiles O connues comme abritant un champ magnétique global ont la configuration d'un rotateur oblique avec un champ magnétique dipolaire (voir revue par Wade & Collaboration MiMeS 2015).

Cependant, David-Uraz *et al.* (2014) ont exploré en détail cette possibilité, en tentant de chercher des champs magnétiques dans 13 étoiles O clés dont les propriétés des DACs sont relativement bien connues. Ils n'ont pu détecter de champ magnétique dans toutes ces étoiles, mais les limites supérieures qu'ils trouvent ont 95.4% de chances de correspondre à $\eta_\star < 1$ et 68.3% de chance de correspondre à $\eta_\star < 0.1$ (voir leur Figure 5), indiquant que les champs magnétiques dipolaires globaux de ces étoiles (si elles en ont) seraient trop faibles pour influer significativement sur le comportement du vent. En d'autres termes, les DACs ne peuvent pas être dues à des champs magnétiques dipolaires globaux, ce qui corrobore le scénario de leur génération par la présence de

structures à grande échelle dans le vent stellaire, elles-mêmes pouvant être engendrées ultimement par la présence de perturbations photosphériques (Cranmer & Owocki 1996; David-Uraz *et al.* 2017).

4

Structures photosphériques chez les étoiles O

Avant de se lancer dans la quête des éventuelles sources photosphériques des structures dans les vents des étoiles massives de type spectral O évoquées précédemment, il est judicieux de faire au préalable l'inventaire des structures photosphériques que ces étoiles peuvent présenter, ce qui fait l'objectif de ce chapitre. Il ne s'agit pas du tout ici de se forger des idées préconçues, mais de faire l'état de l'art de nos connaissances actuelles sur les variétés de structures qui peuvent être présentes au niveau de la photosphère des étoiles O et les variabilités qu'elles peuvent engendrer. Il va sans dire que ces différentes structures se doivent d'être décrites séparément, bien qu'elles peuvent être évidemment physiquement présentes simultanément à la photosphère, de même que des structures à petite et à grande échelle peuvent cohabiter dans le vent stellaire.

4.1 Oscillations stellaires non-radiales

Les pulsations non-radiales ('non-radial pulsations' – abrévié 'NRPs' par la suite) constituent une catégorie importante de structures pouvant être présentes à la surface d'une étoile massive de type spectral O. À ce propos, il est naturel de vouloir savoir en quoi consistent ces NRPs (Section 4.1.1), comment elles se manifestent (Section 4.1.4), et comment elles permettent de contraindre les propriétés stellaires (Section 4.1.5).

4.1.1 Modes normaux d'oscillations stellaires

Les premières observations d'étoiles pulsantes remontent à plus de deux siècles, avec les détections des variations de lumière de η Aquilae A (F6Iab) rapportées par Pigott (1785) et celles de δ Cephei A (F5Iab:) rapportées par Goodricke (1786), bien que les natures pulsantes de ces étoiles ont été sujettes à un long débat jusqu'aux prémices des théories des pulsations stellaires conduites par Eddington (1917, 1918, 1919) éliminant pour de bon les possibilités de la rotation, de la binarité, et des structures nébuleuses circumstellaires comme origine des variations observées. Ces deux étoiles sont maintenant considérées comme les prototypes d'une classe d'étoiles pulsantes particulière, les Céphéides, montrant des oscillations radiales dominantes, c'est-à-dire subissant périodiquement des contractions et des expansions radiales au cours desquelles la symétrie sphérique est préservée. Ainsi, de tels types d'oscillations stellaires *ne peuvent pas* être considérées comme correspondant à des structures à la photosphère (parce que c'est toute l'étoile qui grossit et rétrécit périodiquement), et ne peuvent induire ni des grumeaux (générés de manière stochastique) ni des CIRs (qui sont des structures sphériquement asymétriques) dans les vents des étoiles O. Ainsi, si des pulsations à la surface stellaire étaient à l'origine de ces structures dans le vent, elles seraient nécessairement des NRPs. Les raisons pour lesquelles j'aborde la notion de pulsation stellaire

par cette petite historique sur les oscillations radiales des Céphéides sont que, d'une part leurs modes d'oscillation sont les plus simples à imaginer et sont les plus 'simples' qu'une étoile peut montrer, et d'autre part ça donne un bon aperçu de comment la théorie des pulsations stellaires a pris naissance.

Qu'elles soient radiales ou non, les pulsations stellaires sont les modes normaux de vibrations en trois dimensions d'une étoile, grossièrement analogues aux oscillations en une dimension d'une corde de guitare, aux oscillations en une dimension de l'air dans les tuyaux d'une flûte de Pan, ou encore aux modes normaux de vibrations de la membrane d'un djembe. Cependant, dans ces trois derniers cas, le milieu de propagation (corde, air, membrane) est homogène, c'est-à-dire que les modes normaux d'oscillations sont les solutions de l'équation d'onde classique sous les contraintes imposées par les conditions aux frontières: des ondes acoustiques se propageant à la vitesse du son $c_s = \omega/k$ (ω étant la fréquence angulaire et k le nombre d'onde), qui est une constante caractéristique du milieu homogène. Les intérieurs des étoiles, au contraire, sont évidemment fortement inhomogènes, et les équations impliquées pour l'étude de leurs comportements oscillatoires sont les trois équations fondamentales de l'hydrodynamique appliquées à un élément de fluide stellaire en présence de la gravité (Cox 1980; Aerts *et al.* 2010):

$$\text{l'équation du mouvement:} \qquad \rho\left(\frac{\partial}{\partial t} + \vec{v}\cdot\vec{\nabla}\right)\vec{v} = -\vec{\nabla}P - \rho\vec{\nabla}\Phi, \tag{4.1}$$

$$\text{l'équation de continuité:} \qquad \frac{\partial\rho}{\partial t} + \vec{\nabla}\cdot(\rho\vec{v}) = 0, \tag{4.2}$$

$$\text{l'équation de Poisson:} \qquad \nabla^2\Phi = 4\pi\rho G, \tag{4.3}$$

où ρ est la densité, P la pression, $\vec{v} = \vec{v}(\vec{r},t)$ la vitesse du fluide et Φ le potentiel gravitationnel relié à la gravité par $\vec{g} = -\vec{\nabla}\Phi$.

Une perturbation infinitésimale $\vec{\xi}(r,t)$ est alors introduite dans ce modèle statique.

La résolution de ce problème au complet sous son aspect non-linéaire n'est pas encore faisable. En général, le traitement théorique se fait en linéarisant les équations de l'état perturbé, c'est-à-dire en considérant des perturbations sinusoïdales et de très faible amplitude par rapport aux échelles caractéristiques de l'étoile.

D'une manière générale, tant que la question de la stabilité des modes n'est pas abordée, les calculs précis des fréquences d'oscillations peuvent être effectués dans l'approximation adiabatique, consistant à supposer qu'il n'y a pas d'échanges de chaleur entre les éléments de matière et leur environnement lors d'un cycle de pulsation. Sous cette approximation, et en supposant en plus que les effets de la rotation, du champ magnétique et du vent stellaire sont négligeables par rapport à ceux des oscillations, le vecteur déplacement de l'élément de fluide en coordonnées sphériques s'exprime par (Aerts *et al.* 2010):

$$\boldsymbol{\delta\vec{r}} = \sqrt{4\pi} \cdot \Re \left\{ \left[\xi_r(r) Y_l^m(\theta,\phi)\vec{\boldsymbol{a}}_{\boldsymbol{r}} + \xi_h(r) \left(\frac{\partial Y_l^m}{\partial\theta}\vec{\boldsymbol{a}}_{\boldsymbol{\theta}} + \frac{1}{\sin\theta}\frac{\partial Y_l^m}{\partial\phi}\vec{\boldsymbol{a}}_{\boldsymbol{\phi}} \right) \right] \exp\left(-i2\pi\nu t\right) \right\}, \qquad (4.4)$$

où ξ_r et ξ_h sont les déplacements radial et horizontal, ν la fréquence d'oscillation et $Y_l^m(\theta,\phi)$ la notation standard pour les harmoniques sphériques:

$$Y_l^m(\theta,\phi) = (-1)^m \sqrt{\frac{2l+1}{4\pi}\frac{(l-m)!}{(l+m)!}} P_l^m(\cos\theta)\exp(im\phi), \qquad (4.5)$$

les $P_l^m(\cos\theta)$ représentant les polynômes de Legendre. Le degré l (entier naturel) de l'harmonique sphérique représente le nombre de surfaces nodales, tandis que l'ordre azimutal m (entier relatif dans l'intervalle $[-l;+l]$) est tel que $|m|$ correspond au nombre de surfaces nodales qui forment des lignes de longitudes à la surface stellaire. Vu qu'il s'agit d'un problème à trois dimensions, il y a un troisième nombre quantique qui est ici l'ordre radial n, spécifiant le nombre de noeuds dans la direction radiale.

Les modes radiaux sont ceux pour lesquels $l = 0$. Comme évoqué tantôt, c'est le mode de pulsation usuel retrouvé dans les Céphéides (et les pulsateurs de type RR Lyrae; Smith 2004). Ce sont les modes de degré $l \geq 1$ qui correspondent à des pulsations non-radiales. En outre, concernant l'ordre azimuthal m, la présence du terme en $\exp(im\phi)$ dans les harmoniques sphériques $Y_l^m(\theta, \phi)$ fait que le vecteur déplacement de l'équation 4.4 a ultimement une dépendance en $\exp[-i(2\pi\nu t - m\phi)]$. Cela est particulièrement intéressant parce que ça indique que les modes tels que $m = 0$ sont des ondes stationnaires, tandis que les modes pour lesquels $m \neq 0$ correspondent à des ondes progressives: pour $m > 0$ les oscillations se propagent dans le sens de rotation de l'étoile (modes prograde) tandis que pour $m < 0$ la propagation se fait en sens inverse de la rotation de l'étoile (modes rétrogrades).

Toujours dans le thème de la catégorisation, les modes normaux d'oscillations stellaires peuvent être classés en deux principaux types: les modes p et les modes g. Une manière de comprendre en quoi ces deux modes sont spécifiques est d'aller puiser dans deux types de perturbations que peuvent subir un élément de fluide stellaire au repos au sein d'une étoile: d'une part une légère compression, et d'autre part un léger déplacement (par exemple vers le haut). En effet, dans la situation où la perturbation sur l'élément de fluide consiste en une compression (Figure 4.1, panneau du haut), il est naturel, en vertu de la troisième loi de Newton, de s'attendre à ce qu'une force de rappel s'opposant à cette compression se crée. Cette force en question est proportionnelle au contraste de densité entre l'élément de fluide et son milieu environnant, c'est-à-dire proportionnelle au gradient de pression. C'est grâce à cette force de rappel que, après décompression, l'élément de fluide va naturellement subir des oscillations en volume – et donc en densité et pression – autour de son état d'équilibre initiale. Ces oscillations, qui définissent alors la catégorie des modes p ('p' pour pression), s'effectuent à une

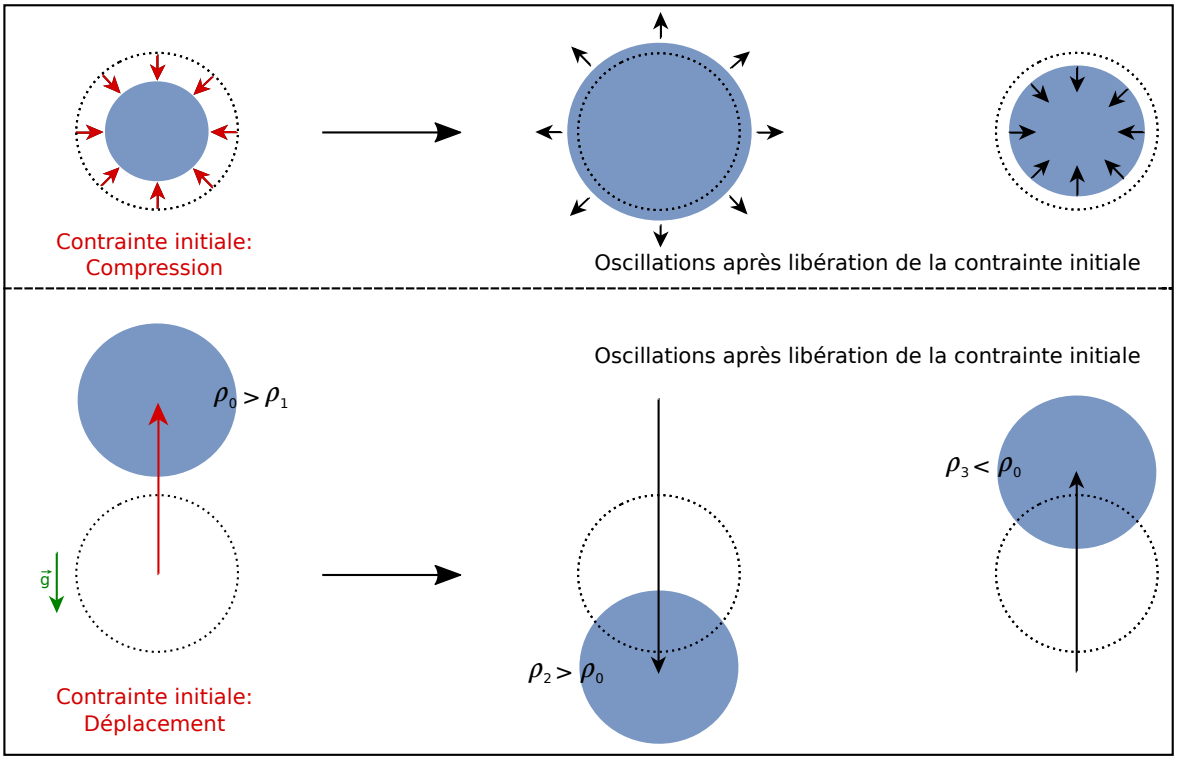

Figure 4.1: Schématisation des deux principaux types de perturbations pouvant être subites par un élément de fluide stellaire: une compression (*panneau du haut*; résultant aux modes de pression) et un déplacement vertical (*panneau du bas*; résultant aux modes de gravité). Les lignes pointillées indiquent l'état d'équilibre.

fréquence caractéristique, la fréquence de Lamb (1909):

$$L_l^2 = \frac{l\,(l+1)}{r^2} c_S^2, \tag{4.6}$$

où $c_s = \Gamma_1 P/\rho$ est la vitesse du son adiabatique locale, dont l'expression fait intervenir l'exposant adiabatique Γ_1, défini par:

$$\Gamma_1 = \left(\frac{\partial \ln P}{\partial \ln \rho}\right)_{\rm ad}. \tag{4.7}$$

La deuxième situation où la perturbation consiste en un déplacement de l'élément de fluide vers le haut (Figure 4.1, panneau du bas) revient à le mettre dans un milieu moins dense (dans une étoile, globalement la densité décroît en fonction de la distance par rapport au centre de l'étoile). L'élément de fluide, alors plus lourd que son milieu ambiant, va tendre à revenir vers sa configuration d'équilibre initiale sous l'action de la gravité. Quand il est lâché de sa position perturbée, les rapports de forces entre son poids et la poussée d'Archimède le font osciller autour de sa position d'équilibre à une fréquence caractéristique qui est la fréquence de Brunt-Väisälä:

$$N^2 = g\left[\frac{1}{\Gamma_1}\frac{d\ln P}{dr} - \frac{d\ln\rho}{dr}\right], \tag{4.8}$$

qui dépend des conditions physiques locales au point d'équilibre. De telles oscillations forment les modes g ('g' pour gravité).

Il va sans dire que les effets de la pression et ceux de la gravité ne peuvent pas être rigoureusement séparés complètement. De ce fait, les fréquences d'oscillations des modes dépendront à la fois des profils de la fréquence de Lamb et de la fréquence de Brunt-Väisälä dans l'intérieur stellaire. C'est ainsi qu'il est souvent dit que les modes normaux de vibrations stellaires correspondent essentiellement à des ondes sismiques de type gravito-acoustique qui se propagent au sein des étoiles.

4.1.2 Mécanismes d'excitation des modes

Pour maintenir les oscillations stables à l'intérieur de l'étoile, il faut qu'il y ait des mécanismes particuliers apportant régulièrement de l'énergie aux oscillations stellaires. Parmi de tels mécanismes, les plus importants connus jusqu'à présent sont le mécanisme κ, le mécanisme ϵ, le mécanisme d'excitation stochastique, et le mécanisme de génération des modes dites 'étranges'.

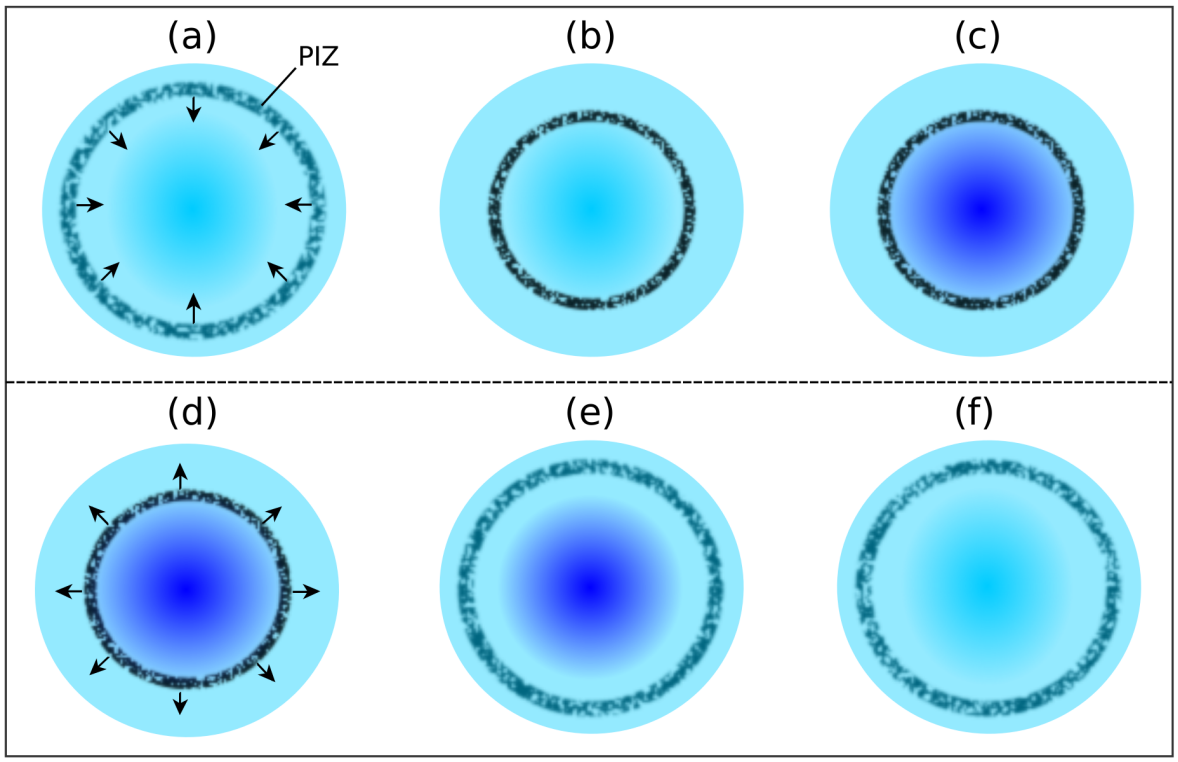

Figure 4.2: Schématisation du mécanisme κ. Voir texte pour la description.

4.1.2.1 Le mécanisme κ

Comme son nom l'indique, ce mécanisme est étroitement lié aux comportements de l'opacité dans des régions très particulières de l'intérieur stellaire. Ces zones bien spécifiques ne sont autres que les zones d'ionisations partielles ('partial ionization zones' – PIZs par la suite) d'éléments abondants décrites à la Section 2.1.2 du Chapitre 2: par exemple celle de l'ionisation partielle du Fer à $T \simeq 170$ kK, ou encore celle de la deuxième ionisation partielle de l'helium à $T \simeq 50$ kK. Qu'est-ce que ces zones ont de si particulier en terme du comportement de l'opacité? En général, la dépendance de

l'opacité sur la densité et la température suit la loi d'opacité de Kramers:

$$\kappa \propto \rho T^{-3.5}. \tag{4.9}$$

Cela veut dire qu'en général, lorsqu'un élément de fluide stellaire subit une compression, même si sa température et sa densité tendent à augmenter, son opacité va diminuer à cause de la forte dépendance sur la température. Par contre, quand une PIZ subit une compression, cela génère de l'énergie qui va permettre d'ioniser plus de particules au lieu de faire augmenter la température. Puisque la température de la PIZ varie très peu tandis que sa densité augmente lors de la compression, cela correspond inévitablement à une augmentation de son opacité (Figure 4.2, panneaux (a) et (b)). Il s'ensuit que la radiation provenant des couches sous-jacentes est bloquée, provoquant un réchauffement et une augmentation de la pression de ces couches sous-jacentes (Figure 4.2, panneau (c)). Ce comportement tend alors à repousser la PIZ vers l'extérieur (Figure 4.2, panneau (d)). Sous cet effet, cette dernière subit une expansion, pendant laquelle de l'énergie est de nouveau produite par la recombination des ions avec les électrons de la PIZ (Figure 4.2, panneau (e)). Donc dans cette phase d'expansion, la température dans la PIZ varie très peu, mais la densité quant à elle diminue. Par conséquent, l'opacité de la PIZ diminue, et la radiation provenant des couches sous-jacentes peut s'échapper à travers la PIZ (Figure 4.2, panneau (f)). À leur tour, la pression dans les couches sous-jacentes diminue, et la PIZ va tendre à nouveau à s'affaisser, et le cycle recommence. Ce processus, dénomé 'mécanisme κ', est ainsi souvent considéré comme l'analogue d'une machine thermique, où le rôle de la vapeur est pris par la radiation, le pistion est joué par la PIZ, et la valve est représentée par le comportement de l'opacité.

4.1.2.2 Le mécanisme ϵ

Ce mécanisme est lié à la perturbation du taux de réactions nucléaires ϵ. Les seuls cas où, potentiellement, ce mécanisme pourrait produire des instabilités vibratoires correspondent à des phases évolutives avancées dans lesquelles le brûlage nucléaire se produit en couche. À ce jour, aucune étoile pulsante n'a été recensé dont le mode d'excitation se fait seulement par ce mécanisme.

4.1.2.3 Le mécanisme d'excitation stochastique

Dans ce cas, des modes de pulsation sont excités par de l'énergie générée stochastiquement. Comment y parvenir? Une manière de générer de l'énergie de manière aléatoire dans une étoile est par les mouvements des cellules convectives dans les zones où le transport d'énergie peut se faire par convection. Notamment, dans les étoiles à enveloppe convective, les mouvements turbulents des cellules convectives s'avèrent être efficace pour créer stochastiquement de l'énergie acoustique déposée proche de la photosphère et induire des oscillations à durées de vies finies (Stein 1968; Goldreich & Keeley 1977). C'est le mécanisme généralement accepté comme responsable des pulsations observées dans le Soleil et dans les pulsateurs de type solaire montrant des modes p à durées de vies finies (Houdek 2006).

Dans ce même contexte, les ondes de gravité internes constituent aussi des exemples d'oscillations excitées de manière stochastique. Les ondes de gravité sont des phénomènes très communs. Il y en a plusieurs manifestations sur la Terre: les vagues (ondes de gravité de surface), les nuages de type altostratus undulatus, les ondes se propageant dans différentes couches océaniques à fortes gradients de salinité (ondes de gravité internes). Il serait même envisageable de créer des ondes de gravité internes dans un cocktail black velvet... En effet, en général les ondes de gravité se forment

dans un milieu stratifié où il y a un gradient de densité verticalement: si une perturbation de type 'déplacement' (comme décrite à la Section 4.1.1) s'applique à une partie de fluide dans le milieu, celle-ci va subir des oscillations à cause des rapports de forces entre son poids et la poussée d'Archimède. Cela est donc bien envisageable aussi dans une étoile où il y a un gradient de densité relativement important. Dans ce cas, des ondes de gravité internes seraient initiées et excitées au niveau de l'interface entre une zone convective et une zone radiative où les perturbations stochastiques (mais permanentes) pourraient être causées par des tourbillons de turbulences dans la zone convective proche de l'interface (Kumar *et al.* 1999), et/ou des dépassements convectifs sous formes de panaches (Ansong & Sutherland 2010; Rogers & MacGregor 2011). Dans le cas des étoiles à coeur convectifs et enveloppes radiatives, Rogers *et al.* (2013) ont testé ces deux types de mécanisme et ont trouvé entre autres que la contribution des deux expliquerait le comportement à basses fréquences des spectres en amplitudes des oscillations, tandis que le comportement à hautes fréquences serait plutôt dominé par l'excitation par les dépassements convectifs sous formes de panaches.

4.1.2.4 Les modes de pulsations 'étranges'

Comme leur nom l'indique, les modes qualifiés d''étranges' sont des modes qui apparaissent de manière inattendue dans les spectres de fréquences d'oscillations stellaires. Ils apparaissent dans les analyses théoriques de la stabilité non-linéaire adiabatique des modes de pulsations dans les étoiles près de la limite d'Eddington. Il a été proposé que l'apparition de ces modes pourrait être étroitement liée à un phénomène d'inversion de densité au sein d'une zone de convection sub-surfacique, auquel s'ajouterait la dominance de la pression de radiation liée au fait que l'étoile se trouve près de la limite d'Eddington (Glatzel & Kiriakidis 1993; Glatzel 2009; Saio 2009). Dans le cas des

étoiles massives, les phases concernées seraient donc les phases supergéantes, WR et les étoiles LBVs.

4.1.3 Zones d'instabilité dans le diagramme H–R

La Figure 4.3 résume les zones d'instabilité liées aux oscillations stellaires prédites à ce jour dans la partie haute du diagramme H–R:

[i] les modes p de degré $l = 0 - 2$ typiques des pulsateurs de type β Cep qui sont des étoiles typiquement de type spectral B0-2 V-III, de masse $7-20 M_{\odot}$, oscillant à des modes p non-radiales de périodes de l'ordre de $2 - 6$ h (Stankov & Handler 2005) excités via le mécanisme κ opérant dans la PIZ du fer à $T \simeq 170$ kK (Dziembowski & Pamyatnykh 1993; Gautschy & Saio 1993; Pamyatnykh 1999);

[ii] les modes g d'ordre $l = 1-2$ rencontrés généralement dans les étoiles B à pulsation lentes ('slowly pulsating B stars' – SPBs), excités par le mécanisme κ associé au pic d'opacité du fer à $T \simeq 170$ kK (Dziembowski *et al.* 1993; Pamyatnykh 1999) et dont les périodes sont de l'ordre de $0.8 - 3$ d;

[iii] les modes d'oscillations étranges.

Il faut noter l'ouverture large de la zone d'instabilité des modes d'oscillations des variables de type β Cep vers la partie haute du diagramme H–R. Cette ouverture pourrait être à l'origine de la détection de cette catégorie de pulsations dans quelques étoiles O tardives (voir Section suivante).

4.1.4 Observations des pulsations chez les étoiles O

Tout d'abord, comment se manifestent les pulsations dans la variabilité intrinsèque d'une étoile? En photométrie, elles se manifestent par des variations (multi-)périodiques de la lumière, constituée alors de superpositions de sinusoïdes (Figure 4.4, panneau

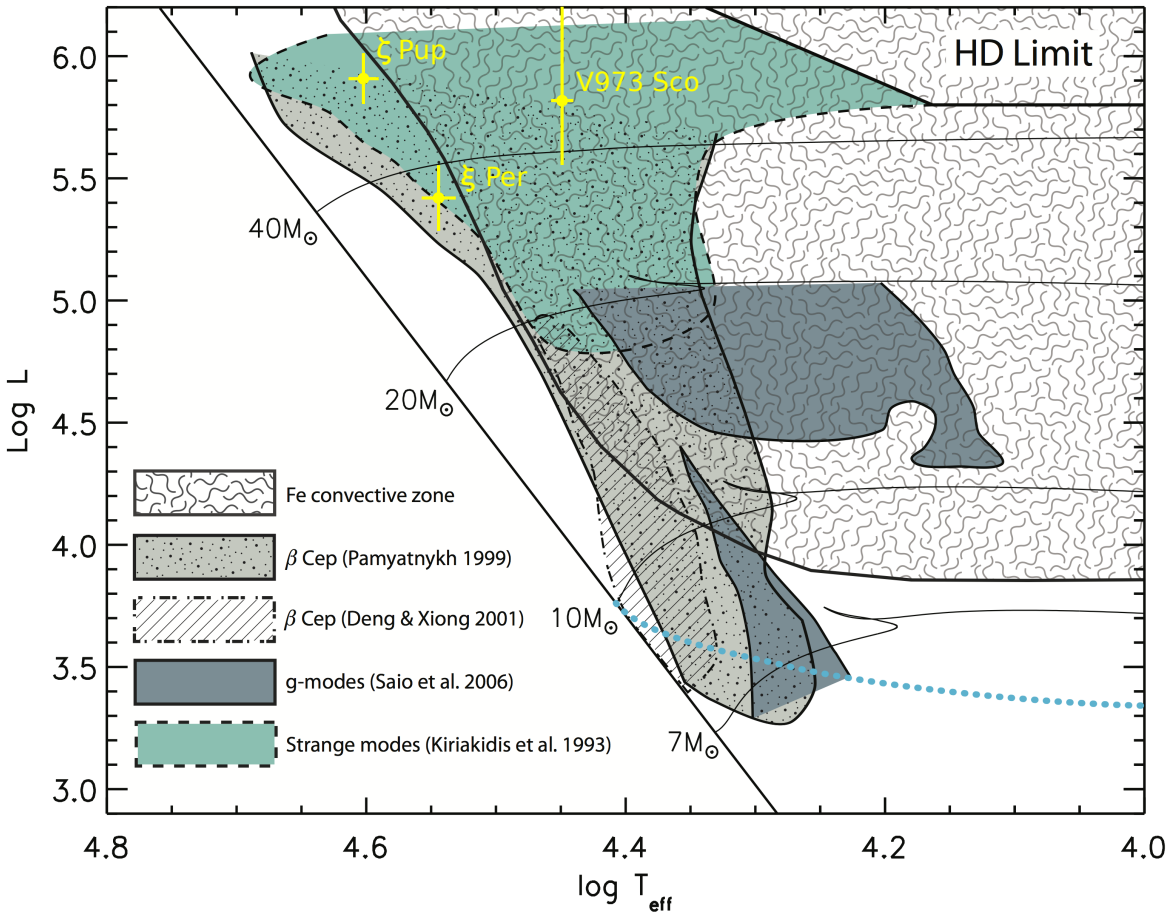

Figure 4.3: Compilation des zones d'instabilités oscillatoires théoriques dans la partie haute du diagramme H–R faite par Cantiello (2009). Schématisées sur cette figure sont la zone d'instabilité des pulsations de type β Cep [grise], celle des modes g de degré $l = 1 - 2$ typiques des SPBs [bleue-grise], et la zone où les modes étranges sont prédits d'apparaître [verte]. Les trois étoiles clés considérées dans ce projet de recherche y sont aussi marquées. La région du diagramme H–R où la FeCZ peut avoir lieu se situe au-dessus de la ligne bleue pointillée, tandis que la zone brouillée indique les régions d'apparition du FeCZ telles que les vitesses des cellules convectives dépassent 2.5 km s^{-1}. Figure tirée de Cantiello (2009).

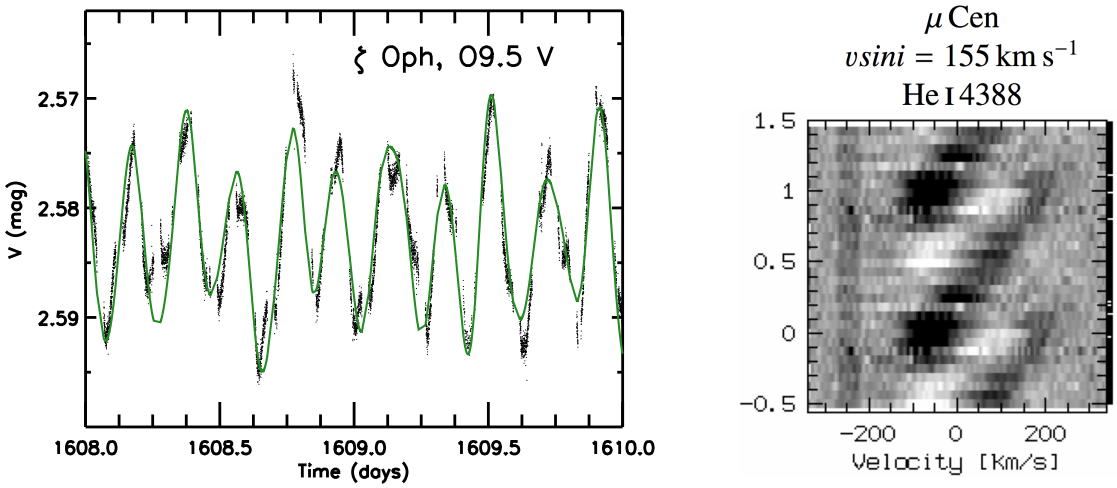

Figure 4.4: *Gauche:* Courbe de lumière *MOST* du pulsateur de type β Cep ζ Ophiuchi (O9.5V) (Adaptée de Walker *et al.* 2005). *Droite:* Variations de profils de raies photosphériques de l'étoile μ Centauri (B2Ve) attribuées à des pulsations non-radiales. Figure tirée de Rivinius *et al.* (2003).

latéral gauche). En spectroscopie, les pulsations non-radiales se révèlent par des LPVs des raies photosphériques, caractérisées par des bosses qui se propagent du côté bleu vers le bord rouge de la raie (Figure 4.4, panneau latéral droit) pour des modes prograde, et dans le sens inverse pour les modes rétrogrades. L'angle d'inclinaison i de l'étoile par rapport à la ligne de visée a évidemment une influence dans le comportement de la propagation de ces bosses: un mode peut se manifester par des bosses qui se propagent dans les deux sens si l'inclinaison de l'étoile par rapport à la ligne de visée est relativement petite.

L'analyse Fourier de ces variations permet d'extraire les périodes, les amplitudes apparentes et les phases relatives des modes détectés. De ces trois quantités, les périodes contiennent l'information la plus complète quant à la structure globale et interne de l'étoile en question (voir Section 4.1.5).

Les pulsations dans les étoiles massives de type spectral O sont moins bien établies par rapport à celles des étoiles B. Parmi les premiers efforts de suivis photométriques d'un grand nombre d'étoiles O à partir du sol figurent celui de Balona (1992), révélant aucuns signes clairs de pulsations mais seulement des variations de luminosité de faibles amplitudes qui ne sont pas toujours périodiques. Jusqu'à présent, les campagnes d'observations photométriques à relativement longs termes ont recensé seulement environ une dizaine d'étoiles O qui présentent des pulsations stables probablement excitées via le mécanisme κ lié au pic d'opacité du fer à $T \simeq 170$ kK (De Cat *et al.* 2007; Pigulski & Pojmański 2008; Rauw *et al.* 2008; Walker *et al.* 2005; Briquet *et al.* 2011; Buysschaert *et al.* 2015). La plupart de ces pulsateurs sont des étoiles O tardives, probablement à cause de l'extension de la bande d'instabilité des variables de type β Cep dans cette zone (Figure 4.3). Les périodes de pulsations les mieux établies sont attribuées à l'étoile O9.5V ζ Oph (Figure 4.4), pour laquelle les observations photométriques à haute précision à partir de l'espace avec les missions *MOST* (*Microvariability and Oscillations of STars*; Walker *et al.* 2003; Matthews *et al.* 2004), *WIRE* (*Wide-field InfraRed Explorer*; Buzasi 2000) et *Coriolis/SMEI* (*Coriolis/Solar Mass Ejection Imager*; Eyles *et al.* 2003) ont détecté une douzaine de périodes d'oscillations non-radiales de type β Cep allant de 2 à 20 h (Walker *et al.* 2005; Howarth *et al.* 2014).

Toujours dans le thème de la photométrie à haute précision menée à partir de l'espace, la mission *CoRoT* (*Convection, Rotation et Transits planétaires*; Baglin *et al.* 2006; Auvergne *et al.* 2009) a étudié la variabilité de six étoiles O dans l'amas ouvert NGC 2244 et dans une association d'étoiles OB, Mon OB2 (Degroote *et al.* 2010b; Blomme *et al.* 2011; Briquet *et al.* 2011; Mahy *et al.* 2011), tandis que la mission *Kepler* (Borucki *et al.* 2010) n'a observé qu'une étoile O (HD 188209; Aerts *et al.* 2017). Ces observations ont mené à des résultats particulièrement intéressants dans les sens où elles ont révélé

des cas de NRPs probablement excitées de manière stochastique chez les étoiles O, à savoir des modes p à durées de vies finies (HD 46149; Degroote *et al.* 2010b) et des modes g à durées de vie finies qualifiés d'ondes de gravité internes (HD 46223, HD 46150, HD 46966 et HD 188209; Blomme *et al.* 2011; Aerts & Rogers 2015; Aerts *et al.* 2017).

En spectroscopie, les observations des variations de profils de raies photosphériques les plus aptes à être qualifiées de NRPs sont très rares. Plus exactement, il n'y en a que trois cas: celui de ζ Pup pour laquelle une possibilité de NRPs de degré $l = 2$ et d'ordre azimuthal $m = -2$ oscillant à la période de 8.54 ± 0.05 h a été rapporté par Reid & Howarth (1996); et ceux de ξ Per et λ Cep pour lesquelles des NRPs de degrés respectivement $l = 3$ (avec une période de $P = 3.5$ h) et $l = 3, 5$ (avec des périodes de $P = 12.3$ h et $P = 6.6$ h) ont été rapporté par de Jong *et al.* (1999).

Un petit tour chez les étoiles au stade LBV: leurs variabilités photosphériques sont très diverses (voir revue effectuée par van Genderen 2001), mais des possibilités d'existence de pulsations ne sont pas complètement exclus. Des variations de lumière d'amplitudes inférieures à 0.1 mag s'effectuant sur des échelles de temps de l'ordre de quelques jours à quelques semaines chez les étoiles dans la phase LBV s'avèrent être similaires à celles observées dans les supergéantes chaudes et pourraient être liées à des oscillations stellaires. Des modes g ont été proposés comme causes de ces variations dans les étoiles LBVs (Lamers *et al.* 1998), bien qu'une possibilité de modes étranges a aussi été évoquée (Saio *et al.* 2013). À ce propos, il est à remarquer que la Figure 4.3 montre que théoriquement les modes étranges pourraient affecter les étoiles O, bien que jusqu'à présent il n'existe aucune preuve observationnelle confirmant cette possibilité. Ce qui est sûr c'est que, à ce jour, les pulsations dans les étoiles LBVs restent encore très peu connues au niveau observationnel. Même du point de vue théorique, le fait qu'elles se situent près de la limite d'Eddington introduit beaucoup d'incertitudes sur les prédic-

tions de leurs oscillations et leurs effets sur la perte de masse et les éruptions.

Pour couronner le recensement des observations des pulsations chez les étoiles O, des possibilités d'oscillations induites par effets de marée ont été rapportés dans certaines étoiles O impliquées dans des systèmes multiples. Il s'agit des cas de δ Ori Aa, ι Ori et η Car (Pablo *et al.* 2015, 2017; Richardson *et al.* 2018). Évidemment, si des pulsations étaient à l'origine des structures dans les vents des étoiles O, ce ne serait *sûrement pas exclusivement* ces genres d'oscillations induites par effets de marée, tout simplement parce que les structures dans les vents des étoiles O se retrouvent aussi dans les étoiles O simples (et en cavale) telles que ξ Per, λ Cep et ζ Pup. La mention de ces oscillations induites par effets de marée est faite ici seulement pour compléter l'état de l'art des observations des pulsations chez les étoiles O.

4.1.5 L'astérosismologie pour contraindre la structure interne stellaire

Il va de soi que les structures induites par les oscillations stellaires non-radiales à la photosphère ne sont que la continuation du comportement interne de ces oscillations. C'est pour cela que les propriétés de ces dernières peuvent être déduites des variations associées à ces structures telles qu'observées au niveau de la photosphère. Aussi, pour une étoile pulsante donnée, différents modes d'oscillations non-radiales atteignent différentes profondeurs de l'intérieur stellaire, ce qui fait que les différentes fréquences de ces modes permettent d'étudier différentes couches de l'intérieur stellaire. La science qui exploite les informations contenues dans ces modes d'oscillations stellaires pour contraindre la structure interne des étoiles est l'astérosismologie, la soeur de la sismologie terrestre qui étudie les ondes sismiques de la Terre pour sonder et mieux comprendre sa structure interne. La procédure de base sur laquelle repose l'astérosismologie est donc

la suivante: essayer de détecter des signes de pulsations dans une étoile donnée, et dans le cas où il y en a, comparer les périodes d'oscillations observées avec les périodes de pulsations théoriques évaluées à partir de modèles stellaires, l'objectif ultime étant de pouvoir trouver un modèle unique le plus fidèle possible aux observations.

Plus les modes d'oscillations détectés sont nombreux, plus l'analyse astérosismologique a de la chance de permettre de contraindre les paramètres stellaires fondamentaux tels que la masse, l'âge, la métallicité, la température effective, la luminosité et la gravité de surface. En principe l'astérosismologie devrait aussi être capable de sonder la structure interne de l'étoile, en apportant par exemple des contraintes sur l'abondance en hydrogène du coeur (X_c), le profil de rotation interne, et même la taille du dépassement du coeur convectif (donnée par le paramètre α_{ov}). Dans la majorité des cas, il existe déjà à priori des estimations approximatives des paramètres de l'étoile en question (obtenues par spectroscopie, photométrie ou astrométrie par exemple) et l'objectif est de contraindre ces mesures.

Une fois les fréquences d'oscillations extraites de la courbe de lumière ou des LPVs, l'analyse sismique s'effectue en deux phases (Aerts *et al.* 2010):

1. Identification des modes d'oscillations, en constituant une série de modèles stellaires $\mathcal{M}^{(j)}=\{\alpha_{ov}^{(j)},\ M^{(j)},\ Z^{(j)},\ X_c^{(j)},\ X_{init}^{(j)}\}$ et en générant le spectre des fréquences théoriques associé à chaque modèle. Cela permet de déterminer le modèle $\mathcal{M}^{(i)}$ le plus proche des fréquences observées et donc d'associer des ordres l et m à ces dernières. Un exemple de cette étape dans le case du pulsateur de type β Cep V836 Cen est illustrée à la Figure 4.5.

2. Génération de chemins évolutifs pour des modèles proches du modèle $\mathcal{M}^{(i)}$, en fixant dans un premier temps les paramètres (X, α_{ov}). Cela permet de choisir le modèle qui ajuste au mieux la fréquence dominante, donnant une valeur de M et Z. En d'autres termes, il s'agit d'une association entre l'espace 2D des paramètres (X, α_{ov}) et l'espace 3D des paramètres (Z, M, âge). En faisant un ajustement à

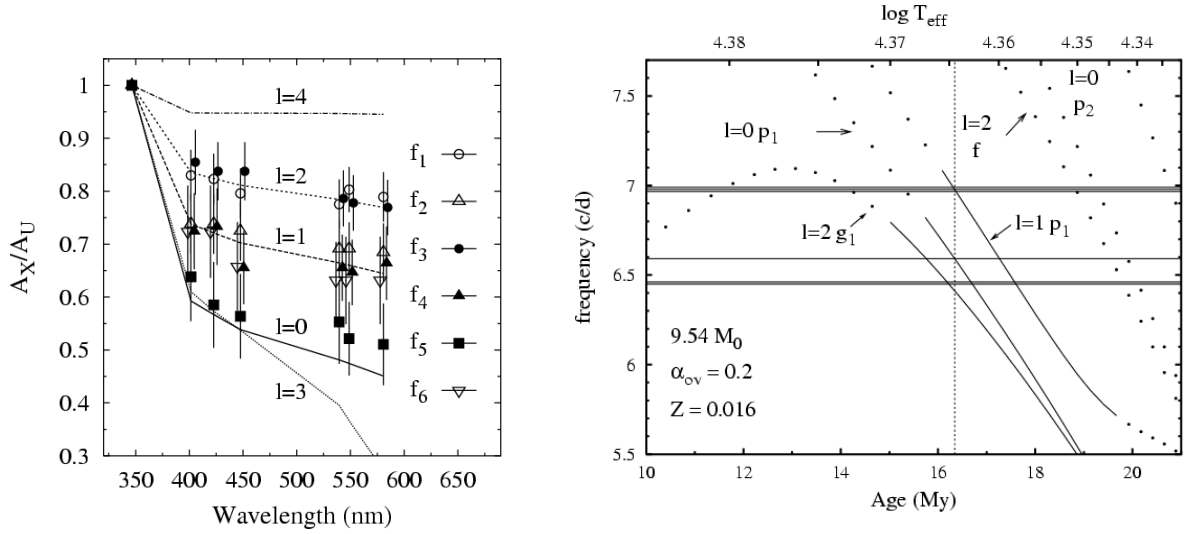

Figure 4.5: Analyse astérosismique du pulsateur de type β Cep V836 Centauri (B3V). *Gauche*: Identification des modes pour six fréquences extraites de la photométrie multi-couleur. Les amplitudes des fréquences observées A_X par rapport à l'amplitude dans la bande U (A_U) sont comparées aux prédictions des modèles théoriques. *Droite*: Exemple de diagramme d'évolution des fréquences en fonction de l'âge pour différents modes. Figure tirée de Dupret *et al.* (2004).

partir de deux fréquences, il est possible, par exemple, d'associer l'espace 3D des paramètres (X, α_{ov}, Z) et l'espace 2D des paramètres (M, âge), donnant une relation masse-métallicité pour chaque couple (X, α_{ov}) considéré.

Ainsi, la détection de fréquences d'oscillations qui sondent différentes régions de l'intérieur stellaire permet de bien contraindre les cinq paramètres (M, X, X_c, Z, α_{ov}). Cela a été fait pour quelques étoiles massives pulsantes de types spectraux B précoces (Saio *et al.* 2000; Thoul *et al.* 2003; Dupret *et al.* 2004; Briquet *et al.* 2007; Handler *et al.* 2009), mais *jamais été fait pour une étoile O!* Pour les étoiles plus massives, qu'elles soient sur la séquence principale ou dans des phases plus évoluées (SGRs, LBVs, WR), l'obstacle réside sur les incertitudes dans les modèles stellaires existants, ainsi que

l'identification des modes, même si le nombre de fréquences détectées est élevé. C'est en l'occurrence le cas de la supergéante HD 163899 (B2 Ib/II), pour laquelle l'analyse de la courbe de lumière *MOST* a fait ressortir 48 fréquences dominantes (Saio *et al.* 2006). Seules les paramètres $M \simeq 15 - 20 \mathrm{M}_{\odot}$ et $\log T_{\mathrm{eff}} \in [4.36; 4.41]$ ont pu être contraintes, due à l'insuffisance d'informations plus précises sur la température effective, la luminosité et la vitesse de rotation stellaire.

En plus de la capacité à bien contraindre les paramètres stellaires, l'astérosismologie constitue le seul moyen de sonder le profil de rotation interne des étoiles. Cela est relativement bien établi en héliosismologie (voir revue faite par Thompson *et al.* 2003). Dans le cas des étoiles massives, le facteur limitant est essentiellement la capacité à détecter des multiplets de fréquences.

Dans une étoile à symétrie sphérique, les fréquences d'un mode de degré l sont dégénéré $2l + 1$ fois, puisque m est un entier relatif entre dans l'intervalle $[-l; +l]$. La rotation stellaire constitue la cause physique la plus importante de la brisure de la symétrie sphérique de l'étoile, entrainant la levée de cette dégénérescence. La perturbation des fréquences due à la rotation est alors quantifiée, en coordonnées sphériques, par (Aerts *et al.* 2010):

$$\delta\omega_{nlm} = \omega_{nlm} - \omega_{nl0} = m \int_0^R \int_0^{\pi} K_{nlm}(r,\theta)\, \Omega(r,\theta)\, r \mathrm{d}r\mathrm{d}\theta \tag{4.10}$$

où $\Omega(r,\theta)$ est la fréquence angulaire de rotation de l'étoile, ω_{nlm} la fréquence angulaire de pulsation associée à l'ordre m, R le rayon stellaire et $K_{nlm}(r,\theta)$ une fonction poids dépendant du mode considéré. Cette fonction est une mesure de l'importance du mode de degrés n, l, m à un point $P(r,\theta)$ dans l'étoile (Aerts *et al.* 2010). Elle détermine jusqu'à quelle profondeur un mode donné est capable de sonder l'intérieur stellaire. La

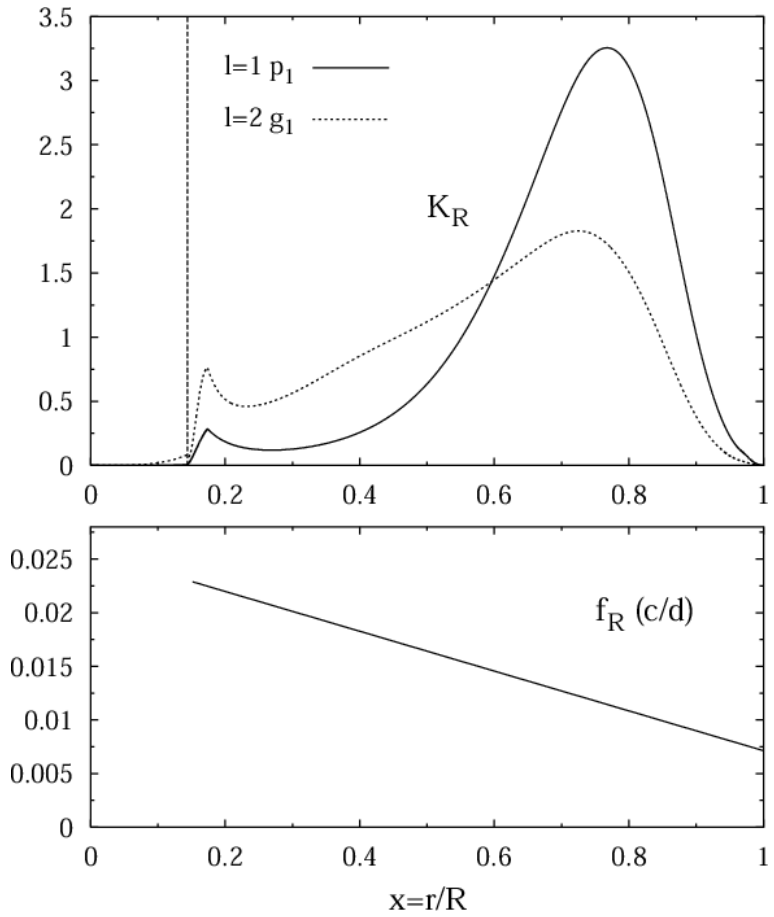

Figure 4.6: Facteur K_{nlm} pour le mode p_1 d'ordre $l = 1$ (triplet) et le mode g_1 d'ordre $l = 2$ (quintuplet) du pulsateur de type β Cep V836 Centauri (*Haut*), ainsi que le profil linéaire de rotation différentielle radiale de l'étoile établi à l'issu de l'analyse sismique (*Bas*). Figure tirée de Dupret *et al.* (2004).

Figure 4.6 montre les variations radiales de la fonction poids K_{nlm} pour les multiplets détectés dans le pulsateur de type β Cep V836 Cen (B3V). Pour cette étoile, le quintuplet $l = 2$, g_1 permet de sonder la rotation différentielle plus profondément que le triplet $l = 1$, p_1.

La rotation différentielle latitudinale et radiale $\Omega(r, \theta)$ peuvent être étudiées en évaluant la compatibilité des séparations des fréquences données par l'équation 4.10 avec les nouveaux paramètres stellaires globaux dérivés lors de l'analyse sismique. Ainsi, par exemple la possibilité d'une rotation rigide peut être explorée, auquel cas la rotation de l'étoile se traduirait par:

$$\Omega = \frac{\delta\omega_{nlm}}{\int_0^R m K_{nlm}(r, \theta)\, r \mathrm{dr}} \tag{4.11}$$

Il est aussi possible d'envisager une rotation différentielle entre le coeur convectif et l'enveloppe radiative. Dans ce cas, l'intégrale 4.10 se sépare en deux termes, un pour le coeur avec $\Omega = \Omega_c$ et un autre terme pour l'enveloppe avec $\Omega = \Omega_e$.

La précision sur le profil de rotation $\Omega(r, \theta)$ dépend du nombre de multiplets disponibles. Par exemple, dans le cas de l'analyse sismique de V836 Cen où deux multiplets seulement ont été détectés (un quintuplet et un triplet), une dépendance linéaire du profil de rotation interne $\Omega(r)$ a pu être déterminé (Figure 4.6).

4.2 Taches stellaires

Quand il s'agit de structures à la surface d'une étoile, il est inconcevable de ne pas évoquer le phénomène des taches. Les propriétés des taches photosphériques, leurs variabilités (cycles, temps de vies, etc...), ainsi que la variabilité qu'elles induisent dans les propriétés observables de leurs étoiles hôtes, sont relativement bien étudiées – non seulement du point de vue théorique mais aussi au niveau observationnel – dans le cas du Soleil et des étoiles de faible masse dont les coeurs sont radiatifs et les enveloppes

convectives (Solanki 2003; Alekseev 2005). Les taches de ces étoiles sont les manifestations photosphériques de leurs activités magnétiques. Par exemple dans le cas du Soleil, le champ magnétique est ultimement généré par des frictions ayant lieu au niveau de la tachocline solaire, c'est-à-dire l'interface coeur radiatif–enveloppe convective. Un des modèles qui expliquent la formation du champ magnétique solaire est celui de Babcock-Leighton (Babcock 1961; Leighton 1964), dans lequel un champ magnétique dipolaire prenant naissance au niveau de la tachocline subit des effets de la rotation différentielle solaire pour former une configuration toroïdale. Des parties des tubes de champ magnétique ainsi formées peuvent remonter graduellement vers la surface sous l'effet turbulent de la convection, au point où elles peuvent ressortir complètement de la photosphère, apparaissant donc comme des boucles de tubes de champ magnétique dans la chromosphère solaire (visibles dans l'UV et dans le domaine des rayons X par les particules à hautes énergies qu'elles entrainent). Un boucle de tube de champ émergent donné inhibe localement le transport convectif d'énergie au niveau des deux régions qu'il transperce proches de la photosphère. Ces deux régions apparaissent plus froides que la photosphère environnante, ce qui est visible par une paire de taches sombres par rapport au reste de la surface (Figure 4.7, panneau latéral gauche).

Dans le cas des étoiles massives, la situation est très différente. Jusqu'à la fin de la première décennie du XXI^{e} siècle, il était de coutume d'admettre qu'il serait impossible d'avoir des taches à la surface des étoiles chaudes et massives, en se basant essentiellement sur le fait que ces étoiles possèdent des énormes enveloppes radiatives. Ce courant de pensée a été ébranlé par la découverte théorique du FeCZ par Cantiello *et al.* (2009b, voir aussi la Section 2.1.2 du Chapitre 2). De manière plus importante, Cantiello & Braithwaite (2011) ont remarqué que cette zone de convection sub-surfacique pourrait même générer un champ magnétique global toroïdal dont les tubes de champ peuvent occasionnellement remonter et transpercer la surface stellaire. Ces remontées de tubes

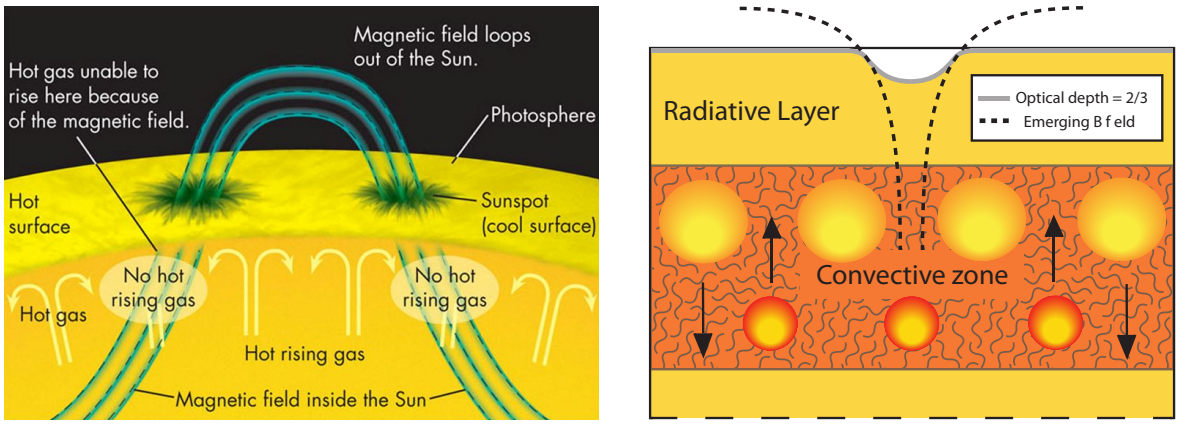

Figure 4.7: Schématisations de la formation d'une paire de taches solaires sombres magnétiques (*Gauche*; Crédits: McGraw-Hill Education) et de la possibilité de génération d'une tache claire magnétique à la photosphère d'une étoile massive (*Droite*; Figure tirée de Cantiello & Braithwaite 2011).

de champ devraient former nécessairement des boucles magnétiques[1]. Les régions correspondant aux 'pôles' d'une boucle émergente donnée laissent voir des couches plus profondes – et donc plus chaudes – de la mince zone radiative située au-dessus de la FeCZ, formant des taches magnétiques plus claires que le reste de la photosphère avoisinante (Figure 4.7, panneau latéral droit). Ces études restent théoriques, et les premières contraintes observationnelles sur l'existence de taches claires dans les étoiles O proviennent des résultats des efforts observationnels entrepris dans le présent projet. Bien entendu, les descriptions détaillées de ces efforts et de leurs résultats font les objets des Chapitres 5 et 6.

La présence de taches à la photosphère d'une étoile peut engendrer des variations dans les profils des raies photosphériques de l'étoile, comme illustrées par la Figure 4.8. Au fur et à mesure qu'une tache est entrainée par la rotation de l'étoile, les moments

[1]Car il n'y a pas de monopole magnétique – au moins jusqu'à preuve du contraire...

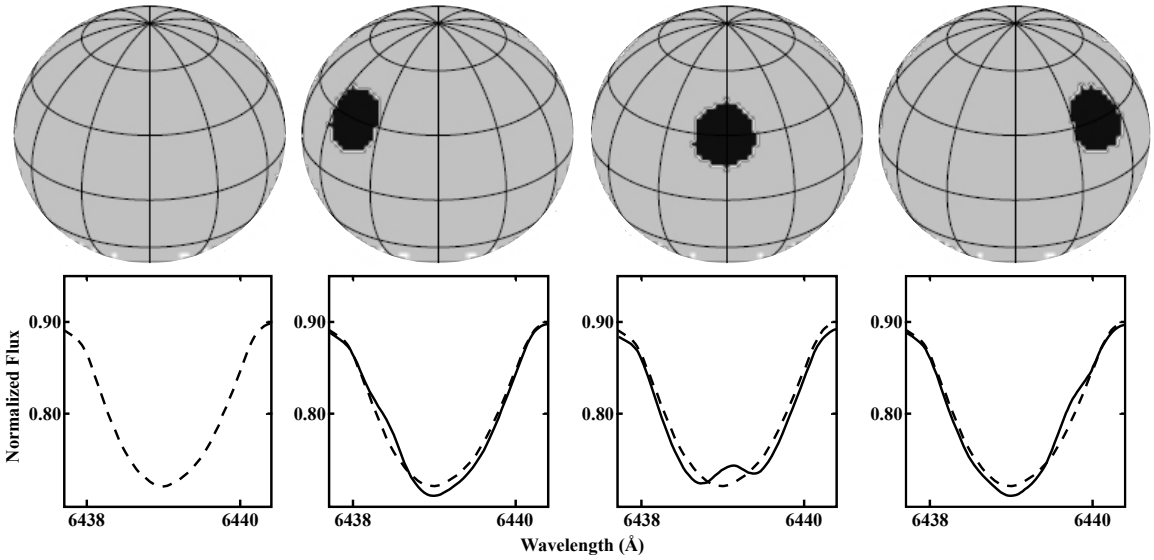

Figure 4.8: Séquence temporelle montrant des modèles de variations du profil d'une raie photosphérique (Ca I λ6439) synthétique dues à la présence d'une tache sombre en corotation sur la surface d'une étoile de faible masse. La courbe discontinue montre le profil de la raie quand la tache n'est pas visible par l'observateur, tandis que la courbe pleine montre le profil de la raie quand la tache est visible par l'observateur. Figure tirée de Berdyugina (2005)

où la tache est visible par l'observateur correspondent à l'apparition de bosses (moins d'absorption) dans les profils des raies photosphériques tels que la raie du Ca I λ6439 chez les étoiles de faible masse.

Mais la manière la plus connue de déceler la présence de taches à la surface d'une étoile est sans doute par leurs signatures en photométrie: une tache sombre entrainée par la rotation de l'étoile va induire une baisse de la luminosité de l'étoile aux phases rotationnelles où elle est visible par l'observateur. Par exemple, comme adopté par Lanza *et al.* (2003) pour la modélisation des variations de l'irradiance solaire totale dues à la présence des taches solaires, l'intensité de lumière provenant d'une étoile

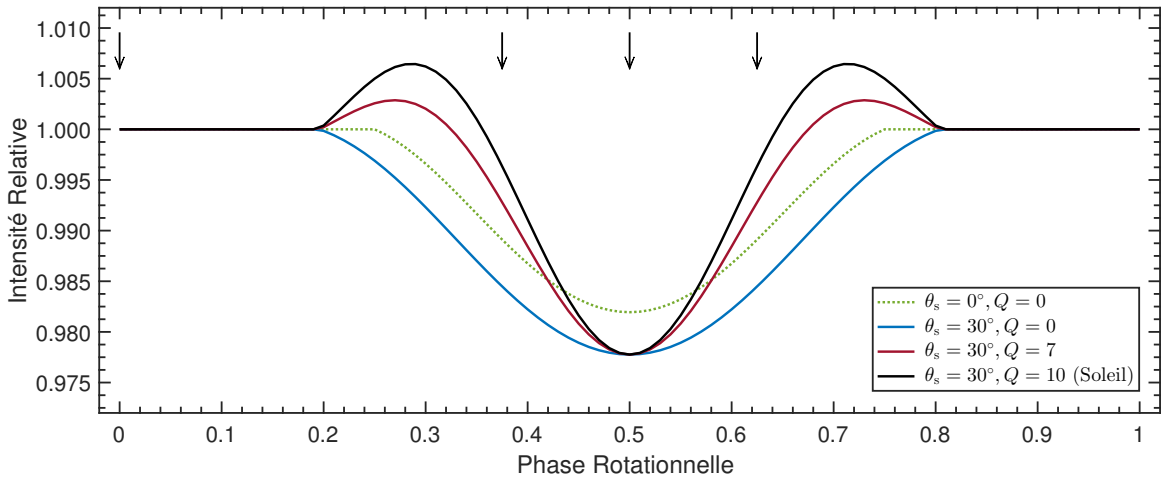

Figure 4.9: Modèles analytiques de variations de la lumière d'une étoile de faible masse dues à la présence d'une tache sombre à sa surface (équations 4.12 et 4.13), correspondant à la situation illustrée sur la Figure 4.8 (tache à $\theta_s = 30°$ de latitude et étoile inclinée de $i = 60°$ par rapport à la ligne de visée), avec trois cas d'étendue de facule ($Q = 0$: sans facules; $Q = 10$: cas du Soleil; $Q = 7$: cas intermédiaire). La situation d'une tache à l'équateur et sans facule est aussi illustrée à des fins comparatifs. Les flèches indiquent les moments correspondants aux quatre prises de vues de la séquence de la Figure 4.8.

montrant un nombre fini N de taches peut prendre la formulation analytique suivante:

$$S = S_0 + S_r + S_0 C \sum_{\substack{n=1 \\ \mu_n > 0}}^{N} A_n \mu_n \mathcal{L}(\mu_n) \left[(c_s - 1) + Q \left(c_f + c'_f \mu_n - 1 \right) \right], \tag{4.12}$$

où S_0 représente l'intensité quand il n'y a pas de taches, S_r l'intensité due à d'autres sources (par exemple du bruit blanc gaussien, du bruit rouge, ...), A_n le pourcentage de surface stellaire couvert par la n-ième tache, $\mathcal{L}(\mu_n)$ la quantité d'assombrissement-bord au niveau de la n-ième tache, généralement exprimée en fonction de $\mu_n = \cos \psi_n$ avec ψ_n l'angle entre la normale à la tache et la ligne de visée. Le facteur C représente l'intensité spécifique quand il n'y a pas de taches, et est étroitement lié à la loi d'assombrissement

centre-bord. Aussi, le contraste d'intensité entre les taches et la photosphère est spécifié par le paramètre c_s.

La formulation 4.12 permet aussi de tenir en compte l'éventuel présence de facules, via le paramètre Q qui est le rapport entre l'aire de la facule et celle de sa tache associée. Dans ce cas, c_f représente le contraste d'intensité entre les facules et la photosphère, tandis que c'_f permet de tenir compte de l'éventuelle dépendance de la luminosité des facules en fonction de l'angle d'où elles sont vues.

Comme indiqué dans l'équation 4.12, la sommation est effectuée seulement sur la partie visible de l'étoile, c'est-à-dire quand $\mu_n > 0$. À propos de cet angle, la loi des cosinus donne:

$$\mu_n = \cos i \sin\theta_n + \sin i \cos\theta_n \cos\left[\phi_n + \frac{2\pi}{P(\theta_n)}t - \phi_0\right], \tag{4.13}$$

avec i l'angle d'inclinaison de l'étoile par rapport à la ligne de visée, θ_n et ϕ_n la latitude et la longitude de la tache sur l'étoile, $P(\theta_n)$ la période de rotation stellaire (pouvant donc dépendre de la latitude s'il y a rotation différentielle latitudinale), t le temps, et ϕ_0 une phase de référence (au besoin).

La Figure 4.9 illustre par exemple les variations de lumière synthétiques de l'étoile tachetée considérée précédemment sur la Figure 4.8, en adoptant une loi d'assombrissement centre-bord quadratique $\mathcal{L}(\mu_n) = a_0 + a_1\mu_n + a_2\mu_n^2$, avec $a_0 = 0.36$, $a_1 = 0.84$, $a_2 = -0.20$, $C = [(1/4)(a_0 + 2a_1/3 + a_2/2)]^{-1} = 4.88$, et $Q = 10$, $c_s = 0.67$, $c_f = 1.115$, $c'_f = -0.115$ dans le cas du Soleil, mais en considérant une rotation rigide de l'étoile. La présence des facules se manifeste notamment (pas de manière inattendue) par un léger excès d'intensité quand la tache arrive aux bords du disque stellaire, ainsi que des baisses de lumière moins prononcées que dans le cas où n'y a pas de facules.

L'approche sus-décrite fait partie des approches directes de modélisation des taches.

Un exemple d'approche inverse est décrite en détail à la Section 6.4.4.3.1 du Chapitre 6. D'ailleurs, les avantages et les inconvénients de ces deux approches seront aussi discuté à la Section 6.4.4.3 du Chapitre 6.

4.3 Microturbulences et macroturbulences

La notion de turbulences photosphériques a été initialement introduite essentiellement par soucis de commodité afin expliquer l'élargissement additionnel des raies photosphériques en sus de l'effet d'élargissement dû à la rotation stellaire (Struve & Elvey 1934; Gonczi & Roddier 1971). Cette notion a connu des difficultés à être acceptée initialement (comme tout nouveau paradigme émergent), mais est maintenant généralement agrée en raison de l'incapacité des modèles d'atmosphère stellaire actuels à reproduire par le seul effet de la rotation stellaire les observations à hauts rapport signal sur bruit et à haute résolution spectrale des raies photosphériques de plusieurs variétés d'étoiles (Howarth *et al.* 1997; McErlean *et al.* 1998; Villamariz & Herrero 2000; Markova & Puls 2008).

En somme, les turbulences photosphériques sont des phénomènes associés à des champs de vitesses photosphériques nécéssaires pour expliquer les élargissement des raies photosphériques observées. Formellement, elles sont généralement classées en deux catégories principales selon l'échelle de distance à laquelle elles ont lieu (Gray 2005):

- les microturbulences: décrivant les champs de vitesses ayant lieu sur des échelles de distance plus courtes que le libre parcours moyen des photons dans l'atmosphère stellaire;
- les macroturbulences: pour les champs de vitesses opérant sur des échelles plus grandes que le libre parcours moyen des photons dans l'atmosphère stellaire.

Les champs de vitesses associées à la microturbulence ont des composantes allant de quelques kilomètres par secondes à $\sim$ 15 km s^{-1}, tandis que la macroturbulence peut impliquer des vitesses allant jusqu'à $\sim$ 90 km s^{-1}.

Dans le cas des étoiles à enveloppe convective, les turbulences photosphériques sont généralement associées aux mouvements convectifs dans l'enveloppe. Par contre, chez les étoiles massives les mécanismes physiques pouvant donner lieu aux turbulences photosphériques restent un mystère. Des propositions solides ont été seulement faites relativement récemment: il a été proposé que la macroturbulence pourrait résulter de l'effet combiné de plusieurs modes g à faibles amplitudes excités via le mécanisme κ (Aerts *et al.* 2009) ou d'ondes de gravité internes générées dès l'interface coeur convectif–enveloppe radiative (Aerts & Rogers 2015); tandis que Cantiello *et al.* (2009a,b) ont proposé que la microturbulence, elle aussi, pourrait être due à des ondes de gravité internes mais générées au niveau d'une zone de convection sub-surfacique.

4.4 Éruptions sporadiques

Il va sans dire que des étoiles sujettes à des éruptions sporadiques de matière peuvent montrer des variations associées à ces évènements, au moins dans leurs luminosités. L'illustration la plus simple de cette situation est le comportement du Soleil, dont les éruptions occasionnelles se traduisent par de brèves augmentations de son irradiance (et donc de sa luminosité) à travers presque tout le spectre éléctromagnétique (voir revue donnée par Fletcher *et al.* 2011). Dans le cas des étoiles massives, des éruptions occasionnelles de matière stellaire se rencontrent surtout chez les étoiles proches de la limite de Humphreys-Davidson, à savoir les hypergéantes jaunes et les étoiles LBVs.

4.4.1 Les hypergéantes jaunes

Comme leurs noms l'indique, les hypergéantes jaunes ne peuvent pas être considérées comme directement liées aux étoiles O. Pourquoi alors en parler ici? Parce qu'elles ont des types spectraux très variables, justement à cause des évènements éruptives auxquels elles sont sujettes. En effet, les étoiles hypergéantes jaunes présentent occasionnellement de grosses éruptions à la suite desquelles leur vent stellaire se refroidit et devient optiquement épais. Plus ces éjections de matière sont massives et fréquentes, plus l'étoile est poussée vers la partie bleue du diagramme de Hertzsprung-Russell (donc vers le type spectral O – bien qu'elles atteignent rarement le régime O). Quand le vent stellaire redevient optiquement mince, il peut y avoir éventuellement un retour à l'état SGR jusqu'à ce qu'une autre grosse éruption apparaît. Ces allers-retours entre les phases SGR et hypergéante jaune sont donc associées aux pertes de masse par éruptions suivies d'un refroidissement du vent stellaire optiquement épais (de Jager & Nieuwenhuijzen 1997).

Les éruptions des hypergéantes jaunes ont lieu sur une échelle de temps allant de quelques années à quelques décennies et peuvent atteindre des taux de perte de masse similaires à ceux des grosses éruptions des étoiles LBVs (c'est-à-dire $\dot{M} \sim 10^{-2}$ $M_\odot$ an^{-1}). C'est par exemple le cas de ρ Cassiopeiae qui a subi trois éruptions pendant le siècle dernier, et dont la dernière éruption correspond à un taux de perte de masse $\dot{M} \simeq 5.4 \times 10^{-2}$ $M_\odot$ an^{-1} (Lobel *et al.* 2003), comparable aux grosses éruptions de l'étoile LBV η Car.

L'origine des éruptions des hypergéantes jaunes reste encore très incertaine, mais serait probablement liée à des instabilités dynamiques de l'étoile dues aux effets accrus de la pression de radiation dans des PIZs dans l'enveloppe stellaire (Stothers & Chin 2001).

4.4.2 Les étoiles lumineuses, bleues, variables

Les étoiles LBVs montrent occasionnellement des éruptions qui peuvent être classées en deux catégories selon leurs amplitudes et l'échelle de temps sur lesquelles elles ont lieu (van Genderen 2001, voir aussi Figure 4.10): les grosses éruptions ('S Dor-eruptions' ou 'SD-eruptions') et les éruptions moyennes ('S Dor-phases' ou 'SD-phases').

Les grosses éruptions accompagnées de violentes éjections de masse entrainant un changement de magnitude de plus de 2 mag, ont lieu rarement, au plus une à deux fois par siècle (panneau latéral droit de la Figure 4.10) mais dans la plupart des cas elles se comptent même par millénaire. L'origine de ces grosses éruptions reste encore incertaine. Elles pourraient être liées à des oscillations stellaires ou à d'autres types d'instabilités provenant de l'existence d'une zone de convection due à un pic d'opacité. La conjecture générale est que ces grosses éruptions ont lieu quand les étoiles approchent la limite d'Eddington. Cela a été confirmé par les modèles hydrodynamiques d'éjections bipolaires établis par Langer *et al.* (1999). Ces simulations ont aussi révélé les implications du taux de rotation stellaire initial et du moment angulaire initial dans le déclenchement des éruptions des étoiles LBVs.

Les éruptions de moyennes amplitudes ou phases SD des étoiles LBVs, se traduisant par un changement de $1-2$ mag en magnitudes, ont lieu environ tous les $10-40$ ans. Ces variations s'avèrent être cycliques et ne doivent pas être confondues avec les grosses éruptions mentionnées plus haut. En effet, les phases SD seraient plutôt associées à de larges variations du rayon et de la température stellaire, liées probablement à des pulsations et à l'état de l'étoile au-delà de la limite d'Eddington.

Les étoiles LBVs les plus actives (variations de magnitude de 0.5 à 2 mag lors des phases SD) occupent une bande d'instabilité dans le diagramme H–R lorsqu'elles sont

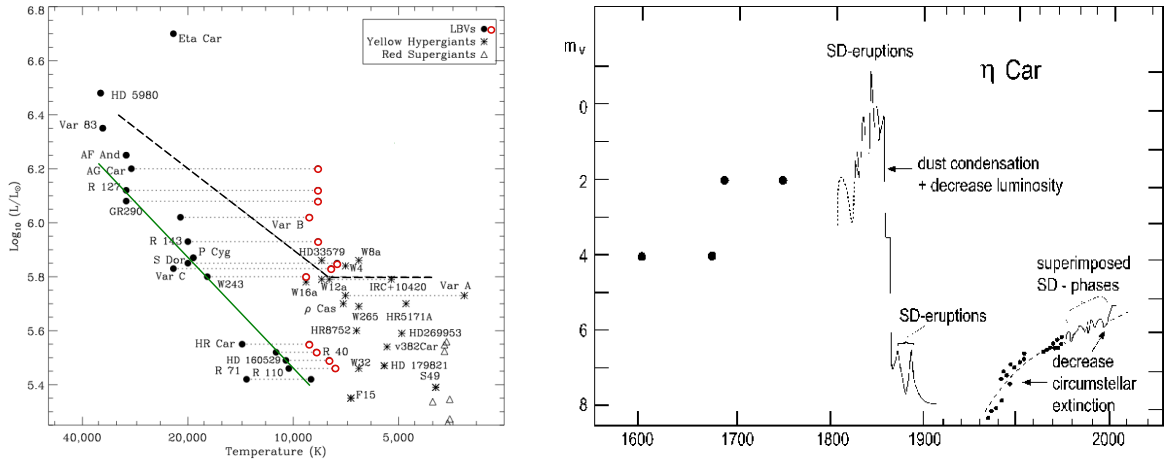

Figure 4.10: *Gauche:* Zones d'instabilités dynamiques dans la partie haute du diagramme H–R avec quelques exemples d'hypergéantes jaunes, d'étoiles LBVs et de SGRs. La ligne verte est la limite inférieure de la zone d'instabilité des étoiles LBVs (voir texte). La ligne discontinue représente la limite de Humphreys-Davidson (Figure adaptée de Oudmaijer *et al.* 2009). *Droite:* Courbe de lumière de l'étoile LBV η Car sur 400 ans, indiquant notamment les phases SD et les éruptions SD. Figure tirée de van Genderen (2001).

'au repos' (Figure 4.10). Cette zone d'instabilité a été introduite pour la première fois par Wolf (1989) et sa limite inférieure vérifie la relation empirique:

$$\log (L/L_{\odot}) = 1.37 \log T_{\rm eff} - 0.03 \tag{4.14}$$

Aussi, la Figure 4.10 indique clairement que les déplacements des positions des étoiles LBVs lors des phases SD se font plus ou moins horizontalement et que les étoiles se retrouvent sur une bande verticale quand elles sont en activité. En outre, plus l'étoile est lumineuse, plus elle montre de grands décalages en température lors des phases SD.

Finalement, certaines éruptions des étoiles LBVs peuvent parfois être confondues avec des explosions supernovae à effondrement de coeur. Ces étoiles sont communément désignées comme 'imposteurs supernovae' (Kochanek *et al.* 2012).

4.5 La recherche entreprise dans le cadre de cette thèse

Maintenant que les bagages nécessaires sont bien pliés, notre quête des origines photosphériques des structures dans les vents des étoiles chaudes et lumineuses peut commencer. Dans cette optique, les trois chapitres qui suivent exposent les résultats des efforts – essentiellement de nature observationnel – menés sur trois étoiles O clés, ξ Persei, ζ Puppis, et V973 Scorpii. Ces résultats ont fait l'objet de trois articles qui ont été publiés dans le mensuel *Monthly Notices of the Royal Astronomical Society*.

4.5.1 ξ Persei

Le Chapitre 5 est consacré à l'analyse de la photométrie à haute précision et résolue dans le temps de la géante ξ Persei [O7.5III(n)((f))] telle qu'observée par le microsatellite *MOST*. Le temps d'observation *MOST* a été initialement demandé et obtenu par

Anthony F. J. Moffat. L'extraction de la courbe de lumière *MOST* de ξ Per à partir des images brutes a été effectuée par Victoria Antoci, et une analyse Fourier préliminaire a été effectuée par André-Nicolas Chené. J'ai ensuite effectué l'analyse Fourier complète, l'analyse temps-fréquence, ainsi que le développement des simulations de courbes de lumière dues à la présence de taches claires en corotation avec la surface stellaire en adoptant l'approche analytique (similaire aux Équations 4.12 et 4.13 de la Section 4.2, mais dans le cas de taches claires équatoriales, sans facules, et en incorporant une loi de croissance et de décroissance linéaires de l'apparition et de la disparition des taches). Une brève analyse sur la meilleure estimation de la période de rotation de ξ Per a été effectuée en étroite collaboration avec Huib F. Henrichs qui a initialement proposé l'idée. L'interprétation finale de la variabilité observée ainsi que la rédaction de l'article ont été effectuées conjointement avec Anthony F. J. Moffat. Comme dans les cas de toutes les publications utilisant les données *MOST*, nous étions contraints à inviter tous les membres de l'équipe *MOST* (Jason F. Rowe, Jaymie M. Matthews, Rainer Kuschnig, Werner W. Weiss, Dimitar Sasselov, Slavek M. Rucinski, et David B. Guenther) à se joindre comme co-auteurs de l'article.

4.5.2 ζ Puppis

Le Chapitre 6 est le fruit d'une grande campagne d'observations photométrique et spectroscopique sans précédent dans le visible que nous avons mené sur la supergéante ζ Puppis [O4I(n)fp]. La composante photométrique de la campagne d'observation est constituée de la photométrie à haute précision obtenue pendant environ cinq mois et demi à travers les deux filtres spécifiques des nanosatellites de la mission spatiale *BRITE* opérant dans le bleu et dans le rouge. Ce temps d'observation *BRITE* a été demandé et acquis par Anthony F. J. Moffat. La seule personne chargée de l'extraction des courbes

de lumière de la mission *BRITE* à partir des images brutes est Adam Popowicz. Une fois extraites, les courbes de lumière doivent être décorrélées par rapport à de potentiels effets d'origines instrumentales, une opération qui a été faite par Herbert Pablo et Andrzej Pigulski dans le cas des courbes de lumière de ζ Pup obtenues lors de cette campagne d'observations. J'ai ensuite effectué l'analyse proprement dite des courbes de lumière. J'ai également récupéré la courbe de lumière *Coriolis/SMEI* de ζ Pup (fournie par Ian D. Howarth et Ian R. Stevens; publiée par Howarth & Stevens 2014) et effectué les mêmes analyses que celles que j'ai faites sur ses courbes de lumière *BRITE* afin de déterminer le comportement à long terme de sa variabilité photométrique. En outre, j'ai effectué la modélisation de la variabilité observée à travers les courbes de lumière moyennant un algorithme d'inversion de courbe de lumière développé par Robert Harmon (Harmon & Crews 2000). Un modèle d'atmosphère pour ζ Pup a été généré avec le code PoWR (Potsdam Wolf–Rayet) par Tomer Shenar afin de confirmer que les observations photométriques sondent bien essentiellement la photosphère stellaire.

Quant à la composante spectroscopique de la campagne d'observations, huit sites d'observation au sol, relativement bien réparties autour du globe (dans l'hémisphère sud), ont été impliqués afin d'assurer au mieux la continuité du suivi spectroscopique du comportement dans le vent de ζ Pup en parallèle avec les observations *BRITE*. J'ai mené les demandes de temps d'observation au téléscope de 1.9 m de la South-African Astronomical Observatory (SAAO) et à celui de 1.5 m de la Cerro Tololo Inter-American Observatory (CTIO), et effectué les observations à la SAAO. Les six autres sites d'observation sont ceux des astronomes amateurs P. Luckas (Australie), B. Heathcote (Australie), J. Powles (Australie), T. Bohlsen (Australie), M. Locke (Nouvelle-Zélande), et P. Cacella (Brésil) qui ont eux-même effectué leurs observations et réduit leurs données. J'ai effectué la réduction des données spectroscopiques récoltées à la SAAO et au CTIO, puis procédé à la normalisation homogène et à l'analyse des

1054 spectres que nous avons pu récolter durant la campagne d'observations. Additionnellement, j'ai récupéré et réduit les données spectroscopiques d'archive de ζ Pup initialement publiées par Eversberg *et al.* (1998, les données étant récupérables au centre canadien des données astronomiques), notamment afin de les analyser pour vérifier la similarité entre la composante stochastique de la variabilité spectroscopique détectée dans le passé et celle détectée lors de cette campagne d'observations. Aussi, pour les données de la campagne d'observations, j'ai pu effectuer la modélisation des manifestations spectroscopiques des CIRs détectées dans la raie d'He II λ4686 de ζ Pup grâce à un code de modélisation analytique de CIRs développé par Richard Ignace. Enfin, la revue des scénarios d'évolution de ζ Pup pouvant expliquer son statut actuel d'étoile en cavale et sa très courte période de rotation a été possible avec la collaboration et l'expertise de Dany Vanbeveren.

La section de l'article expliquant la génération du modèle d'atmosphère pour ζ Pup (Section 6.4.2) a été rédigée par Tomer Shenar. Une partie de la section de discussion et conclusion (Section 6.6) évoquant la possibilité de la nature turbulente du grumelage du vent stellaire a été rédigée par Anthony F. J. Moffat. Le reste de l'article a été rédigé par moi-même. À l'instar de la politique de publication des données *MOST*, nous étions tenus d'inviter tous les membres du comité exécutif scientifique de la mission *BRITE* (*BRITE* Executive Science Team – BEST) qui seraient intéressés à devenir co-auteurs et nous fournir des commentaires sur l'article. Les membres de BEST ainsi devenus co-auteurs de l'article sont Rainer Kuschnig, Gerald Handler, Werner W. Weiss, Gregg A. Wade, Slavek M. Rucinski, et Konstanze Zwintz.

4.5.3 V973 Scorpii

Le Chapitre 7 est dédié à la variabilité photosphérique de la supergéante V973 Scorpii [O8Iaf] telle que sondée par *BRITE*. Le temps d'observation *BRITE* de V973 Sco a été initialement demandé et acquis par Anthony F. J. Moffat. L'opération d'extraction de la courbe de lumière à partir des images brutes est attribuée à Adam Popowicz. Tomer Shenar a généré un modèle d'atmosphère pour V973 Sco, tandis que Rathish Ratnasingam et Tamara M. Rogers m'ont fourni leur modèle de spectre d'amplitudes associé à des ondes de gravité internes pour une étoile ZAMS de $3M_{\odot}$ (Rogers *et al.* 2013). J'ai effectué la décorrelation de la courbe de lumière *BRITE* de V973 Sco par rapport aux effets d'origines instrumentales, effectué l'analyse Fourier et l'analyse temps-fréquence de la courbe de lumière, développé la méthode de caractérisation des signaux sinusoïdaux transitoires formant la variabilité stochastique de l'étoile, et effectué la rédaction de l'intégralité de l'article. Compte tenu de la règle de publication d'articles utilisant des données *BRITE*, des membres de BEST (Rainer Kuschnig, Andrzej Pigulski, Gerald Handler, Gregg A. Wade, Konstanze Zwintz, et Werner W. Weiss) se sont joints en tant que co-auteurs de l'article.

5

La Géante ξ Persei

MOST Detects Corotating Bright Spots on the Mid-O-Type Giant ξ Persei*†

Tahina Ramiaramanantsoa[1,2], Anthony F. J. Moffat[1,2], André-Nicolas Chené[3,4,5], Noel D. Richardson[1,2], Huib Henrichs[6], Sébastien Desforges[1,2], Victoria Antoci[7], Jason F. Rowe[8], Jaymie M. Matthews[9], Rainer Kuschnig[9,10], Werner W. Weiss[10], Dimitar Sasselov[11], Slavek M. Rucinski[12], and David B. Guenther[13]

[1]Département de physique, Université de Montréal, C.P. 6128, Succ. Centre-Ville, Montréal, QC, H3C 3J7, CANADA
[2]Centre de Recherche en Astrophysique du Québec (CRAQ), CANADA
[3]Gemini Observatory, Northern Operations Centre, 670 North A'ohoku Place, Hilo, HI96720, USA
[4]Departamento de Física y Astronomía, Universidad de Valparaíso, Av. Gran Bretaña 1111, Caslla 5030, CHILE
[5]Departamento de Astronomía, Universidad de Concepción, Casilla 160-C, CHILE
[6]Astronomical Institute "Anton Pannekoek", University of Amsterdam, Science Park 904, 1098 XH Amsterdam, THE NETHERLANDS
[7]Stellar Astrophysics Centre, Dept. of Physics and Astronomy, Aarhus University, Ny Munkegade 120, DK-8000 Aarhus C, DENMARK
[8]NASA Ames Research Center, Moffett Field, CA 94035, USA
[9]Department of Physics and Astronomy, University of British Columbia, 6224 Agricultural Road, Vancouver, BC V6T 1Z1, CANADA
[10]Institute for Astronomy, University of Vienna, Türkenschanzstrasse 17, A-1180 Vienna, AUSTRIA
[11]Harvard-Smithsonian Center for Astrophysics, 60 Garden Street, Cambridge, MA 02138, USA
[12]Department of Astronomy and Astrophysics, University of Toronto, 50 St George Street, Toronto, ON M5S 3H4, CANADA
[13]Institute for Computational Astrophysics, Department of Astronomy and Physics, St Mary's University Halifax, NS B3H 3C3, CANADA

Published in the *Monthly Notices of the Royal Astronomical Society, Volume 441, Issue 1, pages 910–917,* 11 June 2014 (Online 02 May 2014)

*Based on data from the *MOST* satellite, a Canadian Space Agency mission jointly operated by Dynacon Inc., the University of Toronto Institute for Aerospace Studies and the University of British Columbia, with the assistance of the University of Vienna.

†This paper is dedicated to the memory of Dr. Vincent Fesquet.

5.1 Abstract

We have used the *MOST (Microvariability and Oscillations of STars)* microsatellite to obtain four weeks of contiguous high-precision broad-band visual photometry of the O7.5III(n)((f)) star ξ Persei in November 2011. This star is well known from previous work to show prominent DACs (discrete absorption components) on time-scales of about 2 d from UV spectroscopy and non-radial pulsation with one (l = 3) p-mode oscillation with a period of 3.5 h from optical spectroscopy. Our *MOST*-orbit (101.4 min) binned photometry fails to reveal any periodic light variations above the 0.1 mmag 3σ noise level for periods of a few hours, while several prominent Fourier peaks emerge at the 1 mmag level in the two-day period range. These longer period variations are unlikely due to pulsations, including gravity modes. From our simulations based upon a simple spot model, we deduce that we are seeing the photometric modulation of several corotating bright spots on the stellar surface. In our model, the starting times (random) and lifetimes (up to several rotations) vary from one spot to another yet all spots rotate at the same period of 4.18 d, the best-estimated rotation period of the star. This is the first convincing reported case of corotating bright spots on an O star, with important implications for drivers of the DACs (resulting from CIRs - corotating interaction regions) with possible bright-spot generation via a breakout at the surface of a global magnetic field generated by a subsurface convection zone.

5.2 Introduction

Despite their rarity, luminous hot (massive) stars account for a dominant fraction of the recycling of energy and enriched stellar material back to the interstellar medium which can then form further generations of stars and planets. This occurs both from winds during the whole stellar lifetimes and supernova explosions at the end of their lives.

Models of the most massive stars near or on the main sequence, the O stars, predict that pulsations should occur via the iron-bump κ mechanism due to the extension of the β Cep instability strip at least to the late-O type stars (Cox *et al.* 1992; Pamyatnykh 1999). This would be indispensable to probe their internal structure. But such pulsations are not observed photometrically in the majority of O stars (Balona 1992, 2010) which is often the easiest way to probe the variability. On the other hand, spectroscopic surveys for variability in O stars (Fullerton *et al.* 1996) indicate that the vast majority of O stars show photospheric line profile variations (LPV) that can probably be attributed to pulsation. In the hottest stars, modes of high-l spherical harmonics are excited in preference to those of low l, thus, possibly explaining the decline in detectable light variations for stars hotter than B0 (Balona 2010). Photometry is most sensitive to very low-l oscillations because of resolution problems and partial cancellation effects at high l. Indeed, even if the variations of the partial cancellation factor as a function of l do not behave monotonically, its values decrease at least by a factor of 10 for $l \geq 4$ compared to the dipole mode, and converge towards zero for $l \geq 9$, the effect being also more important on odd modes than on even modes (see Equation 6.29 and Figure 6.4 of Aerts *et al.* 2010).

Strange-mode pulsations are also predicted to occur in the upper part of the Hertzsprung–Russell diagram (Kiriakidis *et al.* 1993; Glatzel 2009), but it seems that these modes

mainly concern stars close to the Humphreys–Davidson limit and observations have not established yet that strange modes are present in O stars.

Most of the few known pulsating O stars are late-O-type stars (see Henrichs 1999; Walker *et al.* 2005; De Cat *et al.* 2007; Pigulski & Pojmański 2008; Rauw *et al.* 2008; Howarth *et al.* 2014), two of them having the best-established oscillation periods: ζ Ophiuchi, the best studied of all the O stars by *MOST (Microvariability and Oscillations of STars)* photometry (Walker *et al.* 2005; Howarth *et al.* 2014), and HD 93521 (Rauw *et al.* 2008), both O9.5V. The ζ Oph *MOST* light curve is dominated by non-radial pulsations (NRP) in at least a dozen frequencies in the range $1-10$ d^{-1}, with dominating period $P = 4.6$ h and amplitudes reaching 7 mmag. ζ Oph and HD 93521 are also amongst the most rapidly rotating stars known, with $v \sin i \simeq 400$ km s^{-1} for ζ Oph and 390 km s^{-1} for HD 93521. So even if they show low-amplitude β Cep-like pulsations, they should be considered as exceptional members of the so-called class of β Cep stars (Stankov & Handler 2005).

Two hotter, mid-O-type stars are of particular interest: ξ Persei [O7.5III(n)((f))] and λ Cephei [O6I(n)fp], which exhibit short-period LPV, implying NRP with $l = 3 - 5$ based on high-precision time-dependent spectroscopic monitoring (de Jong *et al.* 1999). λ Cep is unfortunately not observable by *MOST*.

The *COnvection ROtation and planetary Transits* satellite (*CoRoT*, Baglin *et al.* 2006; Auvergne *et al.* 2009) has also been used to study variability in six O stars in a (relatively short for *CoRoT*) run targeting O stars in the young cluster NGC 2244 and its surrounding association Mon OB2 (Degroote *et al.* 2010a; Blomme *et al.* 2011; Briquet *et al.* 2011; Mahy *et al.* 2011). These data reveal diverse and highly uncertain origins for the variability, ranging from possible pulsations for those (cooler O) stars closest to the β Cep strip (dominated by early-type B stars) to intrinsic red noise mainly for the hotter O stars, with rotation also possible in some cases.

With regard to their winds, detailed examination of P Cygni absorption troughs of resonant UV lines frequently used to determine mass-loss rates and terminal wind speeds of hot luminous stars, reveals time-variable structures called discrete absorption components (DACs). From their *International Ultraviolet Explorer (IUE)* snapshot survey of 203 targets, Howarth & Prinja (1989) found that narrow absorption components (NACs) in the P Cygni absorption troughs of unsaturated UV resonance lines are virtually universal among O stars. Subsequent time series observations established that NACs are the end states of propagating DACs, thus implying that DACs are also ubiquitous among O-type stars. More extended data sets of individual stars (e.g. Massa *et al.* 1995a,b; Howarth *et al.* 1995; Prinja *et al.* 1995; Kaper *et al.* 1996), led to the conclusion that DACs can start out relatively close to the stellar surface as broad absorptions, which accelerate to ever narrower features at higher velocities, asymptotically approaching the terminal wind speed of typically ∼2000 km s^{-1}. At any given epoch for an average O star, there are on average two dominating DACs per rotation cycle (Kaper *et al.* 1999). DACs tend to repeat on a rotation period, yet do not preserve coherency over time-scales greater than a few rotations. In the case of ξ Per, Henrichs *et al.* (1994) used high-time-resolution *IUE* UV spectroscopy of this star to conclude that the variability of its wind takes place in a wide velocity range and most importantly that the observed DACs start out at very low velocities. This was later confirmed by simultaneous Hα (close to the stellar surface) and UV wind (far out) observations of ξ Per by de Jong *et al.* (2001) who showed that the DACs are really tied to a region very close to the photosphere.

Concerning the origin of DACs, Mullan (1986) suggested that they probably emerge from corotating interaction regions (CIRs) in the stellar wind. These large-scale structures are observed and well studied in the solar corona (Hundhausen 1972), where regions of open magnetic field accelerate local parcels of wind plasma ultimately to

higher speeds, and the interaction of these streams with the ambient wind, combined with rotation, leads to corotating spiral-like wind perturbations. Mullan (1986) extended this paradigm to the case of hot stars and the origin of DACs was associated with CIR compressions within the stellar wind.

Kaper & Henrichs (1994) discussed magnetic footprints as the source of DACs in O-type stars. They suggested a low-amplitude, variable dipole magnetic field as the seed of a large-scale wind structure that can be responsible for the emergence of DACs. Later, Cranmer & Owocki (1996) established models of CIRs in which it turns out that DACs come from extended velocity plateaux forming ahead of the dense CIR compressions. In the simulations of Cranmer & Owocki (1996), bright spots at the stellar surface produce plateau speeds in the wind and absorption features that match with the characteristics of the observed DACs, whereas dark spots generate plateau speeds in the wind that are at $4000 - 5000$ km s^{-1} (see their figure 8a) which are not consistent with the slow-moving observed DACs (Owocki, private communication). The source of the bright spots needed to create the DACs, however, remained a mystery, with NRP or hypothetical magnetic spots remaining as the most likely candidates, with some preference for the latter as the required magnetic field strength would match typical values of the wind confinement parameter η for an O star (Ud-Doula *et al.* 2008; Henrichs 2012). In addition to that, only magnetic spots will corotate with the star; NRPs will not be corotating, propagating in prograde or retrograde modes.

ξ Per is the brightest single O star in the Northern hemisphere, with the most extensive observational record regarding wind and atmosphere connection, DAC information, pulsation information, and with a magnetic upper limit (59 G, model-dependent surface dipole polar field strength for ξ Per, David-Uraz *et al.* 2014), but with high-precision photometry desperately missing. Photometry is especially relevant because if DACs arise from corotating magnetic spots, the latter should be detectable in optical contin-

uum light, which is the main goal of this investigation.

We have observed ξ Per using *MOST* in an attempt to photometrically reveal its NRP (despite the only known mode so far, a p mode with $l = 3$, $P = 3.5$ h according to the spectroscopic monitoring of de Jong *et al.* 1999) and any other variability that might be present (e.g. corotating bright spots). It was hoped that this may reveal other pulsation modes, too, which would help clinch the p modes expected in O stars (and possibly even reveal longer period g modes from the core region). We also obtained contemporaneous optical spectra in the range $4000 - 5000$ Å at the highest resolution available ($\sim$0.4 Å pixel^{-1}, $\Delta v \sim 60$ km s^{-1}) and $S/N \sim 150$ at the Observatoire du Mont Mégantic, in order to attempt to match up with the *MOST* photometry and to verify the LPV previously seen in this star (Kaper *et al.* 1996; de Jong *et al.* 1999, 2001). Unfortunately, due to the insufficient signal-to-noise (S/N) in our spectra and the sparsity of the time coverage, no obvious link could be established between the spectral changes and the simultaneous *MOST* light variations. More extensive spectral coverage will be needed in the future to probe this interesting aspect. Thus, this paper focuses on the outcome of our analysis of the *MOST* light curve of ξ Per.

5.3 Observations

The photometry presented here was obtained by the *MOST* microsatellite, which houses a CCD photometer fed by a 15-cm Maksutov telescope through a custom broad-band optical filter ($350 - 750$ nm). The satellite's Sun-synchronous polar orbit (period = 101.4 min, corresponding to a frequency of 14.20 d^{-1}) enables uninterrupted observations of stars in its continuous viewing zone ($-18^o <$ Dec $< +36^o$) for up to eight weeks. A pre-launch summary of the mission is given by Walker *et al.* (2003) and on-orbit science operations are described by Matthews *et al.* (2004).

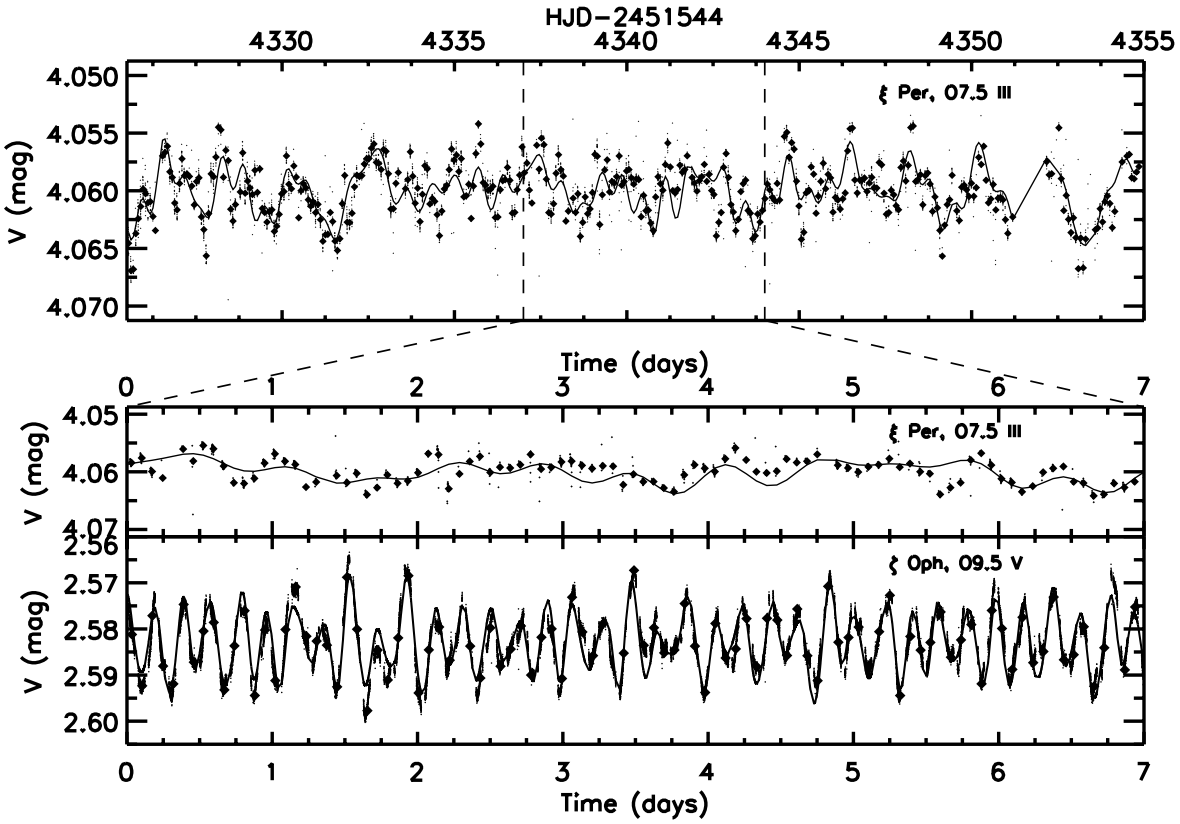

Figure 5.1: *MOST* photometry. The diamonds are orbital means, whereas the small points represent raw data. *Top:* Light curve of ξ Per obtained with four contiguous weeks of *MOST* photometry in November 2011. The continuous curve is a fit with the 12 frequencies listed in Table 5.I. *Middle:* 7-d subsample of the above light curve. *Bottom:* 7-d subsample of the *MOST* light curve of the O9.5 dwarf ζ Oph for which Walker *et al.* (2005) reported the detection of short-period radial and non-radial pulsations. The continuous curve is a 13 frequency fit from table 1 of Walker *et al.* (2005). Note that the middle and the bottom panels have exactly the same horizontal and vertical scales.

ξ Per ($V = 4.06$, RA[2000] = 03:58:57.90, Dec[2000] = +35:47:27.7) was observed during four contiguous weeks of space-based *MOST* photometry between 2011 November 04 and 2011 December 04 (HJD 2,455,869.5 – 899.5). The observations lasted ~20 min of each *MOST* orbit, the remaining orbital time being devoted to two other targets. The data were obtained in Fabry mode and extracted using the technique of Reegen *et al.* (2006). With such time gaps and no urgent need to look above the *MOST*-orbit Nyquist frequency (or below $P = 2 \times 101$ min = 3.37 h), we calculated orbital means to create a final light curve (Figure 5.1). The standard deviation of each mean point is ~0.3 mmag.

5.4 Results

5.4.1 Rotation period of ξ Per

The rotation period is a crucial parameter in this investigation. Even if the recurrence of the DACs in ξ Per happens at a time-scale of $P_{\rm DACs} = 2.09$ d, the best estimate of the stellar rotation period is twice that period, i.e. $P_{\rm rot} = 4.18$ d (de Jong *et al.* 2001).

Theoretically, the rotation period is simply related to the stellar radius R and the rotational velocity as $P_{\rm rot} = 2\pi R/v$. The top panel of Figure 5.2 shows a plot of the maximum rotation period $P_{\rm max}$ as a function of R, for a given value of $v \sin i$. The two extreme values of $v \sin i$ of ξ Per were taken: 192 km s^{-1} (from Penny 1996, who found $v \sin i = 204 \pm 12$ km s^{-1}) and 225 km s^{-1} (from Howarth *et al.* 1997, who found $v \sin i = 213 \pm 12$ km s^{-1}). For an assumed radius of $14^{+2.1}_{-1.8} R_\odot$ (derived by Repolust *et al.* 2004) and the lowest $v \sin i = 192$ km s^{-1}, the period should still be less than 3.6 d. For higher $v \sin i$ values, the period should be even shorter. A 4.18-d rotation period implies a stellar radius greater than $\sim 16 R_\odot$. So the adopted radius is critical to accommodate $P_{\rm rot} = 4.18$ d. From the bottom panel of Figure 5.2, we can see that if $R \simeq 16 R_\odot$, a

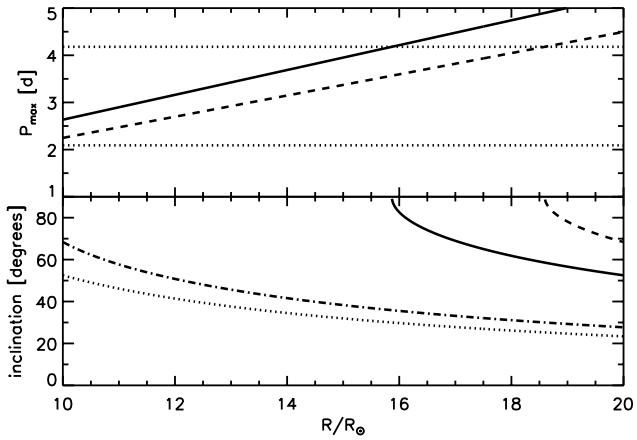

Figure 5.2: *Top*: Maximum rotation period as a function of the stellar radius for $v \sin i$ = 192 km s^{-1} (solid) and $v \sin i$ = 225 km s^{-1} (dashed). The horizontal dotted lines indicate where $P_{\rm max}$ = 2.09 d and $P_{\rm max}$ = 4.18 d. *Bottom*: Inclination angle as a function of the stellar radius for $v \sin i$ = 192 km s^{-1} and $P_{\rm rot}$ = 4.18 d (solid), $v \sin i$ = 192 km s^{-1} and $P_{\rm rot}$ = 2.09 d (dotted), $v \sin i$ = 225 km s^{-1} and $P_{\rm rot}$ = 4.18 d (dashed), $v \sin i$ = 225 km s^{-1} and $P_{\rm rot}$ = 2.09 d (dash-dotted).

rotation period of 4.18 d corresponds to an inclination angle of 90° whereas a rotation period of 2.09 d yields an inclination angle of ∼30°. The same reasoning applies for the highest $v \sin i$ = 225 km s^{-1}: a 4.18-d rotation period implies a stellar radius greater than $\sim 18.5 R_{\odot}$, and when $R \simeq 18.5 R_{\odot}$, a rotation period of 2.09 d yields an inclination angle of ∼30°. However, an inclination angle of the order of 30° is not consistent with the fact that we see NRP travelling bumps only going from blue to red in the dynamic quotient spectra of ξ Per data (see figures 2 and 3 of de Jong *et al.* 1999).

So this analysis, along with previous spectroscopic analyses by de Jong *et al.* (1999) shows that the longer period $P_{\rm rot}$ = 4.18 d is indeed favoured, and the shorter 2.09 d period is more or less excluded. This analysis also gives a lower limit on the stellar radius. Our preferred value of $18.5 R_{\odot}$, at a distance of 380 pc (*Hipparcos*, van Leeuwen 2007), implies that the angular diameter of ξ Per is roughly 0.45 mas, a diameter that

would be measurable using interferometry (e.g. Boyajian *et al.* 2013).

5.4.2 Photometry

The outcome of our time–frequency analysis of the *MOST* data is plotted in Figure 5.3. On the overall Fourier power spectrum, we see a 3σ background noise limit of about 0.1 mmag at $f = 2$ d^{-1} dropping to 0.03 mmag at the Nyquist frequency of 7.13 d^{-1}.

Then, below 2 d^{-1}, we see a series of about 10 peaks between $f = 0.8$ d^{-1} [$P = 1.25$ d] and $f = 1.7$ d^{-1} [$P = 0.59$ d] with amplitudes up to 0.3 mmag, and half a dozen peaks between $f = 0.20$ d^{-1} [$P = 5$ d] and $f = 0.55$ d^{-1} [$P = 1.82$ d] up to 1.0 mmag. The time-dependent part of Figure 5.3 also shows that power peaks at a given frequency do not last more than a couple of rotations.

These impressions are quantified in Table 5.I, which lists the 12 most significant frequencies from the whole data set, using Period04 (Lenz & Breger 2005). The three significant peaks (f_1, f_2, f_3) with S/N > 4.0 occur in a narrow range from $f = 0.40$ d^{-1} [$P = 2.5$ d] to 0.55 d^{-1} [$P = 1.82$ d], which coincides with the dominating DACs frequency at $f = 0.48$ d^{-1} ($P = 2.09$ d, de Jong *et al.* 2001); with two nearly equal DACs on average per rotation cycle, this corresponds to the best estimate of the rotation period of 4.18 d. Two possibly significant frequencies with S/N between 3.0 and 4.0 occur at about half and four times this frequency, respectively. Seven frequencies are marginal (S/N = 2.5 – 3.0) and occur mostly at simple multiples of the primary group of frequencies at $f \sim 0.5$ d^{-1}. Beyond $f = 2$ d^{-1}, no outstanding peaks are seen.

In particular, we fail to see the $l = 3$ p mode from the spectroscopic analysis of de Jong *et al.* (1999), which is not surprising, given that photometry is usually blind to all but the lowest order pulsations, of which there appear to be none. The question then arises whether *MOST* may be seeing longer period (low-order) g-mode pulsations. While

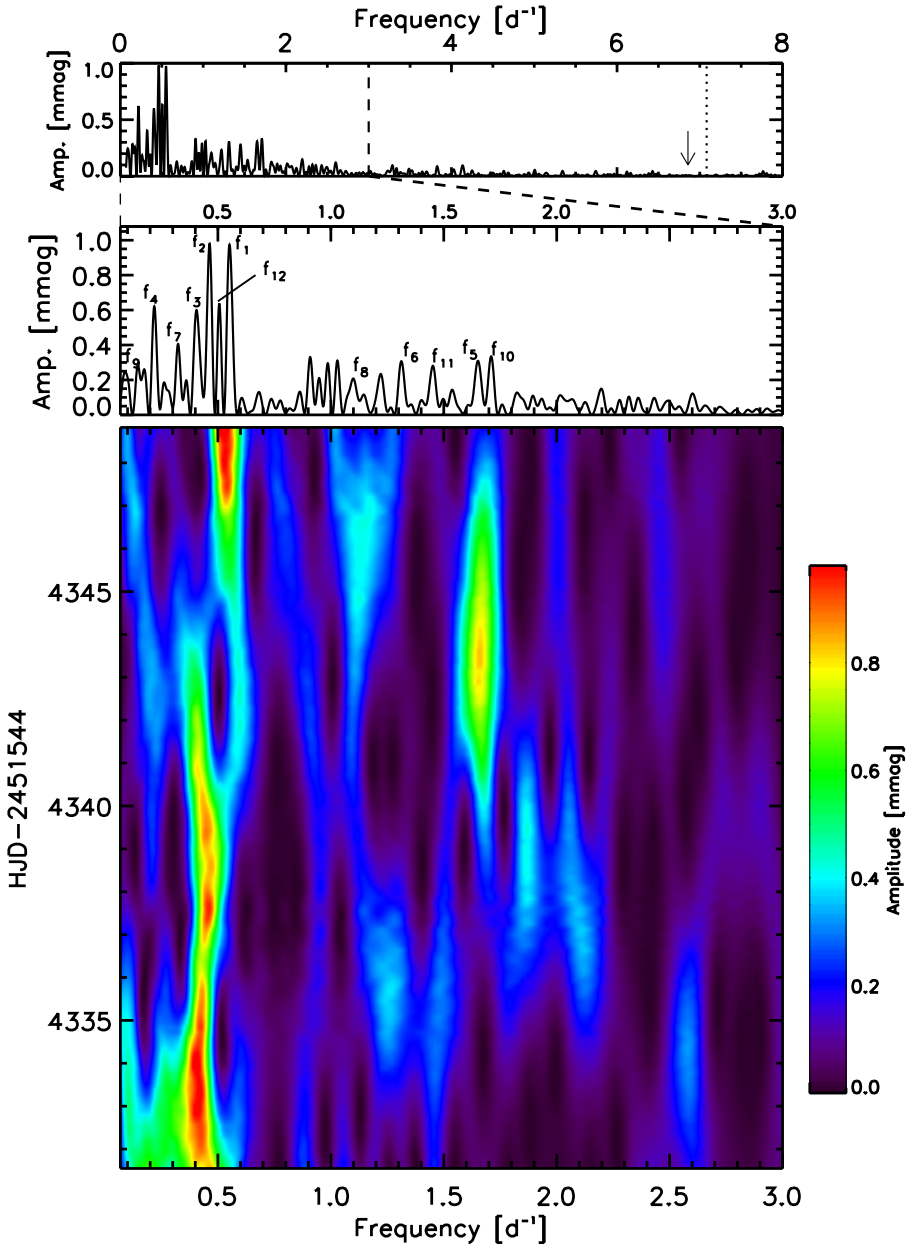

Figure 5.3: *Top*: Lomb–Scargle periodogram of the full binned *MOST* light curve of ξ Per, out to and beyond the Nyquist frequency shown as a vertical dotted line at 7.08 d^{-1}. The arrow indicates that there is no peak at $f = 6.86$ d^{-1} ($P = 3.5$ h). *Middle*: Zoom on the frequencies below 3 d^{-1}. The 12 frequencies from Table 5.I are indicated. *Bottom*: Time–frequency diagram corresponding to the middle panel.

Table 5.I: List of the 12 most significant frequencies from the global Fourier analysis (PERIOD04) of the *MOST* light curve. The starting time for phase values is HJD–2451544 = 4325.547363.

	Frequency [d^{-1}]	Period [d]	Amplitude [mmag]	Phase	S/N
f_1	0.55 ± 0.003	1.82 ± 0.01	0.90 ± 0.11	0.58 ± 0.02	4.9
f_2	0.46 ± 0.006	2.17 ± 0.03	0.98 ± 0.11	0.47 ± 0.02	5.2
f_3	0.41 ± 0.003	2.44 ± 0.02	0.93 ± 0.11	0.64 ± 0.02	5.0
f_4	0.22 ± 0.003	4.55 ± 0.06	0.70 ± 0.11	0.61 ± 0.03	3.8
f_5	1.65 ± 0.004	0.61 ± 0.001	0.66 ± 0.11	0.88 ± 0.03	3.6
f_6	1.31 ± 0.004	0.76 ± 0.002	0.56 ± 0.11	0.96 ± 0.03	3.0
f_7	0.32 ± 0.005	3.13 ± 0.05	0.50 ± 0.11	0.06 ± 0.04	2.8
f_8	1.10 ± 0.004	0.91 ± 0.003	0.55 ± 0.11	0.43 ± 0.02	2.9
f_9	0.09 ± 0.004	11.11 ± 0.49	0.55 ± 0.11	0.11 ± 0.03	2.9
f_{10}	1.71 ± 0.004	0.58 ± 0.001	0.53 ± 0.11	0.98 ± 0.04	3.0
f_{11}	1.45 ± 0.005	0.69 ± 0.002	0.50 ± 0.11	0.36 ± 0.04	2.7
f_{12}	0.50 ± 0.007	2.00 ± 0.03	0.52 ± 0.11	0.92 ± 0.02	2.8

no definitive answer can be given, we do note that we see no recognizable frequency patterns among those peaks that were seen (see Table 5.I) that would support this. Also, fitting the three best frequencies (or even all 12 from Table 5.I) to the light-curve in Figure 5.1 leads to a relatively poor match, with significant stochastic residuals. If pulsations dominated the variability, this kind of curve would match the observed power spectrum very well with negligible residuals, as is the case with the rapidly rotating, pulsating O9.5V star ζ Ophiuchi (Walker *et al.* 2005). This is not the case for ξ Per, so even longer period g mode pulsations do not seem likely.

An alternate hypothesis might be that we are seeing variations due to surface bright spots. But then why several frequencies instead of only one dominating frequency? One conceivable reason might be due to differentially rotating spots at different latitudes overlapping in time. However, even if there are spots stretching from the equator

to near the pole, differential rotation in massive stars is not enough to explain the spread in frequency of even just the three strongest frequencies in Table 5.I in the range $f = 0.40 - 0.55$ ($\Delta f/f \simeq 30\%$). Actually, considering the models of fast-rotating early-type stars established by Espinosa Lara & Rieutord (2013), the surface differential rotation curves as a function of stellar mass tend to be flat beyond $14 M_{\odot}$ (see their figure 15) and an extrapolation up to $40 M_{\odot}$ leads to a difference of at most 10% in rotation periods between the equator and the poles.

Therefore, we attempted to test whether we could reproduce the observed main frequencies with a simple model of spots forming and fading, but always with the same rotation period $P_{\rm rot} = 4.18$ d. Panels (a) and (b) of Figure 5.4 show examples of idealized model light curves with $11-12$ spots at the equator with $i = 90^{\circ}$ of varying intensity and duration. In these model light curves, we can identify 11-12 main peaks from rotating spots at independent starting times. Each spot lasts a maximum of $2 - 3$ rotations. This was chosen to be consistent with the behaviour of the time-dependent part of Figure 5.3. This is also consistent with theoretical predictions that the lifetime of the magnetic field that could be generated in the sub-surface convective zone of massive stars is the turnover time of this convective layer (Cantiello & Braithwaite 2011) which, although a priori independent of rotation, turns out to be of the same order as the rotation period. Cantiello & Braithwaite (2011) also predicted a lower limit of the order of hours for the lifetime of such magnetic spots in a hot massive star, as well as an upper limit of ~50 yr for a $20 M_{\odot}$ star and ~4 yr for a $60 M_{\odot}$ star. It is worth noticing that compared to the Sun, the spot lifetimes considered here are similar to that of large sunspots and sunspot groups (Ringnes 1964; Foukal 2004; Henwood *et al.* 2010).

In our model light curves, each small spot is assumed to follow an intensity law of the form $\cos\theta$, where θ is the angle subtended by the spot as seen from the centre of

the star, and depends on the rotational phase. The factor of $\cos\theta$ allows for projection effects. Because the intensity should be zero when the spot disappears behind the star, the analytical expression of this function for the ith spot is then:

$$f^{(i)}(t) = \max\left\{A^{(i)}_{\max}\cos\left[\frac{2\pi}{P_{\rm rot}}\left(t - t^{(i)}_{\max}\right)\right], 0\right\} \tag{5.1}$$

where $P_{\rm rot}$ is the rotation period and $t^{(i)}_{\max}$ the time at which the spot reaches its maximum amplitude $A^{(i)}_{\max}$. This main function is modulated by the growth law and the decay law. In the case of the Sun, sunspots emerge fast on a time-scale of a few hours (see e.g. Solanki 2003) and start to decay right after their emergence. The decay law of sunspots was initially thought to be linear (e.g. Bumba 1963; Moreno-Insertis & Vazquez 1988) but quadratic laws were also proposed (e.g. Petrovay & van Driel-Gesztelyi 1997). In our simulations, the growth law and the decay law are assumed to be simply linear, resulting in an envelope function of the form

$$\mathcal{E}^{(i)}(t) = \begin{cases} \dfrac{1}{\tau^{(i)}_{\rm rise}}\left[t - t^{(i)}_{\max} + \tau^{(i)}_{\rm rise}\right] & \text{for } t \leq t^{(i)}_{\max} \\ -\dfrac{1}{\tau^{(i)}_{\rm dec}}\left[t - t^{(i)}_{\max} - \tau^{(i)}_{\rm dec}\right] & \text{for } t > t^{(i)}_{\max} \end{cases} \tag{5.2}$$

where $\tau^{(i)}_{\rm rise}$ and $\tau^{(i)}_{\rm dec}$ are the *duration* of the growth and the decay phases, respectively. The growth time of a spot is taken to be a tenth of the duration of the decay phase, so that these two parameters are not independent and can be both constrained when defining the lifetime $\tau^{(i)} = \tau^{(i)}_{\rm rise} + \tau^{(i)}_{\rm dec}$ of the spot. Also, by analogy to the Gnevishev–Waldmeier relation for the Sun, which states the proportionality between the maximal area $\mathcal{S}_{\max}$ of a sunspot group and its lifetime τ ($\mathcal{S}_{\max}/\tau = 10$ millionth of the solar hemisphere per day, Gnevyshev 1938; Waldmeier 1955) and whose validity for individual

Table 5.II: Parameters for each spot in model 1 and model 2. The labels are those used to identify each single spot in Figure 5.4. For each spot having a lifetime τ, $t_{\max}$ is the time when the spot reaches its maximum amplitude $A_{\max}$.

	Model 1			Model 2		
Spot label	$t_{\max}$ [HJD-2451544]	$A_{\max}$ [mmag]	τ [d]	$t_{\max}$ [HJD-2451544]	$A_{\max}$ [mmag]	τ [d]
1	4325.76	9.0	11.26	4327.63	9.6	12.06
2	4327.84	10.1	12.67	4329.72	7.2	9.01
3	4333.06	5.6	7.04	4331.81	1.8	2.25
4	4334.52	7.5	9.39	4335.35	7.2	9.01
5	4337.44	7.9	9.86	4337.23	6.0	7.51
6	4340.36	6.4	7.98	4338.27	2.4	3.00
7	4342.44	7.5	9.39	4342.24	4.8	6.01
8	4344.74	8.3	10.33	4344.32	6.0	7.51
9	4346.41	5.3	6.57	4347.24	5.4	6.76
10	4347.45	3.8	4.69	4349.33	8.4	10.51
11	4349.54	7.5	9.39	4351.41	7.2	9.01
12	4351.62	11.3	14.08	-	-	-

sunspots was established by Petrovay & van Driel-Gesztelyi (1997), the ratio $A^{(i)}_{\max}/\tau^{(i)}$ is assumed to be constant in our simulations. The constant of proportionality was assessed by assuming that the largest spot that can induce a variation of up to ~10 mmag in the light curve (see Figure 5.1) would last three rotations. This yields a constant of proportionality of 0.8 mmag d^{-1} between $A^{(i)}_{\max}$ and $\tau^{(i)}$.

Finally, the synthetic light curve containing N spots is defined by $\mathcal{I}(t) = \sum_{i=1}^{N} f^{(i)}(t) \cdot \mathcal{E}^{(i)}(t)$. We also include white Gaussian noise in our simulations. No assumptions were made concerning the exact shape of the spots and their angular extent in two dimensions, assuming that the definitions of $f^{(i)}(t)$ and the envelope function $\mathcal{E}^{(i)}(t)$ for each spot are sufficient to study the light variations that they induce in the continuum. Also, it is worth noticing that our simulations do not include limb-darkening effects. Table 5.II summarizes the parameters ($t^{(i)}_{\max}$, $A^{(i)}_{\max}$, $\tau^{(i)}$) for each individual spot in the synthetic light curves presented in Figure 5.4. Although we do not expect the simulated

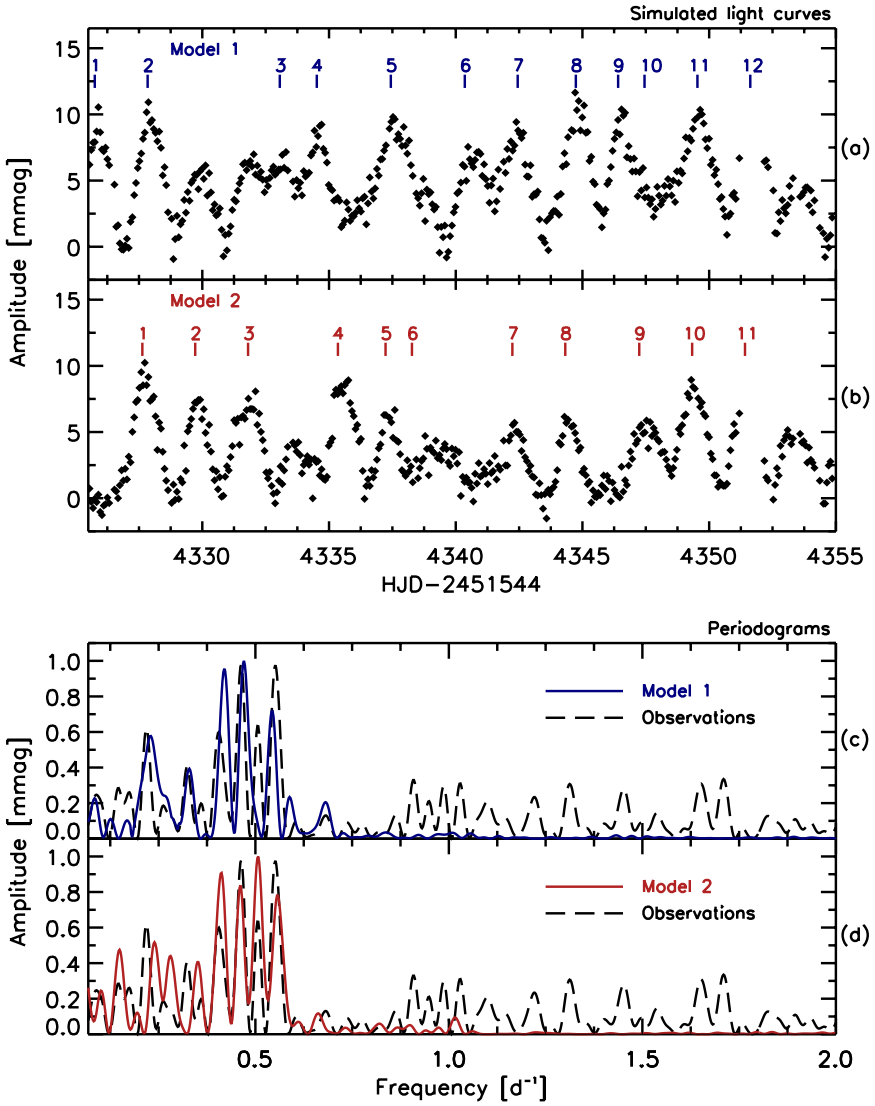

Figure 5.4: *Panels (a) and (b)*: Two model light curves with $11 - 12$ different spots each lasting typically $2 - 3$ rotations and with random starting times over the same time interval as the actual *MOST* observations. The labelled vertical dashes indicate where each spot reaches its maximum brightness. *Panels (c) and (d)*: Periodograms of the spot models (blue and red solid curves for model 1 and model 2, respectively) compared to the periodogram of the *MOST* light curve of ξ Per (black, dashed). The power peaks beyond $f = 0.8$ d^{-1} in the observed data are marginally significant and might be accounted for by harmonics or aliases of the main peaks around 0.5 d^{-1} or by adding more smaller spots.

light curves to match the observed one in any exact way, the power spectra in panels (c) and (d) of Figure 5.4 reveal four significant power peaks in a similar range as observed for the main frequencies. The remaining peaks in the simulations are harmonics of the stronger peaks. It should be emphasized that this is not a unique solution; true simulation of the observed light curve is a formidable task, with many parameters (e.g. spot number, intensity-distribution, starting time, duration, decay law, etc) for which we have no real independent constraints. Treating this as an inverse problem would also be impractical, given the complexity and uncertainty of the nature of the spots. Nevertheless, we are content to have found two solutions which at least qualitatively match what we see; in fact, there are many more possible solutions. Note that the time–frequency analysis shows wandering frequencies, compatible with the idea of a multitude of interfering spots with different start times and durations but all rotating at the same rate, or nearly so.

5.5 Discussion

Our analysis (Section 5.4.2) shows that the *MOST* photometric variability is predominately driven by rotating surface bright spot modulations. The largest question is the origin of such spots. If these spots are corotating, they must be fixed to the stellar surface like sunspots and thus not be related to NRP. If non corotating, the spots may be related to low g mode NRP, either prograde or retrograde. The former interpretation (corotation) is more consistent with the behaviours of the *MOST* light curve and its periodogram showing that the rotation time-scales match the estimated stellar rotation period of $P_{rot} = 4.18$ d. However, at this point, it is worth noting that our models which reproduce the Fourier spectrum (see Figure 5.4) involve more than two corotating spots per rotation cycle. This may suggest that there could be many more

DACs of progressively lower amplitudes in ξ Per, in contrast to the dominant two-DAC per rotation view of ξ Per that has been seen with *IUE* (Kaper *et al.* 1999). The detectability of these DACs of lower strengths requires high signal-to-noise, high spectral resolution ultraviolet spectroscopy.

In the *MOST* light curve, one might wonder if instead we are seeing the photometric modulations directly of DACs/CIRs and not the bright spots that might cause them. However, for the low density wind of ξ Per ($\dot{M} \leq 1.2 \times 10^{-6} M_{\odot}$ yr^{-1} including clumping corrections, Puls *et al.* 2006), the stellar wind does not emit continuum light in the optical. A study of the spectral energy distributions of Be stars and evolved massive stars showed that, apart from the cases of extremely strong $\dot{M}$ or disc, the flux excess is not important in the optical (Touhami *et al.* 2010). The stellar wind only becomes important at long wavelengths where free–free and bound–free emission processes begin to dominate and cause larger amounts of flux excess. The stellar wind only scatters continuum light from the central star, which then becomes highly diffused.

The connection of the light variations to corotating spots is surprising because such hot stars were long thought not to have convection zones except deep in their interior core region where highly temperature-dependent nuclear fusion is going on. This has changed, however, with the modelling work of Cantiello *et al.* (2009b), who find for the first time a subsurface convection zone due to partial ionization (PIZ) near $T \sim 170000$ K of the abundant Fe-like elements. This zone is capable of driving acoustic and gravity waves, which reach the stellar surface through a radiative skin and in turn could create turbulence in the strong stellar winds from hot luminous stars, which manifest themselves as wind clumps. This PIZ may also be the source of a global magnetic field, winding up toroidally with stochastic buoyancy breakouts at the surface causing corotating magnetic bright spots at the surface of the star (Cantiello & Braithwaite 2011). Such spots would normally occur in close north–south polarity pairs, as on the

Sun, and would not be easily detectable via Zeeman splitting with current spectropolarimeters due to cancellation effects of the close bipolar field. Kochukhov & Sudnik (2013) estimated the detectability of a longitudinal magnetic field in early-type stars by putting random magnetic spots on the stellar surface and using results of the recently completed Magnetism in Massive Stars survey (MiMeS; Wade *et al.* 2011b, 2012). Under a number of conditions such magnetic spots are not detectable with the best available instruments (CFHT/ESPaDOnS, TBL/NARVAL, ESO/HARPSpol). Even the global field could be below current detection limits (59 G upper limit for ξ Per as mentioned in Section 5.2). However, when these spots (unlike the optically dark spots on the Sun) rotate with the star, they presumably cause some of the photometric (continuum light) modulations that we see in some O stars.

These corotating magnetic spots were also proposed to be at the base of the so-called 'stellar prominences' that trigger the cyclical variabilities observed in the wind lines of some O stars, e.g. the case of the O6 supergiant λ Cep (Sudnik & Henrichs 2016). Concerning the latter, Uuh-Sonda *et al.* (2014) recently reported an intensive spectroscopic study of this star in search of the two pulsation frequencies found by de Jong *et al.* (1999). Focusing on lines stronger than the HeI λ4713 line studied by de Jong *et al.* (1999), their spectra with S/N lower than that of the data used by de Jong *et al.* (1999) failed to reveal any stable frequency which might be connected to pulsations. Given that λ Cep and ξ Per share many similar properties, including the presence of strong DACs that do not repeat exactly from one rotation to the next, we suggest that the complex behaviours of the LPVs reported by Uuh-Sonda *et al.* (2014) are the results of rotating spots. These spots come and go on time-scales of up to several times the rotation period similar to the spots we observed on ξ Per.

5.6 Conclusion and future work

Some recent observations of high-precision photometric monitoring, especially from space where one can collect large amounts of precise, high-cadence, uninterrupted data, are revealing the presence of rotating spots on the surfaces of hot luminous OB stars (e.g. Degroote *et al.* 2010b; Aerts *et al.* 2013) and their descendant Wolf–Rayet (WR) stars (Chené *et al.* 2011; Moffat et al., in prep.). Most likely, we are seeing the detection of corotating bright spots at or near the stellar surface. ξ Per is the first clear case of corotating bright spots on an O star along with a plausible link to DACs. Because the case of ξ Per is not unique regarding UV DACs, this kind of photometric covariability should be observable and should be similar in other O-type stars showing DACs.

More work is needed to detect corotating bright spots in other O stars, preferably using high-precision photometric monitoring from space. Most late-type O stars are still in the β Cep instability strip, so their light curves could be dominated by NRP, like that of ζ Oph (Walker *et al.* 2005; Howarth *et al.* 2014). Thus, it would be more appropriate to look at early/mid-type O stars. The next generation of nanosatellites for asteroseismology, *BRIght Target Explorer* (*BRITE-Constellation*, http://www.brite-constellation.at/), consisting of a network of six independent 30-mm space telescopes, is expected to photometrically monitor 36 O stars with $V < 6$ mag at a precision level of ~20 ppm in Fourier space. Fourteen of these targets are early/mid-type O stars. The mission will then contribute in determining if the corotating bright spots phenomenon is universal among O stars. Such bright spots may be the drivers of DAC activity, ubiquitous to all O and maybe also their descendant WR and other types of evolved massive stars.

Acknowledgments

We gratefully acknowledge useful conversations with Paul Charbonneau, Nicole St-Louis, Stan Owocki, and Alex Fullerton in relation to this project. DBG, JMM, AFJM, and SMR are supported by NSERC (Canada), with additional support to AFJM from FQRNT (Québec). ANC gratefully acknowledges support from the Chilean Centro de Astrofísica FONDAP no. 15010003 and the Chilean Centro de Excelencia en Astrofísica y Tecnologías Afines (CATA). ANC also received support from the Comite Mixto ESO-Gobierno de Chile and GEMINI-CONICYT no. 32110005. VA acknowledges the Stellar Astrophysics Centre (SAC) funded by The Danish National Research Foundation. VA also received support from the ASTERISK project (ASTERoseismic Investigations with SONG and Kepler) funded by the European Research Council (Grant agreement no.: 267864). RK and WWW are supported by the Austrian Space Agency and the Austrian Science Fund. NDR acknowledges his CRAQ (Centre de Recherche en Astrophysique du Québec) fellowship.

6

La Supergéante ζ Puppis

BRITE-Constellation[*] High Precision Time-Dependent Photometry of the Early O-Type Supergiant ζ Puppis Unveils the Photospheric Drivers of its Small- and Large-Scale Wind Structures

Tahina Ramiaramanantsoa[1,2], Anthony F. J. Moffat[1,2], Robert Harmon[3], Richard Ignace[4], Nicole St-Louis[1,2], Dany Vanbeveren[5], Tomer Shenar[6], Herbert Pablo[1,2], Noel D. Richardson[7], Ian D. Howarth[8], Ian R. Stevens[9], Caroline Piaulet[1], Lucas St-Jean[1], Thomas Eversberg[10], Andrzej Pigulski[11], Adam Popowicz[12], Rainer Kuschnig[13], Elżbieta Zocłońska[14], Bram Buysschaert[15,16], Gerald Handler[14], Werner W. Weiss[13], Gregg A. Wade[17], Slavek M. Rucinski[18], Konstanze Zwintz[19], Paul Luckas[20], Bernard Heathcote[21], Paulo Cacella[22], Jonathan Powles[23], Malcolm Locke[24], Terry Bohlsen[25], André-Nicolas Cené[26], Brent Miszalski[27,28], Wayne L. Waldron[29], Marissa M. Kotze[27,28], Enrico J.Kotze[27], and Torsten Böhm[30,31]

(Affiliations are listed at the end of the chapter)

Published in the *Monthly Notices of the Royal Astronomical Society, Volume 473, Issue 4, pages 5532–5569,* 01 February 2018 (Online 13 October 2017)

[*]Based on data collected by the *BRITE-Constellation* satellite mission, designed, built, launched, operated and supported by the Austrian Research Promotion Agency (FFG), the University of Vienna, the Technical University of Graz, the Canadian Space Agency (CSA), the University of Toronto Institute for Aerospace Studies (UTIAS), the Foundation for Polish Science and Technology (FNiTP MNiSW), and National Science Centre (NCN).

6.1 Abstract

From 5.5 months of dual-band optical photometric monitoring at the 1 mmag level, *BRITE-Constellation* has revealed two simultaneous types of variability in the O4I(n)fp star ζ Puppis: one single periodic non-sinusoidal component superimposed on a stochastic component. The monoperiodic component is the 1.78-d signal previously detected by *Coriolis/Solar Mass Ejection Imager*, but this time along with a prominent first harmonic. The shape of this signal changes over time, a behaviour that is incompatible with stellar oscillations but consistent with rotational modulation arising from evolving bright surface inhomogeneities. By means of a constrained non-linear light-curve inversion algorithm, we mapped the locations of the bright surface spots and traced their evolution. Our simultaneous ground-based multi-site spectroscopic monitoring of the star unveiled cyclical modulation of its He II λ4686 wind emission line with the 1.78-d rotation period, showing signatures of corotating interaction regions that turn out to be driven by the bright photospheric spots observed by *BRITE*. Traces of wind clumps are also observed in the He II λ4686 line and are correlated with the amplitudes of the stochastic component of the light variations probed by *BRITE* at the photosphere, suggesting that the *BRITE* observations additionally unveiled the photospheric drivers of wind clumps in ζ Pup and that the clumping phenomenon starts at the very base of the wind. The origins of both the bright surface inhomogeneities and the stochastic light variations remain unknown, but a subsurface convective zone might play an important role in the generation of these two types of photospheric variability.

6.2 Introduction

Spaceborne high-precision photometric monitoring of stars as a means to probe their intrinsic light variations and trace back the underlying physical mechanisms has only emerged over the past two decades (Buzasi 2000; Buzasi *et al.* 2000). Particularly, this practice is even less frequent on hot luminous massive O-type stars (with $M_{\rm init} \gtrsim 20 M_{\odot}$), partly because of their scarcity which is reflected in the decreasing initial stellar mass function (IMF) following a power law of index -2.35 for masses between 1.25 and $150 M_{\odot}$ (Salpeter 1955; Bastian *et al.* 2010). Nevertheless, with their strong radiation-driven stellar winds and their termination as supernovae, O stars and their descendant Wolf-Rayet stars are important drivers of the chemical enrichment of galaxies and the Universe. Understanding the physical origin of their intrinsic variations may provide constraints not only on their internal properties (e.g. convective core overshoot, possible existence of a sub-surface convection zone, and magnetic fields) but also their global wind properties, and the complex physics of their photosphere-wind interface.

6.2.1 Space photometry of O stars

So far a total of 18 O stars have been monitored through space photometry (table 3 of Buysschaert *et al.* 2015, adding the recently reported photometric observations of the δ Orionis system by Pablo *et al.* 2015, the ι Orionis binary system by Pablo *et al.* 2017, the magnetic hot supergiant ζ Orionis Aa by Buysschaert *et al.* 2017, and the late-O-type supergiant HD 188209 by Aerts *et al.* 2017). The *Wide-field InfraRed Explorer* (*WIRE*, Buzasi 2000) was the pioneer of this practice by including the late-O-type subgiant ζ Oph in its sample of 90 targets (Bruntt 2007). Then followed contributions from the *Microvariability and Oscillations of STars* microsatellite (*MOST*, Walker *et al.* 2003), the *COnvection ROtation and planetary Transits* satellite (*CoRoT*, Baglin *et al.*

2006; Auvergne *et al.* 2009), the *Solar Mass Ejection Imager* (*SMEI*, Eyles *et al.* 2003) instrument onboard the *Coriolis* satellite, and the *Kepler* spacecraft (Borucki *et al.* 2010; Howell *et al.* 2014). Various types of intrinsic variations were reported from these space-based photometric observations, namely β Cep-like pulsations for the late-O-type stars (ζ Oph, Walker *et al.* 2005, Howarth *et al.* 2014; HD 46202, Briquet *et al.* 2011; HD 256035, Buysschaert *et al.* 2015), one case of the presence of p-modes with finite lifetimes analoguous to solar-like oscillations (HD 46149, Degroote *et al.* 2010b), two cases of tidally influenced pulsations (δ Ori Aa, Pablo *et al.* 2015; ι Ori, Pablo *et al.* 2017), one case of a possible oscillatory convection g-mode (ζ Pup, Howarth & Stevens 2014), six cases of possible internal gravity waves (IGWs: HD46223, HD46150, HD 46966, Blomme *et al.* 2011; Aerts & Rogers 2015; HD44597, HD 255055, Buysschaert *et al.* 2015; HD 188209, Aerts *et al.* 2017) and five cases of possible rotational modulation (HD 46149, Degroote *et al.* 2010b; HD 46223, Blomme *et al.* 2011; ξ Per, Ramiaramanantsoa *et al.* 2014; EPIC 202060097, EPIC 202060098, Buysschaert *et al.* 2015). Notably, some stars show simultaneously different types of intrinsic variations. With its sample of 36 O stars brighter than $V = 6$, the recently launched, commissioned and now operational nanosatellites forming *BRIght Target Explorer* (*BRITE-Constellation*, Weiss *et al.* 2014; Pablo *et al.* 2016) will almost triple the current numbers and improve the view on this broad range of O star intrinsic variability.

6.2.2 ζ Puppis

Standing out from the aforementioned restricted sample of O-type stars is the hot, bright, rapidly-rotating, single, runaway supergiant ζ Puppis (Table 6.I). Owing to its brightness, proximity and status as a single star, ζ Pup has become a key object for understanding the properties of O-type stars and hot stellar winds. Therefore, it is not

Table 6.I: Stellar parameters for ζ Puppis (HD 66811). The parameter β denotes the exponent of the usual β-law velocity generally adopted in hot stellar winds, while f_∞ denotes the asymptotic value of the clumping filling factor at the outer boundary of the stellar wind.

Parameter		Value	References
Spectral type		O4I(n)fp	[1]
V		2.256 ± 0.019	[2]
$B-V$		-0.276 ± 0.012	[2]
$U-B$		-1.108 ± 0.013	[2]
$v_\mathrm{e} \sin i$	[km s^{-1}]	219 ± 18	[3]
v_rad	[km s^{-1}]	-23.9 ± 2.9	[4]
v_tan	[km s^{-1}]	55.0 ± 16.6	[5]
Distance	[kpc]	0.46 ± 0.04	[6]
Age	[Myr]	$3.2^{+0.4}_{-0.2}$	[6]
$\log(L/L_\odot)$	[cgs dex]	5.91 ± 0.1	[6]
T_eff	[kK]	40.0 ± 1.0	[6]
$\log g$	[cm s^{-2}]	3.64 ± 0.1	[6]
R	[$R_\odot$]	18.99 ± 3.80	[7]
M	[$M_\odot$]	$56.1^{+14.5}_{-11.6}$	[6]
$\dot{M}$	[$M_\odot$ yr^{-1}]	$1.9 \pm 0.2 \times 10^{-6}$	[6]
v_∞	[km s^{-1}]	2300 ± 100	[6]
β		0.9	[6]
f_∞		0.05	[6]

[1]Galactic O-Star Gatalog: Sota *et al.* (2014), [2]Maíz-Apellániz *et al.* (2004), [3]Howarth *et al.* (1997), [4]Gontcharov (2006), [5]Moffat *et al.* (1998), [6]Bouret *et al.* (2012), [7]Martins *et al.* (2005)

surprising why several observational studies have been conducted on ζ Pup across a wide range of wavelength: in the X-ray (e.g. Hervé *et al.* 2013; Nazé *et al.* 2013, and references therein), in the ultraviolet (UV, Prinja *et al.* 1992; Howarth *et al.* 1995), in the optical (Davis *et al.* 1970; Reid & Howarth 1996; Howarth & Stevens 2014), as well as in the radio and submillimetre (Blomme *et al.* 2003). Amongst these studies, time-resolved spectroscopic and photometric observations have unveiled a number of variabilities on time-scales ranging from hours to a couple of days (table 1 in Howarth & Stevens 2014).

The first variability reported on ζ Pup came from the monitoring of the central absorption reversal of its Hα wind emission line profile which was seen to vary non-sinusoidally with a period of 5.075 ± 0.003 d (Moffat & Michaud 1981). Subsequent ground-based optical photometric observations in the Strömgren b filter (Balona 1992), as well as UV spectroscopic studies (Howarth *et al.* 1995) revealed periods compatible with this one ($\sim$5.2 d). Up to this time this 5.1 d period was attributed to the rotation period of the star, which, combined with the measured projected rotational velocity and the radius (Table 6.I), implies that the star is seen almost equator on.

Also, photospheric line-profile variations (LPVs) that were best interpreted as non-radial pulsations (NRPs) with $l = -m = 2$ were detected in ζ Pup, occurring as bumps moving redward across some optical He I, He II, N IV and C IV lines of the star with a period of 8.54 ± 0.05 h (Baade 1986; Reid & Howarth 1996). Additionally, a possibility for the presence of low-order oscillatory convection modes with a period of 1.780938 ± 0.000093 d and semi-amplitude of 6.9 ± 0.3 mmag has been reported from four contiguous years ($2003 - 2006$) of *Coriolis/SMEI* photometric monitoring of the star (Howarth & Stevens 2014).

From the point of view of wind variability, ζ Pup is often used as a laboratory to study the time-dependent properties of wind structures in O-type stars. Such wind structures

are classified in two distinct categories with respect to their spatial extent: small-scale density inhomogeneities dubbed clumps; and large-scale spiral-like structures corotating with the stellar photosphere, the so-called corotating interaction regions (CIRs). Both of these phenomena are now believed to be essentially ubiquitous in O stars (Puls *et al.* 2008).

Observational evidence for the presence of clumps in hot luminous star winds was initially detected in stars in the He-burning, He-rich Wolf–Rayet phase (Schumann & Seggewiss 1975; Moffat *et al.* 1988), a late stage in the evolution of O-type stars (e.g. Lamers *et al.* 1991). In the case of O stars, a phenomenological model consisting of a population of radiatively driven blobs in the wind of ζ Pup was first proposed to explain its observed X-ray luminosity (Lucy & White 1980). Later ζ Pup became the first O-type star confirmed to have a clumpy wind: spectroscopic monitoring of its wind-formed He II λ4686 line profile revealed excess bumps at the ~5% level of the line intensity, propagating from the centre towards the edges of the line, which is a signature of the kinematics of clumps randomly appearing in the inner stellar wind (Eversberg *et al.* 1998). Subsequent studies confirmed these interpretations and detected similar behaviour in other hot stars (Lépine & Moffat 2008).

The physical origin of these clumps still remains to be determined, with two coexistent paradigms to be considered: the first scenario involves line-driving instability that could generate inverse shocks locally compressing wind material to form clumps in a less dense inter-clump medium (Lucy & Solomon 1970; Owocki *et al.* 1988; Feldmeier 1995; Dessart & Owocki 2003), whereas the second one involves a contribution from IGWs that could be excited within a subsurface convection zone and induce the formation of clumps near the photosphere-wind interface (Cantiello *et al.* 2009b) which could then be subsequently enhanced by the first mechanism further out in the stellar wind.

Besides that, the absorption troughs of unsaturated P Cygni profiles of UV resonance

lines of O-type stars are the sites for the appearance and blueward propagation of spectral features called discrete absorption components (DACs), a more general form of features initially called narrow absorption components (Prinja 1988; Howarth & Prinja 1989; Howarth 1992b; Howarth *et al.* 1995; Kaper *et al.* 1999). These features are best interpreted as the spectroscopic manifestations of the presence of Corotating Interaction Regions (CIRs) in the winds of O stars (Mullan 1986), such as those that are also found in the solar wind (Hundhausen 1972). ζ Pup was one of the three program stars observed during extensive UV spectroscopic monitoring with the *International Ultraviolet Explorer (IUE)* (Massa *et al.* 1995a; Howarth *et al.* 1995). A mean DAC recurrence period of 19.23 ± 0.45 h was measured from the analysis of their propagation in the Si IV $\lambda\lambda 1394, 1403$ doublet line of the star. With a 5.1 d rotation period as was believed at that time, ζ Pup would exhibit on average $5 - 6$ DACs per rotation cycle (figure 1 in Howarth *et al.* 1995), which is much more than the average of two dominating DACs per rotation cycle observed in other O stars (Kaper *et al.* 1999).

As for the origin of these CIRs, the canonical hydrodynamical model in O stars involves photospheric perturbations such as corotating bright spots or NRPs which initially enhance the local stellar wind speed, generating wind plasma of a different speed that interacts with the ambient wind to produce compressed material shaped as large spiral arms as they corotate with the star (Cranmer & Owocki 1996). Velocity plateaus forming ahead of the CIR arms are seen as propagating DACs in the absorption troughs of UV P Cygni resonance lines such as C IV $\lambda 1548$ or Si IV $\lambda\lambda 1394, 1403$. Observational evidence for the presence of bright spots on an O star with possible link to its known DACs recurrence period recently emerged from *MOST* photometric monitoring of the single runaway mid-O-type giant ξ Per (Ramiaramanantsoa *et al.* 2014). This discovery raised a motivation to determine if the presence of bright photospheric spots is universal among O stars (like the NAC/DAC phenomenon) and how they are linked to

CIR/DAC activities in the stellar wind. Primarily driven by this purpose, we conducted a coordinated optical observing campaign on ζ Pup spanning $\sim$5.5 months, consisting of space-based photometric monitoring with *BRITE-Constellation* during an observing run on the Vela/Puppis field (December 11, 2014 – June 02, 2015), and contemporaneous multi-site ground-based spectroscopic monitoring of the He II λ4686 line profile of the star. Our *BRITE* observations probe light variations at the level of the stellar photosphere in two passbands, not achievable by any previous space-based mission, while our spectroscopic observations of the He II λ4686 wind emission line allow us to trace any possible activities related to CIRs and clumps in the inner stellar wind.

6.3 Observations

6.3.1 High-precision space photometry

6.3.1.1 *BRITE-Constellation* photometry

BRITE-Constellation (Weiss *et al.* 2014; Pablo *et al.* 2016) as originally planned consists of a network of six nanosatellites each housing a 35-mm format KAI-11002M CCD photometer fed by a 30-mm diameter $f/2.3$ telescope through either a blue filter (390 – 460 nm) or a red filter (545 – 695 nm): *BRITE-Austria (BAb)*, *Uni-BRITE (UBr)*, *BRITE-Heweliusz (BHr)*, *BRITE-Lem (BLb)*, *BRITE-Toronto (BTr)* and *BRITE-Montréal (BMb)*, the last letter of the abbreviations denoting the filter type ("b" for blue and "r" for red). With the exception of *BMb* which failed to detach from the upper stage module of its Dnepr launch vehicle, all the satellites were launched into Low Earth Orbits of orbital period of the order of 100 min, commissioned and now fully operational. With a $\sim 24^\circ \times 20^\circ$ effective field of view, each component of *BRITE-Constellation* performs simultaneous monitoring of 15 – 30 stars brighter than $V \simeq 6$.

A given field is observed typically over a ∼6 month time base and, as far as possible, at least two satellites equipped with different filters are set to monitor the field to ensure dual-band observations.

The seventh field monitored by *BRITE* was the Vela/Puppis field, for which photometry of 32 stars was extracted, ζ Pup being the sole O-type star (not counting the primary component of the WC+O system γ^2 Velorum, as the binary is not resolved by *BRITE*, the *BRITE* detector pixel size being ∼27.3″). Observations of this field were performed by *BAb*, *BTr* and *BHr* (Table 6.II) during ∼5.5 months between December 11, 2014 and June 02, 2015 (HJD $2,457,003.40-176.31$). Short 1 s exposures were taken at a median cadence of 15.3 s during $\sim 1-30\%$ of each ∼100 min *BRITE* orbit, the remaining time unused due to stray light interferences, blocking by the Earth, and limited data download capacity. Observations were performed in stare mode for all satellites and then switched to chopping mode (Pablo *et al.* 2016; Popowicz 2016; Popowicz *et al.* 2017) for *BAb* and *BTr* for the second half of the observing run. Onboard stacking of three consecutive frames was performed only for the first three setups of the *BTr* observations. Raw light curves were extracted using the reduction pipeline for *BRITE* data which also includes corrections for intra-pixel sensitivity (Popowicz *et al.* 2017). Then post-reduction decorrelations with respect to instrumental effects due to CCD temperature variations, centroid position and orbital phase were performed on each observational setup for each satellite according to the method described by Pigulski *et al.* (2016), and flux variations due to changes in point spread function shape as a function of temperature were performed according to the method described by Buysschaert *et al.* (2017). In the resulting final decorrelated light curves, we do not notice any obvious variations on time-scales shorter than the *BRITE* orbital period ($t \lesssim 100$ min) that could be qualified as intrinsic to the star rather than pure instrumental noise. Therefore in order to gain in precision we calculated satellite-orbital mean fluxes to create the final

Table 6.II: *BRITE* photometry of ζ Pup – Journal of observations. N_s indicates the number of frames stacked onboard. Quantities listed in columns $6-9$ were assessed at post-decorrelation stage: $N_{\rm p,tot}$ is the total number of data points, $N_{\rm p,orb}$ is the median number of points per orbit (along with the range of values), $t_{\rm cont}$ is the median contiguous time per orbit during which observations were performed (along with the range of values), and $\sigma_{\rm rms}$ is the quadratic mean value of mean standard deviations per orbit assessed from linear fits of the flux values within the orbits.

Satellite	Start date [HJD-2451545]	End date	Observing mode	$N_{\rm s}$	$N_{\rm p,tot}$	$N_{\rm p,orb}$	$t_{\rm cont}$ [min]	$\sigma_{\rm rms}$ [mmag]
BRITE-Austria	5458.402	5527.991	Stare	1	16198	25 [4 – 48]	6.9 [0.8 – 12.4]	1.41
	5527.920	5621.152	Chopping	1	22981	30 [6 – 40]	11.6 [2.3 – 13.6]	1.19
BRITE-Toronto	5465.758	5535.193	Stare	3	15744	23 [4 – 30]	16.8 [2.2 – 22.0]	1.36
	5535.135	5624.967	Chopping	1	54135	56 [8 – 60]	15.1 [2.3 – 15.6]	0.75
BRITE-Heweliusz	5553.059	5631.313	Stare	1	44747	78 [8 – 161]	15.9 [2.1 – 30.1]	1.40

light curves in the two filter bands. We note that we also perform removal of outliers during the decorrelation process, such that it is reasonable to adopt orbital mean fluxes instead of median fluxes or trimmed mean fluxes or mean flux values within 1/4 and 3/4 quartiles. Then, to extract the orbital means, we tested two different methods : (1) a simple average of the flux values taken within an orbit, and (2) an average taken to be the mid-point of a linear fit of the flux values within an orbit. We noticed no significant difference between the resulting root mean square (rms) values of the mean standard deviations obtained from the two methods, the second one being only slightly better. Therefore we adopted the second method to generate the final binned light curves in the two filter bands which we use to extract information on the intrinsic variability of the star (Figure 6.1).

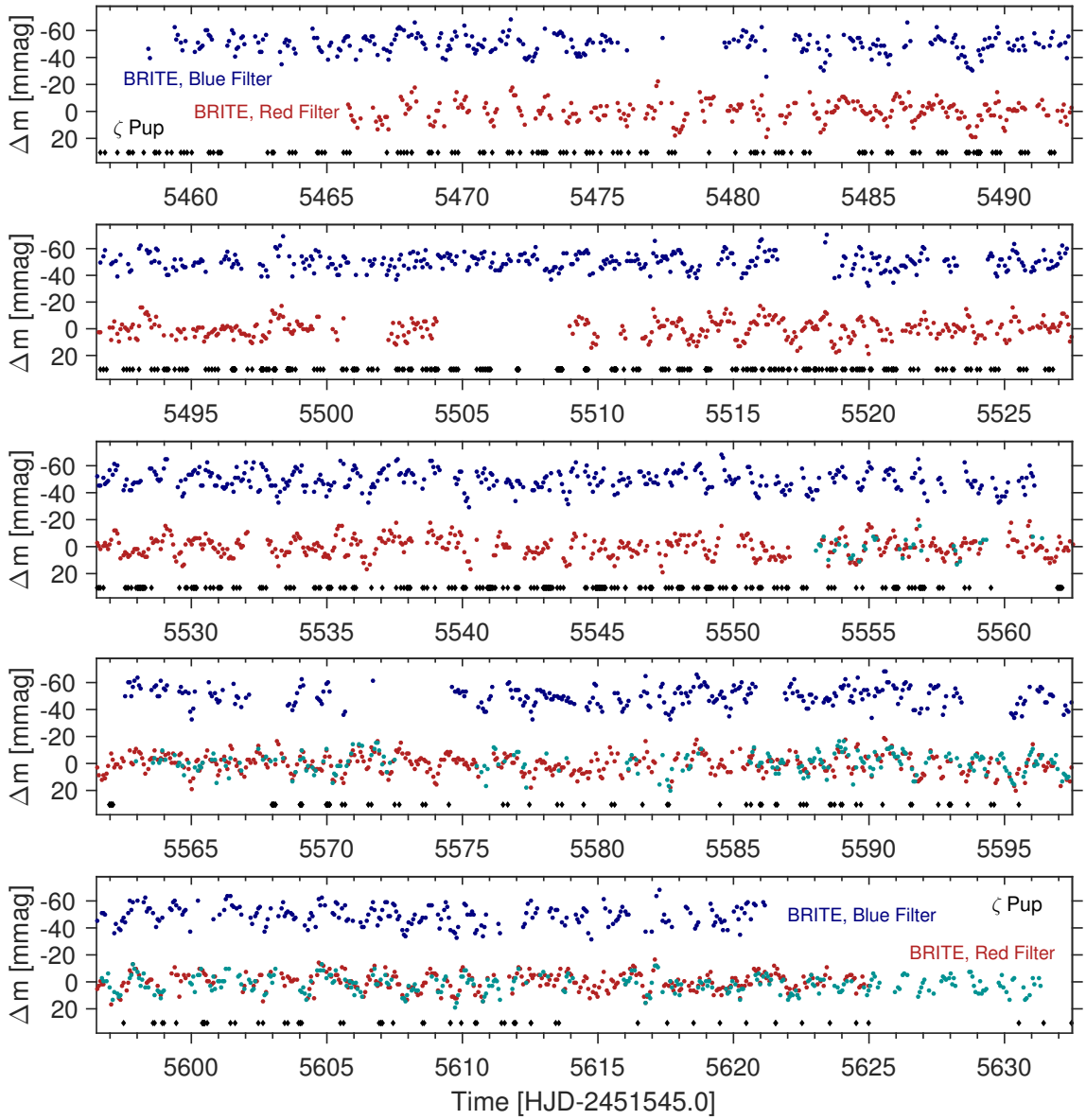

Figure 6.1: Two-colour time series *BRITE* photometry of ζ Pup binned over each *BRITE* orbit. The observations obtained from *BAb*, *BTr* and *BHr* are in blue, red and dark cyan respectively. For better visibility, an offset of 50 mmag was added to the light curve in the blue filter. The temporal coverage of the contemporaneous ground-based spectroscopy is also depicted as small diamonds below the *BRITE* light curves.

Table 6.III: Basic characteristics of the spectroscopic observations involved in our campaign. The facilities are ordered according to East longitude, starting from the closest to the Greenwich meridian. Amateur facilities members of the Southern Astro Spectroscopy Email Ring (SASER; http://saser.wholemeal.co.nz) at the time of the campaign are indicated by a star. Estimates of the typical S/N per spectrum were taken in a portion of continuum in the closest vicinity of He II λ4686.

Observatory	PI/Observer	East longitude	Telescope	Instrument	R	λ range (Å)	N_{sp}	S/N
SAAO	T. Ramiaramanantsoa	20°48′37″	1.9 m	GIRAFFE	39000	4249 – 6513	24	370
Shenton Park ⋆	P. Luckas	115°48′54″	0.35 m	Lhires III	8364	4579 – 4729	257	590
Domain ⋆	B. Heathcote	144°59′21″	0.28 m	Lhires III	8529	4590 – 4738	106	700
Latham ⋆	J. Powles	149°01′41″	0.25 m	Spectra L200	8774	4549 – 4879	65	500
Mirranook ⋆	T. Bohlsen	151°30′35″	0.28 m	Spectra L200	6361	4484 – 5022	1	320
R. F. Joyce ⋆	M. Locke	172°20′59″	0.4 m	Spectra L200	8432	4453 – 4809	22	725
CTIO	T. Ramiaramanantsoa	290°48′23″	1.5 m	CHIRON	24000	4578 – 8762	415	725
Dogsheaven ⋆	P. Cacella	312°05′20″	0.51 m	Lhires III	5780	4550 – 4777	164	420

6.3.1.2 *Coriolis/SMEI* photometry

We also use the archival light curves of ζ Pup recorded by *Coriolis/SMEI* during its 2003 – 2006 seasonal observing runs, published by Howarth & Stevens (2014). The characteristics of the *Coriolis/SMEI* light curves of ζ Pup are described in detail in section 2.1 of Howarth & Stevens (2014).

6.3.2 Ground-based multi-site optical spectroscopy

In parallel with the *BRITE* run, we conducted multi-site ground-based spectroscopy of ζ Pup focusing on the He II λ4686 line in order to monitor possible signatures of CIR/DAC activities in the inner stellar wind. The temporal coverage of the ground-based observations is depicted in Figure 6.1 and the characteristics of the observations are listed in Table 6.III.

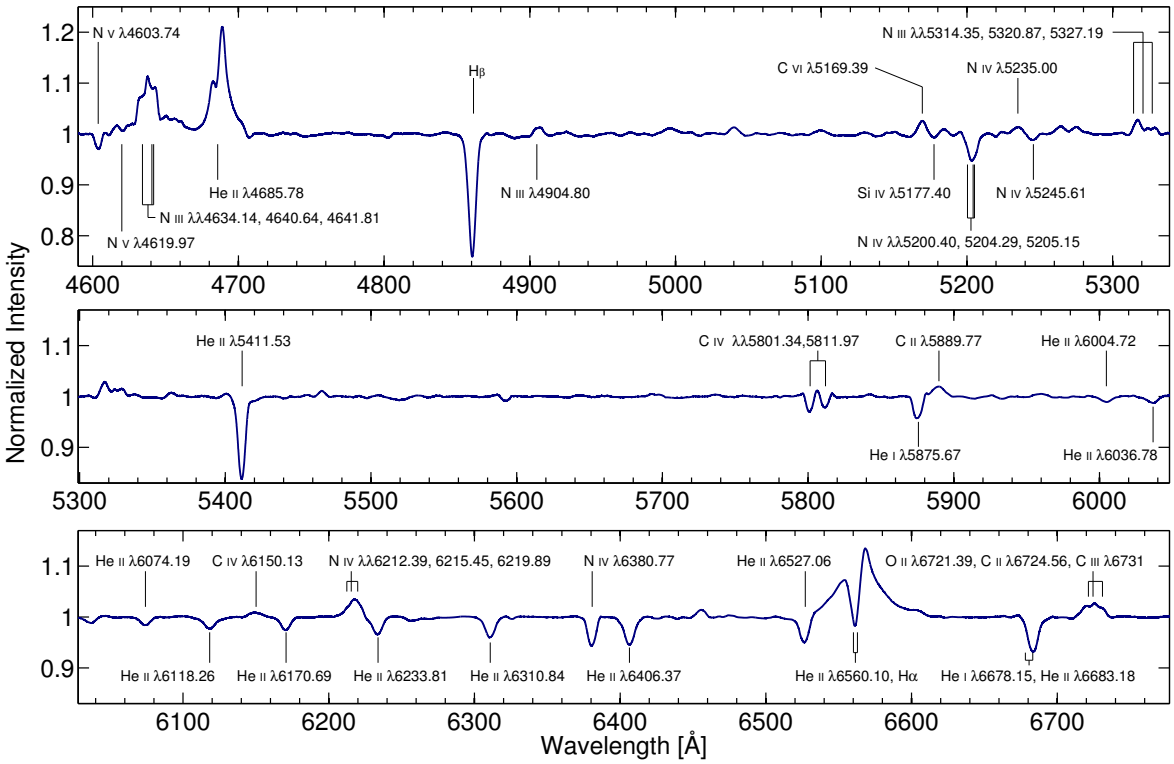

Figure 6.2: Mean high-resolution ($R \sim 80000$) CTIO-SMARTS 1.5m/CHIRON spectrum of ζ Pup. S/N $\sim$ 2500 in the continuum close to the vicinity of the He II λ4686 line profile.

6.3.2.1 CTIO-SMARTS 1.5m/CHIRON

We acquired a total of 415 spectra of ζ Pup spanning $4578 - 8762$ Å with the CHIRON échelle spectrograph (Tokovinin *et al.* 2013) mounted on the Cerro Tololo Inter-American Observatory's (CTIO) 1.5 m telescope operated by the Small and Moderate Aperture Research Telescope System (SMARTS) consortium (NOAO Proposal IDs: 2014B-0082, 2015A-0002; PI: T. Ramiaramanantsoa). We adopted a cadence of $2 - 6$ visits per night on ζ Pup (depending on the observability of the star), between November 28, 2014 and June 20, 2015. Each visit consists of $4 - 6$ consecutive 15 s sub-exposures taken in slicer mode ($R \sim 80000$), that we stacked and re-binned down to $R \sim 24000$ so that one single spectrum has an S/N ~ 725 pixel^{-1} in the continuum close to the He II λ4686 line. In order to correct for the instrumental blaze function, we normalized the extracted one-dimensional wavelength-calibrated spectra of ζ Pup through a division by cubic spline fits to each of the orders of the spectrum of the B9.5V star HR4468 ($V = 4.7$) obtained during the campaign with the same instrument configurations (slicer mode, fixed cross-disperser position). We chose HR4468 for this purpose as it is relatively close to ζ Pup, relatively bright enough and does not have many strong metal lines. Figure 6.2 illustrates the normalized, unbinned ($R \sim 80000$) CTIO-SMARTS 1.5m/CHIRON mean spectrum of ζ Pup over the entire campaign with identification of its strongest spectral lines.

6.3.2.2 SAAO 1.9m/GIRAFFE

We collected 24 optical spectra of ζ Pup during 14 nights between January 28, 2015 and February 10, 2015 at the South-African Astronomical Observatory (SAAO) with the Grating Instrument for Radiation Analysis with a Fibre Fed Échelle (GIRAFFE) spectrograph hosted in the coudé chamber of the 1.9 m Grubb Parsons telescope (PI:

T. Ramiaramanantsoa). Given the two available cross-disperser prisms optimized for the blue domain (3791 – 5459 Å) and the red domain (4094 – 9397 Å) with typical $R \sim 39000$, we chose to use the red prism in order to better match with the CTIO-SMARTS 1.5m/CHIRON wavelength coverage. Camera flat-fields, fibre flat-fields, bias frames and arc exposures were obtained in the usual way and the data reduced using the PYTHON-based pipeline for GIRAFFE data extraction, INDLULAMITHI. Exposure times range from 4 min to 12 min depending on the weather conditions and the airmass of the star. We adopted a cadence of 2−5 visits per night well-spread in time, alternating with visits on another primary target (γ^2 Velorum) and the B9.5V star HR4468 which was used to correct for the instrumental blaze function in the spectra of the two primary targets. Each visit on ζ Pup consists of 4 – 6 consecutive spectra that we later stacked in order to get an S/N ∼ 370 in the continuum near He II λ4686.

6.3.2.3 SASER

Optical spectra covering the He II λ4686 region were obtained by amateur observatories members of the Southern Astro Spectroscopy Email Ring (SASER) located in Australia (Shenton Park observatory, Domain Observatory, Latham Observatory, Mirranook Observatory), New-Zealand (R. F. Joyce Observatory) and Brazil (Dogsheaven Observatory). Data reduction (bias, flat-field, dark and sky background correction) and extraction of one-dimensional wavelength-calibrated unnormalized spectra were performed with the Integrated Spectrographic Innovative Software (ISIS) and the MAXIM DL software. Then, by means of the Image Reduction and Analysis Facility (IRAF[1], Tody 1986, 1993) software, we performed final homogeneous continuum normalization

[1]IRAF is distributed by the National Optical Astronomy Observatories, which are operated by the Association of Universities for Research in Astronomy, Inc., under cooperative agreement with the National Science Foundation

of the 615 spectra collected by SASER together with the 415 spectra obtained from CTIO-SMARTS 1.5m/CHIRON and the 24 SAAO 1.9m/GIRAFFE spectra.

6.3.2.4 CFHT 3.6m/Reticon

We re-extracted the 50 archival optical spectra of ζ Pup taken with the (now decommissioned) spectrograph mounted at the coudé focus of the 3.6 m Canada–France–Hawaii Telescope (CFHT) during the nights of December 10/11 and December 12/13, 1995 (PI: Moffat) and published by Eversberg *et al.* (1998) in order to compare the properties of the line profile variations (LPVs) that they observed in He II λ4686 to those that we detected during our campaign. Details on the characteristics of these spectra are described in section 2 of Eversberg *et al.* (1998).

6.4 Photometric variability

6.4.1 Amplitudes of the observed light variations

As depicted in Figure 6.1, the light variations of ζ Pup appear to be coherent in the two *BRITE* filters, with qualitatively the same amplitudes. In order to quantitatively check the validity of this visual impression, we plotted the observed blue versus red amplitude variations (Figure 6.3). Since the measurements from the two filters were not acquired exactly simultaneously, interpolation over the common time sampling grid of the two light curves is required in order to construct such a diagram (which we shall hereafter call a '*BRITE-b* versus *BRITE-r* diagram'). Therefore, a proper treatment of gaps in the time series needs to be considered, since interpolation over a large gap (such as the extreme case of the ∼5-d gap during the time interval [5504 – 5509]) would lead to wrong estimates of the correlation coefficient, whereas if the gap tolerance is too short the number of points that remain in the diagram would be too small to al-

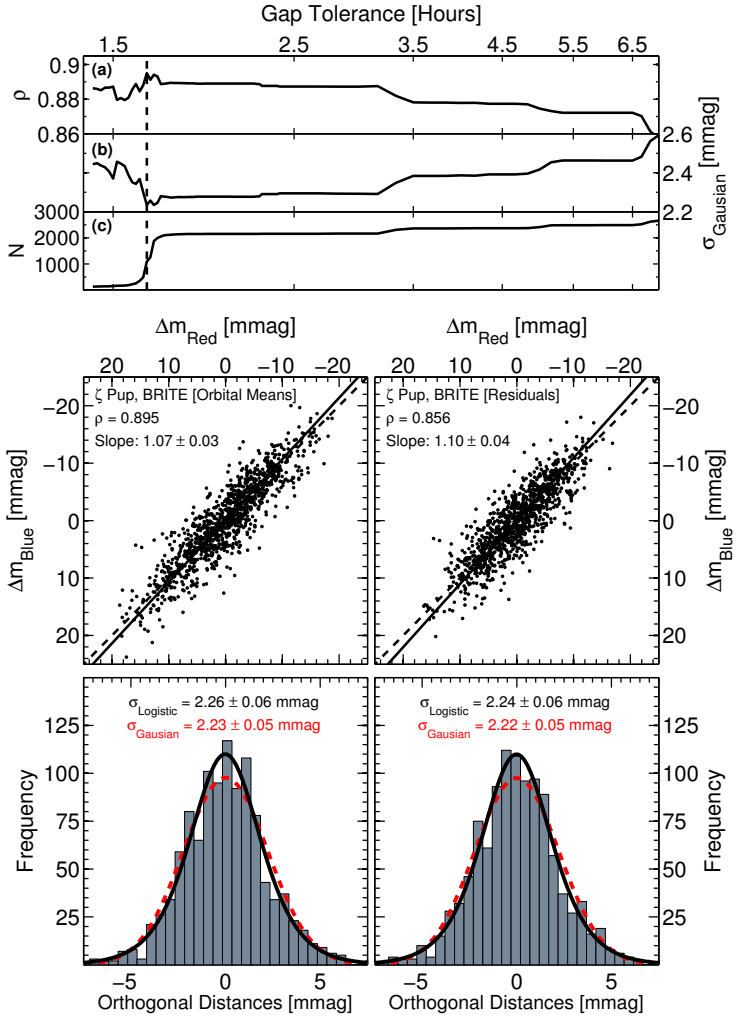

Figure 6.3: Comparison of the amplitudes of the variations of ζ Pup observed through the two *BRITE* optical filters. *Top:* Evolution of (a) the Pearson correlation coefficient, (b) the standard deviation of the distribution of orthogonal distances, and (c) the number of points involved, as a function of gap tolerance for the linear interpolation process. The vertical dashed line indicates the location of the optimal gap tolerance value (1.65 h). *Middle:* Comparison diagrams for (left) the *BRITE* light curves presented in Figure 6.1 and (right) the residual light curves after removal of the main periodic signal intrinsic to the star (Sections 6.4.4 and 6.4.5). The dashed lines indicate the reference slope = 1. *Bottom:* Distributions of distances perpendicular to the direction of correlation. The dashed red curves are Gaussian fits to the distributions whereas the continuous black ones are logistic distribution fits.

low for the extraction of meaningful slope and correlation coefficient values. The ideal case would be to consider a gap tolerance of the order of a *BRITE* orbit, which is acceptable only if the time samplings in the two light curves are such that a reasonable number of points remain for the interpolation. Thus, we scanned a grid of gap tolerance values and measured the Pearson correlation coefficient ρ, the standard deviation of the distribution of distances orthogonal to the direction of correlation σ, and the total number of points N involved in these estimates. The first three upper panels of Figure 6.3 trace the evolution of these three quantities over the considered range of gap tolerance values, and show that at a gap tolerance of 1.65 h (which is of the order of a *BRITE* orbit), ρ reaches its global maximum ($\rho_{\max} = 0.895$), σ its global minimum ($\sigma_{\min} = 2.23 \pm 0.05$ mmag) and N is large enough to make these values meaningful ($N = 1092$). We established our diagram with this gap tolerance value (middle panels of Figure 6.3). Thus, we confirm that the variations observed in the blue and the red filters are strongly correlated ($\rho = 0.895$), while the orthogonal linear regression yields a slope indicating that the amplitudes of the variations of ζ Pup in the blue filter are only 7 ± 3 % higher than the amplitudes measured through the red filter (middle-left panel of Figure 6.3). This relatively small difference could be due to the fact that the wavelength coverages of the *BRITE* filters both fall in the domain of validity of the Rayleigh–Jeans approximation for a hot star like ζ Pup, where different wavelengths react essentially identically to temperature changes.

Besides these considerations on the amplitudes of the light variations of ζ Pup measured in the two *BRITE* filters, it is worth noting that the distributions of orthogonal distances depicted in the bottom panels of Figure 6.3 are slightly leptokurtic (excess kurtosis ~0.7), such that these orthogonal distances can be better described as logistically distributed rather than normally distributed. More importantly, the value of the standard deviation $\sigma_{\text{Logistic}} = 2.26 \pm 0.06$ mmag is indicative of the expected scatter of

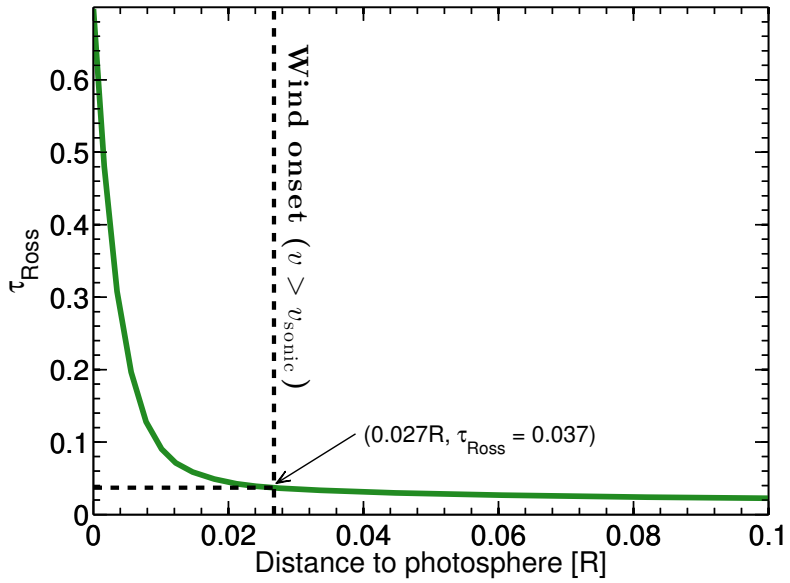

Figure 6.4: How $\tau_{\rm Ross}$ varies as a function of the radial extent from the photosphere (defined at $\tau_{\rm Ross} = 2/3$), as predicted by the *PoWR* stellar atmosphere code. Radii beyond the vertical dashed line correspond to supersonic expansion velocities, i.e. the wind domain.

instrumental origin in the *BRITE* light curves of ζ Pup. Assuming that the three satellites involved in the observations provide the same data quality, the expected scatter of instrumental origin is $\sigma_{\rm Logistic}/\sqrt{2} = 1.60 \pm 0.04$ mmag, which is in line with the rms scatter listed in the last column of Table 6.II, the rms of these values being ∼1.25 mmag.

6.4.2 *BRITE* and *Coriolis/SMEI* probe the stellar photosphere

In view of the typical $10 - 20$ mmag light variations of ζ Pup as detected in the photometric observations, the next crucial point that we investigate is the stellar domain in which the observed variability originates. In principle, the variability could originate in either the photosphere or the wind of ζ Pup (or even both), since some fraction of the photospheric continuum photons interact with matter in the wind. To estimate the

fraction of scattered photons in the wind, we calculate a model atmosphere for ζ Pup using the non-local thermodynamic equilibrium (non-LTE) Potsdam Wolf–Rayet (*PoWR*) tool, applicable for any hot star, including OB-type stars (e.g. Oskinova *et al.* 2011; Shenar *et al.* 2015; Sander *et al.* 2015). As described in detail by Hamann & Gräfener (2003, 2004) and Todt *et al.* (2015), the tool solves the radiative transfer and rate equations in expanding atmospheres under the assumption of spherical symmetry and stationarity of the flow.

To construct the model, we used the stellar and wind parameters of ζ Pup listed in Table 6.I: $\log(L)$, $T_{\rm eff}$, $\log g$, M, $\dot{M}$, v_∞, β and f_∞, all derived by Bouret *et al.* (2012). Figure 6.4 depicts the evolution of the Rosseland mean optical depth $\tau_{\rm Ross}$ as a function of the radial distance to the photosphere (defined at $\tau_{\rm Ross} = 2/3$), as predicted by *PoWR*. We also mark the radius at which the stellar wind initiates, which is defined at the point where $v(r)$ exceeds $v_{\rm sonic}$. It is worth noting that, in the wind domain, $\tau_{\rm Ross}$ is virtually identical to the Thomson optical depth τ_{th} which originated in the scattering of photons off free electrons.

It is evident from Figure 6.4 that the wind optical depth is $\tau_{\rm Ross,wind} = 0.037$. This corresponds to a scattering of $1 - e^{-\tau} \approx 3.5\%$ of the photospheric continuum light in the wind. This is therefore the maximum amount of variability that is expected to originate from scattering of photospheric photons in the wind. However, since some lines generated primarily in the wind, such as He II λ4686, are variable on the $\sim 5 - 10\%$ level (Section 6.5.1.1, Figure 6.15, and Section 6.5.2.1, Figures 6.20 and 6.21), the wind can contribute at most 0.35% to the variability in the continuum. This means that in the typical $10 - 20$ mmag light variations observed by *BRITE* and *Coriolis/SMEI* in ζ Pup, only $0.035 - 0.07$ mmag may originate from the wind. We therefore conclude that the variability we observe in the photometric measurements originates primarily in the photosphere of ζ Pup.

6.4.3 Search for periodic signals

We performed a Fourier analysis of the *BRITE* light curves of ζ Pup using the discrete Fourier transform (DFT)-based software package PERIOD04 (Lenz & Breger 2005), suitable for the extraction of individual sinusoidal components in multiperiodic unevenly sampled time series through a prewhitening procedure, with the possibility to perform iterative Monte Carlo simulations to assess formal uncertainties on the extracted parameters. A global view of the raw amplitude spectra of the *BRITE* light curves of ζ Pup (Figure 6.5, left-hand panel) shows a gradual increase in power towards lower frequencies, suggesting the presence of a red noise component that happens to have roughly the same amplitudes in the two filters. Therefore, at each stage of the prewhitening we computed the signal-to-noise ratio (S/N) for the detected frequency peak ν_i within an interval spanning $[\nu_i - 1; \nu_i + 1]$ d^{-1} which is a good compromise for a reasonable local estimate of the mean noise level while taking into account the red noise trend. Then we only consider that the frequency peak is significant if its S/N > 4.0, a threshold that was validated both empirically (Breger *et al.* 1993, 1999) and from numerical simulations (figure 4b in Kuschnig *et al.* 1997).

As conspicuously depicted in the amplitude spectra of the *BRITE* light curves of ζ Pup, only two significant frequency peaks are simultaneously detected in the two filters, corresponding to the 1.78 d period previously found in *Coriolis/SMEI* observations of ζ Pup, but this time its first harmonic is also prominent. This visual impression is quantified in Table 6.IV in which we report all the Fourier components that are either detected simultaneously in the observations through the two *BRITE* filters regardless of their statistical significance, or are significant but detected only in one filter. Only the 1.78 d component (denoted by ν_0 in Table 6.IV) and its first harmonic have S/N > 4 *and* are detected in both filters. We also point out in Table 6.IV that a pair of frequencies,

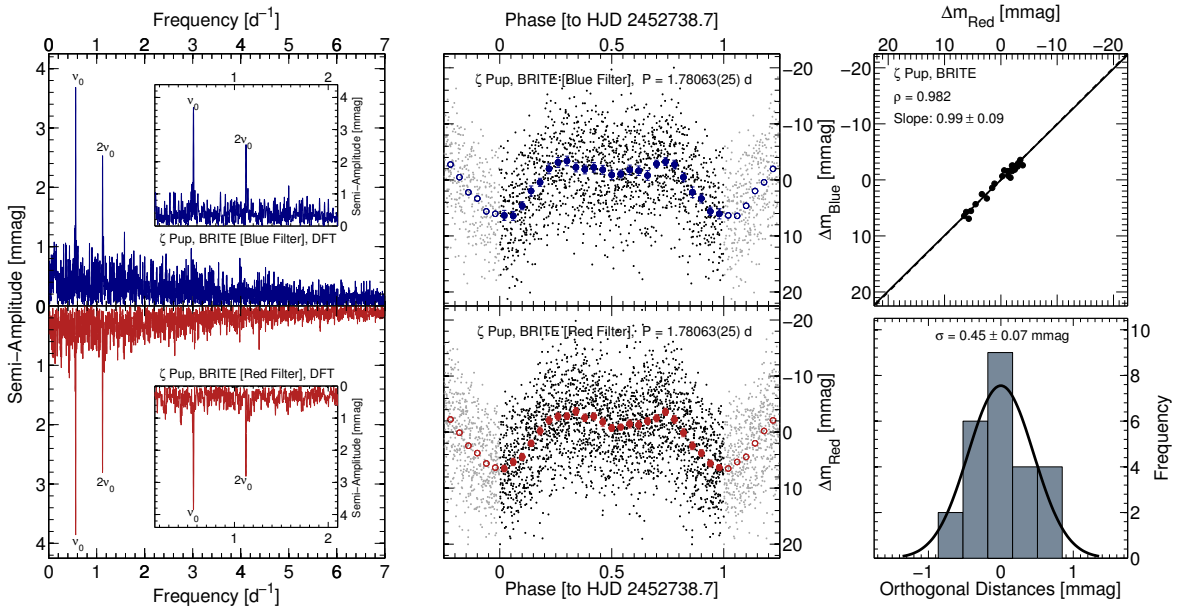

Figure 6.5: *Left:* Discrete Fourier Transform (DFT) of the *BRITE* light curves of ζ Pup, with the insets showing zooms on the two significant frequency peaks. For ease of direct comparison, the vertical axis for the DFT of the red filter data (bottom panel) is reversed. *Middle:* Rotation of ζ Pup as observed during the *BRITE* observing run, the value of the rotation period $P = 1.78063(25)$ d assessed as the weighted mean of the values of the 1.78 d period detected during the *Coriolis/SMEI* and *BRITE* runs (Table 6.IV). The original light curves are displayed (small grey points) as well as averages over bins of 0.04 in phase (large blue/red points) along with their 1σ uncertainties. The reference epoch HJD 2452738.7 was chosen to fall before the beginning of the *Coriolis/SMEI* 2003–2004 observing run and to allow for an easy monitoring of the evolution of the pattern of two consecutive bumps in the light curves (Section 6.4.4.2, Figure 6.7) and the 'S' patterns detected in the He II λ4686 wind emission line (Section 6.5.1.1, Figure 6.15). *Right:* Comparison diagram for the phased light curves of ζ Pup observed through the two *BRITE* optical filters (top), together with the distribution of distances orthogonal to the direction of correlation and its Gaussian fit (bottom).

Table 6.IV: Fourier analysis of the *Coriolis/SMEI* and *BRITE* light curves of ζ Pup. The second column indicates the frequency resolution for each observing run. Formal 1σ uncertainties on the parameters were estimated from 100 Monte Carlo simulations. S/N values were estimated within intervals spanning 2 d^{-1} centred on each frequency. For *BRITE*, all frequencies that are detected in both the red and the blue filters are listed even if their S/N < 4.

Observing run	ν_{res} [d^{-1}]	Frequency [d^{-1}]	Period [d]	Semi-amplitude [mmag]	S/N	Denotation
Coriolis/SMEI						
2003 – 2004	0.00246	0.56116 ± 0.00011	1.78202 ± 0.00035	6.64 ± 0.48	7.3	ν_0
2004 – 2005	0.00473	0.56148 ± 0.00019	1.78101 ± 0.00060	7.38 ± 0.50	8.3	ν_0
2005 – 2006	0.00569	0.56181 ± 0.00031	1.77996 ± 0.00098	6.27 ± 0.52	6.1	ν_0
2003 – 2006	0.00093	0.56150 ± 0.00002	1.78094 ± 0.00006	6.61 ± 0.23	12.2	ν_0
BRITE 2014 – 2015						
		0.56249 ± 0.00024	1.77781 ± 0.00076	3.85 ± 0.03	8.7	ν_0
		1.12087 ± 0.00102	0.89216 ± 0.00081	2.33 ± 0.16	6.7	$\nu_0' \sim 2\nu_0$
		1.12694 ± 0.00120	0.88736 ± 0.00094	1.86 ± 0.17	4.1	$\nu_0'' \sim 2\nu_0$
Blue filter	0.00615	1.14385 ± 0.00100	0.87424 ± 0.00076	1.14 ± 0.03	3.4	ν_1
		1.28213 ± 0.00121	0.77995 ± 0.00074	0.89 ± 0.03	2.7	ν_2
		1.72701 ± 0.00236	0.57904 ± 0.00079	0.99 ± 0.03	2.9	ν_3
		1.77456 ± 0.00094	0.56352 ± 0.00030	0.89 ± 0.03	2.8	ν_4
		0.56250 ± 0.00017	1.77778 ± 0.00054	3.88 ± 0.22	9.6	ν_0
		1.12151 ± 0.00213	0.89166 ± 0.00169	2.78 ± 0.33	7.8	$\nu_0' \sim 2\nu_0$
		1.12813 ± 0.00264	0.88642 ± 0.00207	1.10 ± 0.23	3.4	$\nu_0'' \sim 2\nu_0$
Red filter	0.00604	1.14242 ± 0.00087	0.87533 ± 0.00067	1.03 ± 0.25	3.0	ν_1
		1.28509 ± 0.00085	0.77816 ± 0.00051	0.84 ± 0.18	2.5	ν_2
		1.72947 ± 0.00170	0.57821 ± 0.00057	0.86 ± 0.20	2.6	ν_3
		1.76946 ± 0.00101	0.56514 ± 0.00032	0.76 ± 0.18	2.6	ν_4
		4.38282 ± 0.00768	0.22816 ± 0.00040	0.71 ± 0.20	4.3	ν_5
		0.56241 ± 0.00015	1.77806 ± 0.00047	3.86 ± 0.16	10.1	ν_0
		1.12111 ± 0.00047	0.89197 ± 0.00037	2.46 ± 0.36	8.0	$\nu_0' \sim 2\nu_0$
		1.12714 ± 0.00078	0.88720 ± 0.00061	1.50 ± 0.34	4.3	$\nu_0'' \sim 2\nu_0$
Two filters combined	0.00579	1.14280 ± 0.00065	0.87504 ± 0.00050	1.05 ± 0.16	3.1	ν_1
		1.28323 ± 0.00678	0.77928 ± 0.00412	0.80 ± 0.15	2.6	ν_2
		1.72788 ± 0.00172	0.57874 ± 0.00058	0.77 ± 0.34	2.7	ν_3
		1.77440 ± 0.00090	0.56357 ± 0.00029	0.76 ± 0.17	2.7	ν_4
		4.38313 ± 0.00101	0.22815 ± 0.00005	0.58 ± 0.15	4.0	ν_5

$\{\nu_0'; \nu_0''\}$, is closely spread around the true value of the first harmonic. It is known that a new frequency extracted at one stage of the prewhitening procedure could be very close to a component that was found during one of the previous stages (e.g. Blomme *et al.* 2011). That behaviour is not surprising and is easily conceivable if for instance the physical phenomenon responsible for that signal is subject to a phase shift during the time of the observations. In all cases, one must adopt a resolution criterion in order to decide if a frequency peak is truly unique. In the present case, we use the criterion of Loumos & Deeming (1978) stating that two frequencies must be separated by at least 1.5 times the resolution frequency to be considered unique. The resolution frequency for each set of observations is also provided in Table 6.IV. Using this criterion, we conclude that the pair $\{\nu_0'; \nu_0''\}$ represents the same frequency, namely the first harmonic of the fundamental frequency ν_0.

We also note that one frequency peak, $\nu_5 = 4.38313(101)$ d^{-1} [$P = 5.47560(126)$ h], is detected with an S/N = 4.3 in the observations in the red filter *but undetected in the blue filter*. This periodicity has never been found in previous observational campaigns on ζ Pup. At this point caution must be exercised as for the physical interpretation of this frequency. Future observations will confirm whether this signal is intrinsic to the star or an artefact of instrumental origin in our set of observations in the red filter.

Finally, we detect a set of frequencies, labelled $\{\nu_1; \nu_2; \nu_3; \nu_4\}$ in Table 6.IV, corresponding to periods in the range $\sim$13.5 – 21 h, that are present in the two filters but with a rather low significance (S/N $\sim$ 2.5 – 3.5).

Since the 1.78-d signal was discovered for the first time in *Coriolis/SMEI* observations of ζ Pup spanning 2003 – 2006 (Howarth & Stevens 2014), for comparison purposes and in order to explore the stability of this signal (Section 6.4.4.2) we also revisited the *Coriolis/SMEI* light curves and report in Table 6.IV the values of all frequencies detected with S/N > 4 from the Fourier analysis of the three seasonal observing runs

taken separately (2003 – 2004, 2004 – 2005, and 2005 – 2006), and the ensemble of the observations spanning 2003 – 2006. We confirm that the only significant periodicity that is present in the *Coriolis/SMEI* light curves of ζ Pup is the 1.78-d period, and that the first harmonic of that period is not detected with a high significance level when taking the three seasonal observing runs separately nor when considering the entire data set as a single light curve as did Howarth & Stevens (2014). In the latter case, the values that we obtained for the fundamental frequency and its amplitude as well as their formal uncertainties are in full agreement with the values reported by Howarth & Stevens (2014) even if (1) they used a date-compensated DFT algorithm (DCDFT, Ferraz-Mello 1981) instead of the classical DFT that we adopted in our analyses, and (2) their formal 1σ uncertainties were assessed from 10000 iterations of Monte Carlo simulations of synthetic data whereas ours were extracted from only 100 iterations.

6.4.4 The 1.78-day period

Here we investigate the properties of the 1.78-d monoperiodic signal in ζ Pup by first determining its origin (Section 6.4.4.1), then tracking its evolution during the *Coriolis/SMEI* and *BRITE* observing runs (Section 6.4.4.2), and finally modelling the photospheric source causing it (Section 6.4.4.3).

6.4.4.1 Stellar pulsations versus rotational modulation

As already mentioned in Section 6.2, Howarth & Stevens (2014) proposed an interpretation of the 1.78-d periodic signal detected by *Coriolis/SMEI* in ζ Pup as possibly due to low-order ($0 < l \leq 2$) oscillatory convection (non-adiabatic g^-) modes. The discovery of oscillatory convection modes with high-order azimuthal degree ($l \gtrsim 10$) in theoretical pulsation models for stars with $\log L/L_\odot = 5.0$ and $3.65 \leq \log T_{\rm eff} \leq 4.0$

was first reported by Shibahashi & Osaki (1981). Later the *theoretical* work of Saio (2011) unveiled the possibility for the excitation of low-order ($0 < l \leq 2$) oscillatory convection modes in luminous stars with higher effective temperatures ($\log L/L_{\odot} \gtrsim 4.5$ and $\log T_{\rm eff} \gtrsim 4.0$), necessarily associated with a subsurface convection zone caused by the opacity peak due to the partial ionization of iron-group elements near $\log T \sim 5.3$. In their thorough analysis of the *Coriolis/SMEI* light curves of ζ Pup, Howarth & Stevens (2014) encountered the classical dilemma 'pulsations versus rotational modulation' for the interpretation of the newly discovered 1.78-d signal. Such a situation is not uncommon and, depending on the amount of information available it may not be straightforward to draw a conclusion (e.g. Degroote *et al.* 2010b, 2011; Aerts *et al.* 2013; Ramiaramanantsoa *et al.* 2014). In the case of ζ Pup, Howarth & Stevens (2014) concluded that the 1.78-d monoperiodic signal could arise from stellar oscillations rather than rotational modulation for the following reasons:

[i] the period was found to be 'marginally consistent with the shortest possible rotation period'

[ii] there was only a 'minor periodogram peak' at the first harmonic of the 1.78 d period, such that the resulting phase-folded light curve was 'only slightly non-sinusoidal' showing only one dominant bump (figure 2 in Howarth & Stevens 2014)

[iii] the observed pulsation constant ($Q = P\sqrt{\bar{\rho}/\bar{\rho}_{\odot}} \simeq P\sqrt{M/M_{\odot}/(R/R_{\odot})^3}$, $\bar{\rho}$ and $\bar{\rho}_{\odot}$ being the mean stellar and solar densities) implied by the 1.78 d period is of the order of $0.1-0.2$ d, which is consistent with the predictions in the models of Saio (2011) for low-order oscillatory convection modes ($Q \sim 0.2-0.3$ d).

However, now the *BRITE* observations provide us with additional information, the most remarkable of which being the change of shape of the phased light curves (Figure 6.5, middle panel; see also Figure 6.7, Section 6.4.4.2) with respect to the single-

bumped modulation observed during the *Coriolis/SMEI* observing run (figure 2 in Howarth & Stevens 2014; see also Figures 6.23, 6.24, 6.25): the *BRITE* light curves phase-folded on the 1.78 d period are highly non-sinusoidal, characterized by a pattern of two consecutive bumps separated by $\Delta\phi \sim 0.4$ which explains why the first harmonic is prominent in the Fourier spectra. The highly non-sinusoidal nature of this monoperiodic signal, coupled with the change of shape of the phased light curves during the two observing runs are strong indications that it cannot arise from pulsations but rather a signature of rotational modulation. Note that the monoperiodic and non-sinusoidal nature of the signal alone are not sufficient for drawing any conclusion on whether it comes from stellar oscillations or from rotational modulation, as some radial pulsators are known to exhibit highly non-sinusoidal modulation of their light curves (e.g. Abt 1952, Natale *et al.* 2008, Szabó *et al.* 2010). Also, it is worth noting that the shape-changing property of the light curve alone could be qualified as grossly similar to the shape-changing nature of the observed light variations in RV Tau variables (e.g. Pollard *et al.* 1996), which are pulsators showing the period doubling effect (Moskalik & Buchler 1990). To date, all the pulsators known to exhibit this effect are radial pulsators, although in theory the pulsation modes involved do not necessarily need to be radial but need to satisfy the half-integer resonance criterion, i.e. two modes A and B satisfying $(2n + 1)\nu_A = 2\nu_B$ with n integer (Moskalik & Buchler 1990). In that case, due to resonant phase locking, mode B is not observed as an independent frequency: in the amplitude spectrum, mode A manifests at its frequency ν_A along with its harmonics, whereas mode B manifests through sub-harmonic frequencies of ν_A. Therefore, if the 1.78-d variability in ζ Pup were to be explained in terms of the period doubling effect, the main pulsation mode A has to be the one oscillating at the ∼21.4 h period, while mode B would manifest as the 1.78 d period. But then, in that situation, the fact that there are no signs of any sub-harmonics of the ∼21.4 h period (except the

1.78 d period) in any of the observing runs remains unexplained, and more importantly the ∼21.4 h period itself is quasi-absent during the ∼4 yr of *Coriolis/SMEI* observing run (figure 2 in Howarth & Stevens 2014; Figures 6.23, 6.24, 6.25). Based on all these considerations, we conclude that the highly non-sinusoidal nature of this monoperiodic shape-changing 1.78 d signal in ζ Pup is incompatible with stellar oscillations but can be naturally explained as arising from rotational modulation due to the presence of bright spots appearing and disappearing at different locations on the stellar surface.

The pattern of two consecutive bumps observed in the phase domain during the *BRITE* run is noteworthy. Patterns of two consecutive dips are common in the non-sinusoidally modulated light curves of cool stars having two dominant dark surface spots (e.g. McQuillan *et al.* 2013, Davenport *et al.* 2015), whereas patterns of two consecutive bumps are common in the phased light curves of stars exhibiting bright surface chemical inhomogeneities (Bruntt *et al.* 2009; Bernhard *et al.* 2015a,b; Weiss *et al.* 2016). Over the past decade, an increasing number of light curves of massive OB stars have been seen to show low-frequency non-sinusoidal signal best explained as arising from rotational modulation rather than pulsations as the corresponding phased light curves show a pattern of two consecutive bumps and the periodograms show prominent peaks at the harmonics of the fundamental frequency (De Cat & Aerts 2002; Degroote *et al.* 2010b, 2011; Balona 2016). In the case of ζ Pup, one noticeable property in the frequency domain is the prominence of the fundamental frequency (*Coriolis/SMEI* and *BRITE* observing runs) and the first harmonic (*BRITE* observing run), while higher harmonics are not detected. This behaviour is reminiscent of the findings of Balona (2016) who scanned a sample of OB stars observed during the K2 mission and found that 54% of them show rotational modulation rather than pulsations: 39% of these rotational variables show a single dominant low frequency peak in their periodogram (no harmonics) and 61% have both the fundamental frequency and its

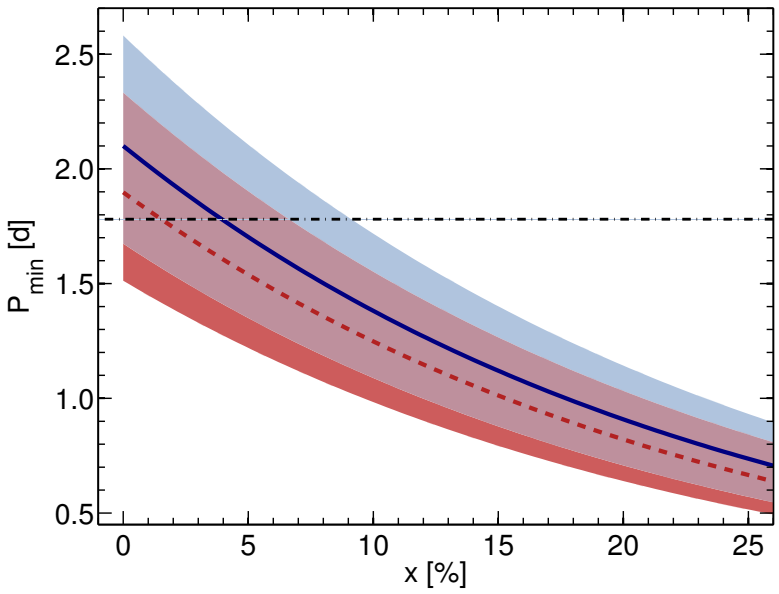

Figure 6.6: Minimum rotation period of ζ Pup (Equation 6.1) as a function of the dimensionless fraction $x = (\log g_{\rm p}/3.64) - 1$ which represents the percentage of deviation of the polar gravity from the value of the effective surface gravity $\log g$ (cm s^{-2}) = 3.64 ± 0.1 derived by Bouret *et al.* (2012). Two cases are considered: $R_{\rm e} = \sqrt{1.5}R$ (solid blue) and $R_{\rm e} = R$ (dashed red). In each case, the shaded area delimits the upper and lower bounds imposed by the uncertainties on the stellar radius and a 2.75% uncertainty on $\log g$. The dashed-dotted horizontal line is the period $P = 1.78063(25)$ d (its 1σ uncertainty is of the order of the thickness of the line itself).

first harmonic prominent in their periodogram while higher harmonics are absent. This particular behaviour reconciles with the theoretical investigations of Clarke (2003) who found that the Fourier series decomposition of stellar light variations due to surface spots is characterized by significant contributions from the fundamental and the first harmonic, with the strengths of the higher harmonics rapidly vanishing as the order increases.

Under these considerations, now that our analyses indicate that the 1.78 signal in ζ Pup is related to rotational modulation rather than pulsations, we revisit the three

Table 6.V: Estimates of the minimum possible rotation period $P_{\rm min}$, the equatorial velocity $v_{\rm e}$, and the inclination angle i of ζ Pup, taking $P = 1.78063(25)$ d for the value of the rotation period and considering the two cases where $R_{\rm e} = \sqrt{1.5}R$ and $R_{\rm e} = R$. The values of $P_{\rm min}$ were calculated for $g_{\rm p} = g$.

Parameter		$R_{\rm e} = \sqrt{1.5}R$	$R_{\rm e} = R$
$P_{\rm min}$	[d]	$2.10^{+0.48}_{-0.43}$	$1.90^{+0.43}_{-0.39}$
$v_{\rm e}$	[km s^{-1}]	661 ± 132	539 ± 108
i	[°]	$19.4^{+7.3}_{-4.7}$	$24.0^{+9.4}_{-5.9}$

points **[i]**, **[ii]** and **[iii]** mentioned above. We note that since the calculation of the pulsation constant mentioned in point **[iii]** involves the stellar mass and radius, which have large uncertainties in the case of ζ Pup due to the large uncertainty in its distance, the last point **[iii]** can only be confirmed or ruled out once a refinement on the value of the distance is available, e.g. with the *Gaia* mission (Lindegren *et al.* 2012; Martín-Fleitas *et al.* 2014). Also, as previously discussed in detail, point **[ii]** is an integral part of the key property that the shape of the light curve changes due to the appearance of spots at different locations on the stellar surface. Finally, point **[i]** also depends on the stellar radius which is affected by the uncertainty in the distance. As pointed out by Howarth & Stevens (2014), in order to maintain a positive equatorial effective gravity in a Roche model, the stellar rotation period must not be shorter than

$$P_{\rm min} = 3\pi \sqrt{\frac{R_{\rm e}}{g_{\rm p}}}, \tag{6.1}$$

where $R_{\rm e}$ is the equatorial radius and $g_{\rm p}$ the gravity at the pole. Note that to date the available values of R and g, which are listed in Table 6.I, were all derived from spherical models (Martins *et al.* 2005; Bouret *et al.* 2012). The values of $P_{\rm min}$ for $g_{\rm p} = g$ and

considering the two cases where $R_e = \sqrt{1.5}R$ and $R_e = R$ are summarized in Table 6.V, indicating that the 1.78-d period is close to the minimum possible value of the stellar rotation period, but not entirely excluded by virtue of the estimated uncertainties. Also, ζ Pup being a fast rotator, if effects of gravity darkening are non-negligible, the value for P_{min} could be lower as the polar gravity would be higher than the value of the effective surface gravity $\log g$ (cm s^{-2}) = 3.64 ± 0.1 listed in Table 6.I. This is clearly illustrated on Figure 6.6: for instance in the case $R_e = \sqrt{1.5}R$, if $\log g_p$ is 10% higher than $\log g = 3.64$, then the minimum rotation period drops to $1.38^{+0.34}_{-0.29}$ d. From all these considerations, we conclude that the three points [**i**]–[**iii**] are compatible with the fact that the 1.78 d signal in ζ Pup comes from rotational modulation.

Given the values of the 1.78 d period yielded by the Fourier analyses of the different data sets of ζ Pup (Table 6.IV), we adopt a unique value of the rotation period throughout our investigation by assessing the weighted average of the values of the 1.78-d period detected in the three *Coriolis/SMEI* seasonal observing runs and the combined *BRITE* light curve. We use the inverse square of the 1σ uncertainties derived from the Monte Carlo simulations as weights on the periods, yielding a final weighted average of $P = 1.78063(25)$ d. Such a relatively short rotation period for ζ Pup is quite surprising at first sight, but is more consistent with the suspected rotational evolution of the star involving past interactions within a massive binary (Vanbeveren *et al.* 1998b; see also Section 6.6 and Figure 6.22) or even a multiple system (Vanbeveren 2012). In all cases, the relatively short rotation period has strong implication on both the value of the stellar inclination angle i with respect to the line of sight and the equatorial velocity v_e. Given the available estimates of the stellar radius $R = 18.99 \pm 3.80\ R_\odot$ and the projected rotational velocity $v_e \sin i = 219 \pm 18$ km s^{-1} (Table 6.I), the stellar inclination angle can

be directly assessed as:

$$i = \arcsin\left(\frac{P v_e \sin i}{2\pi R_e}\right), \tag{6.2}$$

while the equatorial velocity is:

$$v_e = \frac{2\pi R_e}{P}. \tag{6.3}$$

The values of these two parameters are also reported in Table 6.V for the two cases $R_e = \sqrt{1.5}R$ and $R_e = R$. As clearly depicted by the numbers in Table 6.I, we can conclude that the short rotation period implies that the star is seen at a very low inclination angle, but bearing in mind that all these values strongly depend on the stellar radius which remains highly uncertain as a result of the large uncertainty in the distance to the star.

6.4.4.2 Evolution of the 1.78-d signal

As noted in the previous section, the key property leading to the conclusion that the 1.78-d signal in ζ Pup is related to rotational modulation rather than stellar oscillations is the change of shape of the phased light curve from the epoch of the *Coriolis/SMEI* observations to the epoch of the *BRITE* run. This behaviour led us to also investigate the evolution of the amplitude of the 1.78-d signal in ζ Pup through the *BRITE* observing run and through each *Coriolis/SMEI* seasonal run. In order to reduce the effects of high-frequency stochastic variability intrinsic to the star (that we shall characterize in Section 6.4.5), we applied an infinite impulse response (IIR) low-pass 32^{nd}-order Butterworth filter to the light curves, cutting off at $\nu_c = 1.4$ d^{-1}. It is known that Butterworth filters have the advantage of having a monotonic magnitude response that is optimally flat (no ripples) in the passband, which is the prime reason why we chose it over other types of filters, at the cost of a less steep rolloff that is mitigated by increasing the order of the filter. We inspected the reliability of our low-pass Butterworth filter in studying

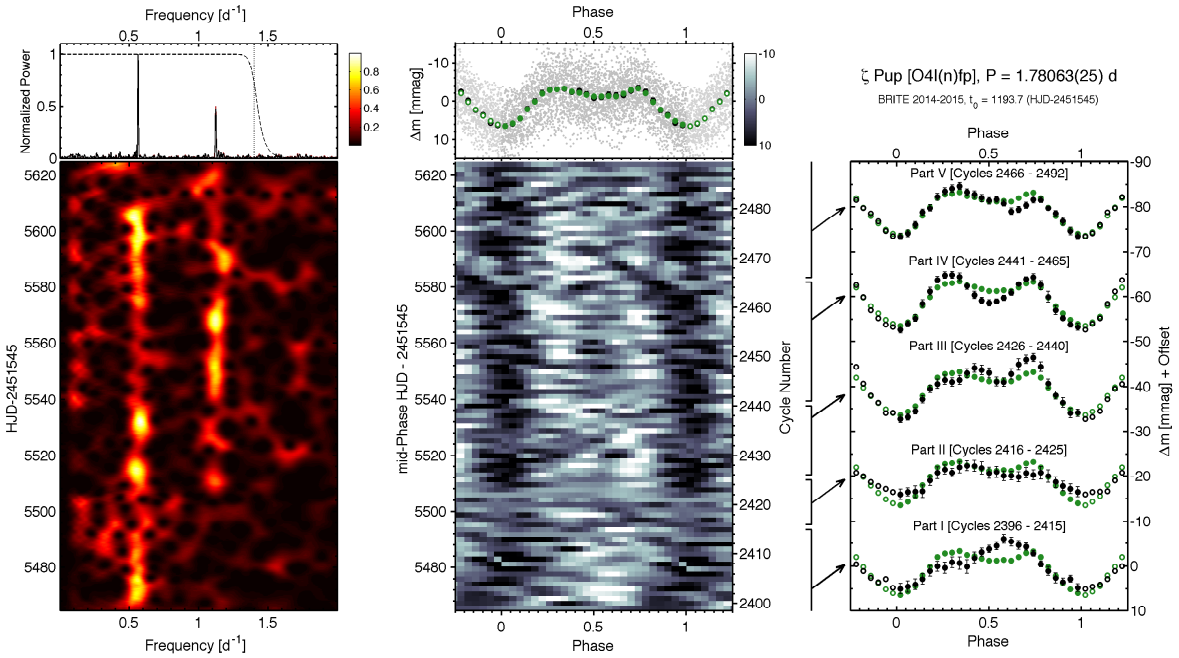

Figure 6.7: Investigation of the evolution of the 1.78-d signal in ζ Pup during the *BRITE* observing run (2014 – 2015). Time increases upwards. *Left:* Time–frequency diagram of the combined filtered *BRITE* light curves constructed from a 12-d sliding window Fourier transform. The upper panel shows the power spectrum of the entire unfiltered light curve (red line) compared to that of the entire filtered light curve (black line), along with the magnitude response of the low-pass filter (dashed line) and the location of its cut-off frequency (vertical dotted line). *Middle:* Continuous dynamic phased light curves of ζ Pup. The upper panel shows the phased light curve for the entire unfiltered data (black filled circles) compared to that from the entire filtered light curve (green filled circles). *Right:* Average shapes of the phased light curve of ζ Pup (black diamonds) over the first 20 rotational cycles (Part I, see the text), the next 10 rotational cycles at the beginning of the transition phase (Part II), the last 15 rotational cycles during the transition phase (Part III), the next 25 rotational cycles (Part IV) and the last 27 rotational cycles (Part V). These shapes are compared to the overall shape of the phased light curve (green filled circles).

the 1.78 d signal in ζ Pup by comparing the power spectra of the original light curve and the filtered light curves (Figure 6.7, upper-left panel). There is globally no significant difference between the two power spectra in the filter bandpass, the loss of *power* being at the ~2% level at the fundamental frequency peak ν_0 and ~8% at the first harmonic $2\nu_0$. Besides, in the time domain, the rms scatter of the residuals between the phased light curve before and after applying the low-pass filter is 0.26 mmag, which is of the order of half the rms value of the 1σ uncertainties of the mean points in the original phased light curve (Figure 6.7, upper-middle panel). From these results we conclude that the low-pass filtering process is reliable to study the evolution of the 1.78 d signal while reducing the contribution of the high-frequency stochastic variations intrinsic to the star which shall be discussed in detail in Section 6.4.5. Thus we performed all of the analyses related to the 1.78 d signal on the filtered light curves.

In the frequency domain, we conducted a Fourier analysis of the *BRITE* light curve in sliding windows over restricted time intervals spanning ΔT = 12 d (with a step of $\Delta T \times 1\%$), thus covering at least ~6 stellar rotational cycles at each step. The lower-left panel of Figure 6.7 depicts the resulting time–frequency diagram, clearly showing that the fundamental frequency is always present from the beginning of the observing run until almost the end (around day 5610.0), while the first harmonic only emerges from day ~5510.0 and remains visible until the end of the observing run. Between days ~5540.0 and ~5575.0, the fundamental frequency is still present but its power is partly absorbed by the first harmonic which is very prominent during that time interval.

Besides the time–frequency analysis, we also tracked the evolution of the 1.78-d signal by splitting the light curve into consecutive rotational cycles and stacking them on top of each other to form the grey-scale diagram in the middle panel of Figure 6.7 as a function of rotational phase and cycle number. Such a diagram is not common practice for analysing periodic/cyclic signals in photometric observations of stars as it requires

a large number of points per cycle, but could be useful in detecting and characterizing subtle variations (e.g. Gies *et al.* 2012, Davenport *et al.* 2015). In our case, the combined filtered *BRITE* light curve of ζ Pup provides us with an increased number of points per rotational cycle and increased S/N so that the diagram turns out to be a very useful complement to the time–frequency analysis as it helps us track events in the light curve that explain the behaviour that we found in the time–frequency diagram. More specifically, before day ∼5490 the phased light curves show one large bump centred around phase 0.6, which is the reason why we only see the fundamental frequency and not the first harmonic during that epoch of the observations. This behaviour could be due to the presence of one relatively large bright spot or a group of smaller bright spots at the photosphere. Then the time between days ∼5490 and ∼5538 is characterized by a transition that eventually leads to the formation of two bumps separated by $\Delta\phi \sim 0.44$ in the phased light curve at the end of the transition. These two bumps are clearly defined between days ∼5540.0 and ∼5575.0, causing the prominence of the first harmonic of the 1.78-d signal during that time interval in the time–frequency diagram. The presence of these two bumps could be the manifestation of two dominant bright spots at the stellar surface, separated by $360^\circ \times \Delta\phi \simeq 158^\circ$ in longitude. The separation of these two bumps in phase seems to become larger towards the end of the observing run, a sign that the surface spots experience a slight migration in longitude, which is then an appropriate explanation for the detection of the pair of frequencies $\{\nu_0'; \nu_0''\}$ closely spread around the true value of the first harmonic during the prewhitening procedure as pointed out in Section 6.4.3. The right-hand panel of Figure 6.7 shows the mean phased light curves over several consecutive rotational cycles, thus summarizing the above descriptions:

[i] the first 20 rotational cycles observed before the transition phase, showing one large bump centred around phase 0.6 (Cycles 2396 – 2415, which we will hereafter refer to as Part I),

[**ii**] the next first 10 rotational cycles during the transition phase (Cycles 2416 – 2425; Part II),

[**iii**] the last 15 rotational cycles during the transition phase (Cycles 2426 – 2440; Part III),

[**iv**] the 25 rotational cycles right after the transition phase, during which the two bumps separated by $\Delta\phi \sim 0.44$ are clearly visible (Cycles 2441 – 2465; Part IV),

[**v**] the last 27 rotational cycles of the observing run (Cycles 2466 – 2492; Part V).

We note that the behaviour of the star during the transition (Parts II and III) is not clearly defined at this point, the two most pertinent scenarios being either that the large spot/spot group in Part I disintegrates and the resulting most dominant parts *migrate* to form the two dominant spots that we see in Part IV at locations on the surface separated by ∼158° in longitude, or the large spot/spot group in Part I gradually disappears while two *new* dominant spots take birth.

Howarth & Stevens (2014) already investigated the stability of the 1.78 d signal during the *Coriolis/SMEI* observing run by performing a DCDFT on the seasonal subsets of the light curve and on 50-d subsets with 50% overlaps. They noticed that the fundamental frequency of the signal does not change, but its amplitude varies by a factor 2 during the observing run, while it experiences a modest phase excursion (figure 3 in Howarth & Stevens 2014). In order to investigate the stability of the 1.78-d signal on the 12 yr time-scale covered by the *Coriolis/SMEI* and the *BRITE* observing runs, we established the same dynamic plots as Figure 6.7 for the *Coriolis/SMEI* seasonal observing runs (Figures 6.23, 6.24 and 6.25). The time–frequency plots show that the fundamental frequency is always detected except at some points where it is so weak that its power is comparable with the noise level (e.g. between HJD−2451545 ∼ 1450 – 1500). Furthermore, the dynamic phased light curves show that the minima wander

within the interval $0.4 - 0.6$, confirming the behaviour reported by Howarth & Stevens (2014). More interestingly, the phased light variations observed during the epoch of the *Coriolis/SMEI* observing run present only one relatively large bump located around phase zero, which could indicate that the surface spots seen during the *Coriolis/SMEI* observing run appear at different longitudes compared to those observed during the epoch of the *BRITE* observations. However, at this point a strict interpretation of the position of the maxima in the phased light curve cannot be ascertained since the exact value of the rotation period remains unknown, and the value of its error bar $\sigma = 0.00025$ d could lead to an apparent phase shift of ~ 0.03 in 1 yr, or ~ 0.35 over the ~ 12 yr covered by the *Coriolis/SMEI* and the *BRITE* observing runs. Nevertheless, even considering such a large phase shift, the clear shape-changing nature of the light variations over these 12 yr, characterized by the presence of one large bump during the *Coriolis/SMEI* observing run and the presence of two dominating bumps during the epoch of the *BRITE* observations, is already a strong indication that the spots seen in $2003 - 2006$ are not the same as the ones seen in $2014 - 2015$.

6.4.4.3 Mapping the spotted stellar surface

Approaches to the modelling of light curves showing effects of rotational modulation associated with the presence of surface spots can be classified into two distinct categories depending on whether the problem is solved in a direct manner or in an inverse manner. The direct method consists in calculating the emerging stellar light variations produced by *a given number of spots* (often taken as a fixed parameter), provided some *a priori* assumptions on their *shape* (often assumed to be circular), their *decay law*, their *size*, and their *location* as well as the *time of their first appearance* on the stellar surface. Then these last three free parameters are refined for each spot until the calculated light

curve reasonably fits the observed light curve. Obviously, in that method a convergence towards a reasonable fit to the observed light curve strongly depends on the assumed number of spots. In practice, one could gradually increase the assumed number of spots until the smallest number that produces a good fit is reached, and then argue that in some sense the simplest acceptable spot distribution has been found. But then the other five parameters for each of the spots are still being assumed. This direct method, also known as the analytical approach, has been used in the modelling of light curves of cool low-mass stars exhibiting active surface regions (e.g. Kipping 2012; Béky *et al.* 2014; Davenport *et al.* 2015) and a few cases of hotter stars (Lüftinger *et al.* 2010; Degroote *et al.* 2011; Ramiaramanantsoa *et al.* 2014), offering the advantage of being fast in terms of computation time but suffering from the disadvantage that the number of spots, their shapes and their decay law have to be assumed a priori along with good estimates of starting points for the other three free parameters for each spot. Alternatively, the inverse approach (Harmon & Crews 2000; Roettenbacher *et al.* 2011, 2013, 2016; Krtička *et al.* 2007; Kolbin *et al.* 2013; Kolbin & Shimansky 2014; Kolbin *et al.* 2015) consists in assessing the distribution of specific intensity at the stellar surface that reasonably fits the observed light curve, with no a priori assumptions concerning the six parameters mentioned previously, the sole assumption being that the stellar surface contains spot-like features. This conceptually constitutes an inverse ill-posed problem and has been proven to require more computation time than the direct approach (thus its designation as the 'numerical approach'), keeping in mind its great advantage of being free from any prior assumption on the five spot parameters enumerated previously.

In order to model the bright spot-induced light variations of ζ Pup as observed by *BRITE* and *Coriolis/SMEI*, we adopted the numerical approach by using a constrained

non-linear light curve inversion algorithm (LI[2], Harmon & Crews 2000). This algorithm for mapping the surface of spotted stars was initially formulated and tested on simulated data by Harmon & Crews (2000), and applied to the analyses of the evolution of dark spots on the K2IV primary component of II Pegasi (Roettenbacher *et al.* 2011) and cool K-type *Kepler* targets (KIC 5110407: Roettenbacher *et al.* 2013; KOI-1003: Roettenbacher *et al.* 2016). Here we apply the algorithm for the first time to map the locations and evolution of bright spots at the surface of a hot massive star.

6.4.4.3.1 Light curve inversion - The algorithm

Let us represent the observed light curve as the time series $\mathbf{I} = \{I(t_k)\}_{1 \leq k \leq K}$, thus containing K measurements. The algorithm as it stands assumes rigid rotation, and thus currently does not explicitly allow for surface differential rotation. Then the basis of LI is to partition the stellar surface into N latitude bands of equal angular size ($\Delta\vartheta = \pi/N$), each n^{th} latitude band containing P_n spherical rectangles having exactly equal area. In addition, the partitioning is made such that all the patches on the stellar surface are of nearly equal area, which is achieved by having P_n proportional to the cosine of the latitude of the centre of the band, subject to the constraint that P_n must be an integer. Thus, at a given time t_k, if say J_{np} is the contribution of the specific intensity along the outward normal for patch $(n; p)$ that subtends a solid angle $\Omega_{np}(t_k)$ as seen from the observer, and $\mathcal{L}_{np}(t_k)$ the value of the limb-darkening at the location of that patch, then to the limit of a large total number of patches, the intensity from the star at that time

[2]Initially denominated "matrix light curve inversion (MLI)" in Harmon & Crews (2000) as it was inspired from a matrix-based algorithm for the inversion of light curves of planetary objects to assess their surface albedo distribution (Wild 1989, 1991). However, the actual implementation of the algorithm no longer involves matrices; thus, we adopt its common current designation: light curve inversion (LI).

takes the discretized form

$$I(t_k) = \sum_{n=1}^{N} \sum_{p=1}^{P_n} \Omega_{np}(t_k) \mathcal{L}_{np}(t_k) J_{np}, \tag{6.4}$$

in which the outer summation needs only to be performed up to $n_s \leq N$, which is the index of the southernmost latitude band that is visible by the observer as a consequence of the inclination of the star (thus $n_s = N$ if the star is seen equator on). Then the idea is to find the set of relative patch intensities $\hat{\mathbf{J}} = \{\hat{J}_{np}\}_{1 \leq n \leq n_s; 1 \leq p \leq P_n}$ that produces a reconstructed light curve $\hat{\mathbf{I}} = \{\hat{I}(t_k)\}_{1 \leq k \leq K}$ such that the rms deviation (expressed in magnitudes) between $\hat{\mathbf{I}}$ and the observed light curve $\mathbf{I}$ is equal to the estimated rms noise in $\mathbf{I}$ (also expressed in magnitudes). The ill-posed nature of the problem clearly appears here, the key component that is involved being the noise in the observations that shows as high-frequency ripples that would be indistinguishable from the effect of a multitude of small bright and dark spots randomly distributed over the stellar surface. Simply trying to find the distribution of patch intensities that best fits the observed light curve, i.e. through a standard minimization of a goodness-of-fit criterion, would inevitably yield a granulated surface dominated by noise artefacts. As in any ill-posed problem, a regularization process must be involved in order to mitigate noise sensitivity and ensure convergence towards a unique solution (Twomey 2013; Craig & Brown 1986). In our case, regularization is achieved by solving for the distribution of patch intensities $\hat{\mathbf{J}}$ through a Lagrange constrained minimization of an objective function defined as a Lagrangian of the form

$$E(\hat{\mathbf{J}}, \mathbf{I}, \lambda, B) = G(\hat{\mathbf{J}}, \mathbf{I}) + \lambda S(\hat{\mathbf{J}}, B), \tag{6.5}$$

in which $G(\hat{\mathbf{J}}, \mathbf{I})$ is the term that measures the goodness-of-fit between the reconstructed and the observed light curves, while the second term $\lambda S(\hat{\mathbf{J}}, B)$ controls the smoothness of the reconstructed stellar surface. The function $S(\hat{\mathbf{J}}, B)$ is therefore called *smoothing function*, such that the lower value it takes the smoother the surface is. Thus, in this context, the Lagrange multiplier λ acts as a *smoothing parameter*, a property that can be easily understood when considering the two asymptotic cases where $\lambda \to 0$ and $\lambda \to +\infty$: the first case amounts to minimizing $E(\hat{\mathbf{J}}, \mathbf{I}, \lambda, B) \simeq G(\hat{\mathbf{J}}, \mathbf{I})$ which would yield solutions dominated by noise artefacts as discussed above, while the second case would yield very smooth solutions that poorly fit to the observed light curve as the term $\lambda S(\hat{\mathbf{J}}, B)$ would dominate over $G(\hat{\mathbf{J}}, \mathbf{I})$. The optimal solution of the inverse problem corresponds to an intermediate value of λ that is the best trade-off between these two limit cases, yielding a reconstructed light curve $\hat{\mathbf{I}}$ that reasonably fits the observed light curve $\mathbf{I}$ while mitigating the tendency of overfitting.

The subtle role of the smoothing function $S(\hat{\mathbf{J}}, B)$ can be understood from its closed-form expression which is a generalized Tikhonov regularizer:

$$S(\hat{\mathbf{J}}, B) = \sum_{n=1}^{n_s} \sum_{p=1}^{P_n} w_n c_{np} \left[\hat{J}_{np} - \langle \hat{J} \rangle \right]^2 , \tag{6.6}$$

where $\langle \hat{J} \rangle$ is the average patch intensity, w_n are latitude-dependent weighting factors, and the coefficients c_{np} incorporate the constraint that the surface exhibits confined discernible spots on a uniform background. This is achieved through the definition:

$$c_{np} = \begin{cases} 1 & \text{if} \quad \hat{J}_{np} < \langle \hat{J} \rangle \\ B & \text{if} \quad \hat{J}_{np} \geq \langle \hat{J} \rangle \end{cases} , \tag{6.7}$$

with B a strictly positive real constant. Keeping in mind that $S(\hat{\mathbf{J}}, B)$ is involved in

the objective function $E(\hat{\mathbf{J}}, \mathbf{I}, \lambda, B)$ to be minimized, two distinct cases arise from this definition of c_{np}: $B > 1$ and $0 < B < 1$. The first case would mean that a patch that tends to be brighter than $\langle \hat{J} \rangle$ by a given amount rather than being dimmer than $\langle \hat{J} \rangle$ by the same amount will increase $S(\hat{\mathbf{J}}, B)$ by a factor of $B > 1$, thus inflicting a penalty in the minimization of $E(\hat{\mathbf{J}}, \mathbf{I}, \lambda, B)$. Conversely, if $0 < B < 1$ the penalty becomes a gain in the minimization of $E(\hat{\mathbf{J}}, \mathbf{I}, \lambda, B)$ as the contribution of the patch to $S(\hat{\mathbf{J}}, B)$ decreases by a factor of $1/B > 1$. In other words, the information on whether we want to model dark or bright spots on a uniform background is incorporated in the coefficients c_{np}: the modelling of dark spots requires $B > 1$ as was adopted in the work of Roettenbacher *et al.* (2011, 2013, 2016), while in this investigation we constrain $0 < B < 1$ to model the bright spots on ζ Pup. Note that for these reasons, $S(\hat{\mathbf{J}}, B)$ is also called *the penalty function* and B the *bias parameter* since it biases the solution in favour of either dark or bright spots.

Also, the presence of the latitude-dependent weighting factors w_n is noteworthy and comes from the necessity to take into account the fact that the maximum projected area of a patch increases the closer to the sub-Earth latitude it is located. Hence, the amount of light modulation induced by any given spot is equivalent to that of a smaller spot located closer to the sub-Earth latitude. This degeneracy would lead the algorithm to a systematic convergence towards solutions with spots lying near the sub-Earth point, as a result of the fact that small spots incur small values of the penalty function $S(\hat{\mathbf{J}}, B)$. To reduce that systematic behaviour, the n^{th} latitude band is weighted by a coefficient w_n that is proportional to the difference between the maximum and minimum values of the product of the projected area and the limb darkening for patches in the band, namely:

$$w_n = \frac{1}{\mathcal{W}} \times \left| \max_{1 \leq p \leq P_n} \{\mathcal{A}_{np}\} - \min_{1 \leq p \leq P_n} \{\mathcal{A}_{np}\} \right|, \tag{6.8}$$

in which $\mathcal{W} = \max_{1 \leq n \leq n_s} \{w_n\}$ is a normalization factor, while $\mathcal{A}_{np}$ is the product of the projected area and the limb-darkening value for the patch $(n; p)$:

$$\begin{aligned} \mathcal{A}_{np} &= \frac{1}{2}\left[\sin i\,(\cos\varphi_1 - \cos\varphi_2)\left(\frac{\pi}{N} + \frac{1}{2}\,(\sin 2\vartheta_1 - \sin 2\vartheta_2)\right)\right. \\ &\quad \left. + \frac{2\pi}{P_n}\cos i\left(\cos^2\vartheta_1 - \cos^2\vartheta_2\right)\right] \times \mathcal{L}_{np}, \end{aligned} \tag{6.9}$$

in which i is the stellar spin axis inclination angle with respect to the line-of-sight, ϑ_1 and ϑ_2 are the colatitudes of the northern and southern edges of the latitude band, whereas φ_1 and φ_2 are the longitudes of the western and eastern edges of the patch. As a matter of fact, $\max_{1 \leq p \leq P_n} \{\mathcal{A}_{np}\}$ is reached at the sub-Earth meridian, while $\min_{1 \leq p \leq P_n} \{\mathcal{A}_{np}\}$ is reached at the anti-Earth meridian. Although it was originally found that the introduction of the latitude weighting coefficients w_n generally resulted in a modest improvement on the latitude resolution and an increased computation time (Harmon & Crews 2000), here we decided to keep them in order to optimize the output of LI.

Finally, the goodness-of-fit term $G(\hat{\mathbf{J}}, \mathbf{I})$ is defined to be the rms deviation in magnitudes of the reconstructed light curve from the observed light curve. Evaluated in units of the estimated noise variance in magnitudes σ^2 in the observed light curve, the closed-form expression for $G(\hat{\mathbf{J}}, \mathbf{I})$ is:

$$G(\hat{\mathbf{J}}, \mathbf{I}) = \frac{(2.5 \log e)^2}{K\sigma^2} \sum_{k=1}^{K} \left(\frac{I(t_k) - \hat{I}(t_k)}{I(t_k)}\right)^2. \tag{6.10}$$

As mentioned earlier, the goal of LI is to find the optimal distribution of patch intensities $\hat{\mathbf{J}}$ that yield a reconstructed light curve $\hat{\mathbf{I}}$ such that the rms variance between $\hat{\mathbf{I}}$ and the observed light curve $\mathbf{I}$ reaches σ^2. In other words, an inversion consists in finding the optimal values of the Lagrange multiplier λ and the bias parameter B, for which we have:

$$G(\hat{\mathbf{J}}(\lambda; B), \mathbf{I}) = 1. \tag{6.11}$$

That is achieved through a two-step process involving a Van Wijngaarden–Dekker–Brent root-finding algorithm (Press *et al.* 2007) to first solve Equation 6.11 for λ for a set of values of the bias parameter B constrained within the interval $[0; 1]$, yielding $\lambda_{\rm opt}(B)$ which is in turn used to find $B_{\rm opt}$ as the root of the function

$$g(B) = \frac{\min\left\{\hat{J}_{np}(\lambda_{\rm opt}(B); B)\right\}}{\langle \hat{J}_{np}(\lambda_{\rm opt}(B); B)\rangle} - \frac{J^{(\rm s)}}{J^{(\rm p)}}, \tag{6.12}$$

where $J^{(\rm s)}$ and $J^{(\rm p)}$ are, respectively, the spot and photosphere specific intensities, two parameters that we determine by evaluating the *Planck* function at the central wavelength of the filter passband for the spot and photosphere temperatures. In principle, a better way to obtain a proxy for these two parameters is to integrate the *Planck* function over the filter passband for the spot and photosphere temperatures, the most ideal way being a numerical integration of the stellar spectral energy distribution (SED) over the filter passband. However, given the typical uncertainty in spot temperatures, the method that we adopted is enough for achieving a nearly optimal precision.

6.4.4.3.2 Spot temperatures

At this point, particular consideration has to be given to spot temperatures: since our *BRITE* observations were performed in two different filters, any amplitude difference between observations through the two filters could be exploited in order to extract potential information on the typical temperatures of the spots. This can be easily conceived by assuming to first order that all the spots that are present on the surface at

a given time t_k are all at the same temperature $T^{(\mathrm{s})}$ (a reasonable approximation if the spots roughly probe the same stellar atmosphere layer), and assuming that their combined area at that snapshot in time is equivalent to a single spot occupying a fractional area f on the stellar surface subtending a limb angle θ as seen from the centre of the star and emitting $I^{(\mathrm{s})}$ per unit area, while the unperturbed stellar photosphere emits $I^{\star}$ per unit area in that filter. This situation amounts to the configuration considered by Clarke (2003) (see his figure 1), so that the observed photometric signal takes exactly the same closed-form expression as his Equation 1:

$$F_j(\theta) = \mathcal{K}\left[I_j^{\star} + f\left(I_j^{(\mathrm{s})} - I_j^{\star}\right)\cos\theta\right], \tag{6.13}$$

in which we have the additional subscript j to indicate observations through filter j (j = 'b' or 'r' in our case). The factor $\cos\theta$ takes into account the foreshortening of the projected area of the spot according to the angle θ, whereas the factor $\mathcal{K}$ is a constant that depends on the stellar radius and the distance to Earth. Furthermore, Equation 6.13 can be expressed in terms of magnitudes and approximated to first order as:

$$m_j - m_j^{\star} \simeq -2.5(\log e)\left(\frac{I_j^{(\mathrm{s})} - I_j^{\star}}{I_j^{\star}}\right) f\cos\theta. \tag{6.14}$$

with $m_j^{\star} = -2.5\log\left(\mathcal{K}I_j^{\star}\right)$ the stellar magnitude in the absence of spots. Therefore, the ratio of the observed variations in the blue filter to the observed variations in the red filter is:

$$\alpha = \frac{\Delta m_b}{\Delta m_r} = \frac{m_b - m_b^{\star}}{m_r - m_r^{\star}} \simeq \frac{I_b^{\star} - I_b^{(\mathrm{s})}}{I_r^{\star} - I_r^{(\mathrm{s})}} \times \frac{I_r^{\star}}{I_b^{\star}}. \tag{6.15}$$

But by definition, this ratio α turns out to be exactly the slope in our *BRITE-b*

versus *BRITE-r* diagrams! In terms of color indices, Equation 6.15 yields:

$$(b-r)_{\rm d} = (b-r)_{\star} - 2.5\log\alpha, \tag{6.16}$$

where $(b-r)_{\rm d}$ is the colour index of the difference between the spot and the photosphere, while $(b-r)_{\star}$ is the colour index for the unperturbed star. In other words, Equation 6.16 remarkably tells us that a simple measurement of the slope in the *BRITE-b* versus *BRITE-r* diagram can give us an estimate of spot temperatures by means of calibrations between $(b-r)$ and effective temperatures. Also, Equation 6.16 can be applied to any dual-band photometric time series observations of any star when appropriate calibrations of colour indices versus effective temperatures are available. Unfortunately, in our situation we measure a slope $\alpha = 0.99 \pm 0.09$ in our *BRITE-b* versus *BRITE-r* diagram for the 1.78-d signal in ζ Pup (right-hand panel of Figure 6.5), which does not allow us to extract any information on spot temperatures. This insensitivity could be due to the fact that the two *BRITE* red and blue filters fall in the domain of validity of the Rayleigh–Jeans approximation for a hot star like ζ Pup. Thus, given the fact that there is no amplitude difference in the observations in the two filters, we performed our inversions on the combined *BRITE* light curve of ζ Pup, allowing us to have decreased errors in the mean points and reduced gaps in rotational phase coverage, even if it has been demonstrated by Harmon & Crews (2000) that the inversion of light curves in multiple filters can improve the spot latitude resolution.

6.4.4.3.3 Mapping the surface of ζ Pup during the *BRITE* 2014 – 2015 observing run

Under all the considerations in § 6.4.4.3.1 and § 6.4.4.3.2, we performed inversions of the *BRITE* light curves of ζ Pup by partitioning the stellar surface into $N = 60$ latitude

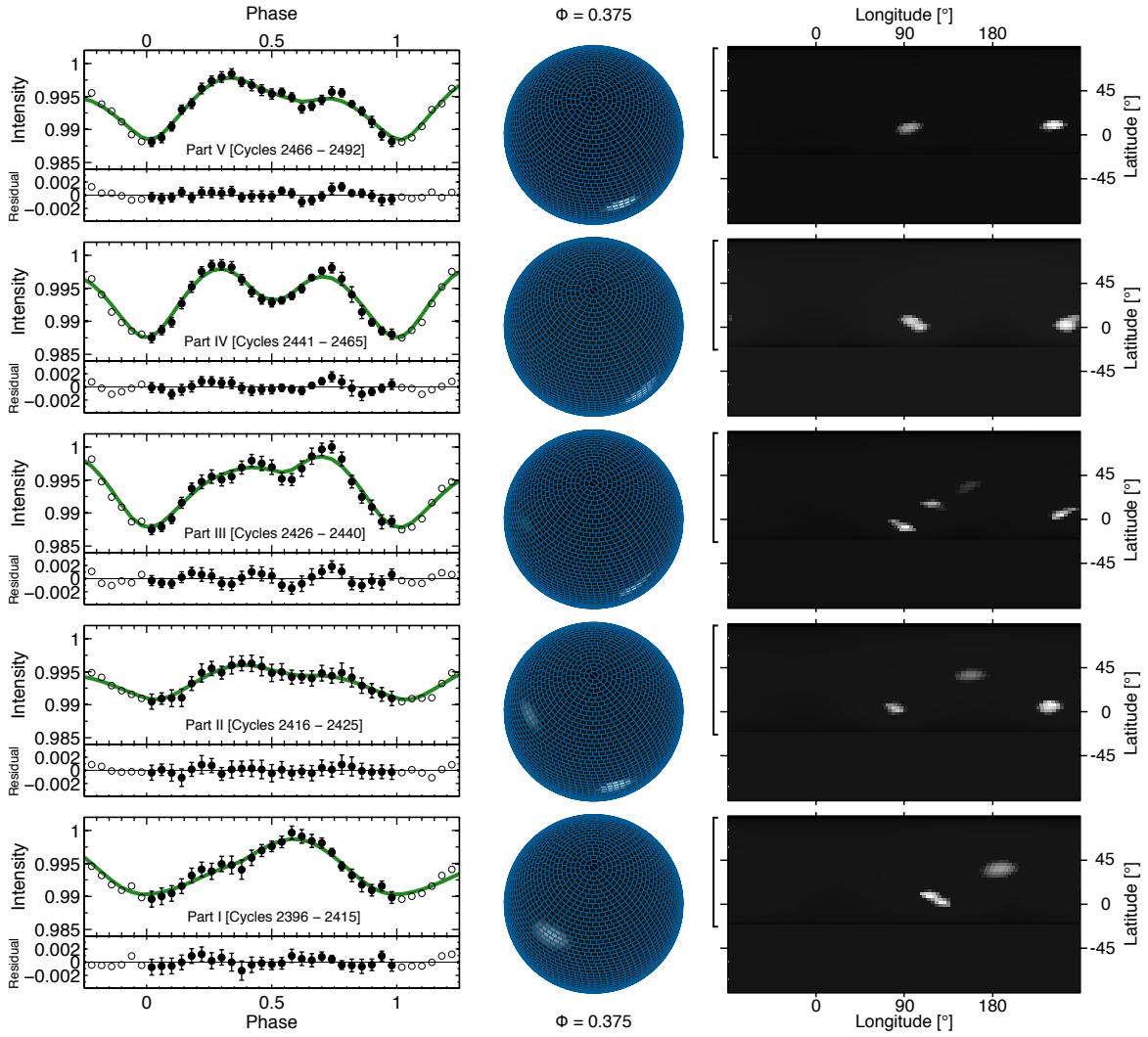

Figure 6.8: Light curve inversion: mapping the photosphere of ζ Pup as observed by *BRITE* in 2014–2015, for $T^{(s)} = 42.5$ kK and a stellar inclination angle $i = 24°$. Time increases upwards. The left-hand panel illustrates the observed light curve (filled circles) during Parts I–V of the *BRITE* observing run as defined on Figure 6.7, Section 6.4.4.2, along with the reconstructed light curve (green line), with the residuals plotted below the light curves. Then follows a view of the star at rotational phase 0.375 (*middle panel*) and the pseudo-Mercator projection of the stellar surface (*right-hand panel*). The vertical open brackets on the left of the pseudo-Mercator projections indicate the range of latitudes visible by the observer. The sub-Earth point is at longitude 0° at rotational phase zero.

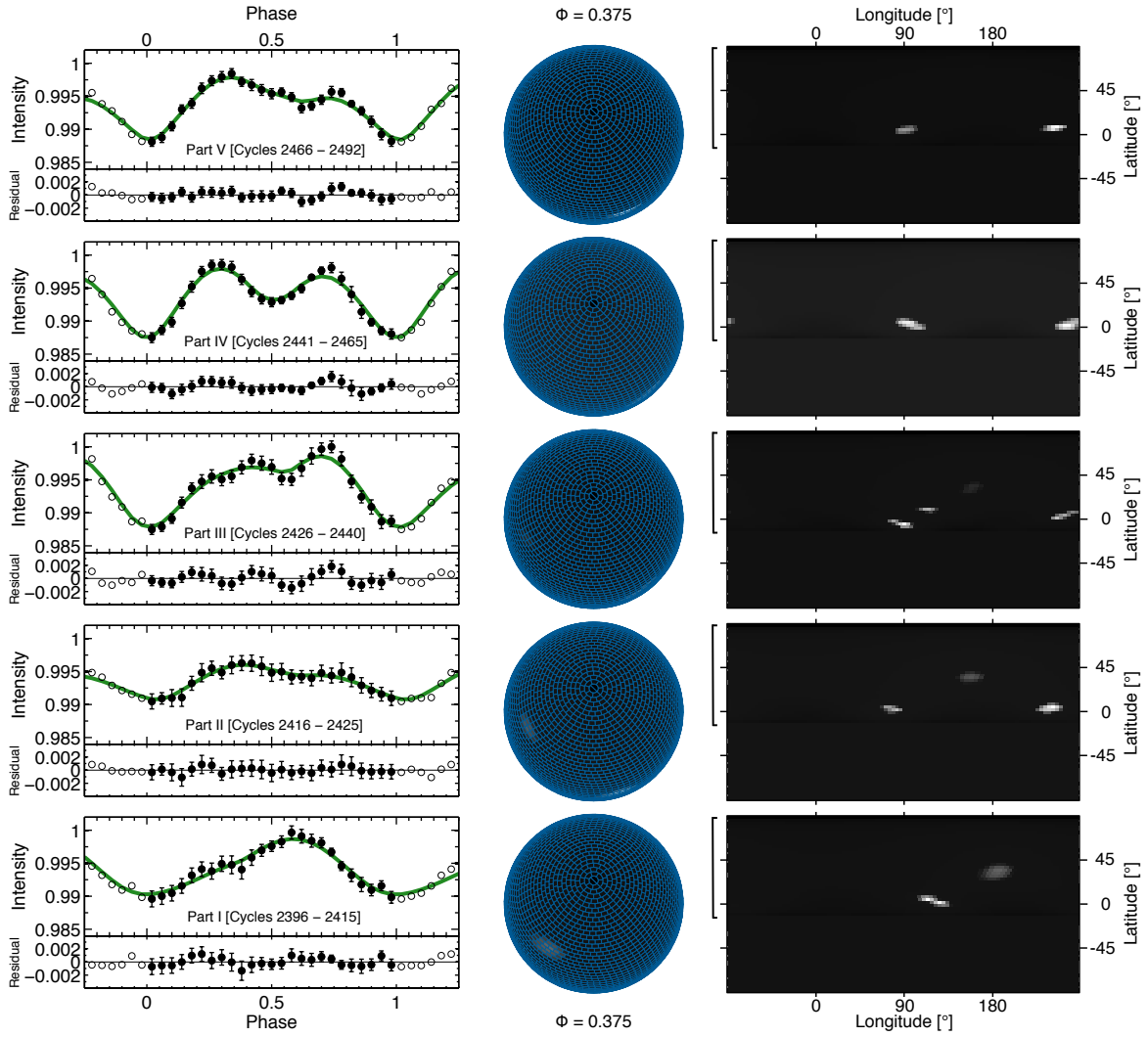

Figure 6.9: Same as in Figure 6.8 but for $i = i_{\min} = 15°$. The locations of the detected spots remain the same as for $i = 24°$ (Figure 6.8), while their shapes appear to be more stretched in longitude.

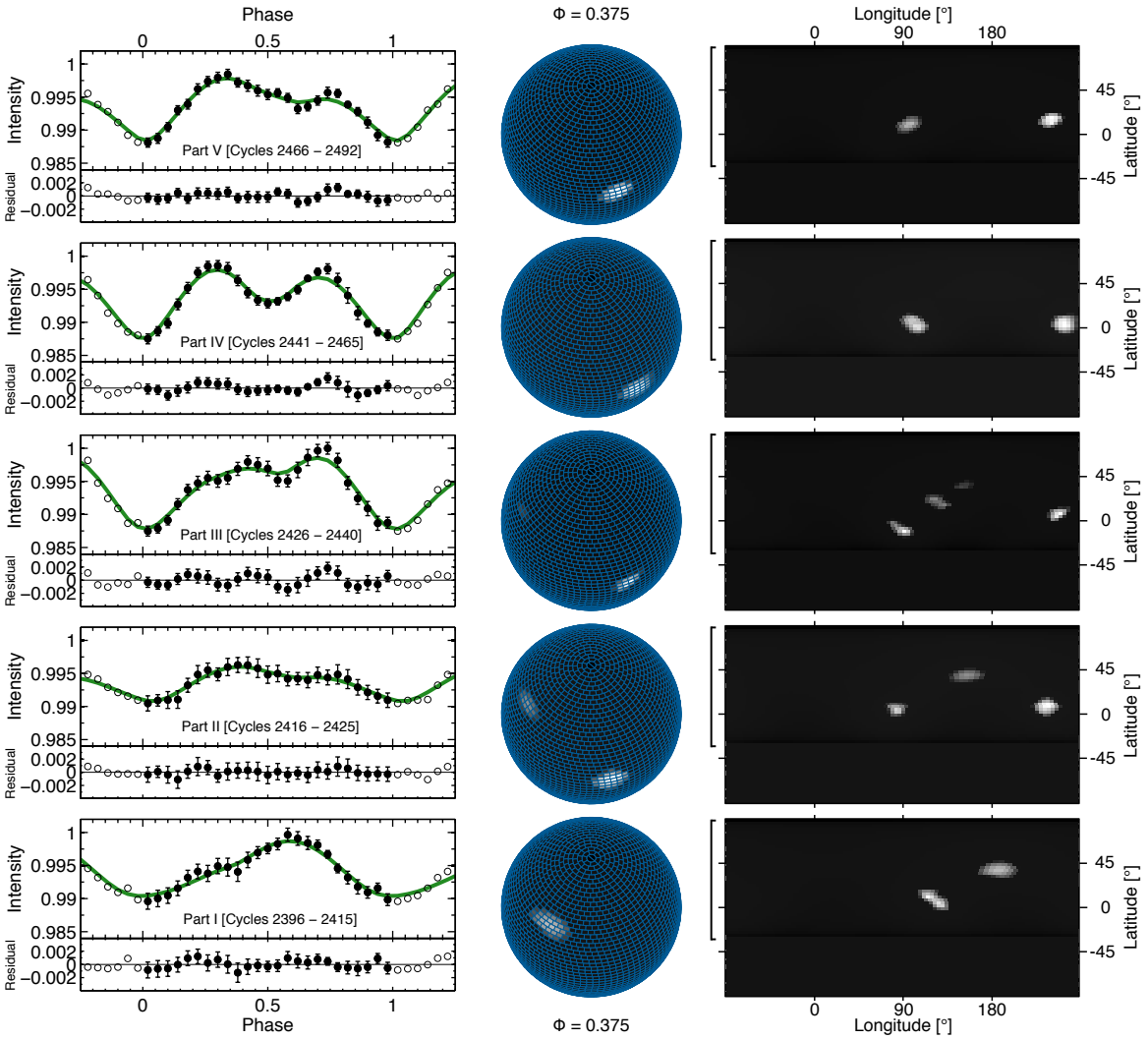

Figure 6.10: Same as in Figure 6.8 but for $i = i_{\max} = 33°$. The locations of the detected spots remain the same as for $i = 24°$ (Figure 6.8), while their shape appear to be rounder.

bands with the first four equatorial bands containing 90 patches, and we adopt as input parameters:

[i] the estimated rms noise σ for the observed light curves split into different parts (Section 6.4.4.2). As mentioned earlier, the goal of LI is to find the "smoothest" solution until the rms residual between the reconstructed and observed light curves reaches the level of σ. It has been demonstrated that in practice (Harmon & Crews 2000; Roettenbacher *et al.* 2011, 2013, 2016), the reconstructed surface will show obvious noise artefacts when the assumed noise level becomes too low. Our criterion for choosing the best solution is thus defined by the effective noise level at which this behaviour starts to occur. Therefore, we only assessed the rms noise in our observed light curves in order to choose the appropriate range of assumed values of σ that need to be considered. We measured σ in the range $1.2 - 0.7$ mmag in the phased light curves of ζ Pup observed by *BRITE*, hence we scanned the following range of σ in our inversions: 1.5, 1.2, 0.9, 0.8, 0.7, 0.6, 0.5 and 0.4 mmag;

[ii] the inclination angle: we performed inversions for $i = 24°$, which is the mean value defined by the limits that we found in Section 6.4.4.1 (Table 6.V), and we also performed inversions for the lower limit $i_{\rm min} = 15°$ and the upper limit $i_{\rm max} = 33°$;

[iii] the photosphere temperature (which we take to be $T_{\rm phot} = T_{\rm eff} = 40.0$ kK: Table 6.I), and a range of discrete values for the spot temperature: $T^{(\rm s)} = 41.5$ kK, 42.5 kK, 45 kK, 47.5 kK and 50 kK;

[iv] limb-darkening coefficients: we adopted a quadratic limb-darkening law and extracted the appropriate coefficients for the stellar parameters of ζ Pup in the Bessel V filter (the closest to the middle of BRITE combined filters) from the grid of limb darkening coefficients calculated by Reeve & Howarth (2016) using non-LTE, line-blanketed TLUSTY model atmospheres.

The first important point that we noticed was that the inversions for the assumed range of spot temperatures only slightly differ in the resulting spot-to-photosphere contrast: higher spot temperatures resulted in slightly brighter spots (which is expected for

the reasonable values of spot temperature that we considered), but negligibly affected the locations and the shapes of the spots found by the algorithm. Figures 6.8, 6.9 and 6.10 illustrate the outcome of our inversions of the *BRITE* light curve of ζ Pup for $T^{(s)} = 42.5$ kK and for $i = 24°$, $i = i_{min} = 15°$ and $i = i_{max} = 33°$ respectively. We clearly note that the range within which the stellar inclination angle varies does not influence the locations of the detected spots on the stellar surface. However, we notice that, as the inclination angle gets lower, the shapes of the spots tend to be more stretched in longitude. In other words, the spots are rounder for $i = 33°$ than for $i = 15°$. The equatorial spots appear to be the most affected by this behaviour, which could then be explained as follows. Given a certain value of the stellar inclination angle, consider an equatorial spot having a certain shape that provides the right amount of light modulation at a given rotational phase: if the stellar inclination is decreased, the lower part of the spot would become less visible (its overall projected area on to the plane of the sky decreases), such that the spot has no other choice than to flatten in order to compensate for that behaviour and provide the same amount of light modulation as in the case of the higher inclination angle. Also, in general it is expected that there should be a tendency for the spots to shift to higher latitudes as the assumed inclination angle decreases, since the sub-Earth latitude moves northward in that case. However, for *small* equatorial spots, which is the case for most of the spots detected by the algorithm here, that tendency will not be as pronounced because a small equatorial spot will be visible for half the rotation period regardless of the value of the inclination angle. This explains why the range within which the stellar inclination angle varies here does not affect the locations of the spots detected by the algorithm. In all cases, our inversions of the *BRITE* light curve of ζ Pup converge towards the following behaviour:

[i] Part I: one spot $\mathcal{S}_1$ is detected lying close to the equator, along with a slightly larger spot $\mathcal{S}_2$ located at mid-latitude (~55.5°). Their separation is ~66° in lon-

gitude.

[ii] Part II: the two spots $\mathcal{S}_1$ and $\mathcal{S}_2$ seem to be subject to a shift in longitude, while a third spot ($\mathcal{S}_3$) appears close to the equator, separated from the previous equatorial spot $\mathcal{S}_1$ by $\sim$158° in longitude.

[iii] Part III: spot $\mathcal{S}_2$ has almost faded away, while the equatorial spots $\mathcal{S}_1$ and $\mathcal{S}_3$ remain there. A fourth spot $\mathcal{S}_4$ seems to be located mid-way between $\mathcal{S}_1$ and the previous location of $\mathcal{S}_2$. We identify three possible scenarios to explain the presence of $\mathcal{S}_4$: either it is exactly $\mathcal{S}_2$ that is migrating towards $\mathcal{S}_1$, or part of the disintegration of $\mathcal{S}_2$ migrating towards $\mathcal{S}_1$, or a completely new spot.

[iv] Part IV: only two dominant equatorial spots, $\mathcal{S}_1$ and $\mathcal{S}_3$, are visible separated by $\sim$158° in longitude.

[v] Part V: the two dominant equatorial spots at $\mathcal{S}_1$ and $\mathcal{S}_3$ remain visible. Both spots seem to have slightly shifted in longitude (by $\sim$6° for $\mathcal{S}_1$ and $\sim$16° for $\mathcal{S}_3$), and their separation becomes $\sim$148° in longitude.

Thus, our inversion of the *BRITE* light curve of ζ Pup has enabled us to map the surface of the star, find the locations of the surface bright spots that best explain the observed variations, and track the evolution of these surface inhomogeneities. We also performed inversions of the light curves of ζ Pup obtained during the three *Coriolis/SMEI* seasonal runs. The resulting surface maps for $T^{(s)} = 42.5$ kK and $i = 24°$ are illustrated on Figures 6.26, 6.27 and 6.28. We detect on average $\sim 2-3$ spots at the equator and at mid-latitudes during the epoch of the *Coriolis/SMEI* observations. The spots clearly appear at different longitudes compared to the *BRITE* observing run, but whenever there are two equatorial spots, their separation seems to be $\sim$148° – 180° in longitude.

6.4.5 Stochastic variability

As mentioned in Section 6.4.3, the sole significant period that emerged from our Fourier analysis of the *BRITE* and *Coriolis/SMEI* light curves of ζ Pup was the 1.78-d signal due to rotational modulation (with the first harmonic of the fundamental period also prominent in the amplitude spectrum of the *BRITE* light curves). In order to check for any signs of other types of variability in the light curves, we therefore removed this 1.78-d periodic signal. Since the shape of this signal changes in time, the standard removal by prewhitening is the least reliable method as it assumes a constant amplitude and phase. Instead of calculating the residual light curve by prewhitening the 1.78-d signal, we performed its removal in the phase domain by subtracting templates of the phased light curves from the different parts of the observing runs: in the case of the *BRITE* observations, we adopted the five different parts of the observing run (Parts I–V; left-hand panel of Figure 6.7), while in the case of the *Coriolis/SMEI* observations we adopted the different parts defined on the left-hand panels of Figures 6.23, 6.24, and 6.25. Then we recomputed the amplitude spectra of the residual light curves to confirm that there is no sign of the 1.78-d signal left and no new significant periodicity introduced during the removal process, thus confirming our previous findings in Section 6.4.3. Now a close inspection of the residual *BRITE* light curves in the two filters reveals variations reaching ~20 mmag in peak-to-peak amplitudes, stochastically generated, but coherent for several hours (Figure 6.11). The first hint indicating that this stochastic signal is intrinsic to the star is the fact that it behaves the same way in the observations in the two *BRITE* filters as clearly seen in Figure 6.11. This is further confirmed by the behaviour of the *BRITE-b* versus *BRITE-r* diagram for the residual light curves in which we measure a strong correlation ($\rho = 0.856$) and a slope $\alpha = 1.10 \pm 0.04$ (right-hand panel of Figure 6.3). Also as already shown in Figure 6.11, our ultimate check that

confirms that this stochastic signal is not of instrumental origin nor due to an artefact introduced during the decorrelation process is a comparison with the *BRITE* light curve of ι Car (HD 80404, A8Ib, V=2.25), which is of similar magnitude as ζ Pup, was also observed by *BRITE* as part of the Vela/Pup observing run, has data that were decorrelated with the same decorrelation routines, and shows no obvious signs of periodic variability from our Fourier analysis. From all these considerations, we conclude that this stochastic signal is intrinsic to the star. We emphasize here the fact that the stochastic nature of this signal describes the way each feature in the signal appears to be generated, while a given feature seems to be well organized (or coherent) for several hours after its generation. Also from these considerations, we can take the liberty to call this signal 'noise', as long as we keep in mind that it is a noise intrinsic to the star and not of instrumental origin. It is thus worth noting that this stochastic behaviour is reminiscent of the findings of Balona (1992) who came to the conclusion that ζ Pup is an irregular microvariable (with amplitudes ∼20 mmag) from ground-based Strömgren b filter photometric monitoring of the star.

The origin of this stochastic signal remains unknown, with potential candidates being unresolved randomly excited p-mode oscillations similar to those discovered in the O-type primary component of the massive binary system HD 46149 (Degroote *et al.* 2010b), or internal gravity waves (IGWs) generated from either a subsurface convection zone (Cantiello *et al.* 2009b) or from the convective core (Aerts & Rogers 2015), the latter case having been proposed to be to date the best interpretation of the red noise components in the *CoRoT* observations of the three O-type dwarfs HD 46223, HD 46150 and HD 46966 in the young open cluster NGC 2244 (Blomme *et al.* 2011). Also, perhaps the set of frequencies $\{\nu_1; \nu_2\nu_3; \nu_4\}$ ($P \sim 13.5 - 21$ h) detected by our Fourier analysis in both the observations in the red and blue filters but with low significance (S/N $\sim 2.5 - 3.5$; Section 6.4.3, Table 6.IV) is part of this stochastic signal, which

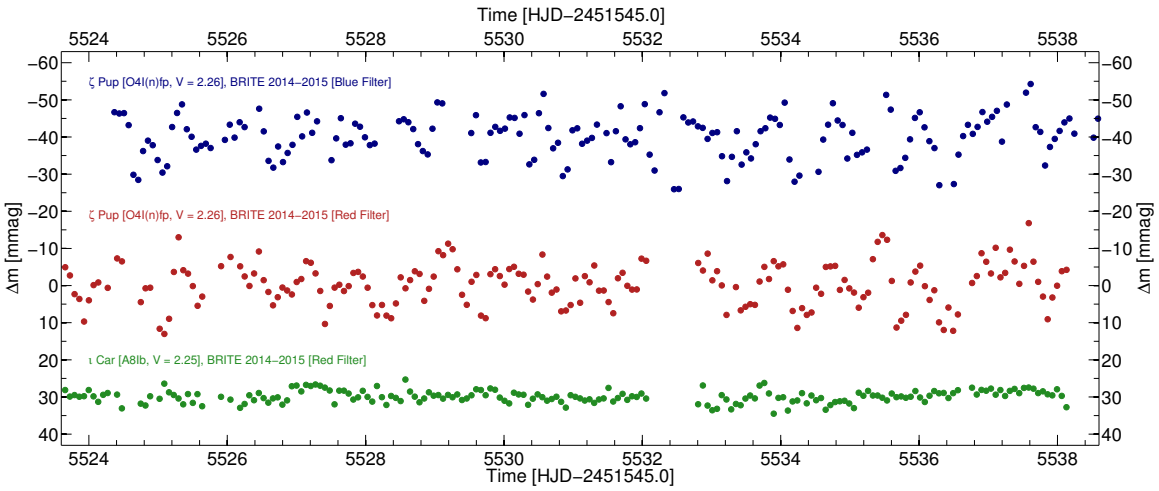

Figure 6.11: A 15-d subset of the residual *BRITE* (2014–2015) light curve of ζ Pup after removal of the 1.78-d periodicity related to rotational modulation, along with the simultaneously observed *BRITE* (2014–2015) red light curve of ι Car (HD 80404, A8Ib, $V = 2.25$) used as a comparison star.

would explain their low significance as they would be present/excited only occasionally and last for a limited time. In all cases, regardless of its origin, in view of its typical amplitudes the quantification of this stochastic variability in terms of its amplitudes and time-scales is as important as the characterization of the 1.78-d periodic rotationally-induced modulation itself.

6.4.5.1 Stochastic variability – Amplitudes

One striking property of this stochastic variability in ζ Pup is that it reaches ~20 mmag in peak-to-peak amplitude during the epoch of the *BRITE* observations (Figure 6.11 and right-hand panel of Figure 6.3), while we should recall that the periodic 1.78-d signal does not exceed ~15 mmag peak-to-peak (Figure 6.5). The overall standard deviation in the amplitudes of the residual *BRITE* light curves of ζ Pup is $\sigma_{\rm BRITE} \simeq 6$ mmag. But as assessed in Section 6.4.1, the scatter of instrumental origin is $\sigma_{\rm BRITE,\ i} = 1.60 \pm 0.04$ mmag.

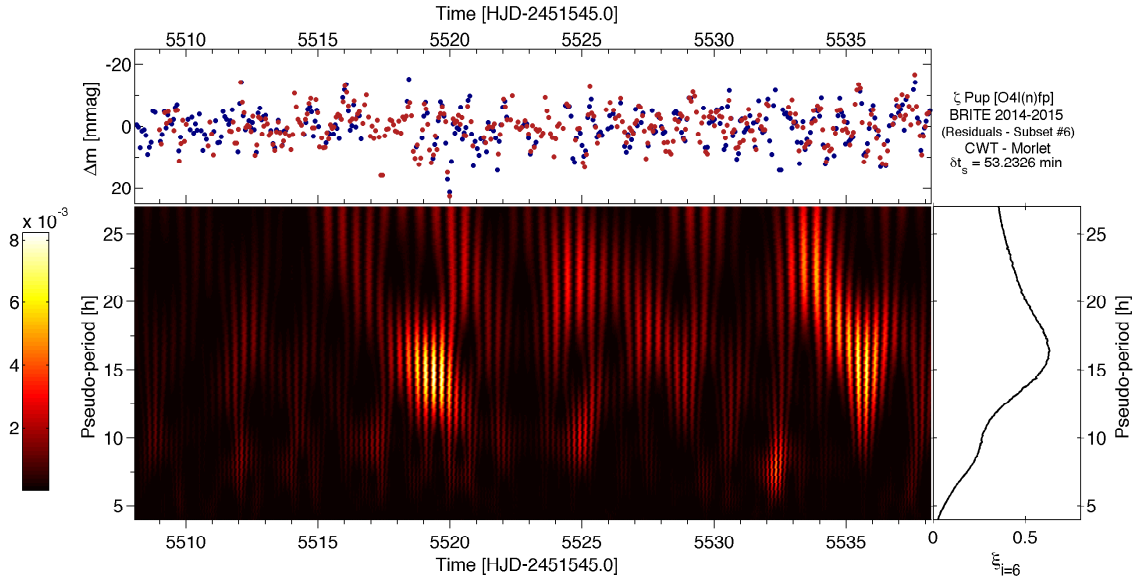

Figure 6.12: Wavelet analysis of a 30-d subset of the combined residual *BRITE* light curve of ζ Pup. The *main panel* depicts the scalogram (percentage of energy for each wavelet coefficient) obtained from a Morlet wavelet family-based continuous wavelet transform (CWT) of the analysed 30-d portion of light curve illustrated on the *top panel*. The *right-hand panel* shows the sum of the percentages of energy per wavelet coefficient over time, thus representing the overall energy distribution of pseudo-periods detected during this subset of the observations.

Since that instrumental scatter is much smaller than the overall scatter in the residual light curve, we can infer that the standard deviation of the amplitudes associated with the stochastic signal intrinsic to the star during the epoch of the *BRITE* observations is of the order of 6 mmag.

Regarding the *Coriolis/SMEI* observations of ζ Pup, the overall standard deviation in the amplitudes of the residual *Coriolis/SMEI* light curve of the star is higher: $\sigma_{\rm SMEI} \simeq 16.8$ mmag. However, the contribution of instrumental effects to this scatter remains ambiguous. Indeed, in view of the *Coriolis/SMEI* observations of the late O-type subgiant ζ Oph (O9.2IVnn; $V = 2.6$) having an rms dispersion of ∼20 mmag dominated by instrumental effects, while contemporaneous *MOST* observations of the star has a dispersion of ∼6 mmag, most of which is intrinsic to the star (Howarth *et al.* 2014), it is impossible to constrain the nature of the stochastic component of the intrinsic variability of ζ Pup during the epoch of the *Coriolis/SMEI* observations.

6.4.5.2 Stochastic variability – Time-scales

As mentioned earlier, the features constituting the intrinsic stochastic signal in ζ Pup seem to be coherent for several hours. In order to characterize the time-scales of these transient features, given the random nature of their generation we performed a continuous wavelet analysis of the residual combined *BRITE* light curves. We tested two cases: (1) application of the 1.10 factor on the amplitudes of the observations in the red filter prior to the generation of the combined light curves, and (2) no amplitude correction prior to the combination of the light curves. We noticed no significant difference in the resulting continuous wavelet transforms (CWT), thus we chose to work on the combined light curves without any amplitude correction. Also it is important to note that in general, the continuous formalism can only be applied on well-sampled and equally

spaced data. Our overall combined *BRITE* light curve of ζ Pup is well-sampled enough, but obviously not regularly sampled. However, by choosing appropriate subsets of the combined light curve that are densely sampled and resampling these subsets with one single sampling interval, it is reasonable to adopt the continuous formalism. Therefore our approach is to subdivide the combined light curve into subsets that contain no gaps greater than 5 h (39 subsets), then refining the selection by keeping only subsets spanning at least 2.5 d, so that we ended up with 11 subsets with time bases between $\sim 3 - 52$ d and mean sampling intervals in the range $53.2 - 75.4$ min. Lastly, through a shape-preserving piecewise cubic interpolation (Sprague 1990), we resampled all the 11 subsets with one single sampling interval taken to be the minimum of the mean sampling intervals of the subsets ($\delta t_s = 53.2326$ min). Once the subsets are defined, we come to the choice of an appropriate wavelet family that will help us optimally and robustly characterize the time-scales of the transient features composing the stochastic signal intrinsic to ζ Pup. Given the facts that the observed variations in the light curve seem to equally have bumps and dips between ± 10 mmag (Figures 6.11 and 6.3), and also since we want to have the most reliable conversion from wavelet scales to pseudo-periods, the wavelet family that is the most appropriate to our case is the family of real-valued Morlet wavelets, for which the mother wavelet is a sinusoid modulated by a Gaussian envelope. Furthermore, this definition itself clearly indicates that this family of wavelets is the most suitable one for the characterization of sinusoidal signals with finite lifetimes, which could be the case of the observed stochastic variations here if it is related to unresolved stochastically excited pulsations with finite lifetimes.

Figure 6.12 shows an example of the outcome of our continuous wavelet transform (CWT) of a 30-d subset of the combined residual *BRITE* light curve of ζ Pup, indicating a gradual increase in power towards longer time-scales, followed by a drop in power for time-scales longer than ~ 17 h. The bump at a pseudo-period of ~ 16.5 h might

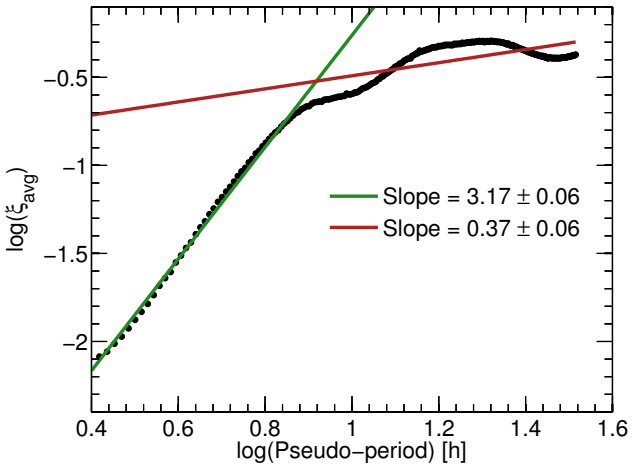

Figure 6.13: Weighted average energy distribution of pseudo-periods resulting from the CWT of the 11 subsets in the combined *BRITE* light curve of ζ Pup (taking as weights the time bases of the subsets), showing a change of slope at a pseudo-period of ∼8 h. The continuous lines are linear fits for pseudo-periods less than 8 h (green) and pseudo-periods beyond 8 h (red).

correspond to the 16.67 ± 0.81 h and 16.90 ± 0.48 h periods reported by Berghoefer *et al.* (1996) from an 11 d simultaneous X-ray and Hα monitoring of ζ Pup. These 'periods' have never been found again since then, and Nazé *et al.* (2013) invoked the possible transient nature of the signal associated with them. In our present investigations, the scalogram on Figure 6.12 clearly shows that the ∼16.5 h pseudo-period is only sporadically present during the *BRITE* observing run, most prominently around time ∼5519.5 and ∼5535.0, and lasts about $\sim 2.5 - 4$ d when it is excited. Also given the width of the bump at the ∼16.5 h pseudo-period, it is not relevant to assign an exact value for it, as for instance a Gaussian fit to the bump yields 16.42 ± 9.5 h. In view of the scalogram on Figure 6.12, we notice a pseudo-period drift from long time-scales (∼22 h) to shorter time-scales (∼12 h), mostly visible between times $\sim 5517.5 - 5521.0$ during which there is a pseudo-period drift from ∼16 h to ∼11 h, and between times

~5533.0 – 5536.0 during which pseudo-periods drift from ~22 h to ~16 h, a behaviour that remains unexplained but could be the cause for the large spread of power around the bump at the ~16.5 h pseudo-period. Finally, we also note a minor pseudo-period bump at ~8 h, which also seems to be only intermittently excited during the observing run, but has a shorter lifetime ($\lesssim$ 1 d) than the ~16.5 h pseudo-period. From all these considerations, it could also be that these two bumps are just part of the spectrum of pseudo-periods constituting the stochastic variability of the star. Therefore, from the CWT of all the 11 subsets that we analysed, we calculated the weighted mean energy distribution of the time-scales (with the lengths of the subsets as weights), best fit with a power-law of index 3.17 ± 0.06 for time-scales less than 8 h while time-scales greater than 8 h follow a less steep power-law of index 0.37 ± 0.06 (Figure 6.13).

6.5 Spectroscopic variability

6.5.1 Large-scale wind structures

6.5.1.1 Searching for periodicity in the He ii λ4686 line

As a first step in our investigations of the variability in the He ii λ4686 wind emission line of ζ Pup, we searched for periodicity in the global time series of difference profiles of the line (with respect to the global average profile) by performing a CLEAN Fourier analysis (Roberts *et al.* 1987) for each Doppler velocity in the range ± 1275 km s^{-1} (Figure 6.14). The resulting power spectrum unveils a dominant peak at $\nu_{0,\mathrm{HeII}} = 0.5615(1)$ d^{-1} [$P_{0,\mathrm{HeII}} = 1.7809(3)$ d], for which we assessed the uncertainty by extracting the half width at half maximum (HWHM) of a Gaussian fit to the peak. This frequency peak, detected across ± 500 km s^{-1} in Doppler velocity and mostly prominent on the blue side of the line profile, corresponds to the rotation frequency of the star that was

also detected in the *BRITE* and *Coriolis/SMEI* observations (Section 6.4.4; Table 6.IV and Figures 6.5 and 6.7). Moreover, the first harmonic $2\nu_{0,\mathrm{HeII}}$ is visible in the power spectrum but with a lower strength. Also some of the aliases of these two peaks are still visible in the power spectrum, such as the peak at $\mid 2\nu_{0,\mathrm{HeII}} - 2 \mid \sim 0.877$ d^{-1} as well as the 1 d^{-1} alias peak, all due to the unavoidable sampling gaps from the ground-based observations. Apart from the rotation period and its first harmonic we do not detect any other significant periodicity in the He II λ4686 line during our campaign. The absence of any sign of the $5.1 - 5.2$-d period through the entire width of the line profile is noteworthy. Furthermore, we do not detect any signs of that period in $H\alpha$ which was only covered by our *CTIO-SMARTS 1.5m/CHIRON* observations. That period was previously detected in $H\alpha$ (Moffat & Michaud 1981) and in UV observations (Howarth *et al.* 1995). However, in view of our findings that the true stellar rotation period is the 1.78-d period and not the $5.1 - 5.2$-d period (Section 6.4.4), the previous interpretations of the latter needs to be revised.

In view of the detection of the stellar rotation period in the variations of the He II λ4686 line profile, we inspected the behaviour of the difference spectra phase-folded on the rotation period, adopting the value $P = 1.78063(25)$ d that we derived from the *Coriolis/SMEI* and *BRITE* photometric observations (Section 6.4.4.1). As we know that the bright spots inducing this signal in the light curve evolve during the observing campaign (Sections 6.4.4.2 and 6.4.4.3), we subdivided the spectroscopic observations according to the five different parts of the *BRITE* observing run, Parts I–V, and looked at the phase-folded dynamic difference spectra for each of these parts. Due to insufficient phase sampling, the phased dynamic difference spectra during the first part of the transition (Part II) and towards the end of the campaign (Part V) did not show any obvious pattern that could be used to characterize the nature of the line profile variations (LPVs) related to the stellar rotation in the He II λ4686 line. The phased

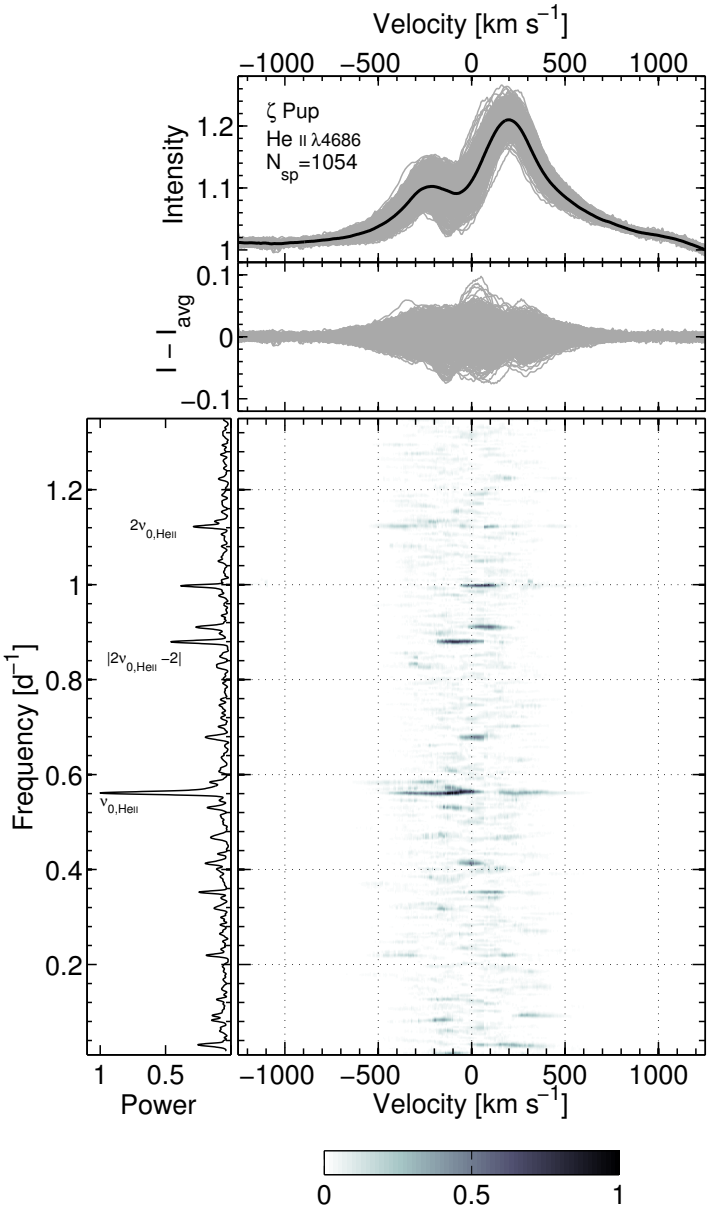

Figure 6.14: Global time series analysis of the He II λ4686 wind emission line profile of ζ Pup. *Top:* The 1054 profiles of the line as recorded throughout the entire campaign (grey) along with their average (black). *Middle:* Difference profiles with respect to the average profile. *Main:* CLEAN periodogram per Doppler velocity within ±1275 km s^{-1} for the time series of difference spectra, obtained after 10 CLEAN iterations. The side panel depicts the normalized integrated periodogram power within Doppler velocities ±500 km s^{-1} where most of the LPVs are detected.

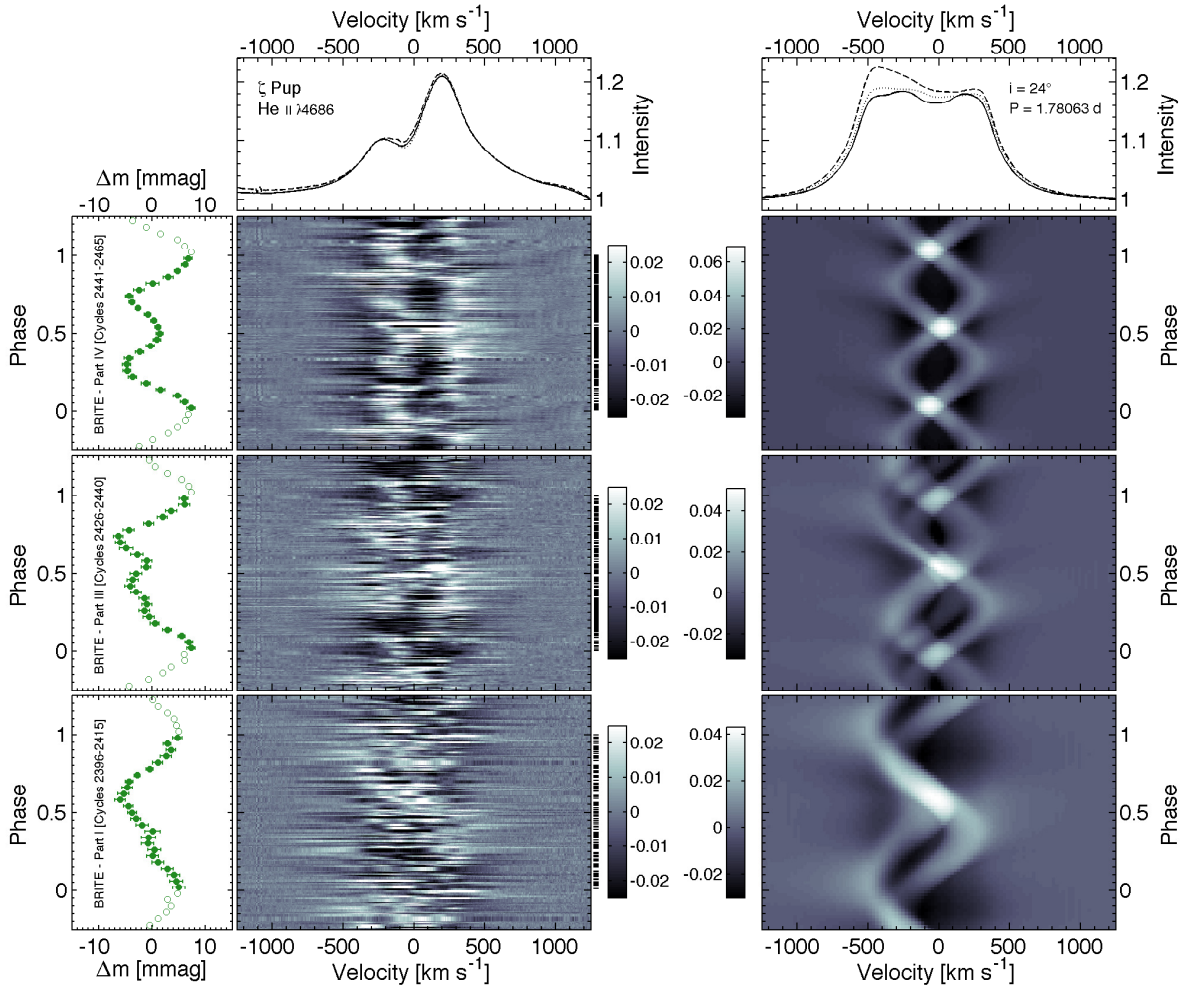

Figure 6.15: Arms of CIRs in the wind of ζ Pup as traced in its He II λ4686 emission line profile in parallel with the *BRITE* 2014–2015 observing run. Time increases upwards. *Left:* Observed dynamic difference spectra of ζ Pup phase-folded on the rotation period P = 1.78063(25) d, during Part I (bottom), Part III (second from the bottom), and Part IV (third from the bottom), along with the corresponding light variations observed by *BRITE* illustrated on the side panels. Small horizontal ticks on the right-hand side of each dynamic diagram indicate the phase sampling. The average profiles of the He II λ4686 line during each of these three parts of the observing campaign are depicted in the top panel (dashed: Part I; dotted: Part III; solid: Part IV). *Right:* Models of CIRs corresponding to each of the three parts of the observing campaign, with an assumed stellar inclination angle i = 24° and taking the locations of the bright spots detected by the light curve inversion algorithm (Section 6.4.4.3; Figure 6.8) as input locations of the photospheric footprints of the CIRs. The top panel depicts the average modelled profiles corresponding to the three parts of the observing run (dashed: Part I; dotted: Part III; solid: Part IV), not accounting for the resonance zone effect as explained in Section 6.5.1.2.3.

dynamic spectra for Part I (before the transition), Part III (end of the transition) and Part IV are illustrated on the left-hand panel of Figure 6.15 in which we note the following behaviour:

[i] Part I: an 'S' pattern in excess emission is mildly visible, reaching maximum redshift around phase 0.35 and maximum blueshift around phase 0.85.

[ii] Part III: the behaviour of the LPVs are fuzzy, but the clearest one is the bump on the red side of the line profile (between $0 - 400$ km s^{-1}) before phase ∼0.5, which appears to be part of the 'S' pattern seen in Part I.

[iii] Part IV: a double 'S' bumped pattern is strikingly visible, wandering between ∼±400 km s^{-1}. Note that this corresponds to the part during which the two bumps in the *BRITE* light curves are clearly visible, caused by the two dominant equatorial surface spots separated by ∼158° in longitude.

The double 'S' pattern that we clearly see during Part IV is a typical sign of the presence of two CIR arms induced by two equatorial perturbations (Dessart & Chesneau 2002), which, according to our findings in Section 6.4.4.3, are the equatorial bright spots separated by ∼158° in longitude observed by *BRITE* during this part of the observing campaign (Figure 6.8). This situation confirms the theoretical predictions of Dessart & Chesneau (2002), as not only did they use the stellar parameters of ζ Pup in all their CIR models, but more importantly our findings for the behaviour in Part IV are remarkably similar to the behaviour that they found in their Model C (figure 3 in Dessart & Chesneau 2002) for which the assumed photospheric perturbations were two equatorial bright spots diametrically opposed on the stellar surface and the assumed stellar inclination angle was 20° (the actual inclination angle of ζ Pup is $i \sim 24°$ according to our findings: Section 6.4.4.1), with the assumed line emission region (LER) extending from $2R$ to $4R$.

6.5.1.2 CIR model

Following the detection of the patterns of manifestations of CIR arms in the phased dynamic difference profiles of the He II λ4686 line, most prominently the double "S" pattern that we see during Part IV of the observing run, we further investigated the consistency of these observed LPVs with models of CIR arms that would be generated by the bright photospheric spots observed by *BRITE* and mapped by LI. To this end, we adopted an analytical approach to determine the behaviour of LPVs induced by a given number of CIR arms in a hot-star wind emission line profile. In our approach, the input parameters consist of:

- **[i]** the inclination angle i of the star, its rotation period P, and its radius R;
- **[ii]** the radius $r_{\rm I}$ at which the stellar wind initiates, as well as the terminal wind speed v_∞;
- **[iii]** two radial functions, one for localizing the LER, and another one for accounting for ionization gradients through the wind;
- **[iv]** the number of CIR arms, each of them specified by its density contrast η with respect to the unperturbed wind, its opening angle ψ, and the location of its photospheric driver on the stellar surface.

Here, we provide a brief description of the basis of this CIR modelling approach and the results that we obtained in the case of ζ Pup, but a more detailed description of the code will be available in a dedicated forthcoming paper (St-Louis *et al.* 2018).

6.5.1.2.1 The emergent line profile for a spherically symmetric wind

In the absence of CIR arms, our calculations of hot-star wind emission-line profiles is performed under the assumption of spherical symmetry, stationarity, and smoothness of the outflow, the latter meaning a stellar wind free of small-scale inhomogeneities. Also

in terms of the velocity field of the wind material, the polar and azimuthal components are assumed to be negligible compared to the radial expansion. Thus, with the geometry depicted in Figure 6.16, a portion of wind material located at point $P(r, \vartheta, \varphi)$ in terms of its spherical coordinates in the stellar reference frame moves outward with a velocity $\vec{v}(\vec{r}) = v_r(r)\vec{e}_r$, assumed to follow the usual β-law:

$$v_r(r) = v_\infty \left(1 - b\frac{r_\mathrm{I}}{r}\right)^\beta, \quad b = 1 - \left(\frac{v_\mathrm{I}}{v_\infty}\right)^{\frac{1}{\beta}} \tag{6.17}$$

with v_I the radial speed at which the stellar wind initiates. As mentioned in Section 6.4.2, $v_\mathrm{I} = v_\mathrm{sonic}$ and is reached at $r_\mathrm{I} \simeq 1.027R$ (Figure 6.4). Thus, the wind domain being in the supersonic regime, calculations of line profiles originating from the wind can be performed under the Sobolev approximation: at a given frequency displacement ν with respect to the line-centre frequency ν_0, the emission is dominated by the contribution from locations in the stellar wind where the local component of the velocity field is in resonance with the frequency ν (see e.g. Equations 38 and 39 in Petrenz & Puls 1996). At a given frequency ν, the monochromatic line flux as received by the observer at distance D from the star is:

$$F_\nu = \frac{1}{D^2} \int_0^{2\pi} \int_0^{\pi} \int_0^{\infty} j_\nu(r) r^2 dr d\cos\vartheta d\varphi, \tag{6.18}$$

involving the emissivity j_ν, which, under the Sobolev approximation, is expressed as (Rybicki & Hummer 1983):

$$j_\nu(r) = \mathcal{F}(r)\mathcal{H}\left(\frac{v_r(r)}{c}\nu_0 - |\nu - \nu_0|\right), \tag{6.19}$$

where the presence of the Heaviside function $\mathcal{H}$ accounts for the resonance zones mentioned previously. This also reflects the fact that at a given radial distance r, the spherical shell of radius r expanding at velocity $v_r(r)$ contributes to the emission as a flat-top profile spanning $\nu_0[1 \pm v_r(r)/c]$, weighted by the quantity:

$$\mathcal{F}(r) = \frac{1}{2\nu_0}\frac{c}{v_r(r)}\kappa(r)S(r)g(r)\mathcal{P}(r), \tag{6.20}$$

the factor $c/2\nu_0 v_r(r)$ arising from wind broadening, $\kappa(r)$ being the integrated line opacity, $S(r)$ the source function, $g(r)$ a function that incorporates all dependencies on temperature variations and changes in ionization throughout the wind, while $\mathcal{P}(r)$ denotes the Sobolev escape probability.

For recombination lines such as the He II λ4686 line in ζ Pup, the product $\kappa(r)S(r)$ scales as the square of the density $\rho(r)$ of the wind. By means of the equation of mass continuity, $\dot{M} = 4\pi r^2 v_r(r)\rho(r)$, the product $\kappa(r)S(r)$ therefore ultimately scales as $1/r^2v_r^2(r)$. As for the function $g(r)$, we assume a dependence of the form $[1-v_r(r)]^{\alpha_0}$, where the exponent α_0 would then counter the $1/v_r^2(r)$ dependence to create an asymmetric bell curve in velocity space that localizes the LER. From the investigations of Hillier *et al.* (2012), we know that one has to go at least up to $\sim 2.5 - 3.5R$ to account for the actual shape of the He II λ4686 line profile in ζ Pup, and the emission falls off slowly beyond that bulk of the wind (D. J. Hillier, private communication). Here we adjust the exponent α_0 to roughly localize the LER, although we note that in reality the departure coefficients from conditions of local thermodynamic equilibrium (LTE) may change rapidly and may not be well represented by the simple form of the $g(r)$ function that we adopted. However, it is a reasonable approximation to adopt in the absence of any detailed constraints on the LER.

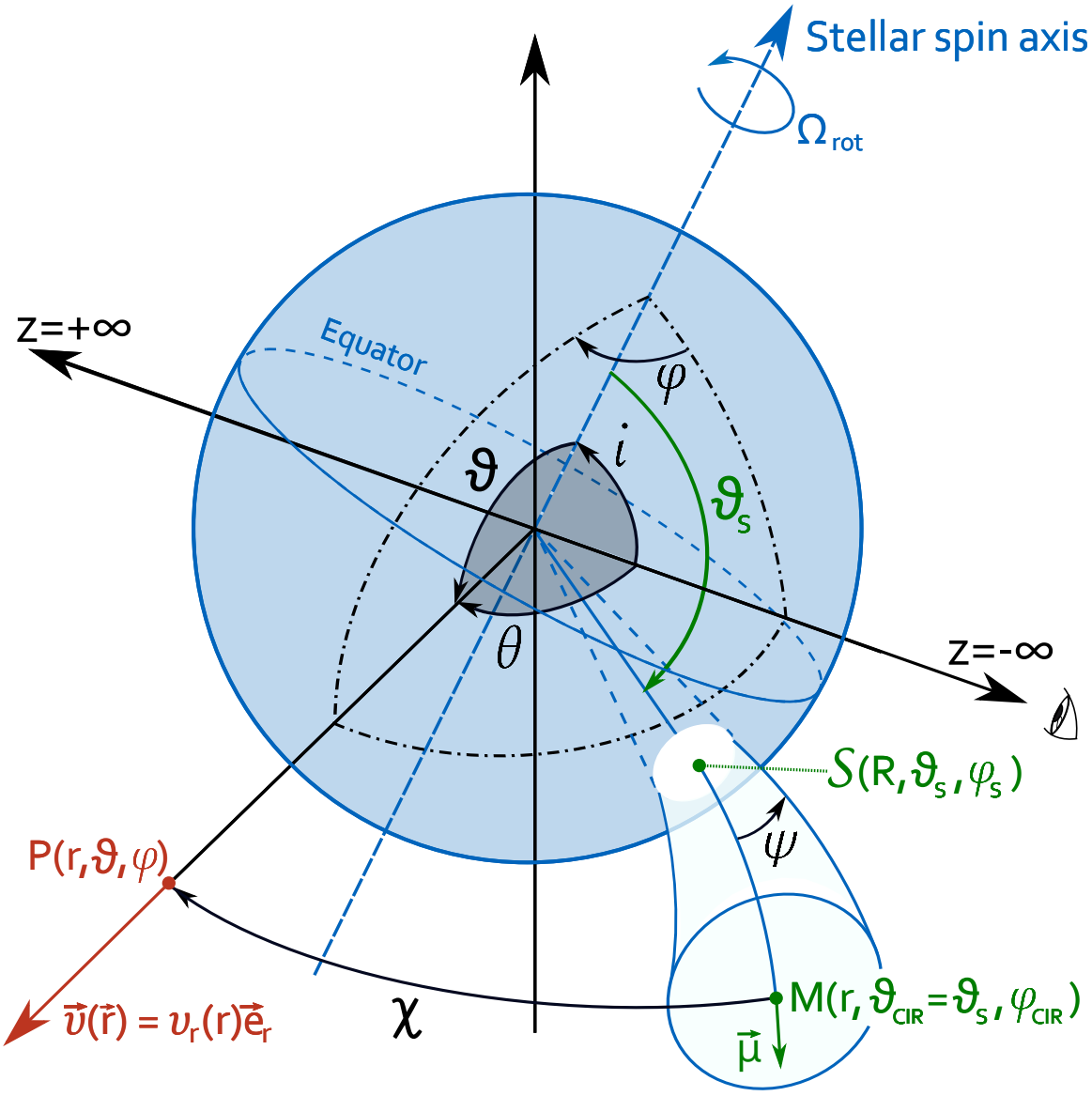

Figure 6.16: Geometry adopted for the simulation of hot-star wind emission line profiles from a spherically symmetric smooth stationary stellar wind and calculation of LPVs induced by the presence of a spiral-shaped CIR compression.

In addition, the Sobolev escape probability $\mathcal{P}(r)$ is given by:

$$\mathcal{P}(r) = \frac{1 - e^{-\tau(\vec{r},\vec{n})}}{\tau(\vec{r},\vec{n})}, \tag{6.21}$$

$\tau(\vec{r},\vec{n})$ being the optical depth evaluated at the point of consideration along the direction specified by the unit vector $\vec{n}$, expressed in the Sobolev approximation as:

$$\tau(\vec{r},\vec{n}) = G(r) \times \frac{\rho^2(r)}{|\nabla_{\vec{n}}(\vec{v}\cdot\vec{n})|}, \tag{6.22}$$

where $|\nabla_{\vec{n}}(\vec{v}\cdot\vec{n})|$ denotes the velocity gradient along direction $\vec{n}$, while the function $G(r)$ accounts for ionization gradients through the wind. Following Lamers *et al.* (1987), we adopt the generalized form $G(r) = v_r^{\alpha_1}(r)\,[1 - v_r(r)]^{\alpha_2}$, in which the exponents α_1 and α_2 are in practice adjusted to match the observed shape of the line profile. Thus, taking also into account the equation of mass continuity, the optical depth takes the form:

$$\tau(\vec{r},\vec{n}) = \mathcal{M} \times \frac{v_r^{\alpha_1-2}(r)\,[1 - v_r(r)]^{\alpha_2}}{r^4|\nabla_{\vec{n}}(\vec{v}\cdot\vec{n})|}, \tag{6.23}$$

with $\mathcal{M} = (\dot{M}/4\pi)^2$. Then, in order to evaluate the Sobolev optical depth, the velocity gradient is measured along the line-of-sight ($\vec{n} = \vec{e}_z$ here) and takes the form (e.g. Rybicki & Hummer 1983; Lamers *et al.* 1987; Mazzali 1990; Petrenz & Puls 1996; Ignace & Hendry 2000; Ignace & Gayley 2003):

$$\nabla_{\vec{n}}(\vec{v}\cdot\vec{n}) = \frac{\partial v_z}{\partial z} = \frac{\partial v_r(r)}{\partial r}\cos^2\theta + \frac{v_r(r)}{r}\sin^2\theta, \tag{6.24}$$

with θ denoting the observer polar angle (i.e. the angle between the line of sight, which is the z axis here, and the position vector $\vec{r}$; Figure 6.16).

Finally, we note that the calculation of the line flux from Equations 6.18 and 6.19

has to be performed excluding part of the stellar wind material located behind the star which remains unseen by the observer. Occultation happens if the angle θ is such that:

$$\cos\theta < -\sqrt{1-\left(\frac{R}{r}\right)^2}, \tag{6.25}$$

in which $\cos\theta$ can be expressed in terms of the azimuth angle φ, the colatitude ϑ and the stellar inclination angle i through the cosine rule:

$$\cos\theta = \cos\vartheta\cos i + \sin\vartheta\sin i\cos\varphi. \tag{6.26}$$

6.5.1.2.2 Presence of CIR arms

In our simulations, the stellar surface is assumed to rotate rigidly at a constant angular frequency $\Omega = 2\pi/P$, and the photospheric source of a CIR arm is assumed to be a bright surface perturbation having a circular shape located at $\mathcal{S}(R, \vartheta_s, \varphi_s + \Omega t)$. The half-opening angle ψ of the CIR is defined to be that of the cone formed by the circular spot and the centre of the star (Figure 6.16). As already pointed out by Dessart & Chesneau (2002), the feature in the CIR that is at the origin of the variability observed in the wind emission lines is the spiral-shaped region of density compression associated with the CIR (region III in figure 5 of Cranmer & Owocki 1996), which in turn can be perceived as a region where the emissivity is increased by a factor $(\eta+1)^2$, with $\eta = (n_{\rm CIR} - n_{\rm sph})/n_{\rm sph}$ being the density contrast between the region of CIR compression of density $n_{\rm CIR}$ and the spherically symmetric smooth wind of density $n_{\rm sph}$. Thus, within the region of CIR compression, the integrand in the calculation of the line flux (Equation 6.18) becomes $r^2(\eta+1)^2 j_v$. Also, in terms of its shape, the region of CIR compression is taken to follow a spiral with increasing radial distance from the centre of the star, while at a given radial distance r the intersection of the spiral-shaped CIR compression and a spherical

shell of radius r is assumed to form a circle. The axis of the region of CIR compression is then defined to be the locus composed by the centres of these circular cross-sections with increasing radial distance r. From all these considerations and from the geometry described in Figure 6.16, the condition for falling within the region of CIR compression is straightforward:

$$\arccos\chi < \psi, \tag{6.27}$$

where χ is the angle between the position vector $\vec{r}$ and the outward normal at the centre M of the circular cross-section of the CIR compression at radial distance r (unit vector $\vec{\mu}$ at point M in Figure 6.16). Again, by means of the cosine rule, this angle can be expressed in terms of the colatitude ϑ and the azimuth angle φ of the position vector, as well as the colatitude $\vartheta_{\rm CIR}$ and the azimuth angle $\varphi_{\rm CIR}$ of the centre of the cross-section of the CIR arm at distance r from the centre of the star:

$$\cos\chi = \cos\vartheta\cos\vartheta_{\rm CIR} + \sin\vartheta\sin\vartheta_{\rm CIR}\cos\left(\varphi_{\rm CIR} - \varphi\right), \tag{6.28}$$

in which $\vartheta_{\rm CIR} = \vartheta_{\rm s}$ at all times and radial distances, whereas the azimuth angle $\varphi_{\rm CIR}$ carries all the information on the time dependence (owing to the stellar rotation) and the shape of the CIR arm:

$$\begin{aligned}\varphi_{\rm CIR} = \varphi_{\rm s} + \Omega t - \frac{\sin\vartheta_{\rm s}}{x_{\rm p}}\Bigg(\frac{r}{R} - 1 + b\ln\left[\frac{r}{R}\right] \\ + \frac{1-b^2}{b}\ln\left[(1-b)\frac{v_\infty}{v_r(r)}\right]\Bigg),\end{aligned} \tag{6.29}$$

a closed-form expression that follows Ignace *et al.* (2009) and Ignace *et al.* (2015) in which it is assumed that $v_\varphi(r) = 0$ for the purpose of solving the spiral shape, due to the complexity of non-radial force considerations and because we do not perform

hydrodynamical calculations in our simulations and do not have any real guidance on $v_\varphi(r)$. Also, it is worth noting that in Equation 6.29, the dimensionless quantity $x_\mathrm{p} = v_\infty/(\Omega R)$ measures the ratio of the distance travelled by the outer boundary of the stellar wind in one rotation period with respect to the stellar equatorial diameter, thus indicative of the asymptotic pitch angle of the spiral-shaped CIR compression.

6.5.1.2.3 Application to the case of ζ Pup

First and foremost, we emphasize again that we generate all our CIR models to check the consistency of the observed CIR patterns (left-hand panel of Figure 6.15) with the bright photospheric spots observed by *BRITE* and mapped by LI. No hydrodynamical calculations and no formal fit of the modelled LPVs to the observed ones are performed here. Moreover, the models have infinite S/N, as no noise of instrumental origin or intrinsic to the star (e.g. due to clumps) was added to the models.

Regarding the observed shape of the He II λ4686 emission-line profile in ζ Pup, the presence of a notch close to the line centre is noteworthy. Since the line is mainly formed in the stellar wind, the radial expansion of the wind itself can contribute to a blue-shifted P Cygni-type absorption in the line. In that respect, the shape of the line profile can be considered as of type III in Beals' (1953) classification of P Cygni-type line profiles. Additionally, ζ Pup being a fast rotator, it has been shown that a proper consideration of the azimuthal velocity field can account for the actual shape of some of its photospheric emission line profiles as well as its wind emission lines such as Hα and He II λ4686 (Hillier *et al.* 2012), the main mechanism involved being the so-called "resonance zone effect" as described in detail by Petrenz & Puls (1996), who found that the introduction of the azimuthal velocity field induces a decrease of the optical depth for Doppler velocities near the line centre as the corresponding resonance zones are twisted away from the star, whereas the optical depth is increased for higher Doppler velocities as the corresponding

resonance zones are twisted towards the star (Figure 6 in Petrenz & Puls 1996). As a consequence, the line emission flux is redistributed towards higher Doppler velocities, resulting in the actual shape of the He II $\lambda 4686$ line having two maxima near $\pm v \sin i$ and a (slightly blue-shifted) notch close to the line centre. Therefore, that notch is a feature associated with the unperturbed wind, and not related to the presence of variable small-scale or large-scale wind structures. Thus, in our simulations we do not take into account the resonance zone effect and consider a velocity field dominated by radial expansion as already stated in Section 6.5.1.2.1.

The right-hand panel of Figure 6.15 depicts the modelled patterns of LPVs corresponding to CIR arms that would be induced by the bright spots detected by the light curve inversion algorithm for Parts I, III and IV of the observing campaign (Section 6.4.4.3.3, Figure 6.8). These models correspond to a stellar inclination angle of $24°$ and the stellar wind parameters of ζ Pup listed in Table 6.I, the values of the density contrast η ranging from $1.5 - 4$ to match with the typical amplitudes of the observed LPVs, and the exponents $(\alpha_0, \alpha_1, \alpha_2) = (1, -14, 5)$.

The modelled LPVs are in good agreement with the observed ones, especially in Part IV where the best phase coverage was achieved in the observations, allowing for the clear detection of the double 'S' pattern due to the two CIR arms. In the modelled CIR patterns corresponding to Part I, we notice that we do not reproduce the apparent bump happening around the line centre around phase ~0.8. This could be due to the fact that the light curve inversion algorithm might have missed detecting a faint/small spot that would have caused a CIR arm responsible for that bump during Part I. However, it has to be noted and emphasized that this part of the observing campaign has the worst phase coverage, which plays an important role in the clear detection and characterization of the LPVs.

6.5.1.3 Variability in other lines

In view of the behaviour in the phased diagrams for He II λ4686, we explored the variability in other line profiles, some photospheric (e.g. He II λ5411) and some forming in the wind (Hα). Our CLEAN Fourier analyses across the lines detected the rotation period in most of them (Figure 6.17), and even the first harmonic of the rotation period is detected in the Balmer lines. However, the phased dynamic difference diagrams for these lines, either by considering the entire time series or by splitting it into different parts, does not show any obvious pattern, which might be an indication on the weakness of the signal in these lines, requiring more S/N for their characterization in phased dynamic difference plots. Particularly, in the case of photospheric lines we do not detect any sign of the ~8.5 h periodicity reported by Baade (1986) and Reid & Howarth (1996), except a possible marginal detection in the blended He I λ6678+He II λ6683 line for which the noise level in its CLEAN periodogram is much higher than those of the other lines.

To further inspect the correlation between the variations observed by *BRITE* and the LPVs, we extracted the time series of the equivalent widths (EW) of He II λ4686, Hα and Hβ (Figure 6.18). Not only is the behaviour of the phased EW variations and the phased light variations strongly correlated, but more importantly a noticeable phase delay is observed in the EW variations in the lines most sensitive to the wind (He II λ4686 and Hα) with respect to the photospheric light variations probed by *BRITE*. Table 6.VI lists the outcome of a cross-correlation analysis of the phased EW measurements with the phased *BRITE* light curve averaged in 0.04 phase bins. From these cross-correlation analyses, we conclude that, besides the noticeable phase delays in He II λ4686 and Hα with respect to the light variations probed by *BRITE*, there appears to be a real phase delay even between He II λ4686 and Hα, and between Hβ and the *BRITE* observations.

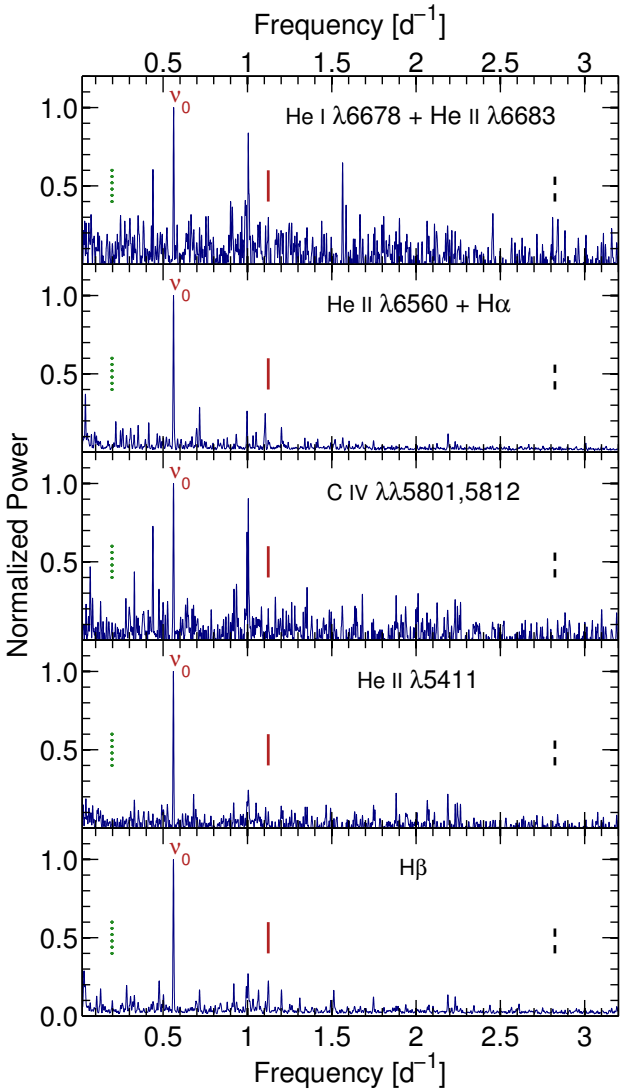

Figure 6.17: Normalized CLEAN power spectra of the time series of difference profiles of some optical lines in ζ Pup, integrated over ± 500 km s^{-1} except for He II λ6560+Hα for which integration was performed over ± 1000 km s^{-1}. The 1.78 d period due to the stellar rotation is detected in all these lines. The vertical red line points to the location of the first harmonic of the rotation period (here detected in the Balmer lines), while the vertical dotted green line indicates the location of the 5.075 ± 0.003 d period (no detection here), and the vertical black dashed line indicates the location of the 8.54 ± 0.054 h period (only a possible marginal detection in the noisy and blended He I λ6678+He II λ6683 lines).

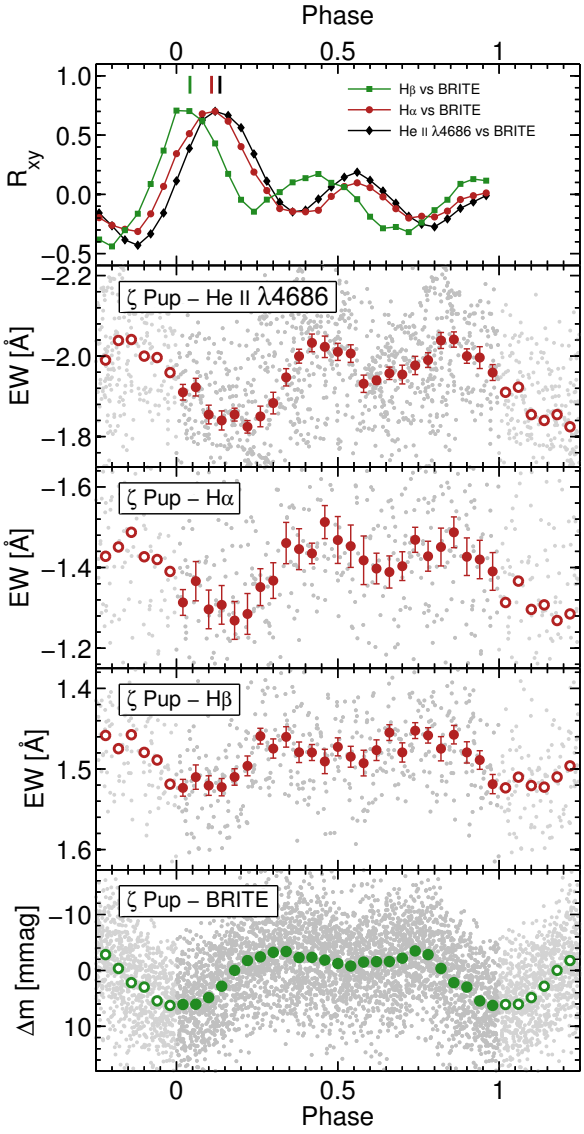

Figure 6.18: First four panels from bottom to top: light variations of ζ Pup as observed by *BRITE* phased with the stellar rotation period, along with the phased time series of EWs of the Hβ, Hα, and He II λ4686 line profiles of the star. The vertical scale on the panel for Hβ is exactly twice larger than the vertical scales on He II λ4686 and Hα. *Upper panel:* Cross-correlation sequences of the EW variations with respect to the light variations observed by *BRITE*. The measured phase delays extracted through Gaussian fits to the first main cross-correlation peaks are indicated by the vertical markers (the Gaussian fits themselves are not overplotted for the sake of visibility).

Table 6.VI: Phase delays measured from the cross-correlations of the phased EW variations of the Hβ, Hα, and He II λ4686 lines of ζ Pup with respect to its phased light variations observed by *BRITE*. The values of the phase delays $\Delta\phi$ were assessed through Gaussian fits to the first main cross-correlation peaks, then translated via Equation 6.29 into the radial extent of the CIR arm (measured from the centre of the star) probed by each line profile.

Line	$\Delta\phi$	r [R]
Hβ	0.04 ± 0.03	1.7 ± 0.7
Hα	0.11 ± 0.01	2.9 ± 0.9
He II λ4686	0.14 ± 0.02	3.5 ± 1.1

More importantly, the phase delays observed in Figure 6.18 and quantified by the cross-correlation analyses are indicative of the azimuthal difference $\Delta\varphi = \varphi_{\rm CIR} - \varphi_{\rm s}$ involved in Equation 6.29, such that we can solve for r in that relation and thus extract the typical radial distance in the wind at which we probe the CIR arms through Hβ, Hα and He II λ4686. The resulting values of r are also listed in Table 6.VI, in which the error bars are the consequences of accounting for the uncertainties on R, v_∞, Ω and $\Delta\varphi$. It is worth noting that the values that we find for r are in good agreement with the extent of the regions of line formation (up to $\sim 2.5 - 3.5R$ for He II λ4686 and Hα as previously mentioned, and closer to the stellar surface for Hβ).

Thus, from all these considerations, we conclude that the 1.78 d cyclic intrinsic light variations observed by *BRITE* in ζ Pup, which we found to occur at the photosphere (Section 6.4.2) and are due to rotational modulation related to the presence of bright photospheric inhomogeneities (Section 6.4.4), are the photospheric drivers of the large-scale CIR arms in the stellar wind as traced by the cyclic variations that we detect in He II λ4686 (and Hα). This implies that our findings constitute the first observational evidence for a direct link between CIRs in the wind of an O-type star and their

photospheric drivers.

6.5.1.4 CIR/DAC recurrence time-scales

As mentioned in Section 6.2.1, the presence and blueward recurrent propagation of DACs observed in the absorption troughs of unsaturated resonance lines of most O-type stars is best interpreted as the spectroscopic manifestation of the presence of CIRs in their winds (Mullan 1986; Cranmer & Owocki 1996). Also, previous *IUE* monitoring of ζ Pup unveiled that the mean DAC recurrence period of the star was 19.23(45) h, so that when it was believed that the stellar rotation period is 5.1 d, the star would exhibit on average $5 - 6$ DACs per rotation cycle (figure 1 of Howarth *et al.* 1995), a behaviour that deviates from that found in most O-type stars for which an average of two DACs per rotation cycle are generally observed (Kaper *et al.* 1999). Now our results that the true rotation period of ζ Pup is much shorter, $P = 1.78063(25)$ d, changes that picture. It is worth noting that the consecutive bumps observed in the phased *BRITE* light curves and in the EW variations of the wind emission lines have a separation that varies between $0.4 - 0.5$ in phase. For instance, a separation of $\Delta\phi = 0.45$ in rotational phase would correspond to two 'events' separated by a time interval of $\Delta t = 19.2308(27)$ h, which is compatible with the DAC recurrence time-scale of 19.23(45) h reported by Howarth *et al.* (1995), but then in that configuration the next 'event' would have to happen after $\Delta\phi' = 0.55$, i.e $\Delta t' = 23.5043(33)$ h later, such that the Fourier analysis of the time series over several cycles would still give rise to a peak at the first harmonic (21.3676(30) h), not at the ∼19.23 h time-scale. Additionally, it has to be considered that Prinja *et al.* (1992) identified a DAC recurrence time-scale of ∼15 h (no error bar available) from the examination of ∼2.2 d of intensive observations within a 5.5-d contiguous *IUE* monitoring of ζ Pup in 1989. Thus, all the information

available to date appears to point out that the average inter-DAC 'period' of ζ Pup has not always been strictly the same over the past three decades. In Figure 6.19, we plot the known 'periodicities' that *might be associated* with CIRs/DACs in ζ Pup. The change in 'periodicity' seems gradual over about two decades, increasing from ∼15 to 21 h, although rapidly at first, then asymptotic later. In this plot, we have also marked the location of the 16.67 ± 0.81 h and 16.90 ± 0.48 h periodicities reported by Berghoefer *et al.* (1996) from a simultaneous X-ray and Hα monitoring of ζ Pup spanning 11 d in 1991, as they appear to follow the global trend in the plot, although at this point the physical origin of these periodicities is not well-established and more importantly has never been formally proven to be related to CIRs/DACs. Also, for the epoch of the *Coriolis/SMEI* observations, we have explicitly marked the location of the first harmonic of the 1.78 d signal, but one has to keep in mind that only the fundamental frequency has a high statistical significance in these data sets.

The global trend in Figure 6.19 is unlikely related to a slowing down (especially if non-uniform in time) of the stellar rotation period: the mass-loss rate is simply too low to allow this and there is no plausible or conceivable internal mechanism to cause such a large change in rotation over such a short time. On the other hand, looking at the behaviour of the Sun in terms of rotation and spot activity, we see clear surface differential rotation from a period of ∼25 d at the equator to ∼35 d at the poles, with spot migration from mid to low latitude over an 11-yr cycle. Among late-type stars in general, one does see both solar-type surface differential rotation (faster rotation at the equator: e.g. Donati & Collier Cameron 1997; Kovári *et al.* 2004; Petit *et al.* 2004; Roettenbacher *et al.* 2011) and anti-solar type of differential rotation (slower rotation at the equator: e.g. Hackman *et al.* 2001; Strassmeier *et al.* 2003; Harutyunyan *et al.* 2016). Inspired by this, we *speculate* that ζ Pup with its very rapid overall rotation could also exhibit differential rotation with the *dominant* spots wandering quickly first from

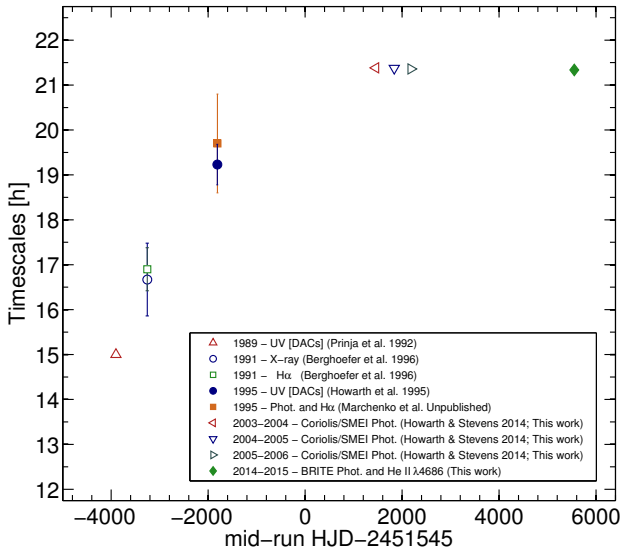

Figure 6.19: Known 'periodicities' that might be related to CIRs/DACs in ζ Pup. Note: The ∼15 h time-scale reported by Prinja *et al.* (1992) does not have an error bar. The results of the simultaneous ground-based photometry and Hα spectroscopy in support of the *IUE* MEGA campaign observations remain unpublished, although they reveal a 19.7(1.1) h periodicity that is consistent with the results of the *IUE* observations.

higher latitudes with faster rotation to spots wandering slowly to lower latitudes with slower rotation at the bulging equator. In that scenario, the *dominant* spots observed at a given epoch of observation would be located around the same latitude, forming an 'active latitude', analogous to the Sun's active latitudes that change over time to form the so-called 'Butterfly diagram' of the Sun's activity cycle. That being said, the surface maps that we obtained through the light curve inversion of the *Coriolis/SMEI* and *BRITE* light curves of ζ Pup also reveal the presence of spots at mid-latitudes. However, one important point that we emphasize here is that the light curve inversion algorithm as it stands currently allows for rigid rotation only, although it still can reveal differential rotation from the relative drifts in spot longitudes between different data sets (Roettenbacher *et al.* 2011). Nevertheless, on this note we leave further speculation in anticipation of future long-term monitoring of this ever-more interesting massive star.

6.5.2 Small-scale wind structures

The densest temporal coverage for the multi-site ground-based spectroscopic monitoring of ζ Pup that we conducted in parallel with the *BRITE* observing run was achieved during ~5 d in February 2015 (HJD $2,457,059.94 - 2,457,065.10$) when we had optimal longitude coverage from facilities at CTIO-SMARTS 1.5m/CHIRON, SAAO 1.9m/GIRAFFE and SASER. We took this opportunity to look for signatures of small-scale wind structures in He II λ4686, as previously found by Eversberg *et al.* (1998).

6.5.2.1 Dynamic difference spectra

Our spectra have a typical S/N ~ 500 in the continuum close to He II λ4686, which is about a factor two lower than the S/N in the CFHT 3.6m/Reticon spectra of ζ Pup

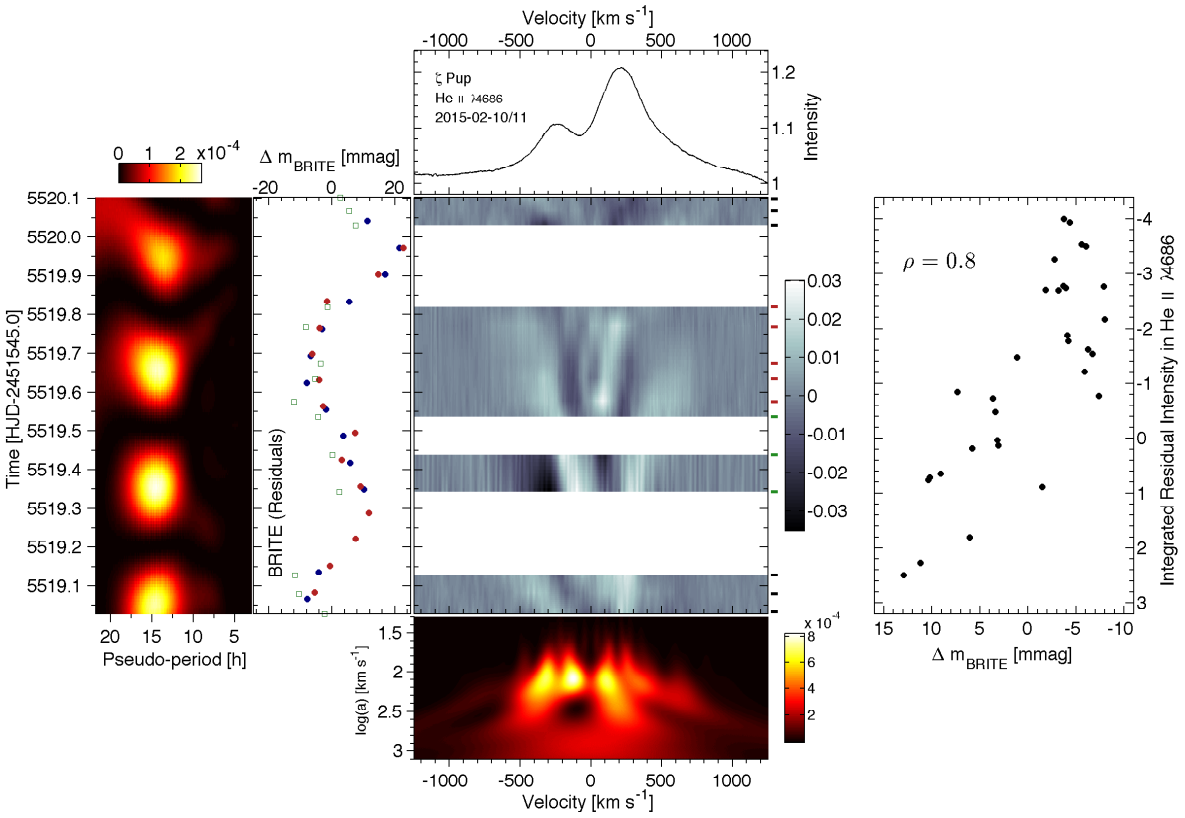

Figure 6.20: Kinematics of outmoving wind clumps in ζ Pup as traced in He II λ4686, along with their photospheric drivers as observed by *BRITE* during the night of February 10/11, 2015. *Top:* Average profile of the He II λ4686 line for the night. *Middle:* Dynamic difference spectra from the average spectrum after removal of the effects of the 1.78-d cyclic variations due to large-scale wind structures (Section 6.5.2.1). Small horizontal ticks on the right side of the diagram indicate the time sampling, with observations performed from Shenton Park Observatory (black), SAAO 1.9m/GIRAFFE (green) and CTIO-SMARTS 1.5m/CHIRON (red). *Bottom:* Average scalogram from the Ricker wavelet-based CWTs of the spectra (in the spatial/wavelength domain). *Left:* Light variations of ζ Pup recorded by *BRITE* in the blue (blue points) and red (red points) filters during the night of February 10/11, 2015. The light curves illustrated here are those free of the effects of the 1.78-d signal associated with rotational modulation (Section 6.4.5, Figures 6.11 and 6.12). Green squares represent the integrated intensity variations in the difference spectra within the velocity range $\pm$1000 km s^{-1}, with the scaling factor $C = -3$ (Equation 6.30, Section 6.5.2.3). *Far Left:* Portion of the scalogram of the residual *BRITE* light curve restricted to that specific night (taken from Figure 6.12), showing that the dominant time-scale during that night was $\sim$14 – 15 h. There seems to be a slight pseudo-period drift during the night, as already noted in Section 6.4.5.2. *Right:* Strong correlation between the integrated intensity variations in He II λ4686 and the light variations observed by *BRITE*.

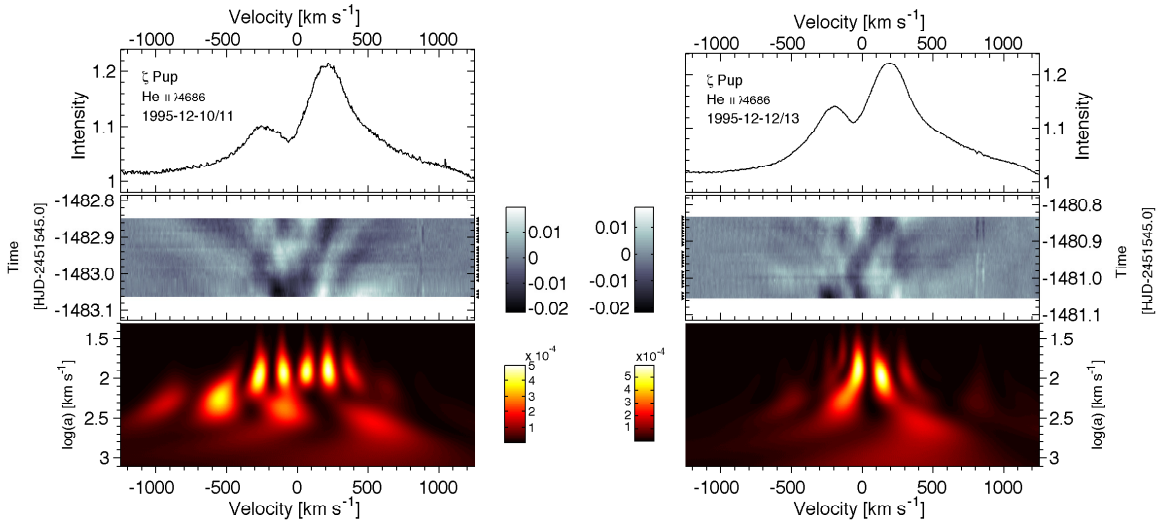

Figure 6.21: Outmoving wind clumps in ζ Pup as first reported by Eversberg *et al.* (1998) from two nights of CFHT 3.6m/Reticon observations (archival data) in December 10/11, 1995 (*Left*) and December 12/13, 1995 (*Right*). For a given night, the *top panel* illustrates the mean spectrum for the night, the *middle panel* shows the dynamic difference spectra from the average spectrum, and the *bottom panel* depicts the average scalogram. The scalogram signatures of the clumps are the same as observed during the *BRITE* 2014 – 2015 observing run, with a dominant scale at $a \sim 10^{2.0} - 10^{2.1}$ km s^{-1}.

in which Eversberg *et al.* (1998) found manifestations of wind clumps. Still, we detect signatures of wind clumps in our observations, as clearly revealed by the dynamic difference spectra in the main panel of Figure 6.20 for the night of February 10/11, 2015 (HJD $2,457,064.03-065.10$) during which the signatures are the most discernible: features in emission excess that appear at random both in Doppler velocity and in time, and propagate away from the line centre towards the red/blue edges while smearing out and dropping in intensity with time until they reach Doppler velocities $\sim\pm500$ km s^{-1} from where they seem to fade away. That the features seem to disappear beyond velocities $\sim\pm500$ km s^{-1} does not necessarily mean that the actual clumps causing these signatures physically vanish, as the LER in which we see their manifestations only spans a limited Doppler velocity range that clearly does not reach the terminal wind speed in the case of He II $\lambda4686$ for ζ Pup which has $v_\infty = 2300 \pm 100$ km s^{-1}. Also, another striking property that we notice in the dynamic difference spectra on the main panel of Figure 6.20 is that the velocity widths are narrower for features located close to the line centre (e.g. those that appear at time ~5519.50) compared to those features that appear at the wings of the emission line, a behaviour also seen in other hot stars (Moffat 1994; Moffat *et al.* 1994; Lépine & Moffat 1999) and best interpreted as the manifestation of anisotropic velocity dispersion seen in Doppler projection.

We note that, at first, from a preliminary look at the dynamic difference spectra we wondered how the cyclic 1.78-d signal associated with large-scale wind structures influences the shape of the features related to clumps. The major difficulty here is the evolutive nature of the CIRs in time (ultimately as a consequence of the evolution of their photospheric drivers as discussed in Sections 6.4.4 and 6.5.1), but more importantly the ~5 d intensive observations including the night of February 10/11, 2015, turn out to be right in the middle of the transition phase in Part III where we only see mild signature of CIRs in the phased diagrams, unlike in Part IV where the CIR signatures

are more clearly defined. Nevertheless, we proceeded with the removal of the observed mild CIR patterns in Part III by adopting the same approach as we used for the removal of the 1.78-d signal in the light curves (Section 6.4.5), but this time performed for each Doppler velocity in the range ±1275 km s^{-1}: we phase-folded the time series spectra in Part III with the rotation period, rebinned them in phase, interpolated over the original phase sampling, subtracted the resulting smoothed pattern from the original phased time series, and then went back in the time domain to compare the resulting corrected time series with the original time series in order to check for possible overcorrections in which case we restarted again the whole procedure with another phase bin size. In general, during the comparison step we noted that the effect of the 1.78-d variability on the ∼1.08 d time span of the February 10/11, 2015 night was a slight increase of intensity between times ∼5519.70 – 5520.10. The phase bin size is the key parameter for controlling overcorrections and undercorrections, since too small phase bin sizes result in templates with relatively large noisy fluctuations (leading to overcorrection), while too large phase bin sizes yield too smooth templates (yielding undercorrection). We found that a phase bin size of 0.05 was a good compromise, yielding the dynamic difference spectra illustrated on the main panel of Figure 6.20.

6.5.2.2 Wavelet analysis

Given the stochastic nature of the appearance of the spectroscopic features associated with the wind clumps, and also their morphology as small features in emission excess superimposed on the wind emission line, the wavelet formalism (here in the spatial/wavelength domain) is very appropriate for the extraction of the properties of the observed clumps, as was already performed in other investigations on spectroscopic observations of WR stars (Lepine 1994; Moffat 1994; Moffat *et al.* 1994; Lépine *et al.* 1996;

Lépine & Moffat 1999). Also, unlike the case of the residual light curve on which we performed a wavelet analysis to characterize the time-scales of the features composing the observed stochastic signal intrinsic to ζ Pup (Section 6.4.5.2), our spectra have a constant dispersion in wavelength[3] and thus are intrinsically equally sampled, such that the continuous formalism can be applied and the CWTs readily calculated. Still, the choice of an appropriate wavelet family to be used needs to be considered. Since the subpeaks that we want to characterize in the difference spectra are excesses in emission often accompanied by less strong side depressions (unlike the features in the light curve that have roughly equal bumps and dips between ±10 mmag), the simplest and most appropriate family of wavelets for this situation is the family of Ricker wavelets, also often called Mexican hat wavelets. The Ricker wavelet function is constructed from a normalization of the second derivative of a Gaussian function. It was also the type of family of wavelets adopted by the studies on observations of clumping in hot stars mentioned previously. Under these considerations we calculated the CWTs of the 14 spectra during the night of February 10/11, 2015 and extracted the mean scalogram which is depicted in the lower panel of Figure 6.20, confirming that the substructures are mostly located between $\sim\pm500$ km s^{-1}, but more importantly that the typical widths of the detected features as indicated in the scalogram are of the order of $10^{2.0} - 10^{2.1}$ km s^{-1} which is slightly higher but remains consistent with the value of $\sim 10^{2.0}$ km s^{-1} found by Lépine & Moffat (1999) for the clumps in WR stars.

Also in order to fully compare the characteristics of the clumps of ζ Pup observed in our campaign with the clumps detected in the star at the epoch of the observations performed by Eversberg *et al.* (1998), we re-extracted the archival CFHT 3.6m/Reticon

[3]In general, raw echelle spectra do not have a constant dispersion through the different orders, but are resampled with a constant dispersion during the process of merging of the orders and extraction of the one-dimensional wavelength-calibrated spectra.

optical spectra of the star taken during the nights of December 10/11, 1995 (HJD $2,450,061.94 - 062.15$) and December 12/13, 1995 (HJD $2,450,063.95 - 064.17$), and calculated the corresponding average Ricker wavelet-based scalograms, which are displayed in Figure 6.21 below the corresponding dynamic difference spectra. The average scalograms for the CFHT 3.6m/Reticon spectra indicate that the typical widths of the features are also $\sim 10^{2.0}$ km s^{-1}, with some isolated minor power detected at larger scales $\sim 10^{2.3}$ km s^{-1}. The presence of such broader features could be due to either nesting effects or contamination from large-scale wind structures, the latter being impossible to remove in the CFHT 3.6m/Reticon spectra since the gap between the two nights of observations is of the order of one rotational cycle and each night only spanned ~ 5 h.

6.5.2.3 Correlated light variations and LPVs

An inspection of the behaviour of the stochastic light variations of ζ Pup as recorded by *BRITE* (Section 6.4.5) during the night of February 10/11, 2015 shows a relatively wide bump that reaches a maximum at time ~ 5519.70 (left-hand panel of Figure 6.20), and the Morlet wavelet-based scalogram of the *BRITE* light curve indicates that the dominant pseudo-period during that night is $\sim 14 - 15$ h with a slight pseudo-period drift towards shorter time-scales during the night (far left-hand panel of Figure 6.20). As already noted in Section 6.4.5.2, that pseudo-period drift, of unexplained origin, is part of a drift that starts from time ~ 5517.5 at time-scales ~ 16 h and finishes at time ~ 5521.0 at time-scales ~ 11 h. Nevertheless, in order to quantify the correlation between the stochastic light variations observed by *BRITE* in ζ Pup and the observed clumps in the wind, we assessed the integrated residual intensity variations in each difference

spectrum over Doppler velocities ±1000 km s^{-1}:

$$\mathcal{I}_k = \frac{C}{v_2 - v_1} \int_{v_1}^{v_2} I_r(v, t_k) dv \tag{6.30}$$

in which $I_r(v, t_k)$ is the residual intensity at Doppler velocity v in the difference spectrum observed at time t_k, and the integration is performed over velocities ranging from $v_1 = -1000$ km s^{-1} to $v_2 = +1000$ km s^{-1}. The constant C is a negative normalization factor accounting for the comparison with the *BRITE* light variations which are expressed in magnitudes. The individual values of $\mathcal{I}_k$ for the 14 spectra in the night are displayed as green squares on the left-hand panel of Figure 6.20 along with the residual *BRITE* light curves, taking $C = -3$. In view of that panel it appears that correlation exists between the two, an impression that is confirmed by the resulting Pearson correlation coefficient value $\rho = 0.8$ (right-hand panel of Figure 6.20).

Since *BRITE* probes the light variations of ζ Pup at the level of its photosphere (Section 6.4.2), we conclude that the stochastic light variations detected by *BRITE* in the star, which we characterized in Section 6.4.5, are the manifestations of the photospheric drivers of the clumps in the stellar wind as traced in He II λ4686.

6.6 Discussion and conclusion

The relatively short rotation period of ζ Pup, $P = 1.78063(25)$ d, that we inferred from the photometric observations has a strong impact on our current understanding of the properties of the star. Most importantly, the now better constrained relatively low stellar inclination angle $i \simeq 24°$ and high equatorial velocity (Section 6.4.4.1) completely change the previous beliefs that the star has a rotation period of ∼5.1 d, is seen almost equator on and spins at $v_e \simeq v_e \sin i = 219 \pm 18$ km s^{-1}. Moreover, as mentioned earlier (Section 6.4.4.1), the short rotation period of ζ Pup is in good agreement with the

suspected rotational evolution of the star, with two proposed scenarios so far: either spin-up during a Roche lobe overflow (RLOF) phase in a WR+O close massive binary followed by ejection from the supernova explosion of the primary component leading to the current status of ζ Pup as a single fast rotator runaway (Vanbeveren *et al.* 1998b), or a spin-up resulting from the merger of at least two massive stars during dynamical interactions within the Vela R2 R-association (Vanbeveren *et al.* 2009; Vanbeveren 2012; Pauldrach *et al.* 2012). In the former case, Vanbeveren *et al.* (1998b) estimated that, with initial binary masses of $40M_{\odot}$ and $38M_{\odot}$ and an initial orbital period of 4 d, the resulting orbital period of the system at the end of the RLOF phase is 2.6 d, in which case tidal effects would be very large and synchronize the components of the system such that the rotation period of the secondary would also be tuned to 2.6 d (figure 14.15 in Vanbeveren *et al.* 1998b, page 232). This is of the same order of magnitude as the actual value of the rotation period that we inferred from the photometric observations in this investigations, $P = 1.78063(25)$ d. The exact values of the initial binary masses implied by this post-RLOF rotation period depend on the exact values of the physical parameters involved during the RLOF, e.g. the exact amount of mass and angular momentum loss from the binary. However, in that scenario, the runaway velocity acquired by the secondary after the supernova explosion (asymmetrical) of the primary has to satisfy (Vanbeveren *et al.* 1998b, Equations 11.4 and 11.17):

$$\|\vec{v}_{\rm rw}\| = \frac{M_{\rm WR}}{\sqrt{M_{\rm WR} + M_{\rm O}}} \left(\frac{\mathcal{G}}{A}\right)^{\frac{1}{2}} \tag{6.31}$$

in which the masses $M_{\rm WR}$ and $M_{\rm O}$, as well as the semi-major axis A are values just before the supernova explosion (here $\mathcal{G}$ denotes the gravitational constant). Assuming pre-supernova masses $M_{\rm WR} = 10M_{\odot}$ and $M_{\rm O} = 56M_{\odot}$, the runaway velocity corresponding to an orbital period of ~1.78 d would be ~107 km s^{-1}, which is too high compared to

the observed runaway velocity of the star ($\|\vec{v}_{\rm rw}\| = 60.0 \pm 16.9$ km s^{-1}), while only an orbital period $\gtrsim 10$ d would yield a runaway velocity that is more compatible with the observed one. The latter case remains a plausible scenario since in that situation tidal effects are very small and the rotation period of the gainer (which was spun-up to ~1.78 d during the RLOF phase) remains unchanged. Additionally, in order to satisfy the observed current mass of ζ Pup, $M = 56.1^{+14.5}_{-11.6} M_{\odot}$ (despite the huge uncertainty on that value), the initial binary masses have to be much larger than those assumed in figure 14.15 of Vanbeveren *et al.* (1998b), e.g. $55 M_{\odot}$ and $50 M_{\odot}$. In that case, it has to be assumed that the $55 M_{\odot}$ primary ends its life with a supernova explosion that disrupted the binary, which is not entirely excluded as there is some evidence that black hole formation (at least for the lowest mass black holes) can be accompanied by a supernova explosion (e.g. Israelian *et al.* 1999). Under these circumstances, the updated scenario is illustrated in Figure 6.22. We emphasize that we performed these calculations only to update this scenario to satisfy the most pertinent values of the stellar parameters of ζ Pup, but at this point no strong constraints is available to help decide which of the two proposed evolutionary scenarios is the most plausible one.

With respect to the physical mechanism at the origin of the photospheric bright spots that give rise to the rotationally modulated light variations observed by *BRITE* and *Coriolis/SMEI*, one possible candidate is the surface emergence of small-scale magnetic fields generated through dynamo action within a subsurface convection zone associated with the iron-opacity bump at $T \sim 150000$ K (FeCZ, Cantiello *et al.* 2009b; Cantiello & Braithwaite 2011). The detection of such small-scale magnetic fields requires high-resolution, high-S/N circular spectropolarimetric observations imposed by the fast rotation of ζ Pup. All previous spectropolarimetric observations of the star ended up with no detection, with an upper limit of 121 G for a dipolar field strength, and longitudinal field error bar of 21 G (David-Uraz *et al.* 2014). Also since most of

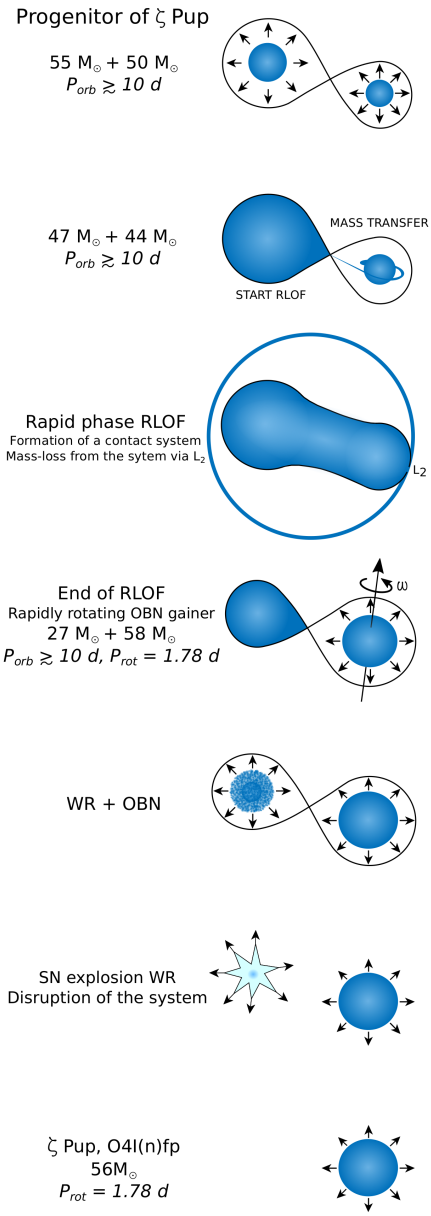

Figure 6.22: Evolutionary history of ζ Pup in the scenario in which the star could have been the secondary component of a massive binary and would have been spun-up during a RLOF phase of the primary component (fourth row from the top). The latter later underwent a supernova explosion, leading to the current fast rotator runaway status of the ζ Pup. Figure adapted from Vanbeveren *et al.* (1998b), updated with a rotation period of 1.78 d, and satisfying the observed runaway velocity $\|\vec{v}_{\rm rw}\| = 60.0 \pm 16.9$ km s^{-1} and the stellar mass $M = 56.1^{+14.5}_{-11.6} M_{\odot}$ listed in Table 6.I.

the spots that we detect during the *BRITE* and *Coriolis/SMEI* observing runs lie near the equator and are separated by $\sim 144 - 180^{\circ}$ in longitude, their magnetic signature (if they are related to small-scale magnetic fields) might cancel out in low-resolution mode as was the case of the spectropolarimetric monitoring of ζ Pup performed by Hubrig *et al.* (2016) who, despite no magnetic detection and no period detection, found marginal signs of modulation of the longitudinal magnetic field measurements when they phase-folded their data with the 1.78 d period (rather than the 5.1 d period). More importantly, as mentioned in Section 6.2.1 previous photometric monitoring of O stars revealed light variations best interpreted as signs of rotational modulation possibly due to surface inhomogeneities, with only the case of ξ Per showing potential link to its CIR/DAC behaviour (Ramiaramanantsoa *et al.* 2014), but our present findings that the bright localized photospheric spots observed by *BRITE* and *Coriolis/SMEI* in ζ Pup are the photospheric drivers of its CIRs/DACs constitutes the first observational evidence for a link between large-scale wind structures in an O-type star and their photospheric origin. This reinforces the need to observe more O-type stars with known CIR/DAC recurrence time-scale (e.g. those studied by Kaper *et al.* 1999) on a long-term through high-precision photometric monitoring and contemporaneous high-S/N mid/high-resolution spectroscopic/spectropolarimetric monitoring, because the near-ubiquity of CIRs/DACs in O-type stars implies that their photospheric drivers must also be a common phenomenon.

Lastly, the detection of the stochastically excited (but coherent for several hours) light variations intrinsic to ζ Pup during the *BRITE* and *Coriolis/SMEI* observations is as important as the cyclic variations related to rotational modulation itself, since we also find for the first time that those randomly excited (but coherent for several hours) light variations are the photospheric drivers of stellar wind clumps. Although the physical nature of these stochastic intrinsic variations at the photosphere remains

unknown, there is a possibility that such variations arise from randomly excited stellar oscillations with finite lifetimes such as IGWs, generated within an FeCZ (Cantiello *et al.* 2009b) or even from the convective core in the case of IGWs as found by Aerts & Rogers (2015). Nevertheless, the fact that these stochastic photospheric variations are linked to the variability associated with wind clumps suggests that the latter are formed even at the very base of the wind. Previous X-ray observations of ζ Pup suggested that only a large number of clumps in the wind ($N > 10^5$) are able to reproduce the observed X-ray variability of the star (Nazé *et al.* 2013). Since the variability scales with the inverse of the square root of the number of clumps involved, we can infer by the optical line flux variability that we observe (∼6%) that it would arise from the contribution of $N \simeq 300$ clumps. The question therefore remains as whether those clumps are of equal size or follow a power law distribution in which there is a relatively small number of strongly emitting clumps which would dominate the variability. The latter case fits naturally into the notion of the scaling laws of turbulence (compressible for hot winds) with a power law of negative slope, making few large clumps along with a rapidly increasing number of smaller ones each of which emits less and less as the size is diminished (e.g. Moffat 1994). This is further supported by the fact that turbulence is a very common phenomenon in astrophysics, e.g. large-scale structures in the Universe, the intergalactic medium (Ly-α clouds towards quasars), galaxies, cloudlets in giant molecular clouds, the discrete nature of stars themselves (as implied by the IMF) or surface granulation in the Sun itself. Also, the fairly clear and distinct observed spectral emission-line excess streaks over several hours must be spatially confined and not due to e.g. a sum of smaller random perturbations anywhere in the wind. However it has also been shown that the first scenario, that is variability that arises from a large number of clumps of equal size, cannot be ruled out (e.g. Davies *et al.* 2007). To further test the hypothesis of turbulence, high-S/N high-resolution spectroscopic observations of a WR star with

strong emission line and high terminal wind speed (e.g. up to ∼5000 km s^{-1}) needs to be performed, the best candidates being one of the WO2 stars in the Milky Way. But given the faintness of these objects, observations with the upcoming generation of extremely large telescopes such as the Thirty Meter Telescope (TMT) would be the most ideal.

Acknowledgements

We gratefully acknowledge fruitful discussions with D. John Hillier, Yaël Nazé and Radosław Smolec in relation to this investigation. We also thank the reviewer, Richard Townsend, for his insights and for providing us with useful constructive remarks. T. Ramiaramanantsoa acknowledges support from the Canadian Space Agency (CSA) grant FAST. A. F. J. Moffat is grateful to the Natural Sciences and Engineering Research Council of Canada (NSERC) and the Fonds de Recherche du Québec – Nature et Technologies (FRQNT) for general financial aid, and to CSA for funding the training of highly qualified personnel associated with the *BRITE* project. N. D. Richardson acknowledges postdoctoral support by the University of Toledo and by the Helen Luedtke Brooks Endowed Professorship. A. Pigulski acknowledges support from the National Science Centre grant no. 2016/21/B/ST9/01126. A. Popowicz acknowledges NCN grant 2016/21/D/ST9/00656. G. Handler acknowledges support from NCN grant 2015/18/A/ST9/00578. The Polish contribution to the *BRITE* mission is supported by the Polish NCN grant 2011/01/M/ST9/05914. G. A. Wade and S. M. Rucinski acknowledge Discovery Grant support from NSERC. K. Zwintz acknowledges support from the Austrian Fonds zur Förderung derwissenschaftlichen Forschung (FWF; project V431-NBL). This project uses observations made from the South African Astronomical Observatory (SAAO). The professional authors of this paper are grateful to the am-

ateur astronomers of the SASER team (also co-authors of this paper), who invested personal time and enthusiasm in this project. Part of the research leading to these results has received funding from the European Research Council (ERC) under the European Union's Horizon 2020 research and innovation programme (grant agreement no. 670519: MAMSIE).

6.7 Appendices

6.7.1 Evolution of the 1.78-day signal during the *Coriolis/SMEI* observing run

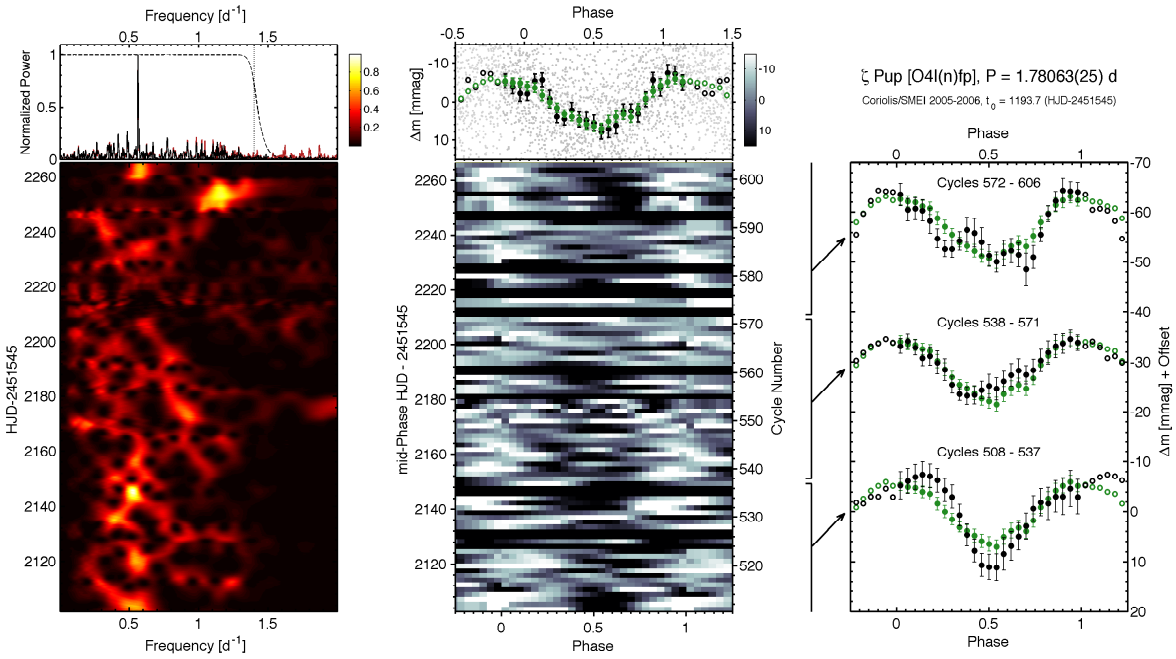

Figure 6.23: Same as Figure 6.7, but for the *Coriolis/SMEI* observing run in 2005-2006.

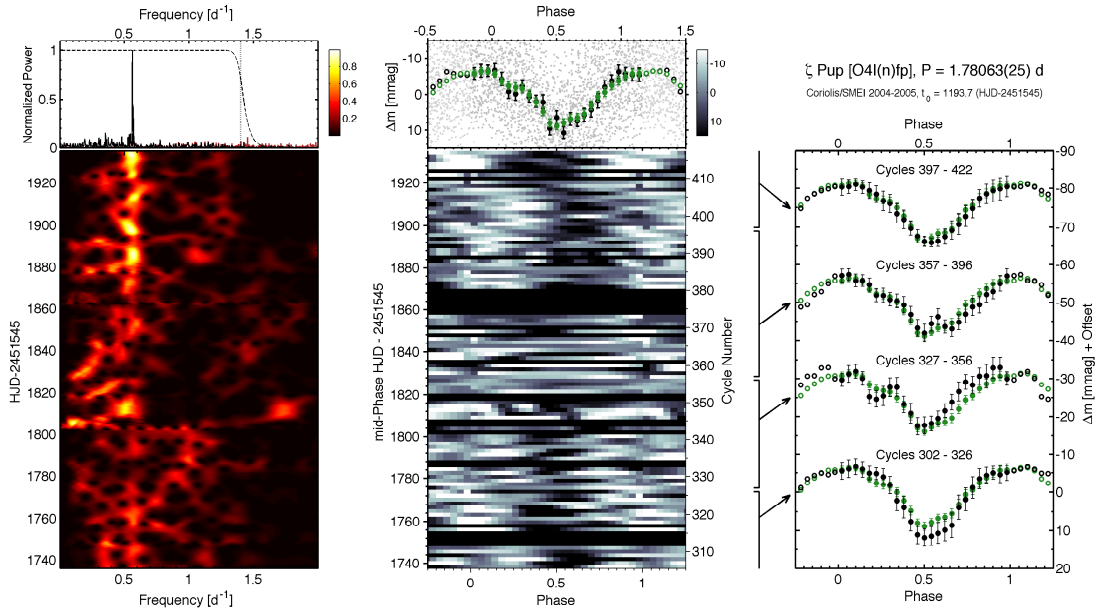

Figure 6.24: Same as Figure 6.7, but for the *Coriolis/SMEI* observing run in 2004-2005.

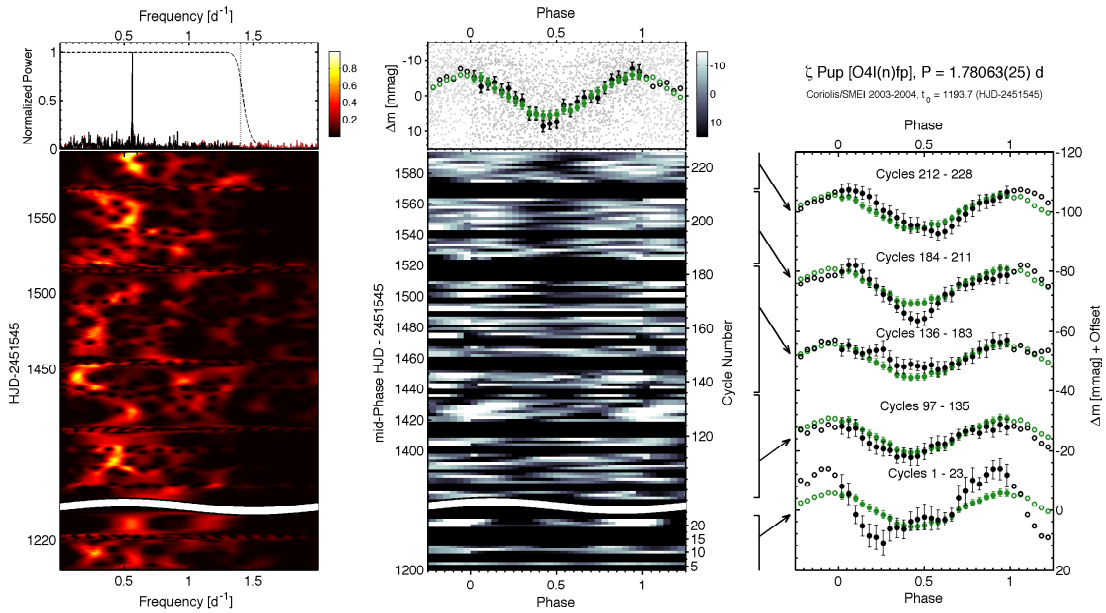

Figure 6.25: Same as Figure 6.7, but for the *Coriolis/SMEI* observing run in 2003-2004.

6.7.2 Light curve inversion: Surface maps of ζ Pup during the *Coriolis/SMEI* seasonal observing runs

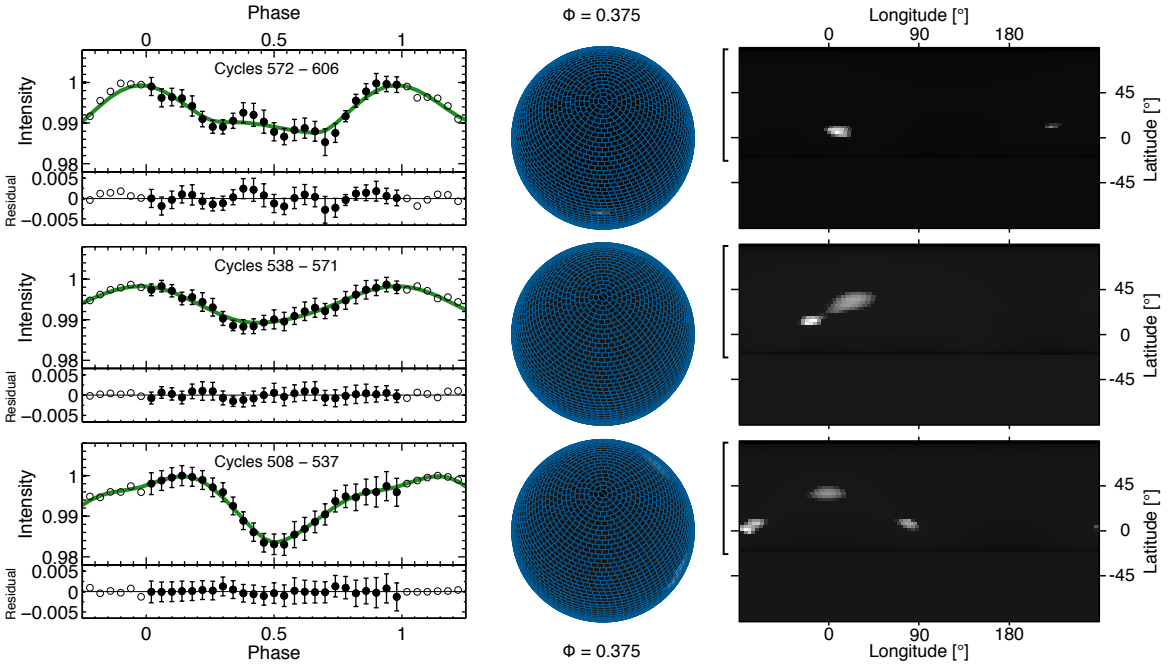

Figure 6.26: Light curve inversion: mapping the photosphere of ζ Pup as observed by *Coriolis/SMEI* in 2005 – 2006, for $T^{(s)} = 42.5$ kK and a stellar inclination angle $i = 24°$. Time increases upwards.

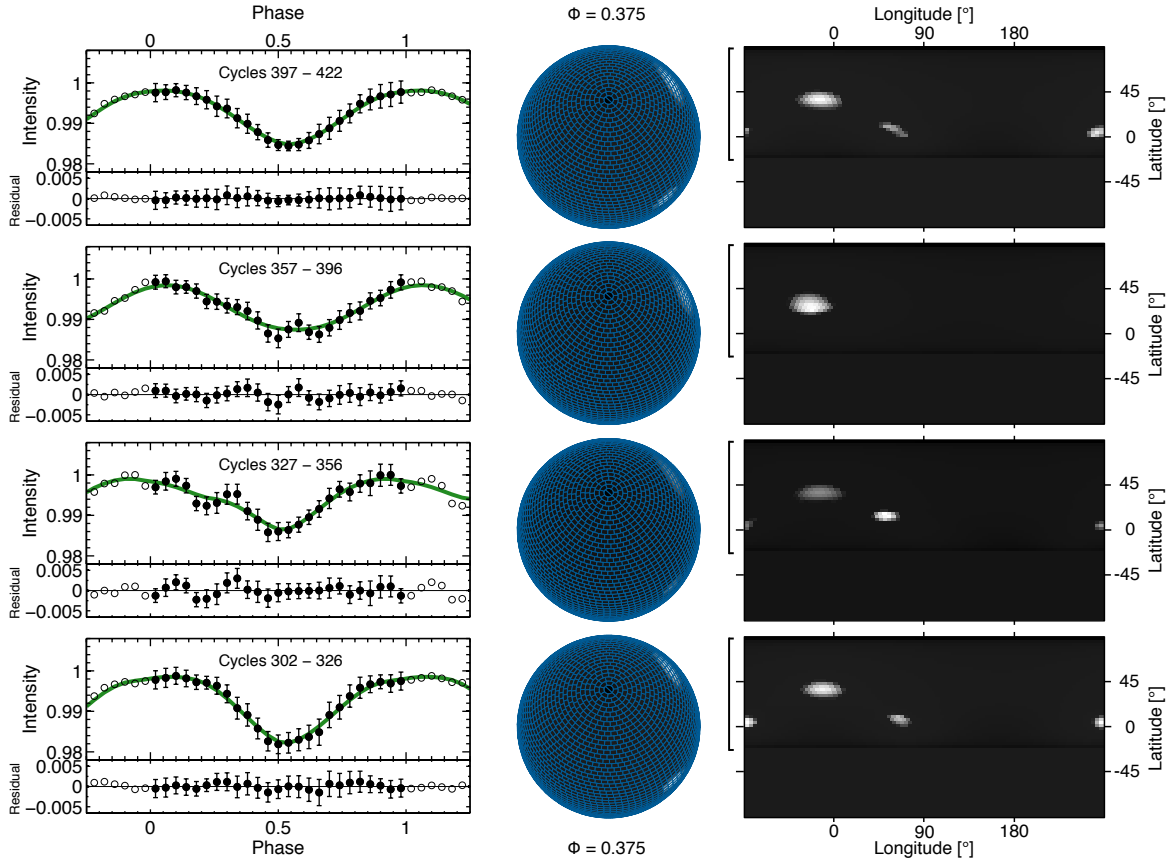

Figure 6.27: Light curve inversion: mapping the photosphere of ζ Pup as observed by *Coriolis/SMEI* in 2004 – 2005, for $T^{(s)} = 42.5$ kK and a stellar inclination angle $i = 24°$. Time increases upwards.

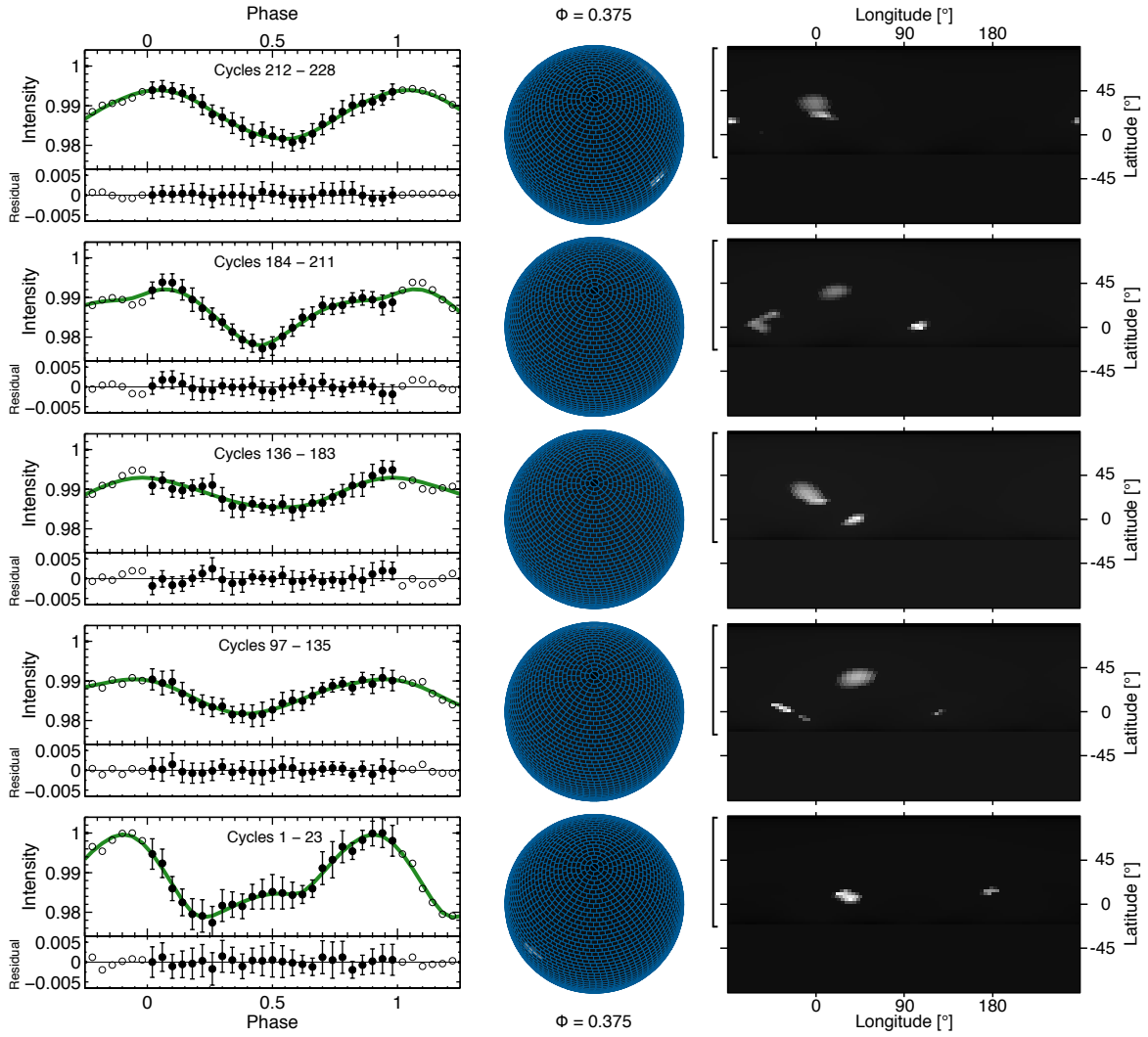

Figure 6.28: Light curve inversion: mapping the photosphere of ζ Pup as observed by *Coriolis/SMEI* in 2003 – 2004, for $T^{(s)} = 42.5$ kK and a stellar inclination angle $i = 24°$. Time increases upwards.

AUTHORS' AFFILIATIONS:

[1] Département de physique, Université de Montréal, CP 6128, Succursale Centre-Ville, Montréal, Québec, H3C 3J7

[2] Centre de Recherche en Astrophysique du Québec (CRAQ), Canada

[3] Department of Physics and Astronomy, Ohio Wesleyan University, Delaware, OH 43015, USA

[4] East Tennessee State University, Department of Physics & Astronomy, Johnson City, TN, 37614, USA

[5] Astrophysical Institute, Vrije Universiteit Brussel, Pleinlaan 2, B-1050 Brussels, Belgium

[6] Institut für Physik und Astronomie, Universität Potsdam, Karl-Liebknecht-Str. 24/25, D-14476 Potsdam, Germany

[7] Ritter Observatory, Department of Physics and Astronomy, The University of Toledo, Toledo, OH 43606-3390, USA

[8] Department of Physics & Astronomy, University College London, Gower St, London WC1E 6BT, United Kingdom

[9] School of Physics and Astronomy, University of Birmingham, Edgbaston, Birmingham B15 2TT, United Kingdom

[10] Schnörringen Telescope Science Institute, Waldbröl, Germany

[11] Instytut Astronomiczny, Uniwersytet Wrocławski, Kopernika 11, 51-622 Wrocław, Poland

[12] Instytut Automatyki, Politechnika Ślaska, Akademicka 16, 44-100 Gliwice, Poland

[13] Institut für Astrophysik, Universität Wien, Türkenschanzstrasse 17, 1180 Wien, Austria

[14] Nicolaus Copernicus Astronomical Center, Bartycka 18, 00-716 Warsaw, Poland

[15] LESIA, Observatoire de Paris, PSL Research University, CNRS, Sorbonne Universités, UPMC Univ. Paris 06, Univ. Paris Diderot, Sorbonne Paris Cité, 5 place Jules Janssen, F-92195 Meudon, France

[16] Instituut voor Sterrenkunde, KU Leuven, Celestijnenlaan 200D, 3001 Leuven, Belgium

[17] Department of Physics, Royal Military College of Canada, PO Box 17000, Station Forces, Kingston,

Ontario, K7K 7B4, Canada

[18] Department of Astronomy & Astrophysics, University of Toronto, 50 St. George Street, Toronto, Ontario, M5S 3H4, Canada

[19] Institut für Astro- und Teilchenphysik, Universität Innsbruck, Technikerstrasse 25/8, 6020 Innsbruck, Austria

[20] International Centre for Radio Astronomy Research, The University of Western Australia, 35 Stirling Hwy, Crawley, Western Australia 6009

[21] SASER Team, Domain Observatory, 269 Domain Road, South Yarra, Vic 3141, Australia

[22] SASER Team, Dogsheaven Observatory, SMPW Q25 CJ1 LT10B, Brasilia, Brazil

[23] SASER Team, Latham Observatory, Australia

[24] SASER Team, R. F. Joyce Observatory, Canterbury Astronomical Society, West Melton, New Zealand

[25] SASER Team, Mirranook Observatory, Booroolong Road, Armidale, NSW, Australia

[26] Gemini Observatory, Northern Operations Center, 670 N. A'ohoku Place, Hilo, Hawaii, 96720, USA

[27] South African Astronomical Observatory, PO Box 9, Observatory, 7935 Cape, South Africa

[28] Southern African Large Telescope, PO Box 9, Observatory, 7935 Cape, South Africa

[29] Eureka Scientific, Inc., 2452 Delmer Street, Oakland, CA 94602, USA

[30] Université de Toulouse; UPS-OMP; IRAP; Toulouse, France

[31] CNRS; IRAP; 14, avenue Edouard Belin, 31400 Toulouse, France

7

La Supergéante V973 Scorpii

A *BRITE** View on the Massive O-Type Supergiant V973 Scorpii: Hints Towards Internal Gravity Waves or Sub-surface Convection Zones

Tahina Ramiaramanantsoa[1,2], Rathish Ratnasingam[3], Tomer Shenar[4], Anthony F. J. Moffat[1,2], Tamara M. Rogers[3,5], Adam Popowicz[6], Rainer Kuschnig[7], Andrzej Pigulski[8], Gerald Handler[9], Gregg Wade[10], Konstanze Zwintz[11], and Werner W. Weiss[7]

[1]Département de physique, Université de Montréal, C.P. 6128, Succ. Centre-Ville, Montréal, QC, H3C 3J7, Canada
[2]Centre de Recherche en Astrophysique du Québec (CRAQ), Canada
[3]Department of Mathematics and Statistics, Newcastle University, Newcastle upon Tyne NE1 7RU, UK
[4]Institut für Physik und Astronomie, Universität Potsdam, Karl-Liebknecht-Str. 24/25, D-14476 Potsdam, Germany
[5]Planetary Science Institute, Tucson, AZ 85721, USA
[6]Instytut Automatyki, Politechnika Ślaska, Akademicka 16, 44-100 Gliwice, Poland
[7]Institut für Astrophysik, Universität Wien, Türkenschanzstrasse 17, 1180 Wien, Austria
[8] Instytut Astronomiczny, Uniwersytet Wrocławski, Kopernika 11, 51-622, Wrocław, Poland
[9] Nicolaus Copernicus Astronomical Center, Bartycka 18, PL-00-716 Warsaw, Poland
[10] Department of Physics and Space Science, Royal Military College of Canada, Kingston, ON K7K 7B4, Canada
[11] Institut für Astro- und Teilchenphysik, Universit tät Innsbruck, Technikerstrasse 25, A-6020 Innsbruck, Austria

Published in the *Monthly Notices of the Royal Astronomical Society, Volume 480, Issue 1, pages 972–986,* 11 October 2018 (Online 19 July 2018)

*Based on data collected by the *BRITE-Constellation* satellite mission, designed, built, launched, operated and supported by the Austrian Research Promotion Agency (FFG), the University of Vienna, the Technical University of Graz, the Canadian Space Agency (CSA), the University of Toronto Institute for Aerospace Studies (UTIAS), the Foundation for Polish Science & Technology (FNiTP MNiSW), and National Science Centre (NCN).

7.1 Abstract

Stochastically-triggered photospheric light variations reaching ~40 mmag peak-to-valley amplitudes have been detected in the O8Iaf supergiant V973 Scorpii as the outcome of two months of high-precision time-resolved photometric observations with the *BRIght Target Explorer (BRITE)* nanosatellites. The amplitude spectrum of the time series photometry exhibits a pronounced broad bump in the low-frequency regime ($\lesssim$0.9 d^{-1}) where several prominent frequencies are detected. A time-frequency analysis of the observations reveals typical mode lifetimes of the order of 5 – 10 days. The overall features of the observed brightness amplitude spectrum of V973 Sco match well with those extrapolated from two-dimensional hydrodynamical simulations of convectively-driven internal gravity waves randomly excited from deep in the convective cores of massive stars. An alternative or additional possible source of excitation from a sub-surface convection zone needs to be explored in future theoretical investigations.

7.2 Introduction

The stellar demographics of galaxies are such that massive O-type stars are heavily outnumbered by long-lived cool low-mass M dwarfs (e.g. Salpeter 1955; Kroupa 2001; Bastian *et al.* 2010). However, hot luminous stars more than compensate for their sparse spatial density by simply constituting the indispensable recycling engines of chemical elements involved in the formation of new stars and new substellar objects. That occurs both through their termination as supernovae and through the production of elements heavier than iron from the kilonovae occasionally induced by binary neutron star mergers (e.g. Drout *et al.* 2017; Kasen *et al.* 2017). Thus, understanding the

physical properties and the structures of massive stars at all their evolutionary stages prior to their deaths is of high interest. To that end, observational endeavours to probe their intrinsic variability (e.g. pulsations, rotational modulations, stochastic variations, episodic events such as flaring) – which can yield constraints on their internal structures (see e.g. Aerts *et al.* 2010) – have been energized by the outcome of long-term, high-quality, high-cadence monitoring provided by space-based observatories (see Ramiaramanantsoa *et al.* 2018 for a recent update on that subject in the particular case of O-type stars).

The late O-type supergiant V973 Sco (HD 151804; Table 7.I) is one of the most luminous stars in the Sco OB1 association (Humphreys 1978). No signs of multiplicity have been found so far for V973 Sco (e.g. Conti *et al.* 1977), putting it at the same rank as other single O-type stars like ξ Per and ζ Pup for constituting good laboratories for probing the intrinsic variability of O-type stars. However, the fainter apparent magnitude of V973 Sco compared to those of ξ Per and ζ Pup makes it less privileged when it comes to O-star variability studies.

The first spectroscopic variability study of V973 Sco was performed by Snow (1977), who inspected two ultraviolet (UV) spectra of the star taken $\sim$1.5 yr apart and found no significant changes in the P Cygni profiles of its C III λ1174$-$1176 and N V $\lambda\lambda$1239, 1242 resonance lines. In that regard, the UV resonance lines of V973 Sco are saturated, such that their absorption troughs do not exhibit variable recurrent blueward-propagating discrete absorption components (DACs – originally called 'narrow absorption components'; Howarth & Prinja 1989; Kaper *et al.* 1999). These DACs are found to be nearly ubiquitous amongst O stars and are best interpreted as manifestations of the presence of large-scale corotating interaction regions in the stellar wind (Mullan 1986; Cranmer & Owocki 1996). Nevertheless, a possible occurrence of DACs has been discovered in the P Cygni profile of the He I λ5876 optical line of V973 Sco from two spectroscopic

Table 7.I: Stellar parameters for V973 Sco. $T_\star$ and $R_\star$ are evaluated at a Rosseland optical depth of 20, whereas the effective temperature $T_{\rm eff}$ corresponds to a radius $R_{2/3}$ where the Rosseland optical depth is 2/3.

Parameter		Value	
		Old	Updated[1]
Spectral type		O8 Iaf[2]	–
V		5.232 ± 0.014[3]	–
$B-V$		0.066 ± 0.013[3]	–
$U-B$		-0.838 ± 0.039[3]	–
$v_{\rm e} \sin i$	[km s^{-1}]	104 ± 14[4]	–
$v_{\rm rad}$	[km s^{-1}]	-46.7 ± 15.0[5]	–
$v_{\rm tan}$	[km s^{-1}]	18.9 ± 13.5[5]	–
Distance	[kpc]	1.91 ± 0.57[5]	$1.63^{+0.87}_{-0.42}$
$\log(L/L_\odot)$		5.90 ± 0.2[6]	$5.82^{+0.38}_{-0.26}$
$\log g$	[cm s^{-2}]	3.00 ± 0.2[6]	–
$T_{\rm eff}$	[kK]	28.1 ± 0.5[6]	–
$T_\star$	[kK]	29.0 ± 0.5[6]	–
$R_{2/3}$	[$R_\odot$]	37.6 ± 1.3[6]	$34.4^{+20.6}_{-9.9}$
$R_\star$	[$R_\odot$]	35.4 ± 1.2[6]	–
$\dot{M}$	[M$_\odot$Myr^{-1}]	6.3 ± 0.1[6]	–
M	[M$_\odot$]	40 ± 5[6]	43^{+67}_{-21}
v_∞	[km s^{-1}]	1445 ± 100[7]	–

[1]Derived from the new parallax measurement provided by the *GAIA* mission ($\Pi = 0.6139 \pm 0.2131$ mas; Gaia Collaboration 2018), [2]Galactic O-Star Catalog: Sota *et al.* (2014), [3]Maíz-Apellániz *et al.* (2004), [4]Howarth *et al.* (1997), [5]Moffat *et al.* (1998), [6]Crowther & Evans (2009), [7]Prinja *et al.* (1990)

variability investigations on the star: the 15 optical spectra collected by Fullerton *et al.* (1992) over ∼6.2 days revealed signs of migrating absorption enhancements in the absorption trough of the He I λ5876 line profile, variability features that were later also found in the more intensive but slightly shorter spectroscopic campaign led by Prinja *et al.* (1996) (64 spectra spread over ∼5 d) who attributed them to DACs, although the length of the campaign did not allow for a derivation of a possible DAC recurrence time-scale. In addition to these variations, the He II λ4686 wind-sensitive emission line of V973 Sco was also found to be variable, showing no signs of periodicity but only fluctuations from one night to the next (Grady *et al.* 1983), a behaviour that could suggest a link to stochastic wind clumping activity.

V973 Sco has also been the subject of some photometric variability studies conducted from the ground that revealed non-negligible light variability (van Genderen *et al.* 1989; Balona 1992). Particularly, the ∼15-d long Strömgren b photometric monitoring of V973 Sco led by Balona (1992) revealed light variations having an rms scatter of ∼15 mmag and happening on time-scales of the order of days. These ground-based observations unfortunately evidently suffered from a limited time base, daily aliases, and large gaps. Here, we report on the outcome of an effort to better determine the nature of the photometric variability of V973 Sco through two months of high-cadence, high-precision optical photometric monitoring from space with the *BRIght Target Explorer (BRITE)* mission.

7.3 BRITE-Constellation photometry of V973 Scorpii

The launch of the first *BRITE* satellites in February 2013 marked the beginning of a generation of nanosatellites fully dedicated to astronomy. The mission rightly takes the name of *BRITE-Constellation* as it currently consists of five operational nanosatel-

lites: *BRITE-Austria (BAb)*, *UniBRITE (UBr)*, *BRITE-Lem (BLb)*, *BRITE-Heweliusz (BHr)*, and *BRITE-Toronto (BTr)*, the small letter appended to each abbreviation indicating the passband in which each satellite operates ("b" for a blue filter covering $390-460$ nm, and "r" for a red filter covering $545-695$ nm). Located in low-Earth orbits with orbital periods of the order of 100 min, each of the $20\times20\times20$ cm *BRITE* nanosatellites is equipped with a 3-cm telescope feeding an uncooled 4008×2672-pixel KAI-11002M CCD, with a large effective unvignetted field of view of $24^\circ\times20^\circ$ to fulfil a single purpose: tracking the long-term photometric variability of bright stars ($V\lesssim6$) in two passbands, typically over $2-6$ months. Full technical descriptions of the mission were provided by Weiss *et al.* (2014) and Pablo *et al.* (2016).

During an observing run on the Scorpius field in 2015, *BRITE* monitored a total of 26 targets, only three of which are of spectral type O: μ Nor (O9.7Iab), V918 Sco (a detached massive O7.5If + ON9.7I binary) and V973 Sco. Four of the five operational *BRITE* satellites were tasked to observe the field. *BAb*, *UBr* and *BLb* were set to observe with the usual 1 s exposure time, while *BHr* was set to take longer 2.5 s exposures to allow for the observation of fainter stars such as V918 Sco and V973 Sco with reasonable photometric precision. Although the entirety of the observing run on the field lasted ~5.5 months (March 17, 2015 - August 29, 2015), V973 Sco was monitored by only one satellite, *BHr*, for only about two months towards the end of the observing campaign, between June 26, 2015 and August 28, 2015 (HJD $2457199.543-2457263.347$), with individual 2.5 s exposure snapshots taken at a median cadence of 27.3 s during $\sim2-20\%$ of each ~97.1 min orbit of *BHr*. Table 7.II summarizes the characteristics of the *BHr* observations of V973 Sco, the last four entries measured after cleaning the raw light curve from instrumental effects, a process that we describe in Appendix 7.8. As illustrated in Figure 7.1, the *BHr* light curve of V973 Sco exhibits clear variations reaching peak-to-valley amplitudes of ~40 mmag.

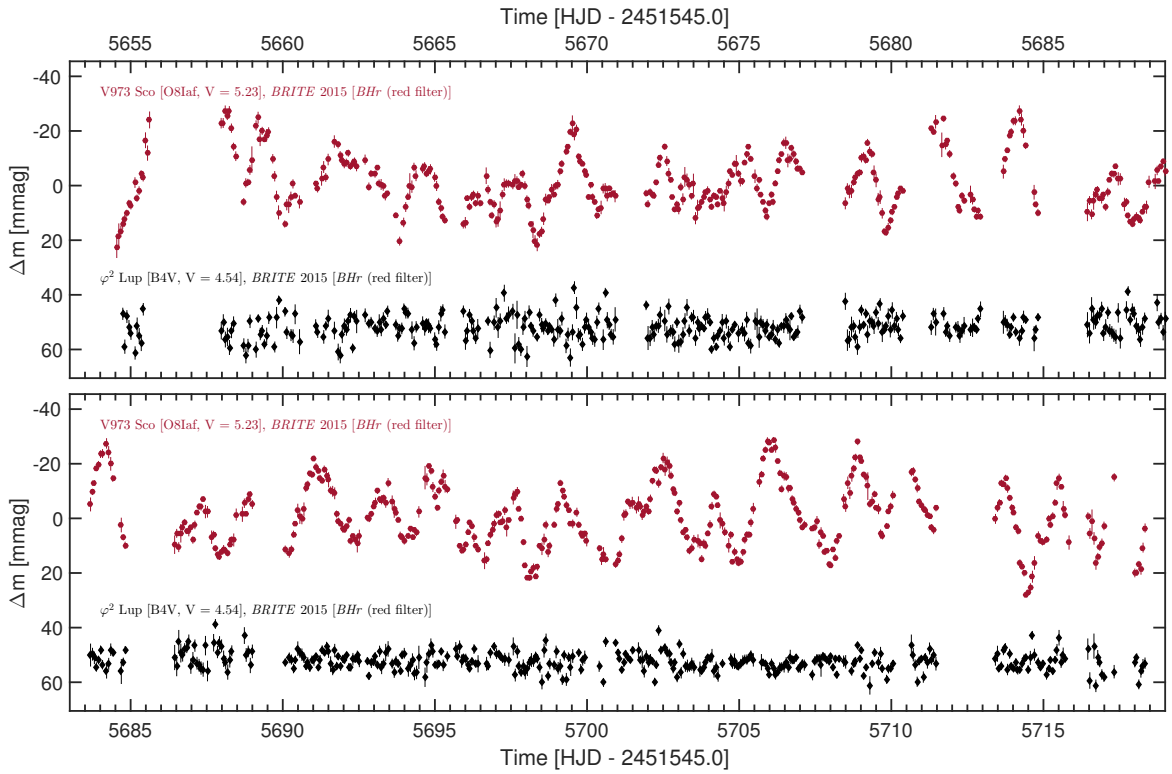

Figure 7.1: The two-month long *BRITE* light curve of V973 Sco (red filled circles) as recorded in 2015 in the red (545 – 695 nm) passband by *BHr*, binned over each ~97.1 min satellite orbit, along with the contemporaneous *BHr* observations of φ^2 Lup (black diamonds, offset by 50 mmag for better visibility), reduced and decorrelated with respect to instrumental effects in the same way as the light curve of V973 Sco but not showing any variability related to those observed in the latter (both in terms of amplitudes and time-scales). Small vertical bars indicate the $\pm 1\sigma$ uncertainties. (Color versions of all figures in this paper are available in the online journal.)

Table 7.II: Characteristics of the *BRITE* observations of V973 Sco. Quantities listed in the last four rows were assessed at post-decorrelation stage. The last entry $\sigma_{\rm rms}$ is the root mean square mean standard deviation per orbit assessed from linear fits of the flux values within the orbits.

Parameter	Value
Satellite	*BRITE-Heweliusz*
Start – End dates [HJD-2451545.0]	5654.543 – 5718.347
Observing mode*	Chopping
Exposure time [s]	2.5
Total number of data points	17374
Number of points per orbit**	30 [6 – 40]
Contiguous time per orbit** [min]	15.9 [2.3 – 18.7]
$\sigma_{\rm rms}$ [mmag]	1.68

* See Pablo *et al.* (2016) and Popowicz *et al.* (2017) for the descriptions of the different modes of observations for *BRITE*.

** Median values. Bracketed values indicate the extrema.

7.4 How much does the stellar wind contribute to the observed light variations?

This has been investigated by Ramiaramanantsoa *et al.* (2018) in the case of the *BRITE* dual-band observations of the hot early O-type supergiant ζ Puppis, for which it turned out that only a negligible fraction ($\lesssim 0.35\%$) of the variability in the continuum could be due to a contribution from the wind, meaning that *BRITE* essentially probed variations at the photosphere of ζ Pup. Although it is expected that the conclusion would not be very different in the case of our *BRITE* observations of V973 Sco, we still redo the same analysis as in Ramiaramanantsoa *et al.* (2018) but with the stellar parameters of V973 Sco. To this end, we assessed the fraction of scattered photons in the stellar

wind by constructing a PoWR (Potsdam Wolf-Rayet; Hamann & Gräfener 2003, 2004; Todt *et al.* 2015; Shenar *et al.* 2015) model atmosphere corresponding to the stellar parameters of V973 Sco (L, g, $T_{\rm eff}$, $\dot{M}$, and v_∞ as listed Table 7.I, all from the investigation led by Crowther & Evans 2009), then plotting the variation of the Rosseland mean optical depth with respect to the distance from the photosphere. We note that PoWR assumes the usual β-law velocity generally adopted in hot luminous stars for the radial component of the wind expansion. However, there is no explicit empirically-derived value of the exponent β available for the case of V973 Sco. Crowther & Evans (2009) found $\beta = 2$ yielded an excellent fit to the Hα profile of **He 3–759** (O8Iaf), which shares very similar properties with V973 Sco. Therefore, we run the PoWR simulations for the cases $\beta = 2$ and $\beta = 1$, the latter being found to be more common for the winds of O-type stars. Additionally, we take wind clumping into account, considering the case of the standard assumption of a clumping filling factor $f = 0.1$ (as also adopted by Crowther & Evans 2009), and $f = 0.05$ (as adopted for ζ Pup; Ramiaramanantsoa *et al.* 2018). Finally, we noticed that the existing estimates of the mass loss rate for V973 Sco (12 $M_\odot$Myr^{-1} without clumping corrections, and 6.3 $M_\odot$Myr^{-1} when accounting for clumping; Crowther & Evans 2009) are curiously larger than typical mass loss rates for O-type stars (even ζ Pup has $\dot{M} = 1.9$ $M_\odot$Myr^{-1}), such that we consider the cases $\dot{M} = 6.3$ $M_\odot$Myr^{-1} and $\dot{M} = 3.2$ $M_\odot$Myr^{-1}. Under these considerations, the outcome of our simulations is illustrated in Figure 7.2, with the values of the resulting wind optical depth indicated for each case. Thus, the worst-case scenario points toward a wind that scatters $1 - e^{-\tau_{\rm sonic}}$ ~11% of the photons coming from the photosphere. Since the optical wind-sensitive lines of V973 Sco are known to be variable at $\lesssim$ 10% of the continuum level (e.g. Prinja *et al.* 1996), we can infer that a maximum of ~1.1% of the variability in the continuum could arise from the wind. Hence, *BRITE* basically monitors the photosphere of V973 Sco.

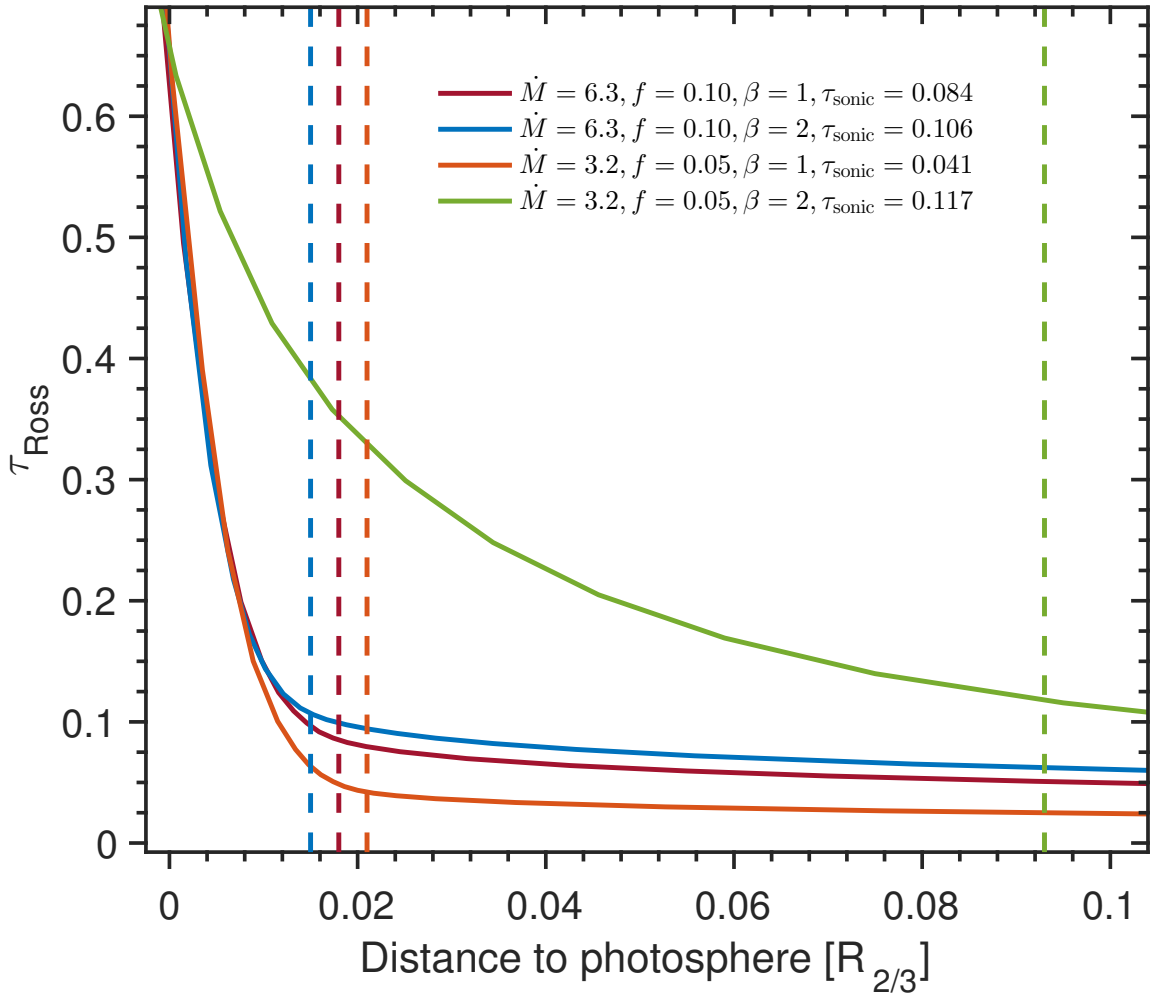

Figure 7.2: PoWR prediction of the evolution of the Rosseland mean optical depth with increasing distance from the photosphere ($\tau_{\rm Ross} = 2/3$), adopting the usual β-law velocity for the radial expansion of the wind, and considering various cases (see Section 7.3). For each case, the vertical dashed line indicates the limit beyond which the expansion becomes supersonic (i.e. the wind domain).

7.5 Frequency analysis

To search for periodic signals in the light variations of V973 Sco, we evaluated the discrete Fourier transform (DFT) of the light curve with the PERIOD04 software package (Lenz & Breger 2005) up to the Nyquist frequency (7.42 d^{-1}), resulting in the amplitude spectrum depicted in the upper panel of Figure 7.3. Immediately visible in this amplitude spectrum is a pronounced increase in amplitude towards low frequencies from ∼1 d^{-1} to ∼0.4 d^{-1}, followed by a decrease below ∼0.4 d^{-1}, resulting in a bump in a confined low-frequency region where several prominent frequency peaks are present. In order to investigate the stability of these frequencies, we performed a time-frequency analysis by evaluating the windowed DFT of the light curve using a Hamming window of width $\mathcal{W} = 20$ d sliding through the time series at a step rate of $\mathcal{W} \times 1\%$, enabling us to cover up to 16 cycles of the frequencies in the region of bumped amplitude at each step[1]. The main panel of Figure 7.4 illustrates the resulting spectrogram, revealing random triggering of the prominent frequencies, which, when excited, are stable only for roughly $5 - 10$ days.

The next step is to quantify the characteristics of these prominent signals: their frequencies, amplitudes and phases. The standard way of achieving this is through the usual iterative prewhitening procedure using the entire time series. However, that procedure is efficient for the extraction of the properties of sinusoidal signals that are present and relatively stable from the beginning until the end of the observations, but remains inappropriate for the characterization of stochastically excited signals with finite lifetimes. This simply comes from the fact that prewhitening a randomly triggered

[1]Different window sizes were initially tested (namely: 15 d, 20 d, 25 d, and 30 d). We chose $\mathcal{W}$ = 20 d for the subsequent analyses as it offered the most reasonable compromise between the frequency resolution at each step, the number of signal cycles covered at each step, and the final time base covered by the spectrogram, which has to begin $\mathcal{W}/2$ after the first measurement in the time series and end $\mathcal{W}/2$ before the last observation.

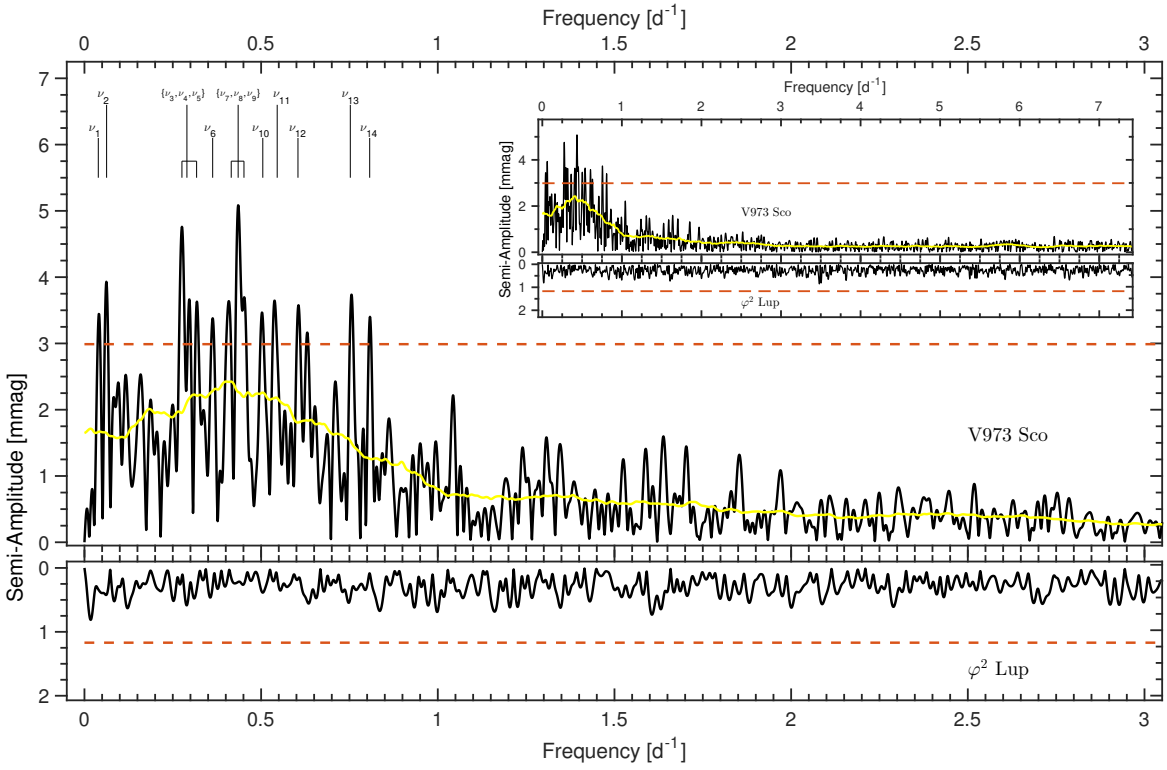

Figure 7.3: DFTs of the *BHr* light curves of V973 Sco and φ^2 Lup, the dashed horizontal lines tracing four times the average noise levels evaluated over the frequency range $[0;4]$ d^{-1}. The inset zooms out on the overall behaviour up to the Nyquist frequency at 7.42 d^{-1}. The DFT of the *BHr* time series photometric observations of V973 Sco is illustrated along with its running average with a binwidth of 0.3 d^{-1}, clearly revealing the bump in the low-frequency regime $[0;0.9]$ d^{-1}.

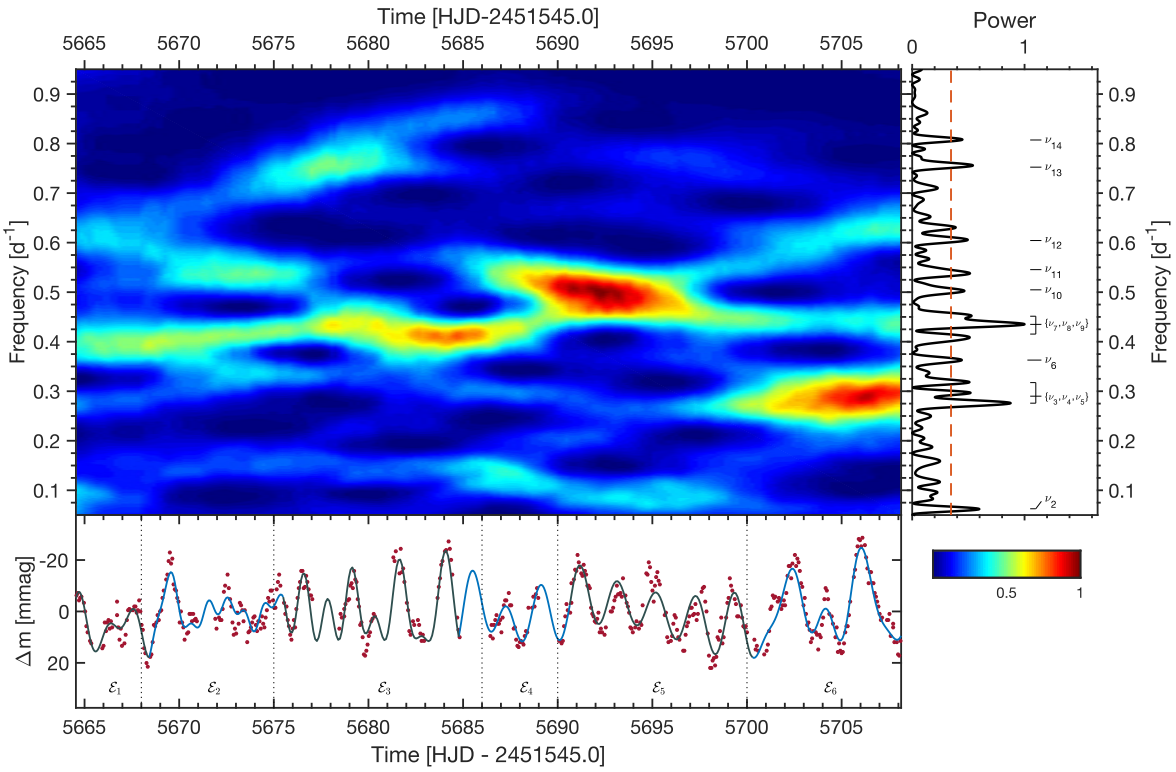

Figure 7.4: Time-frequency analysis of the *BRITE* light curve of V973 Sco. *Main panel:* spectrogram obtained from a 20-d sliding tapered window Fourier transform of the light curve. *Right panel:* Normalized power spectrum of the entire light curve, used as a guide in the determination of which frequencies are prominent during which epoch. The dashed line is the same as that in Figure 7.3, indicating four times the average noise level over $[0;4]$ d^{-1}. *Bottom panel*: Light curve of V973 Sco (red points), with vertical dotted lines delimiting the epochs $\mathcal{E}_m$ obtained at the end of step **[2]** of the method described in Section 7.5. The continuous curves trace the final best fits obtained during each epoch.

sinusoidal signal with finite lifetime using the entire time series would introduce a spurious signal with the same frequency at epochs during which the actual transient signal was not present. For instance, prewhitening the dominant frequency at $\sim$0.5 d^{-1} present in the time interval 5690.0 – 5696.0 in the light curve of V973 Sco would introduce a spurious sinusoidal signal at the same frequency in the time interval 5696.0 – 5710.0. Additionally, such an approach might even partially or totally dilute some other signals at frequencies very close to the one being prewhitened. Alternatively, "local prewhitening" could be done only within subsets of the light curve where the signal is excited and stable enough. However, in that case, iterative prewhitening cannot be necessarily performed efficiently on a given subset, i.e. after prewhitening a signal that is prominent within a subset, one has to choose another subset to look for and characterize other prominent signals because those other signals may only be partly excited within the current subset. Moreover, since the first step of the prewhitening consists of computing the DFT to look for the first prominent signal, doing this on subsets of the light curve means dealing each time with amplitude spectra with poor frequency resolution. Under these considerations, we adopt the following three-step method to extract the characteristics of the transient sinusoidal signals present in the light curve of V937 Sco:

[1] extraction of the values of the dominant frequencies present in the observations through the standard iterative prewhitening procedure using the entire light curve. We do this here *only* to get first estimates of the values of the dominant frequencies, which we use as inputs for the subsequent steps;

[2] determination of the epochs at which each of these signals are excited, followed by a splitting of the time series into subsets according to these epochs. This is performed visually using the information provided by the spectrogram, and the definition of the epochs are primarily driven by times where new signals appear;

[3] multifrequency sine wave fit to the observed variations. For a given subset in which N prominent sinusoidal signals are detected, we quantify the characteristics

of each of these signals through a Levenberg-Marquardt non-linear least-squares fit of the model function $\sum_{n=1}^{N} A_n \sin\left[2\pi\left(\nu_n[t - t_0] + \phi_n\right)\right]$ to the observed variations in the subset. This sum describes the total signal arising from the contribution of the N prominent sinusoidal signals triggered during the subset, each of frequency ν_n, amplitude A_n, and phase ϕ_n with respect to the arbitrary fixed time reference t_0.

The preliminary values of the prominent frequencies that we extracted with PERIOD04 during step [**1**] are listed in the second column of Table 7.III and indicated in Figs. 7.3 and 7.4. We note the detection of three sets of two–three unresolved frequencies, $\mathcal{S}_1 = \{\nu_1, \nu_2\}$, $\mathcal{S}_2 = \{\nu_3, \nu_4, \nu_5\}$ and $\mathcal{S}_3 = \{\nu_7, \nu_8, \nu_9\}$, as $|\nu_1 - \nu_2| = 0.0235$ d^{-1}, $|\nu_3 - \nu_4| = 0.0141$ d^{-1}, $|\nu_5 - \nu_4| = 0.0274$ d^{-1}, $|\nu_7 - \nu_8| = 0.0196$ d^{-1}, and $|\nu_9 - \nu_8| = 0.0164$ d^{-1}, all below or barely above the Loumos & Deeming (1978) threshold which in our case is $1.5/T \simeq 0.0235$ d^{-1} (T being the total time base of the observations). Also, as a consequence of this criterion (and even just considering the Rayleigh criterion), one frequency, $\nu_{11} = 0.5047$ d^{-1} [$P_{11} = 1.9814$ d], could be the occurence of the first harmonic of $\nu_3 = 0.2759$ d^{-1} [$P_3 = 3.6245$ d]. However, the possibility of this being purely coincidental cannot be excluded because there are a dozen prominent frequency peaks packed in the region $\sim[0.2; 0.9]$ d^{-1} and the probability of occurence of combinations increases with the number of detected frequencies. Finally, also as a result of the $1.5/T$ criterion, a set of four frequency peaks, $\mathcal{S}_4 = \{\nu_4, \nu_6, \nu_8, \nu_{10}\}$, appears to share an equal spacing of $\sim$0.07 d^{-1}. This is further confirmed by the autocorrelation of the part of the amplitude spectrum in the range $\sim[0.2; 0.9]$ d^{-1} (Figure 7.5), revealing a frequency spacing of $\Delta\nu = 0.069 \pm 0.006$ d^{-1}. However, again due to the high concentration of frequency peaks in the restricted $\sim[0.2; 0.9]$ d^{-1} region, pure coincidence cannot be ruled out for the origin of this spacing.

Then, in step [**2**] we ended up with the six epochs highlighted in the bottom panel of

Table 7.III: The most prominent sine wave components of the intrinsic light variations of V973 Sco as observed by *BRITE* in 2015. The first column indicates the labels for the parameters of each signal (frequencies ν_n in d^{-1}, amplitudes A_n in mmag, and phases ϕ_n measured with respect to HJD-2451545.0 = 0.0). The second column lists the preliminary frequency values extracted with PERIOD04, with the bracketed numbers indicating their S/N measured in the original DFT over $[0;4]$ d^{-1}. Columns 3 – 8 list the subset epochs $\mathcal{E}_m$ of the observing run resulting from step **[2]** of the method described in Section 7.5, the bracketed numbers indicating their starting and ending dates (HJD-2451545.0). If a signal is prominent during epoch $\mathcal{E}_m$, its frequency, amplitude and phase resulting from the fitting procedure (step **[3]**) are listed in the corresponding column. The last line reports the standard deviation σ_m (in mmag) of the residual light variations in each subset.

Signal		Epoch					
		$\mathcal{E}_1$ [5663.04 – 5668.00]	$\mathcal{E}_2$ [5668.00 – 5675.00]	$\mathcal{E}_3$ [5675.00 – 5686.00]	$\mathcal{E}_4$ [5686.00 – 5690.00]	$\mathcal{E}_5$ [5690.00 – 5700.00]	$\mathcal{E}_6$ [5700.00 – 5710.00]
	PERIOD04						
ν_1	0.03919 [4.6]	–	–	–	–	–	–
A_1	–	–	–	–	–	–	–
ϕ_1	–	–	–	–	–	–	–
ν_2	0.06270 [5.3]	–	–	–	–	0.06225 ± 0.00625	0.06278 ± 0.00856
A_2	–	–	–	–	–	5.35 ± 0.63	3.61 ± 0.59
ϕ_2	–	–	–	–	–	⋆0.5039 ± 0.0186	0.5039 ± 0.0258
ν_3	0.27588 [6.4]	0.27597 ± 0.01055	–	–	–	–	0.27594 ± 0.00121
A_3	–	8.49 ± 0.67	–	–	–	–	25.55 ± 0.59
ϕ_3	–	0.2062 ± 0.0125	–	–	–	–	0.1784 ± 0.0036
ν_4	0.28999 [4.9]	–	–	–	–	–	0.29043 ± 0.00129
A_4	–	–	–	–	–	–	23.88 ± 0.59
ϕ_4	–	–	–	–	–	–	0.0183 ± 0.0039
ν_5	0.31742 [4.9]	–	–	–	–	–	0.31746 ± 0.00268
A_5	–	–	–	–	–	–	11.54 ± 0.59
ϕ_5	–	–	–	–	–	–	0.3339 ± 0.0081
ν_6	0.36287 [4.5]	0.36294 ± 0.01180	–	–	–	–	–
A_6	–	7.59 ± 0.67	–	–	–	–	–
ϕ_6	–	0.2005 ± 0.0140	–	–	–	–	–
ν_7	0.41538 [4.9]	0.41545 ± 0.00493	0.39992 ± 0.00348	0.40918 ± 0.00193	0.41534 ± 0.00538	–	–
A_7	–	18.17 ± 0.67	13.00 ± 0.60	18.54 ± 0.64	14.56 ± 0.60	–	–
ϕ_7	–	0.2618 ± 0.0058	0.2310 ± 0.0074	0.0865 ± 0.0055	0.0117 ± 0.0066	–	–
ν_8	0.43498 [6.8]	–	0.43888 ± 0.00404	0.43385 ± 0.00252	0.43536 ± 0.01488	0.43479 ± 0.00371	0.43508 ± 0.00465
A_8	–	–	11.20 ± 0.60	14.19 ± 0.64	5.26 ± 0.60	9.02 ± 0.63	6.64 ± 0.59
ϕ_8	–	–	0.6858 ± 0.0086	0.5448 ± 0.0071	0.1056 ± 0.0183	0.7952 ± 0.0111	0.0000 ± 0.0140
ν_9	0.45144 [4.9]	–	–	–	0.45104 ± 0.00417	0.45167 ± 0.00319	–
A_9	–	–	–	–	18.79 ± 0.60	10.46 ± 0.63	–
ϕ_9	–	–	–	–	0.4847 ± 0.0051	0.1533 ± 0.0096	–
ν_{10}	0.50473 [4.6]	–	–	–	–	0.50434 ± 0.00221	–
A_{10}	–	–	–	–	–	15.15 ± 0.63	–
ϕ_{10}	–	–	–	–	–	0.4657 ± 0.0067	–
ν_{11}	0.54549 [4.9]	–	0.54553 ± 0.01436	–	0.54556 ± 0.01081	0.54620 ± 0.00554	–
A_{11}	–	–	3.15 ± 0.60	–	7.24 ± 0.60	6.03 ± 0.63	–
ϕ_{11}	–	–	0.0045 ± 0.0305	–	0.0079 ± 0.0133	0.5354 ± 0.0166	–
ν_{12}	0.60427 [4.8]	0.60419 ± 0.00971	–	–	–	–	0.60387 ± 0.00517
A_{12}	–	9.23 ± 0.67	–	–	–	–	5.97 ± 0.59
ϕ_{12}	–	0.2959 ± 0.0115	–	–	–	–	0.1539 ± 0.0156
ν_{13}	0.75239 [5.0]	–	–	0.75237 ± 0.01194	–	–	–
A_{13}	–	–	–	3.00 ± 0.64	–	–	–
ϕ_{13}	–	–	–	0.8084 ± 0.0337	–	–	–
ν_{14}	0.80726 [4.6]	–	–	0.80235 ± 0.00439	–	–	–
A_{14}	–	–	–	8.15 ± 0.64	–	–	–
ϕ_{14}	–	–	–	0.1659 ± 0.0124	–	–	–
σ_m		3.47	4.21	4.33	3.12	5.24	4.83

⋆Phase kept constant as the signal clearly started at the beginning of $\mathcal{E}_5$ and continues in $\mathcal{E}_6$ but with a lower amplitude.

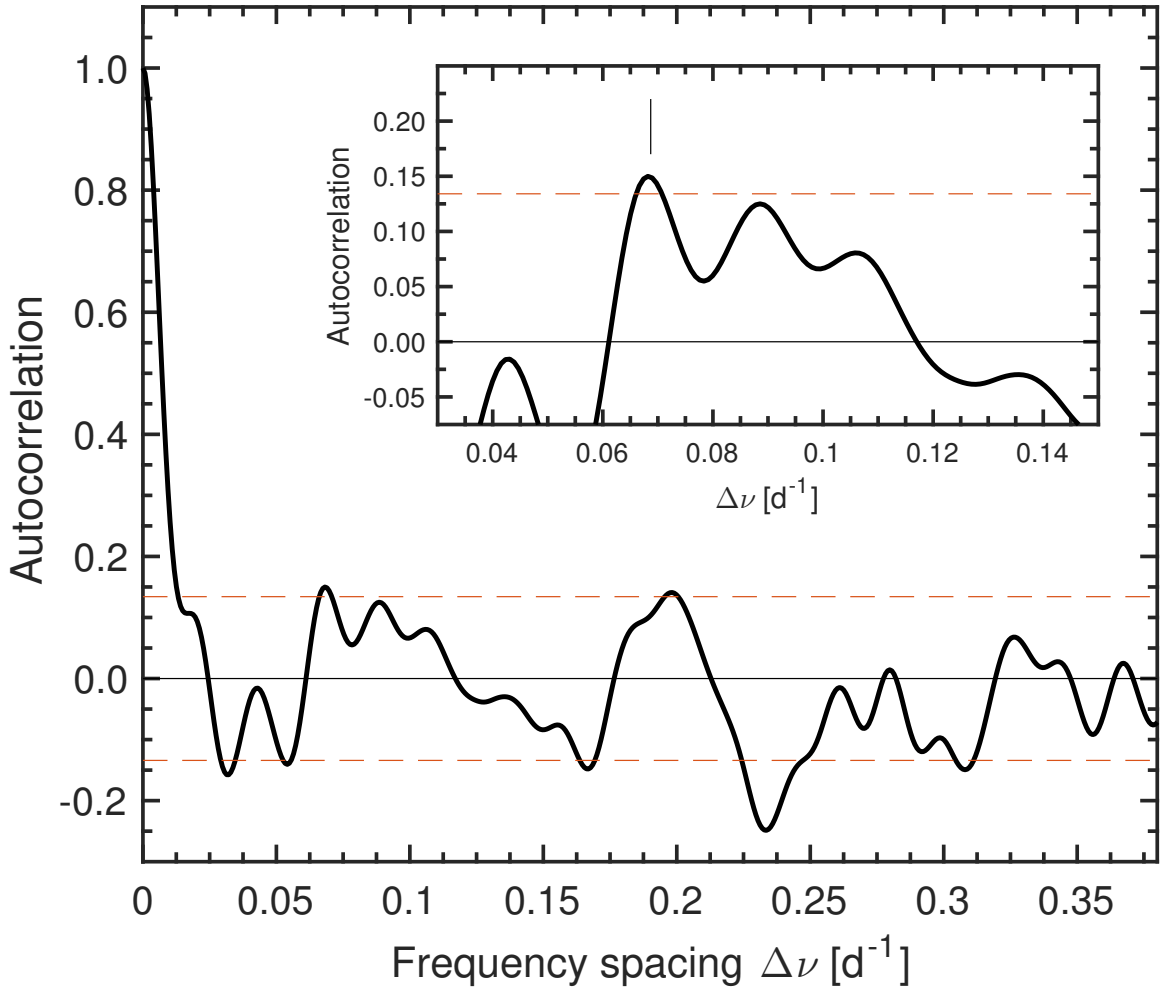

Figure 7.5: Autocorrelation function (ACF) of the $[0.2; 0.9]$ d^{-1} portion of the amplitude spectrum of the *BRITE* observations of V973 Sco (continuous curve), along with the 4σ confidence bounds (dashed horizontal lines), the inset zooming on the region of lags $[0.03; 0.15]$ d^{-1} where a significant peak is detected at a lag of $\Delta\nu = 0.069 \pm 0.006$ d^{-1} corresponding to the frequency spacing apparently exhibited by the elements of set $\mathcal{S}_4 = \{\nu_4, \nu_6, \nu_8, \nu_{10}\}$. The ACF also appears to present another peak at $\sim$0.2 d^{-1} rising slightly above the 4σ threshold but having a relatively large width to be unambiguously considered a true spacing.

Figure 7.4 and listed in columns 3-8 of Table 7.III, with typical time bases in the range $5-11$ days. Table 7.III also summarizes which signal is excited during which epoch. We note that the determination of the epochs of excitation of a prominent signal was not straightforward for some signals that do not have well-resolved frequencies, especially the two signals with frequencies ν_7 and ν_8. Wherever there is an ambiguity about whether such signals are excited or not, we decided to include them, and the result is that they appear to last longer than the other signals (however, their amplitudes clearly change from one epoch to another). Evidently, observations over a much longer time base are needed in the future to better assess the lifetimes of these signals. Speaking of time base, it should be kept in mind that, since the windowed Fourier transforms have to be evaluated starting $\mathcal{W}/2$ after the first observation in the time series and ending $\mathcal{W}/2$ before the last data point in the time series, the spectrogram is limited to that time base, and therefore this analysis is also only based on epochs defined within that time span. Consequently, this approach is not adequate for the characterization of the very low frequency $\nu_1 = 0.0392$ d^{-1} [$P_1 = 25.5102$ d]; but, in any case, since our observations only cover ~2.5 cycles of this signal, further observations over a much longer time base are needed to validate whether this signal is real or an artifact of instrumental origin. Additionally, as already mentioned previously, the current data barely allow us to unambiguously distinguish ν_1 and $\nu_2 = 0.0627$ d^{-1} as two different frequencies.

Finally, at step [**3**] we used the preliminary values of the frequencies determined in step [**1**] as first guesses for the frequencies involved in the fitting procedure. Particularly, in order to account for the Loumos & Deeming (1978) criterion, we let the frequencies vary within $\pm 1.5/T$ of their preliminary guesses, and leave the amplitudes and phases as completely free parameters to be determined. Furthermore, we note another key point that has to be taken care of: continuity at subset boundaries. More precisely, ideally

the transitions at the boundaries need to result in an overall function of class at least C^1 (i.e. differentiable and having a continuous derivative). In order to account for this subtle issue, we adopt the following strategy:

[1] perform the fitting procedure on the different subsets independently;

[2] note the subset $\mathcal{E}_{\rm best}$ which yielded the best fit (highest adjusted R^2 statistic);

[3] consider an adjacent subset $\mathcal{E}_{\rm adj,1}$ and slightly extend its time base to overlap with that of $\mathcal{E}_{\rm best}$, thus obtaining an extended subset $\mathcal{E}^{\rm ext}_{\rm adj,1}$;

[4] approximate the variations in the overlapping zone by the fitted variations from $\mathcal{E}_{\rm best}$, and redo the fit in the extended subset $\mathcal{E}^{\rm ext}_{\rm adj,1}$;

[5] the best fit in subset $\mathcal{E}^{\rm ext}_{\rm adj,1}$ is therefore taken to be the one that has a high-enough adjusted R^2 value and is such that the transition to the fitted variations in subset $\mathcal{E}_{\rm best}$ results in a nearly class C^1 function;

[6] propagate the procedure in adjacent subsets until all epochs are treated.

At the end of step **[3.1]**, it turned out that $\mathcal{E}_{\rm best} = \mathcal{E}_6$ (R^2 ~82%), such that we essentially went backwards in time to treat the subsequent adjacent epochs. The overlaps typically span around $0.5 - 0.75$ d depending on the gaps in the observations, with an exception of a 2-day overlap between subsets $\mathcal{E}_4$ and $\mathcal{E}_3$ due to the relatively large ~1.6-day gap in the observations around this transition, and for which we failed to determine a reasonable behaviour of class C^1, as we only found a continuous but not formally differentiable behaviour. The final fits to the observed variations in the subsets have R^2 values in the range ~$71 - 82$% and are also depicted in the bottom panel of Figure 7.4. The best-fit parameters for each sine wave component in each subset are listed in columns $3 - 8$ of Table 7.III. We also quote the analytical 1σ uncertainties for

these signal parameters (Montgomery & Odonoghue 1999):

$$\sigma(\nu_{n,m}) = \sqrt{\frac{6}{N_m}}\frac{1}{\pi T_m}\frac{\sigma_m}{A_{n,m}}, \quad \sigma(A_{n,m}) = \sqrt{\frac{2}{N_m}}\sigma_m, \quad \sigma(\phi_{n,m}) = \frac{1}{2\pi}\sqrt{\frac{2}{N_m}}\frac{\sigma_m}{A_{n,m}}, \tag{7.1}$$

where N_m is the number of observations during the time span T_m of epoch $\mathcal{E}_m$. In the original formulation of these analytical uncertainties, σ_m represents the root mean square error in the observations. It has to be kept in mind that the resulting formal uncertainties on the signal parameters are known to underestimate the true uncertainties (see e.g. Handler *et al.* 2000). Here we even adopt a more conservative approach by considering σ_m to be the standard deviation of the residual time series after removal of the fitted multiperiodic signal (Lenz & Breger 2005; Aerts *et al.* 2010, p. 367–368), which is typically a factor $\sim 2-3$ higher than the root mean square errors in the observations during each epoch $\mathcal{E}_m$. An even more pessimistic approach could consist in directly adopting those σ_m values (also indicated in Table 7.III) as gross estimates of the uncertainties in the signal amplitudes.

7.6 Origin of the light variations

First of all, the fact that $\nu_{11} \simeq 2\nu_3$ within the limits set by the Loumos & Deeming (1978) criterion (and even just considering the Rayleigh criterion) is noteworthy. Interpreting $\nu_3 = 0.2759$ d^{-1} [$P_3 = 3.6245$ d] as the rotational frequency $\nu_{\rm rot}$ is not evident at all and is highly unlikely because it corresponds to an equatorial velocity very close to the critical rotational velocity. Indeed, adopting $v_{\rm crit} = \sqrt{\mathcal{G}M/R_{\rm eq}}$ (M being the stellar mass, $R_{\rm eq}$ the radius at the equator, and $\mathcal{G}$ the gravitational constant; e.g. Townsend *et al.* 2004), which can be simply re-written as $v_{\rm crit} = \sqrt{gR_{\rm eq}}$ (since $M = gR_{\rm eq}^2/\mathcal{G}$), and taking into account the uncertainties on the values available to date for the surface

gravity and radius of V973 Sco (Table 7.I), the critical rotational velocity would be at 511^{+143}_{-112} km s^{-1}, corresponding to a critical rotational frequency of $0.2689^{+0.0756}_{-0.0589}$ d^{-1}. While this sets an upper limit on $\nu_{\rm rot}$, its lower bound can be obtained from the estimate of the projected rotational velocity available to date. In fact, the minimum value that $\nu_{\rm rot}$ can reach is $v_{\rm e} \sin i/(2\pi R_{\rm e}) = 0.0547^{+0.0096}_{-0.0089}$ d^{-1} (imposed by $\sin i \leq 1$). Hence, under the Loumos & Deeming (1978) criterion, $\nu_2 = 0.06270$ d^{-1} [$P_2 = 15.9490$ d] would be a better candidate for the rotational frequency (in which case V973 Sco would be seen almost equator on). However, as already repeatedly noted in Section 7.5, the two frequencies in set $\mathcal{S}_1 = \{\nu_1, \nu_2\}$ are barely distinguishable. Again, observations over a longer time base are needed in order to check this possibility.

Secondly, as already mentioned in Section 7.5, we noticed the presence of a regular spacing of $\Delta\nu = 0.069 \pm 0.006$ d^{-1} between the elements of set $\mathcal{S}_4$. Three possibilities are to be explored for the origin of this frequency spacing:

[1] large frequency separation exhibited by adjacent pressure modes of the same low degree but different high overtone in the asymptotic approximation (Tassoul 1980, 1990);

[2] small frequency separation of p modes predicted by the asymptotic theory;

[3] rotational splitting of pressure modes of the same degree and same overtone but different azimuthal order (Ledoux 1951).

Regarding (1), for a star as massive and large as V973 Sco, scaling laws (Kjeldsen & Bedding 1995) yield a large frequency separation of about a factor five greater than $\Delta\nu$, meaning that this spacing is unlikely to be a large frequency separation. Then remain possibilities (2) and (3). It is worth noting that if $\Delta\nu$ is related to rotational splitting of p modes, only three adjacent members of set $\mathcal{S}_4$ would be involved, i.e. either $\mathcal{S}'_4 = \{\nu_4, \nu_6, \nu_8\}$, or $\mathcal{S}''_4 = \{\nu_6, \nu_8, \nu_{10}\}$. *However*, before going further into these

interpretations, the first question that needs to be answered is: can the relatively low frequencies involved in set $\mathcal{S}_4$ arise from pressure modes for an evolved hot massive star like V973 Sco? In that regard, it should be pointed out that the stellar parameters of V973 Sco indicate that it falls both in the extreme upper part of the instability strip for low-order p mode oscillations (although far away from the known β Cep variables clustered in the lower part of that instability strip; e.g. figs. 3, 4, 5 in Pamyatnykh 1999; Figure 1 in Saio 2011) and in a confined region of the upper part of the HR diagram where the instability strip corresponding to $l = 1 - 2$ g-mode oscillations reappears (the same modes encountered in slowly pulsating B-type stars, although V973 Sco is obviously far from the cluster of observationally confirmed SPB stars). However, regarding heat-driven pulsations, the matter of whether a given period P might be due to pressure or gravity modes can even be more quantitatively evaluated with the associated value of the pulsation constant $Q = P\sqrt{(M/M_\odot)/(R/R_\odot)^3}$. The pulsation constant is of the order of $0.033 - 0.042$ d for the radial fundamental mode (Davey 1973; Lesh & Aizenman 1974; Fitch 1981; Stankov & Handler 2005), such that any value above this is indicative of gravity modes, while values below this correspond to pressure modes. For a $(45\mathrm{M}_\odot, 36\mathrm{R}_\odot)$ star, $Q \simeq 0.03P$, meaning that heat-driven p modes are expected to have periods shorter than ∼1 d for such stars, whereas periods longer than ∼1 d are likely to be those of g modes. Nevertheless, heat-driven oscillations excited through the κ mechanism operating in the iron opacity bump at T ∼170 kK are typically much more stable than the frequencies in set $\mathcal{S}_4$. Indeed, the spectrogram in Figure 7.4 and better quantified through the analysis summarized in Table 7.III says that, for instance, ν_{10} is only excited during epoch $\mathcal{E}_5$ for ∼10 d and is quasi-absent at other epochs. All these considerations lead us to the conclusion that caution must be exercised as for a strict interpretation of both the origin of the fact that $\nu_{11} \simeq 2\nu_3$ and the origin of $\Delta\nu$, as, again, these could just be incidental owing to the high density of

detected frequency peaks in the restricted $\sim[0.2; 0.9]$ d^{-1} region.

The key information that needs to be considered here is the time-dependency of the different modes: the main sinusoidal signals composing the light variations vary in amplitude, and their appearance seems to occur in no particular organized manner, suggesting a stochastic triggering. After they are excited, they typically last about $\sim 5-10$ days (this does not strictly apply to the signals affected by frequency resolution issues, as we already noted in detail in Section 7.5). Additionally, the presence of the bump in the regime $[0; 0.9]$ d^{-1} where the prominent signals are excited is indicative of stochastically excited modes with finite lifetimes, as is the case for e.g. stochastically excited solar-like oscillations (e.g. Kallinger *et al.* 2010). All these behaviours (several excited frequencies in the range $[0; 0.9]$ d^{-1}, clear bump in that frequency regime, time-dependency and finite lifetime of the modes) point towards three possible explanations for the dominant intrinsic light variations revealed by *BRITE* in V973 Sco:

[i] internal gravity waves (IGWs) excited from deep down at the level of the convective core–radiative enveloppe boundary (Rogers *et al.* 2013; Aerts & Rogers 2015; Aerts *et al.* 2017);

[ii] gravity waves excited at the interface between a sub-surface convection zone and the radiative layer directly above it (Cantiello *et al.* 2009b);

[iii] direct manifestation of turbulent convection in the upper part of a sub-surface convective zone.

Regarding option **[i]**, there have already been interpretations of the dominant stochastic light variations of three main-sequence and subgiant O-type stars observed by the *COnvection ROtation and planetary Transits (CoRoT)* satellite (HD 46223 [O4 V((f))], HD 46150 [O5 V((f))z], and HD 46966 [O8.5 IV]; Blomme *et al.* 2011; Aerts & Rogers 2015) and those of the O9.5Iab star HD 188209 observed by *Kepler* (Aerts *et al.*

2017) as possibly arising from IGWs stochastically-triggered from the convective core. In order to further qualitatively compare the observed amplitude spectrum of V973 Sco with that of IGWs that could be excited from the convective core, we follow the same approach as that adopted by Aerts & Rogers (2015) and Aerts *et al.* (2017), which is based upon the two-dimensional hydrodynamical simulations performed by Rogers *et al.* (2013). We thus consider the case of the $3M_{\odot}$ non-rigidly rotating model D11 of Rogers *et al.* (2013) and apply a scaling factor to convert from tangential velocity to brightness amplitude, followed by a scaling of the frequencies to account for a TAMS supergiant. The validity and caveats in this simple scaling approach were addressed in detail by Aerts & Rogers (2015). Evidently, the first requirement to be met in order to adopt this approach here is the similarity in the overall internal structure of a $3M_{\odot}$ ZAMS massive star and a star as massive and evolved as V973 Sco (i.e. convective core, radiative envelope). In spite of that being the case, it has been pointed out that the propagation of IGWs can be different depending on the stellar mass and evolutionary status. However, that effect might be lessened by the fact that the observable velocity and brightness amplitude spectra of IGWs are more influenced by the convective flux rather than the profile of the Brünt–Väisälä frequency (Rogers *et al.* 2013, equations 14 and 15). But in that regard, the total mass fraction of the convective core and the luminosity to mass ratio could be important parameters for the driving of the waves, and therefore not allow the scaling approach to yield optimal results. Additionally, as already noted by Aerts & Rogers (2015) and Aerts *et al.* (2017), obviously this approach only allows for a qualitative comparison of the overall behaviour of the simulated and observed periodograms, and does not allow a strict comparison of the excited frequencies one by one. Nevertheless, this approach currently remains the only viable one for V973 Sco until new hydrodynamical models of IGWs are available for the appropriate stellar mass range and age.

The conversion from the simulated tangential velocity spectrum to brightness amplitude spectrum simply consists in applying a scaling factor to the amplitudes of the simulated tangential velocity spectrum such that the highest peak in the resulting brightness amplitude spectrum roughly matches the highest peak in the observed brightness amplitude spectrum of V973 Sco. We then find a conversion factor of 19 mmag/(km s^{-1}) to be most appropriate to explain the observed amplitudes of the variability in V973 Sco. This value is about an order of magnitude larger than those found by Aerts & Rogers (2015) for the three main sequence and subgiant stars observed by *CoRoT* (conversion factors in the range $1.5 - 3$ mmag/(km s^{-1})). We note that if the same procedure was to be applied to the cases of the amplitude spectra of the *Kepler* observations of HD 188209 (O9.5Iab; Aerts *et al.* 2017) and the residual light variations of ζ Pup as observed by *BRITE* (O4I(n)fp; and 'residual' means free of any signs of the 1.78-d rotation of the star; Ramiaramanantsoa *et al.* 2018), the conversion factors would be of the order of 4 mmag/(km s^{-1}) for both stars. In that regard, V973 Sco appears to be particularly showing higher IGW brightness variability. Obviously, more observations are needed to confirm this hypothesis and to check whether there is any correlation with spectral type. Also, we note that the observed brightness amplitude spectrum of V973 Sco is $1 - 2$ orders of magnitude larger than the typical IGW-related rms surface brightness fluctuations found by Shiode *et al.* (2013, e.g. their figure 6). This could be due to effects not accounted for in their models, e.g. the effects of rotation which are known to enhance gravity wave amplitudes (Rogers *et al.* 2013).

In terms of the scaling in frequencies, Aerts & Rogers (2015) and Aerts *et al.* (2017) used the results of Shiode *et al.* (2013, their table 1) to find the appropriate scaling factor between the frequencies of $l = 1$ gravity waves of a $3M_{\odot}$ ZAMS star and those for stars having the mass and evolutionary status of their targets. In the case of

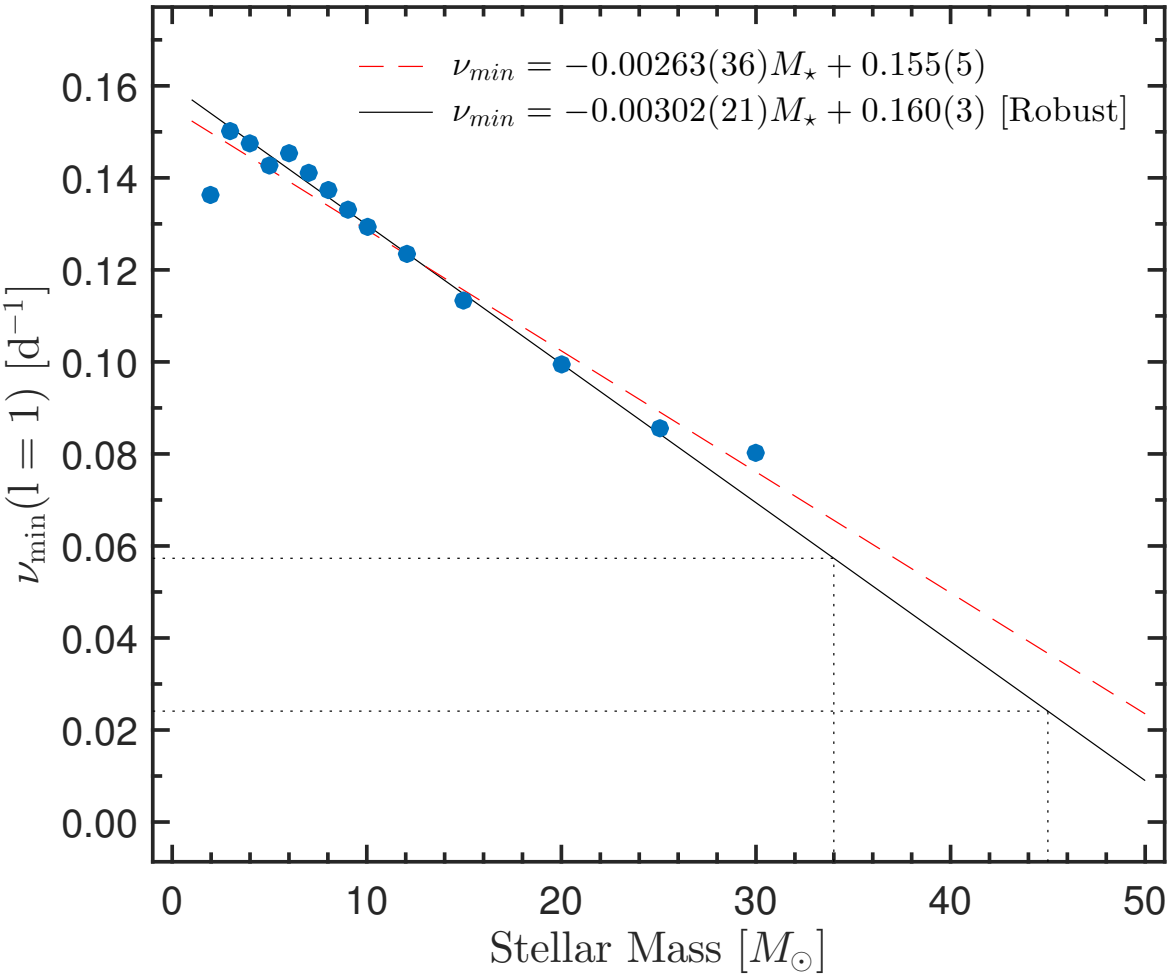

Figure 7.6: Trend followed by the minimum frequency for $l = 1$ standing waves reported by Shiode *et al.* (2013) as a function of stellar mass (pale blue dots), along with its linear least-square fit (dashed thin red line) and its robust linear least-square fit (solid black line). Dotted lines indicate the minimum frequency value for $M = 3\mathrm{M}_\odot$, and those corresponding to $M = 34\mathrm{M}_\odot$ and $M = 45\mathrm{M}_\odot$ as yielded by the robust fit.

V973 Sco, Martins *et al.* (2005) quote a typical mass of ~34$M_\odot$ for an O8.5 supergiant[2], whereas Crowther & Evans (2009) estimated a current mass in the range ~35 – 45$M_\odot$ for V973 Sco. Since the results reported by Shiode *et al.* (2013) do not go beyond 30$M_\odot$, we extrapolate their values by performing a first order (linear) fit to the trend followed by the minimum frequencies for dipole gravity waves as a function of stellar masses, as shown in Figure 7.6. Adopting the robust fit to the trend, we find a scaling factor of 0.16 for a 45$M_\odot$ star and 0.38 in the case of a 34$M_\odot$ star.

Figure 7.7 depicts the outcome of the comparison process, clearly indicating that the 45$M_\odot$ model is favoured as its broad bump in the amplitude spectrum and the associated range of most excited frequencies match well with the ones observed in V973 Sco. We emphasize here that these simulations do not allow a strict comparison of the frequency peaks one by one, but serve as a qualitative comparison of the global shape, trend, and range of excited frequencies of the periodograms.

Concerning options [**ii**] and [**iii**], we note that further investigations need to be conducted on the possibility of IGWs that could be excited from a potential sub-surface convection zone (Cantiello *et al.* 2009b), and/or whether the effects of turbulent convection in such a sub-surface convection zone could be visible up to the level of the photosphere. Adding to that is the fact that, at the moment, it is unclear whether the velocity/brightness amplitude spectrum due to breaking, stochastically-generated IGW (as simulated by Rogers *et al.* 2013) is fundamentally different from the spectrum of turbulent convection. Nevertheless, in both cases evidently the observable effects could become more important the closer to the surface the convective layer is located. In that regard, the current status of V973 Sco turns out to be particularly interesting.

[2]Martins *et al.* (2005) only consider O stars divided up into luminosity classes V, III and I. They do not distinguish luminosity sub-classes Ib, Iab, Ia and Ia+. V973 Sco being of luminosity class Ia, it is brighter than the average luminosity class I considered by Martins *et al.* (2005), thus expected to be more massive than the ~34$M_\odot$ mass they quote for luminosity class I O-type stars.

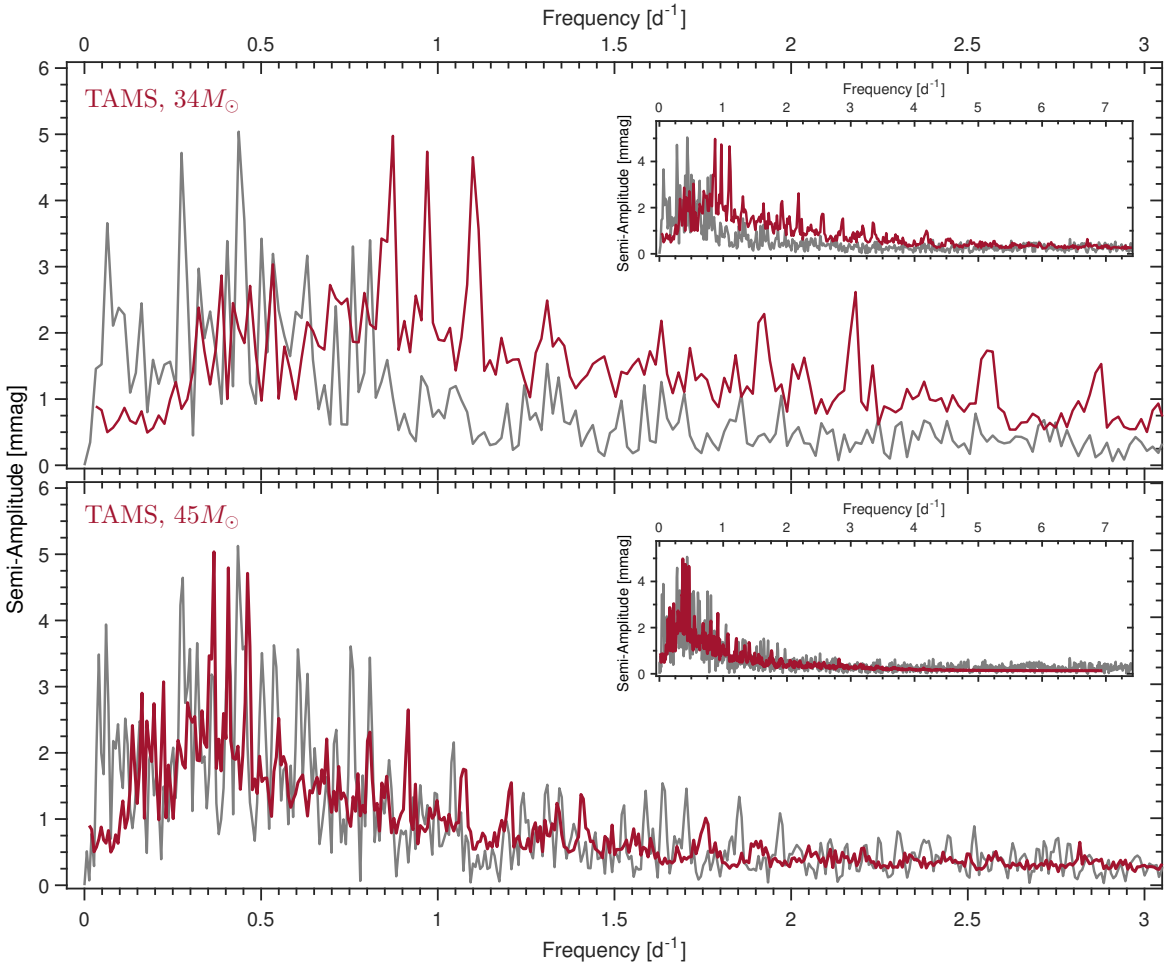

Figure 7.7: The observed amplitude spectrum of the *BHr* light curve of V973 Sco (gray) compared to the emergent amplitude spectrum from 2D HD simulations of IGWs triggered from deep in the convective core (red), corresponding to model D11 of Rogers *et al.* (2013) but properly scaled in frequency to account for the status of V973 Sco as a supergiant and two possibilities for its current mass (~34M$_\odot$ according to Martins *et al.* 2005; ~35−45M$_\odot$ according to Crowther & Evans 2009). Clearly the 45M$_\odot$ model corresponds better to the behaviour of the observed amplitude spectrum. Note that in order to perform a fair comparison between the observed and the modelled amplitude spectra, the former had to be re-evaluated with the same frequency resolution as the latter.

According to the findings of Crowther & Evans (2009), the current mass of V973 Sco is of the order of $35 - 45 M_{\odot}$, which corresponds to an initial mass of about $60 M_{\odot}$ and an age of ~2.7 Myr. This means that V973 Sco would be the ideal archetype of the $M_{ZAMS} = 60 M_{\odot}$ model considered by Cantiello *et al.* (2009b, their figs. 1 and 3). Particularly, the age estimate of ~2.7 Myr corresponds to a stage where a convection layer due to iron opacity bump at $T \simeq 170$ kK plunges further down into the star (therefore, perhaps better qualified as 'intermediate' convective zone rather than 'sub-surface' convective zone), while a sub-surface convective layer due to the helium opacity peak at $T \simeq 50$ kK appears at $\sim 0.12 R_{\odot}$ below the photosphere (figure 3 of Cantiello *et al.* 2009b). These considerations emphasize the need for theoretical investigations on options [**ii**] and [**iii**].

7.7 Conclusions and future work

The *BRITE* time-dependent photometric observations of V973 Sco that we have analyzed in this investigation are the longest and most intensive observations of V973 Sco to date, and revealed for the first time the unambiguous presence of a stochastically-generated intrinsic variability at the photosphere of the star. Stochastic triggering of IGWs from the convective core yields a brightness amplitude spectrum that qualitatively matches the observed amplitude spectrum of the light variations of V973 Sco, especially the bump where the dominant modes are located. The evident next path to be explored from the theoretical standpoint is the investigation of the possibility of stochastic excitation of gravity waves from a sub-surface convection layer, as well as an in-depth investigation of the observable characteristics of turbulent convective motions in such sub-surface convective regions.

On the observational side, despite the fact that for V973 Sco these observations are

unprecedented in terms of their quality, cadence, and time span, we emphasize the (obvious) need for observations on a much longer time base to better quantify the characteristics of the modes involved in these IGWs, especially their lifetimes, the frequency resolution of the current time series photometric observations being still insufficient to clearly distinguish some signals, as we pointed out in Section 7.5. Additionally, future observations of V973 Sco need to explore the connection between these IGWs appearing at the photosphere and wind clumping activity. The four-year long photometric and spectroscopic multi-site campaign conducted by Aerts *et al.* (2017) on the late O-type supergiant HD 188209 revealed that the stellar photospheric variability due to IGWs propagates into the stellar wind. The six-month long *BRITE* observations of the early O-type supergiant ζ Puppis, complemented by contemporaneous ground-based multi-site spectroscopic monitoring of the He II λ4686 wind-sensitive emission line of the star, revealed that large-scale wind structures are driven by bright photospheric spots and that the inner wind clumping activity is triggered by an unknown stochastic mechanism operating at the photosphere and manifesting itself as light variations of stochastic nature (Ramiaramanantsoa *et al.* 2018). The most probable scenario that can be drawn from those two recent investigations is that stochastically excited IGWs seen at the stellar photosphere induce clumping at the very base of the wind. But, clearly, more long-term, multi-wavelength observations (e.g. long-duration, continuous, contemporaneous optical and X-ray monitoring – the X-ray domain being useful to probe shocks that could be related to wind clumps) on a relatively large number of O-type stars is needed in order to obtain a definitive, complete picture on this point. This has already been initiated on ζ Pup, for which a 840 ks *Chandra* X-ray observing run will be executed (PI: Wayne Waldron) in parallel with ground-based spectroscopy and monitoring by *BRITE-Constellation*.

Acknowledgements

AFJM acknowledges support from the Canadian Space Agency (CSA), the Natural Sciences and Engineering Research Council of Canada (NSERC), and the Fonds de Recherche du Québec - Nature et Technologies (FRQNT). APo acknowledges NCN grant 2016/21/D/ST9/00656 and used the infrastructure supported by POIG.02.03.01-24-099/13 grant: GCONiI–Upper-Silesian Center for Scientific Computation. APi acknowledges support from the NCN grant no. 2016/21/B/ST9/01126. The Polish contribution to the *BRITE* mission is supported by a SPUB grant of the Polish Ministry of Science and Higher Education (MNiSW). GH acknowledges support from the Polish NCN grant 2015/18/A/ST9/00578. GAW acknowledges Discovery Grant support from NSERC. TR was supported in part by science funding related to the *BRITE-Toronto* mission, awarded by the CSA to GAW on behalf of the Canadian *BRITE* team. KZ acknowledges support by the Austrian Space Application Programme (ASAP) of the Austrian Research Promotion Agency (FFG).

7.8 Appendix: *BRITE* photometry of V973 Sco: decorrelation with respect to trends of instrumental origin

An initial version of the *BRITE* observations of V973 Sco was extracted from raw images to a time series of flux measurements (corrected for intrapixel variations) using the standard pipeline for *BRITE* data reduction described in Popowicz *et al.* (2017), and was officially released under format "DR3"[3]. That format allows for the correction for possible trends of instrumental origin related to the location $(x_{\rm cen}; y_{\rm cen})$ of the centroid of the stellar point spread function (PSF) on the chip, variations in the temperature

[3]see Table A.1 in Popowicz *et al.* 2017 for the different existing versions of the release formats of *BRITE* light curves.

$T_{\rm CCD}$ of the detector, the satellite orbital phase $\phi_{\rm orb}$ (from the time column and with $P_{\rm orb} = 97.0972$ min), blurring of the stellar PSF that might be due to imperfect satellite stability (characterized by a coefficient named "PSFC"), and effects of random telegraph signal (RTS - indicated by a coefficient named "RTSC"). The most prominent instrumental effect that we noticed in that initial version of the raw *BRITE* light curve of V973 Sco is a sudden drop in flux in some of the orbits, corresponding to a strong blurring of the stellar PSF as indicated by the behaviour of the "PSFC" coefficient (Figure 7.8). This effect could arise from some scattered light coming to the star-tracker, or other issues related to the orientation of the satellite relative to the Sun, the Earth and the Moon. Furthermore, as depicted in Figure 7.8, this effect does not necessarily happen at the same orbital phase, such that decorrelation with respect to $\phi_{\rm orb}$ does not account for this anomaly. Unfortunately, the most appropriate way of dealing with this is to clip off measurements showing strong blurring effect, namely measurements with low "PSFC" values. In that regard, the choice of an appropriate threshold remains an issue and can even be qualified as arbitrary. Adopting a trial-and-error approach (by testing a range of "PSFC" value thresholds and inspecting the resulting remaining measurements taken within each orbit in the time series), we determined a value of 1.9×10^{-3} to be a good limit to adopt (Figure 7.8). However, this obviously results in a sharp cut and removes some points that are only slightly blurred but not affected by a strong flux loss. Given the fact that more recent formats of *BRITE* data releases ("DR4" and "DR5") contain an additional coefficient to better characterize blurring effects, we decided to re-extract the *BHr* observations of V973 Sco using the most updated, improved version of the reduction pipeline for observations performed in chopping mode. This allowed us to extract:

[i] four coefficients to characterize the blurring effect (hereafer $\mathrm{PSFC}_{j=1...4}$);

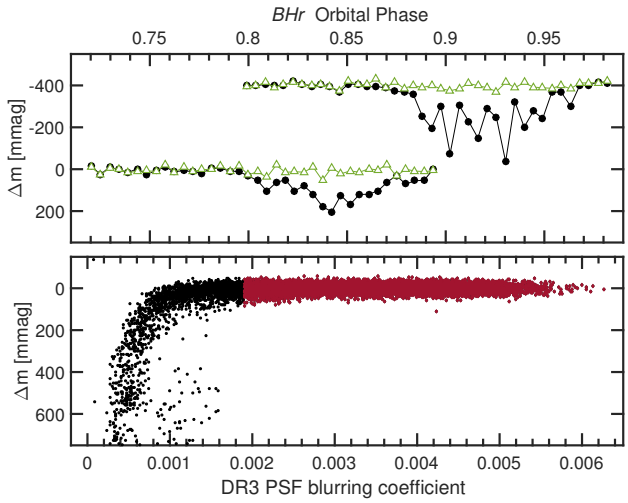

Figure 7.8: Illustration of the occurence of light curve anomalies corresponding to a strong blurring of the PSF in the *BHr* observations of V973 Sco released in the "DR3" format. *Top:* Sample time series taken within two different satellite orbits, respectively centered around HJD 2457204.84851 and HJD 2457218.27183. The second set of observations is offset by 0.4 mag for better visibility. Filled circles correspond to the officially released data, showing the anomalies, while open triangles correspond to the data that we re-extracted using the most updated version of the reduction pipeline. *Bottom:* A view of the officially released data as a function of the "DR3" PSF blurring coefficient. Black points represent the entirety of the data, showing strong flux loss for the most blurred observations, whereas red points correspond to the measurements that would remain when cutting off observations with blurring coefficient values lower than 1.9×10^{-3}.

[ii] the number of pixels $N_{\rm pix}$ considered in the stellar PSF;

[iii] an estimate of intensity offsets $I_{\rm off}$ within the custom aperture enclosing the target;

[iv] an estimate of the background level $B_{\rm diff}$ in difference images.

The motivations for considering blurring effects in *BRITE* observations were presented in detail by Popowicz *et al.* (2017). The parameter PSFC_2 is the same energy-based indicator "PSFC1" defined in equation B.1 by Popowicz *et al.* (2017) for "DR4"

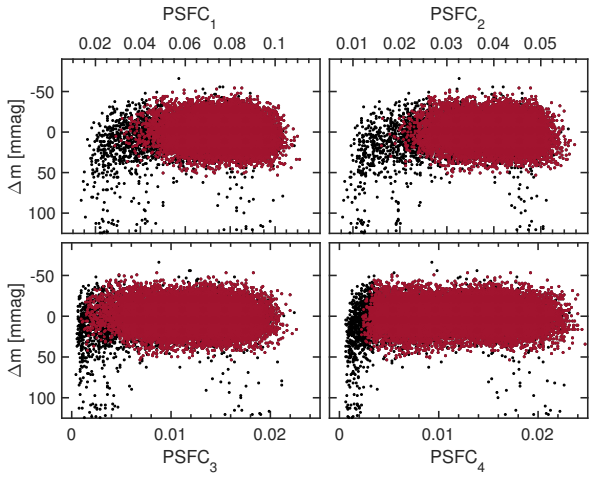

Figure 7.9: Newly extracted raw *BHr* light curve of V973 Sco viewed as a function of the four blurring coefficients $\mathrm{PSFC}_{j=1...4}$, showing fairer results out of the thresholding process. Red points are the raw data, whereas black points represent the remaining points after clipping off measurements that do not satisfy the condition **(C)** defined in the text.

and "DR5" formatted data. The parameters PSFC_3 and PSFC_4 are the decomposed versions of the correlation-based indicator "PSFC2" introduced in "DR4" and "DR5" formatted data (equation B.2 of Popowicz *et al.* 2017), now separately measuring blurring effects in the vertical direction (PSFC_3) and in the horizontal direction (PSFC_4). The only genuinely new blurring coefficient that we have also assessed here is PSFC_1, which simply tracks the ratio of the intensity of the brightest pixel in the stellar PSF to the integrated intensity over the stellar PSF.

Another useful parameter is the estimate of possible intensity offsets within the apertures (I_{off}). For a given observation in which a specific aperture has been assigned to the target, I_{off} considers only the pixels in that aperture and evaluates the sum of their intensity differences between the next observation and the previous one. This is a good proxy for measuring a possible increase of background light within the aperture. We

note that this method for estimating $I_{\rm off}$ is only possible in the chopping mode of observation as a result of the fact that the position of the stellar PSF in the current image is shifted in the x direction with respect to the PSF positions in the precedent and subsequent images.

Finally, the parameter $B_{\rm diff}$ is exactly the same as the parameter "APER0" described by Popowicz *et al.* (2017) for data in "DR4" or "DR5" formats, and could be useful in that it accounts for possible occasional intensity gradients in background between exposures, an effect that could induce some larger scatter within some orbits.

As readily visible in the top panel of Figure 7.8, the new reduction of the *BRITE* light curve of V973 Sco is better than the initial reduction, as some of the anomalies related to the blurring of the PSF are mitigated. The reason for this improvement is chiefly an improved best aperture selection in the latest version of the pipeline, essentially resulting from the fact that corrections for intrapixel variations are now done separately for the two sets of data in the two chopping positions (instead of globally as done in the case of "DR3" formatted data).

In the newly reduced time series of V973 Sco, the first step that we performed was the removal of obvious outliers. In that step, we ended up with the following condition **(C)** for a measurement to be considered for further processing:

$$(\mathrm{PSFC}_1 > 0.05) \vee (\mathrm{PSFC}_2 > 0.03) \vee (\mathrm{PSFC}_3 > 0.006) \vee (\mathrm{PSFC}_4 > 0.0035)$$

$$|B_{\rm diff} - 23| < 27$$

$$|I_{\rm off}| < 1200$$

$$(|x_{\rm cen} + 8.05| < 2.55) \vee (|x_{\rm cen} - 11.00| < 2.00)$$

$$|y_{\rm cen}| < 3.50,$$

with '$\vee$' denoting the inclusive disjunction. Figure 7.9 illustrates the resulting remaining measurements, particularly showing the capability of the four coefficients in keeping some of the measurements having low $\mathrm{PSFC}_{j=1\ldots4}$ values but not affected by strong flux deficit. At this stage of the light curve cleaning procedure we measure $\sigma_{\mathrm{rms}} \simeq 2.28$ mmag for the rms value of the mean standard deviations per orbit.

The next step consists in removing possible trends of instrumental origin affecting the flux measurements by exploring their behaviour as a function of the eleven parameters available, i.e. $(x_{\mathrm{cen}}; y_{\mathrm{cen}})$, T_{CCD}, $\mathrm{PSFC}_{j=1\ldots4}$, N_{pix}, I_{off}, B_{diff}, and ϕ_{orb}. The multivariate nature of the problem and our aim to concurrently describe the possible correlations between the different variables naturally calls for an approach involving principal component analysis (PCA). In fact, our time series of flux measurements of V973 Sco taken along with the estimates of the aforementioned eleven parameters constitute a series of $n = 18841$ measurements of $m = 12$ possibly dependent variables that can be regarded as an $n \times m$ matrix $\mathcal{M}$, each line representing the coordinates of a data point in an m-dimensional space formed by each of the original variables. Then we can use PCA to find the new coordinates of the set of measurements in a new orthogonal basis, the axes of which are directed by the eigenvectors of the covariance matrix $\mathcal{C}$ of $\mathcal{M}$. However, it is worth noting that the *BHr* observations of V973 Sco were performed in chopping mode in the x direction, obviously resulting in a globally bimodal distribution of the values of x_{cen}, such that it would be meaningless to treat this parameter globally together with the other parameters using PCA. Moreover, PCA only accounts for linear correlations, which could pose an issue if some of the trends of instrumental origin are not necessarily linear as in the case of other stars observed by *BRITE* (see e.g. figure A.5 in Pigulski *et al.* 2016). In consideration of these two caveats, we adopted the following three-step strategy:

[**1**] separate the data in two sets corresponding to the two distributions of PSF cen-

troid x position;

[2] perform PCA on these two sets;

[3] recombine the resulting corrected sets and adopt the method described by Pigulski *et al.* (2016) to correct for non-linear trends in the recombined data.

We note that, steps **[2]** and **[3]** could be substituted by a single step involving non-linear PCA (NLPCA; e.g. Kramer 1991; Dong & McAvoy 1994; Scholz 2012). In that case, NLPCA would be applied on the two sets, which are eventually recombined after the nonlinear trends are corrected. However, after testing an implementation of NLPCA based on an auto-associative neural network (Scholz 2012) on the *BRITE* observations of V973 Sco, we found that, not only is it computationally expensive, but it also yielded unsatisfactory results in describing some highly non-linear trends in the data (e.g. the behaviour of flux as a function of orbital phase). Thus, we decided to adopt the strategy involving the aforementioned three steps. Figs. 7.10 and 7.11 depict the outcome of the PCA on the two separate data sets, while Figure 7.12 plots the non-linear trends detected and corrected in the recombined data after the PCA. Finally, we perform a global 4σ clipping to the detrended data, followed by a 2σ orbital clipping, and omit any orbit containing less than five points. The properties of the final light curve at post-decorrelation stage are summarized in the last four entries of Table 7.II and the light curve binned over each *BHr* orbit illustrated on Figure 7.1.

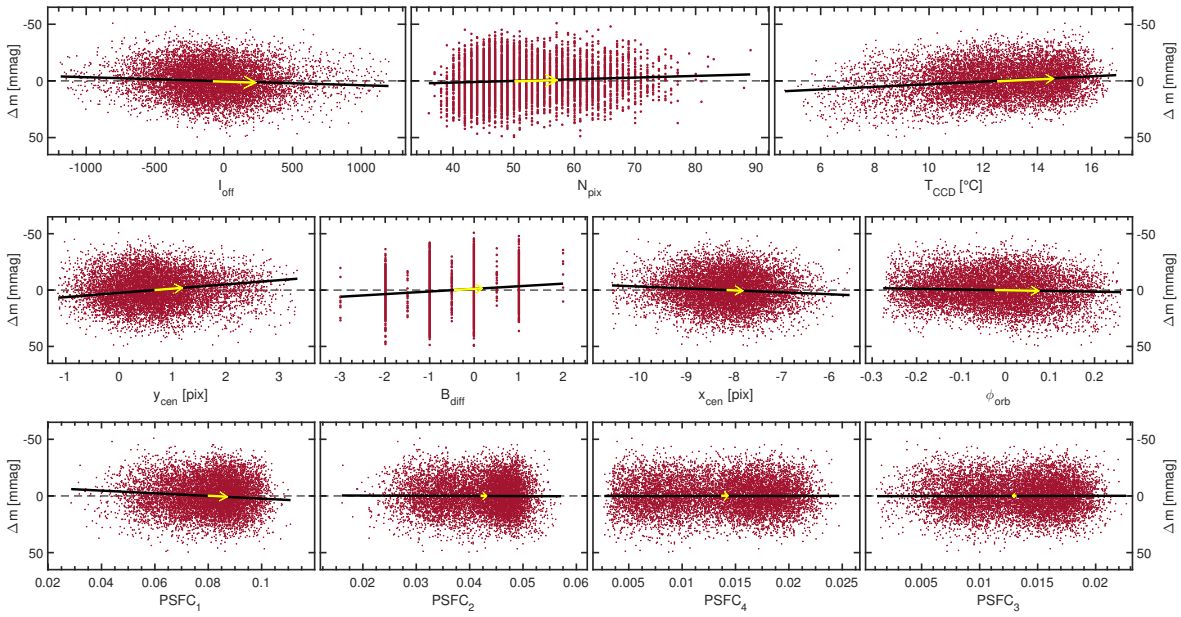

Figure 7.10: Outcome of PCA on the *BRITE* observations of V973 Sco for one of the centroid x position. Each panel illustrates the projection of the observations onto the plane of flux measurements versus one of the eleven instrumental parameters (red points), along with the corresponding direction of linear correlation/anti-correlation found by PCA (black line) as directed by the projection of the corresponding eigenvector (yellow arrow) of the covariance matrix onto that plane.

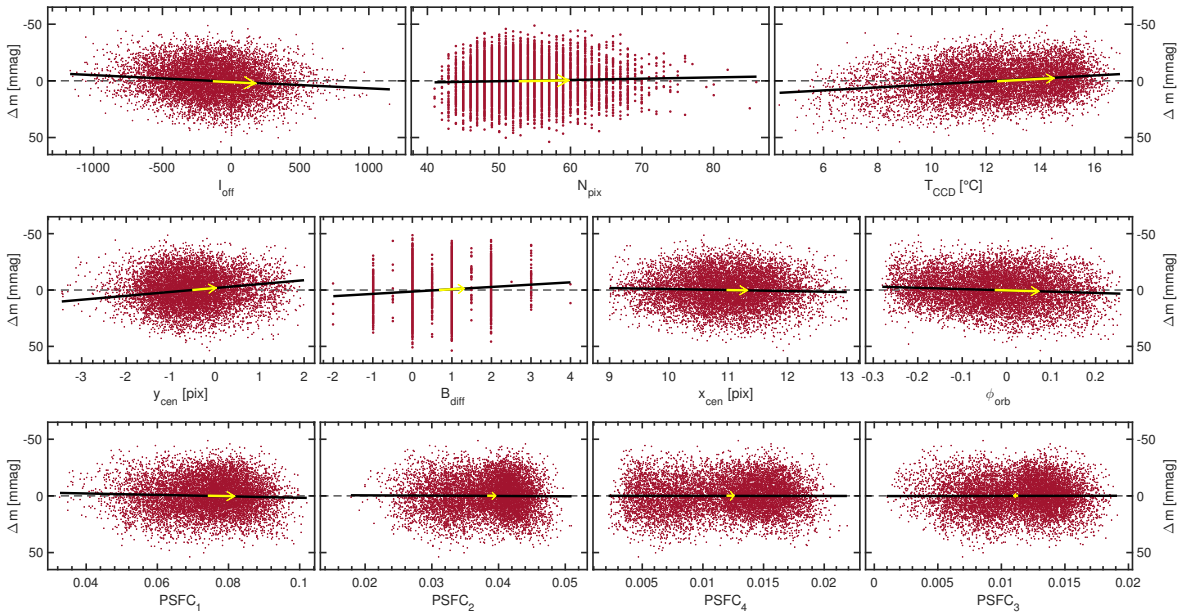

Figure 7.11: Same as Figure 7.10 but for the part of the observations acquired at the other centroid x position.

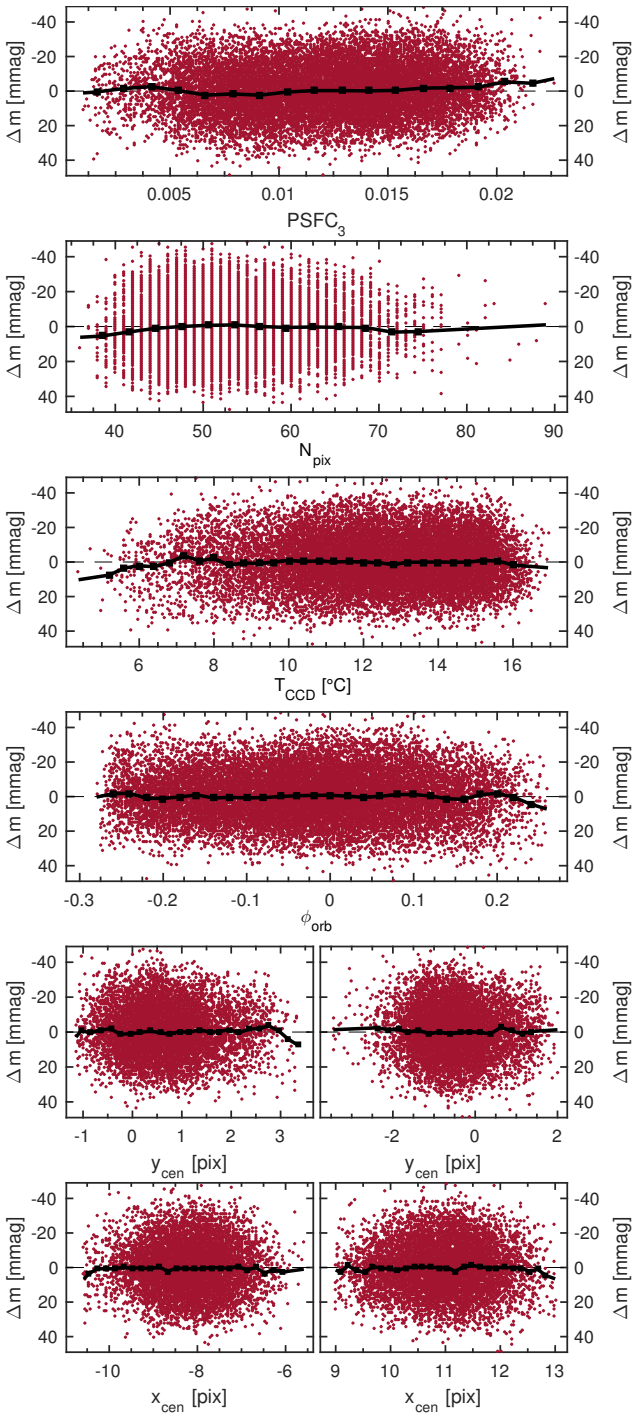

Figure 7.12: Correction of the remaining non-linear trends in the *BRITE* observations of V973 Sco found as a function of some of the instrumental parameters.

8

Conclusions et perspectives

Grâce aux efforts observationnels menés au cours de ce projet de thèse sur les étoiles O clés ξ Per, ζ Pup et V973 Sco, nous avons pu fonder les prémices de notre quête des sources photosphériques des structures à grande et à petite échelles dans les vents des étoiles chaudes et lumineuses de type spectral O.

La détection d'un ensemble de pics de fréquences centré autour de la fréquence de récurrence des DACs de ξ Per dans le périodogramme de sa courbe de lumière *MOST* était un début très encourageant: cela indiquait déjà que la variabilité qui était détectée auparavant dans le vent de l'étoile (DACs/CIRs; $P_{\rm DACs} \simeq 2.09$ d) est aussi détectée au niveau de sa photosphère. L'interprétation de la présence de l'ensemble de (quatre) pics au lieu d'un seul pic de fréquence n'était pas évidente. La possibilité de modes

g n'était pas définitivement exclue, mais le scénario des taches claires en corotation à la photosphère était le plus plausible, auquel cas l'émergence de l'ensemble de pics au lieu d'un seul pic s'est avérée être une manifestation des déphasages entre les époques d'apparitions des différentes taches à la surface. Il faut aussi noter que la propriété la plus flagrante minimisant la possibilité de modes g est la monopériodicité de cette variabilité telle qu'observée dans le vent, une caractéristique qui est encore confirmée récemment par les résultats de l'analyse de 12 ans d'observations spectroscopiques de l'étoile, décelant une période unique à ~ 2.04 d dans sa raie de N IV λ1718 (Sudnik & Henrichs 2018).

Toujours dans le cas des variations de lumière de ξ Per telles que détectées par *MOST*, il est important de noter encore une fois que la modélisation analytique des taches a permis d'expliquer le comportement aux alentours de la fréquence de récurrence des DACs dans le périodogramme, mais ne permet en aucun cas la comparison stricte des courbes de lumière ainsi modélisées à celle observée. Deux raisons fondamentales contribuent à ce fait: d'une part le problème des taches est connu comme étant un problème hautement dégénéré (comme déjà mentionné à la Section 5.4.2 du Chapitre 5); et d'autre part il est irréaliste d'espérer pouvoir faire un ajustement parfait d'un modèle analytique de taches sur une courbe de lumière non remise en phase par rapport à la période de rotation si cette courbe de lumière observée contient des variations additionnelles stochastiques intrinsèques à l'étoile de même ampleur que celles dues aux taches. Cette deuxième considération ne nous est pas venue à l'idée à l'époque où nous avons publié officiellement les résultats sur ξ Per. Nous nous en sommes rendus compte seulement après avoir détécté clairement qu'il existe des variations intrinsèques de nature stochastique dans la courbe de lumière de ζ Pup et V973 Sco, et en revoyant le comportement global de la courbe de lumière *MOST* de ξ Per.

La campagne d'observations que nous avons menée sur ζ Pup est sans aucun doute celle qui s'est avérée être la plus révélatrice. Elle nous a permis à la fois la détection claire de la manifestation de taches claires photosphériques entraînant la formation de CIRs dans le vent stellaire, et la détection de la manifestation de structures photosphériques stochastiques qui sont à l'origine de la formation de grumeaux dès la base du vent stellaire.

En termes de la variabilité cyclique à 1.78063(25) d liée à la rotation de ζ Pup, un mystère attendant d'être élucidé par les futures observations est le fait que la période de récurrence des DACs/CIRs de 19.23(45) h telle que mesurée dans la partie en absorption du doublet de la raie de résonance du Si IV $\lambda\lambda 1394, 1403$ de l'étoile est différente de la première harmonique de la période de rotation stellaire, 21.3676(30) h. Comme déjà mentionné à la Section 6.5.1.4 du Chapitre 6, cela pourrait être la manifestation d'une rotation différentielle de type anti-solaire (rotation moins rapide à l'équateur qu'aux pôles). Qui plus est, cela concorde avec la faible angle d'inclinaison de l'étoile ($i = [24 \pm 9]^\circ$) et le fait que les DACs ne se voient que dans la partie en absorption des profils P Cygni (c'est-à-dire qu'elles ne sont visibles que dans la colonne de matière du vent stellaire située exactement devant le disque stellaire; région D sur la Figure 2.4 de la Section 2.1.3 du Chapitre 2). En d'autres termes, avec la faible angle d'inclinaison de $i = [24 \pm 9]^\circ$ et une rotation différentielle anti-solaire:

- les taches équatoriales induisent des CIRs qui ne se manifestent pas en DACs dans l'UV (car ces bras de CIRs ne passent jamais devant le disque stellaire face à l'observateur);
- les taches à haute altitude induisent des CIRs qui se manifestent en DACs dans l'UV (car ces bras de CIRs passent devant le disque stellaire face à l'observateur), et qui ont une cyclicité plus fréquente que celle des taches et des CIRs équatoriales (à cause de la rotation différentilelle anti-solaire).

Ce comportement reste bien sûr à vérifier avec les futures observations.

Concernant la nature des structures photosphériques stochastiques detectées dans ζ Pup, les mêmes possibilités que dans le cas de V973 Sco s'appliquent: soit il s'agit d'ondes de gravité internes (excitées à partir du coeur convectif ou d'une zone de convection sub-surfacique), soit il s'agit d'une manifestation directe de turbulences dans une zone de convection sub-surfacique. Dans tous les cas, le fait que les comportements de ces structures sont fortement corrélées à ceux des grumeaux dans le vent constitue une preuve concrête de l'origine photosphérique des structures à petite échelle dans le vent stellaire.

Bien que la campagne d'observations sur V973 Sco n'avait pas de composante permettant de sonder le vent stellaire, elle nous a permis de mettre en évidence la dominance des structures générées de manière stochastique à la surface de l'étoile durant l'époque des observations *BRITE*. La ressemblance du comportement du spectre en amplitude observé à celui du modèle d'ondes de gravité internes générées à l'interface coeur convectif–enveloppe radiative est frappante. Cela dit, cette étude observationnelle sur V973 Sco est même plus intéressante dans la mesure où elle lance une motivation pour déterminer théoriquement non seulement la possibilité d'excitations des modes dans une zone de convection intermédiaire ou sub-surfacique, mais aussi la possibilité d'une manifestation directe des mouvements turbulents eux-mêmes dans une zone de convection sub-surfacique.

Un point à noter aussi à propos de l'analyse des variations stochastiques dans la courbe de lumière *BRITE* de V973 Sco est la méthode adoptée pour determiner les caractéristiques (fréquences, amplitudes, phases) des signaux à durées de vies finies ainsi impliqués. Cette méthode est très intuitive et adéquate à la situation, bien que son inconvénient réside dans le fait qu'elle requiert beaucoup d'interventions du chercheur

qui fait l'analyse (quasiment à toutes les étapes, mais surtout à l'étape [**2**]), et donc demanderait beaucoup de patience si la série temporelle est très longue (comme celles des observations *Kepler*). Une amélioration visant à automatiser le plus possible cette méthode fera l'objet d'un sous-projet à part.

Ainsi, dans l'ensemble, ce projet de thèse nous a permis de faire un grand pas dans nôtre quête des origines photosphériques des structures dans les vents des étoiles chaudes et lumineuses, essentiellement grâce aux longues observations photométriques à haute précision et intensives menées à partir de l'espace avec les satellites *MOST* et *BRITE*. Nous avons trouvé ces structures photosphériques, certes, mais (pas de manière inattendue) cela soulève d'autres questions qui vont nous guider à l'établissement des prochaines étapes. Ces questions sont principalement:

[**1**] Est-ce que toutes les autres étoiles O présentent ces taches claires? Cela devrait être le cas, étant donné que le phénomène des DACs se retrouve virtuellement dans toutes les étoiles O. Cependant, pour confirmer cette inférence, la détection concrète de ces taches dans un bon nombre d'étoiles O reste à établir.

[**2**] D'où viennent ces taches claires photosphériques? Est-ce qu'elles sont d'origine magnétique (Cantiello & Braithwaite 2011)?

[**3**] Est-ce que les CIRs et les clumps sont associés à des chocs comme le prédisent les théories (Cranmer & Owocki 1996)?

Ces trois petites questions à elles seules reflètent le fait qu'il s'agit d'une longue quête qui requiert idéalement de considérer un grand nombre d'étoiles O, et, pour chaque étoile, adopter une stratégie observationnelle similaire à celle de la campagne d'observations sur ζ Pup (Section 6.3 du Chapitre 6), à laquelle il faut rajouter un suivi spectroscopique dans l'UV (pour sonder les DACs dans les raies de résonances),

dans le domaine des rayons X (pour sonder les éventuels chocs), et un suivi spectropolarimétrique (afin d'explorer la possibilité que les taches puissent être d'origine magnétique; Cantiello & Braithwaite 2011).

Cependant, afin d'avancer de manière réaliste vis-à-vis de la question **[1]**, la première étape à faire à la suite des campagnes d'observations présentées dans ce projet de thèse est de chercher des possibles signatures de modulation rotationnelle due à des taches dans les courbes de lumières d'autres étoiles O clés (c'est-à-dire à période de récurrence des DACs relativement bien établies; Kaper *et al.* 1999) déjà observées par *BRITE*. Les étoiles O clés ainsi concernées sont λ Cep (O6.5I(n)fp; $P_{\rm DACs} \simeq 1.4$ d), 10 Lac (O9V; $P_{\rm DACs} \simeq 6.8$ d), 68 Cyg (O7.5IIIn((f)); $P_{\rm DACs} \simeq 1.4$ d), et λ Ori A (O8III((f)); $P_{\rm DACs} \simeq 4$ d).

Pour avancer dans les questions **[2]** et **[3]**, comme déjà mentionné vers la fin de la Section 7.7 du Chapitre 7, 360 ks d'observations *Chandra* de ζ Pup vont être exécutées en parallèle avec des observations *BRITE*, de la spectroscopie au sol visant essentiellement le vent stellaire, et de la spectropolarimétrie avec l'instrument ESPaDOnS monté au télescope Canada-France-Hawaii (CFHT). Il n'est pas évident d'obtenir la quantité de temps d'observations spectropolarimétrique adéquate pour parvenir à détecter le champ magnétique faible qui pourrait être associé aux taches dans ζ Pup si elles sont d'origine magnétique. Cela dit, la motivation de la communauté scientifique en général devrait augmenter étant donné l'importance de l'enjeu: ce serait la toute première détection de taches claires d'origine magnétique sur une étoile chaude et lumineuse.

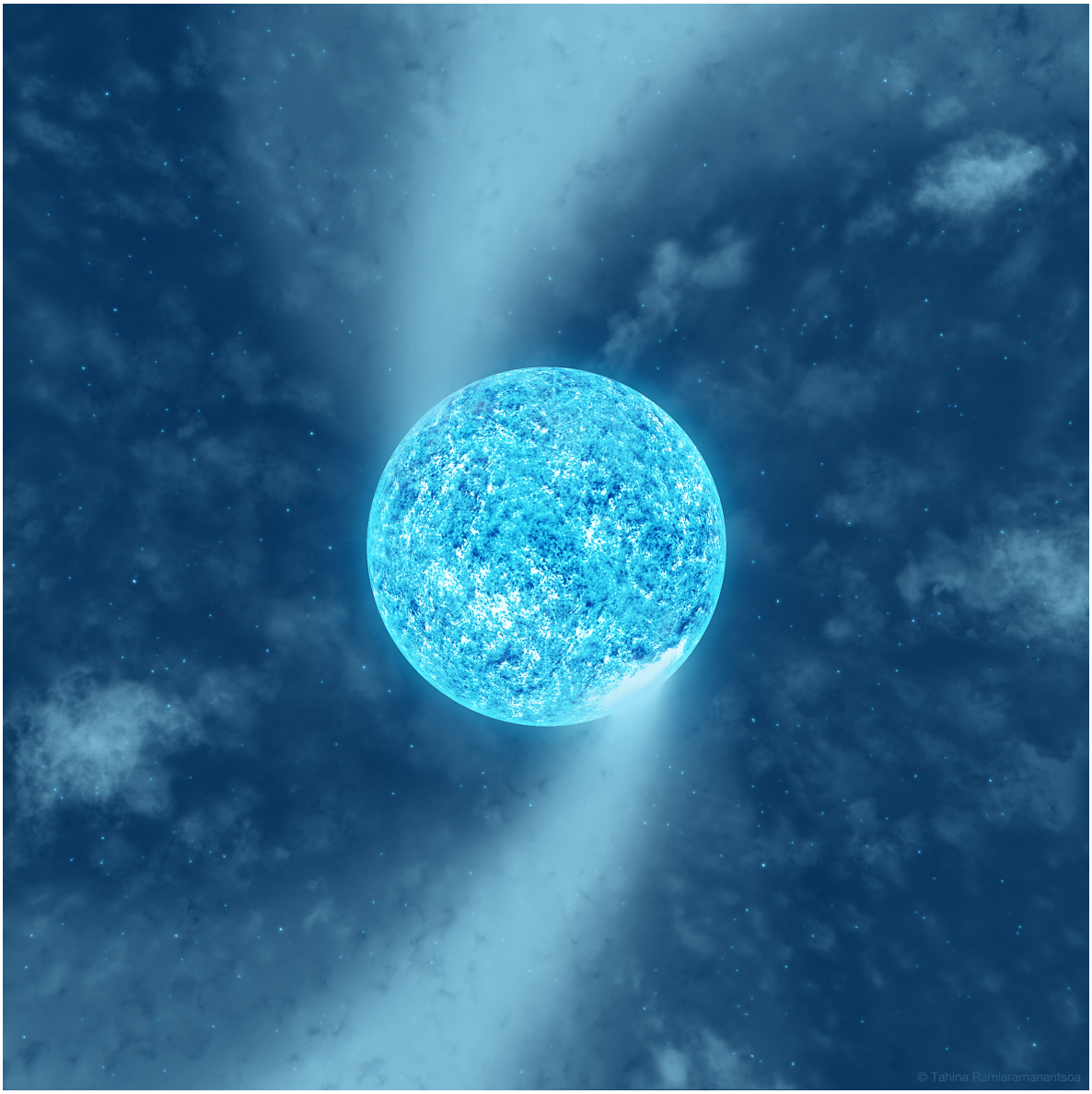

Figure 8.1: Vue d'artiste de ζ Pup inspirée des résultats de ce projet de recherche. Cette vue correspond à la partie IV de la campagne d'observations sur l'étoile telle qu'illustrée aux Figures 6.8 et 6.15 du Chapitre 6 ($i = 24°$ et phase rotationnelle $\phi = 0.375$).

Bibliographie

Abt, A. 1952. An analysis of W Virginis. *AJ*, **57**(Oct.), 158.

Aerts, C., & Rogers, T. M. 2015. Observational Signatures of Convectively Driven Waves in Massive Stars. *ApJ*, **806**(June), L33.

Aerts, C., Puls, J., Godart, M., & Dupret, M.-A. 2009. Collective pulsational velocity broadening due to gravity modes as a physical explanation for macroturbulence in hot massive stars. *A&A*, **508**(Dec.), 409–419.

Aerts, C., Christensen-Dalsgaard, J., & Kurtz, D. W. 2010. *Asteroseismology*.

Aerts, C., Simón-Díaz, S., Catala, C., *et al.* 2013. Low-amplitude rotational modulation rather than pulsations in the CoRoT B-type supergiant HD 46769. *A&A*, **557**(Sept.), A114.

Aerts, C., Símon-Díaz, S., Bloemen, S., *et al.* 2017. Kepler sheds new and unprecedented light on the variability of a blue supergiant: Gravity waves in the O9.5Iab star HD 188209. *A&A*, **602**(June), A32.

Alekseev, I. Y. 2005. Spots, activity cycles, and differential rotation on cool stars. *Astrophysics*, **48**(Jan.), 20–31.

Ansong, J. K., & Sutherland, B. R. 2010. Internal gravity waves generated by convective plumes. *Journal of Fluid Mechanics*, **648**(Apr.), 405.

Auvergne, M., Bodin, P., Boisnard, L., *et al.* 2009. The CoRoT satellite in flight: description and performance. *A&A*, **506**(Oct.), 411–424.

Baade, D. 1986. Observational properties of nonradial oscillations in early-type stars and their possible effect on mass loss: the example of ζ Puppis (O4 If). *Pages 465–466 of:* Gough, D. O. (ed), *NATO Advanced Science Institutes (ASI) Series C*. NATO Advanced Science Institutes (ASI) Series C, vol. 169.

Babcock, H. W. 1961. The Topology of the Sun's Magnetic Field and the 22-YEAR Cycle. *ApJ*, **133**(Mar.), 572.

Baglin, A., Auvergne, M., Barge, P., *et al.* 2006 (Nov.). Scientific Objectives for a Minisat: CoRoT. *Page 33 of:* Fridlund, M., Baglin, A., Lochard, J., & Conroy, L. (eds), *The CoRoT Mission Pre-Launch Status - Stellar Seismology and Planet Finding*. ESA Special Publication, vol. 1306.

Balona, L. A. 1992. Photometric monitoring of O-type stars. *MNRAS*, **254**(Feb.), 403–412.

Balona, L. A. 2010. *Challenges In Stellar Pulsation*.

Balona, L. A. 2016. Rotational modulation in B stars observed by the Kepler K2 mission. *MNRAS*, **457**(Apr.), 3724–3731.

Bastian, N., Covey, K. R., & Meyer, M. R. 2010. A Universal Stellar Initial Mass Function? A Critical Look at Variations. *ARA&A*, **48**(Sept.), 339–389.

Beals, C. S. 1953. The Spectra of the P Cygni Stars. *Publications of the Dominion Astrophysical Observatory Victoria*, **9**, 1.

Béky, B., Holman, M. J., Kipping, D. M., & Noyes, R. W. 2014. Stellar Rotation-Planetary Orbit Period Commensurability in the HAT-P-11 System. *ApJ*, **788**(June), 1.

Berdyugina, S. V. 2005. Starspots: A Key to the Stellar Dynamo. *Living Reviews in Solar Physics*, **2**(Dec.), 8.

Berghoefer, T. W., Baade, D., Schmitt, J. H. M. M., *et al.* 1996. Correlated variability in the X-ray and Hα emission from the O4If supergiant ζ Puppis. *A&A*, **306**(Feb.), 899.

Bernhard, K., Hümmerich, S., Otero, S., & Paunzen, E. 2015a. A search for photometric variability in magnetic chemically peculiar stars using ASAS-3 data. *A&A*, **581**(Sept.), A138.

Bernhard, K., Hümmerich, S., & Paunzen, E. 2015b. Magnetic, chemically peculiar (CP2) stars in the SuperWASP survey. *Astronomische Nachrichten*, **336**(Dec.), 981.

Blomme, R., van de Steene, G. C., Prinja, R. K., Runacres, M. C., & Clark, J. S. 2003. Radio and submillimetre observations of wind structure in zeta Puppis. *A&A*, **408**(Sept.), 715–727.

Blomme, R., Mahy, L., Catala, C., *et al.* 2011. Variability in the CoRoT photometry of three hot O-type stars. HD 46223, HD 46150, and HD 46966. *A&A*, **533**(Sept.), A4.

Borucki, W. J., Koch, D., Basri, G., *et al.* 2010. Kepler Planet-Detection Mission: Introduction and First Results. *Science*, **327**(Feb.), 977.

Bouret, J.-C., Hillier, D. J., Lanz, T., & Fullerton, A. W. 2012. Properties of Galactic early-type O-supergiants. A combined FUV-UV and optical analysis. *A&A*, **544**(Aug.), A67.

Boyajian, T. S., von Braun, K., van Belle, G., *et al.* 2013. Stellar Diameters and Temperatures. III. Main-sequence A, F, G, and K Stars: Additional High-precision Measurements and Empirical Relations. *ApJ*, **771**(July), 40.

Breger, M., Stich, J., Garrido, R., *et al.* 1993. Nonradial Pulsation of the Delta-Scuti Star Bu-Cancri in the Praesepe Cluster. *A&A*, **271**(Apr.), 482.

Breger, M., Handler, G., Garrido, R., *et al.* 1999. 30+ frequencies for the delta Scuti variable 4 Canum Venaticorum: results of the 1996 multisite campaign. *A&A*, **349**(Sept.), 225–235.

Briquet, M., Morel, T., Thoul, A., *et al.* 2007. An asteroseismic study of the β Cephei star θ Ophiuchi: constraints on global stellar parameters and core overshooting. *MNRAS*, **381**(Nov.), 1482–1488.

Briquet, M., Aerts, C., Baglin, A., *et al.* 2011. An asteroseismic study of the O9V star HD 46202 from CoRoT space-based photometry. *A&A*, **527**(Mar.), A112.

Broiles, T. W., Desai, M. I., & McComas, D. J. 2012. Formation, shape, and evolution of magnetic structures in CIRs at 1 AU. *Journal of Geophysical Research (Space Physics)*, **117**(Mar.), A03102.

Bromm, V., & Larson, R. B. 2004. The First Stars. *ARA&A*, **42**(Sept.), 79–118.

Bruntt, H. 2007. Asteroseismology with the WIRE satellite. *Communications in Asteroseismology*, **150**(June), 326.

Bruntt, H., Kurtz, D. W., Cunha, M. S., *et al.* 2009. Asteroseismic analysis of the roAp star α Circini: 84d of high-precision photometry from the WIRE satellite. *MNRAS*, **396**(June), 1189–1201.

Bumba, V. 1963. Development of SPOT group areas in dependence on the local magnetic field. *Bulletin of the Astronomical Institutes of Czechoslovakia*, **14**, 91.

Buysschaert, B., Aerts, C., Bloemen, S., *et al.* 2015. Kepler's first view of O-star variability: K2 data of five O stars in Campaign 0 as a proof of concept for O-star asteroseismology. *MNRAS*, **453**(Oct.), 89–100.

Buysschaert, B., Neiner, C., Richardson, N. D., *et al.* 2017. Studying the photometric and spectroscopic variability of the magnetic hot supergiant ζ Orionis Aa. *A&A*, **602**(June), A91.

Buzasi, D., Catanzarite, J., Laher, R., *et al.* 2000. The Detection of Multimodal Oscillations on α Ursae Majoris. *ApJ*, **532**(Apr.), L133–L136.

Buzasi, D. L. 2000 (Apr.). Experiment Design and Data Reduction for Seismology: Lessons Learned from WIRE. *Page 9 of:* Teixeira, T., & Bedding, T. (eds), *The Third MONS Workshop: Science Preparation and Target Selection*.

Cantiello, M. 2009 (Nov.). *Observational consequences of unstable stellar interiors*. Ph.D. thesis, Utrecht University.

Cantiello, M., & Braithwaite, J. 2011. Magnetic spots on hot massive stars. *A&A*, **534**(Oct.), A140.

Cantiello, M., Langer, N., Brott, I., *et al.* 2009a. On the origin of microturbulence in hot stars. *Communications in Asteroseismology*, **158**(July), 61.

Cantiello, M., Langer, N., Brott, I., *et al.* 2009b. Sub-surface convection zones in hot massive stars and their observable consequences. *A&A*, **499**(May), 279–290.

Carovillano, R. L., & Siscoe, G. L. 1969. Corotating Structure in the Solar Wind. *Sol. Phys.*, **8**(Aug.), 401–414.

Chené, A.-N., Moffat, A. F. J., Cameron, C., *et al.* 2011. WR 110: A Single Wolf-Rayet Star with Corotating Interaction Regions in its Wind? *ApJ*, **735**(July), 34.

Clarke, D. 2003. Period determinations of spotted stars. *A&A*, **407**(Sept.), 1029–1037.

Conti, P. S. 2002. Definitions, summary, and some issues [JD3: Massive star birth]. *Highlights of Astronomy*, **12**, 179–181.

Conti, P. S., Garmany, C. D., & Hutchings, J. B. 1977. Radial velocities of three Of stars - HD 148937, HD 151804, and HD 152408. *ApJ*, **215**(July), 561–567.

Cox, A. N., Morgan, S. M., Rogers, F. J., & Iglesias, C. A. 1992. An opacity mechanism for the pulsations of OB stars. *ApJ*, **393**(July), 272–277.

Cox, J. P. 1980. *Theory of stellar pulsation.*

Craig, I. J. D., & Brown, J. C. 1986. *Inverse problems in astronomy: A guide to inversion strategies for remotely sensed data.*

Cranmer, S. R., & Owocki, S. P. 1996. Hydrodynamical Simulations of Corotating Interaction Regions and Discrete Absorption Components in Rotating O-Star Winds. *ApJ*, **462**(May), 469.

Crooker, N. U., Gosling, J. T., Bothmer, V., *et al.* 1999. CIR Morphology, Turbulence, Discontinuities, and Energetic Particles. *Space Sci. Rev.*, **89**(July), 179–220.

Crowther, P. A. 2007. Physical Properties of Wolf-Rayet Stars. *ARA&A*, **45**(Sept.), 177–219.

Crowther, P. A., & Evans, C. J. 2009. A FEROS spectroscopic study of the extreme O supergiant He 3-759. *A&A*, **503**(Sept.), 985–990.

Davenport, J. R. A., Hebb, L., & Hawley, S. L. 2015. Detecting Differential Rotation and Starspot Evolution on the M Dwarf GJ 1243 with Kepler. *ApJ*, **806**(June), 212.

Davey, W. R. 1973. A Linear Nonadiabatic Analysis of Radial Oscillations in Models for Beta Cephei Stars. *ApJ*, **179**(Jan.), 235–240.

David-Uraz, A., Wade, G. A., Petit, V., *et al.* 2014. Investigating the origin of cyclical wind variability in hot, massive stars - I. On the dipolar magnetic field hypothesis. *MNRAS*, **444**(Oct.), 429–442.

David-Uraz, A., Owocki, S. P., Wade, G. A., Sundqvist, J. O., & Kee, N. D. 2017. Investigating the origin of cyclical wind variability in hot massive stars - II. Hydrodynamical simulations of corotating interaction regions using realistic spot parameters for the O giant ξ Persei. *MNRAS*, **470**(Sept.), 3672–3684.

Davies, B., Vink, J. S., & Oudmaijer, R. D. 2007. Modelling the clumping-induced polarimetric variability of hot star winds. *A&A*, **469**(July), 1045–1056.

Davis, J., Morton, D. C., Allen, L. R., & Hanbury Brown, R. 1970. The angular diameter and effective temperature of Zeta Puppis. *MNRAS*, **150**, 45–53.

De Cat, P., & Aerts, C. 2002. A study of bright southern slowly pulsating B stars. II. The intrinsic frequencies. *A&A*, **393**(Oct.), 965–981.

De Cat, P., Briquet, M., Aerts, C., *et al.* 2007. Long term photometric monitoring with the Mercator telescope. Frequencies and mode identification of variable O-B stars. *A&A*, **463**(Feb.), 243–249.

de Jager, C. 1998. The yellow hypergiants. *A&ARv*, **8**, 145–180.

de Jager, C., & Nieuwenhuijzen, H. 1997. An obstacle to the late evolution of massive stars. *MNRAS*, **290**(Sept.), L50–L54.

de Jong, J. A., Henrichs, H. F., Schrijvers, C., *et al.* 1999. Non-radial pulsations in the O stars XI Persei and lambda Cephei. *A&A*, **345**(May), 172–180.

de Jong, J. A., Henrichs, H. F., Kaper, L., *et al.* 2001. A search for the cause of cyclical wind variability in O stars. Simultaneous UV and optical observations including magnetic field measurements of the O7.5III star <ASTROBJ>xi Persei</ASTROBJ>. *A&A*, **368**(Mar.), 601–621.

Degroote, P., Aerts, C., Samadi, R., *et al.* 2010a. Asteroseismology of OB stars with CoRoT. *Astronomische Nachrichten*, **331**(Dec.), 1065.

Degroote, P., Briquet, M., Auvergne, M., *et al.* 2010b. Detection of frequency spacings in the young O-type binary HD 46149 from CoRoT photometry. *A&A*, **519**(Sept.), A38.

Degroote, P., Acke, B., Samadi, R., *et al.* 2011. CoRoT's view on variable B8/9 stars: spots versus pulsations. Evidence for differential rotation in HD 174648. *A&A*, **536**(Dec.), A82.

Dessart, L., & Chesneau, O. 2002. Interferometric and spectroscopic monitoring of emission lines. Detection of CIRs in hot star winds. *A&A*, **395**(Nov.), 209–221.

Dessart, L., & Owocki, S. P. 2003. Two-dimensional simulations of the line-driven instability in hot-star winds. *A&A*, **406**(July), L1–L4.

Donati, J.-F., & Collier Cameron, A. 1997. Differential rotation and magnetic polarity patterns on AB Doradus. *MNRAS*, **291**(Oct.), 1–19.

Dong, Dong, & McAvoy, T. J. 1994 (June). Nonlinear principal component analysis-based on principal curves and neural networks. *Pages 1284–1288 vol.2 of: American Control Conference, 1994*, vol. 2.

Drout, M. R., Piro, A. L., Shappee, B. J., *et al.* 2017. Light curves of the neutron star merger GW170817/SSS17a: Implications for r-process nucleosynthesis. *Science*, **358**(Dec.), 1570–1574.

Dupret, M.-A., Thoul, A., Scuflaire, R., *et al.* 2004. Asteroseismology of the β Cep star HD 129929. II. Seismic constraints on core overshooting, internal rotation and stellar parameters. *A&A*, **415**(Feb.), 251–257.

Dziembowski, W. A., & Pamyatnykh, A. A. 1993. The opacity mechanism in B-type stars. I - Unstable modes in Beta Cephei star models. *MNRAS*, **262**(May), 204–212.

Dziembowski, W. A., Moskalik, P., & Pamyatnykh, A. A. 1993. The Opacity Mechanism in B-Type Stars - Part Two - Excitation of High-Order G-Modes in Main Sequence Stars. *MNRAS*, **265**(Dec.), 588.

Eddington, A. S. 1917. The pulsation theory of Cepheid variables. *The Observatory*, **40**(Aug.), 290–293.

Eddington, A. S. 1918. Stars, Gaseous, On the pulsations of a gaseous star. *MNRAS*, **79**(Nov.), 2–22.

Eddington, A. S. 1919. On the pulsations of a gaseous star. *MNRAS*, **79**(Jan.), 177–189.

Ekström, S., Georgy, C., Eggenberger, P., *et al.* 2012. Grids of stellar models with rotation. I. Models from 0.8 to 120 $M_?$ at solar metallicity (Z = 0.014). *A&A*, **537**(Jan.), A146.

Espinosa Lara, F., & Rieutord, M. 2013. Self-consistent 2D models of fast-rotating early-type stars. *A&A*, **552**(Apr.), A35.

Eversberg, T., Lépine, S., & Moffat, A. F. J. 1998. Outmoving Clumps in the Wind of the Hot O Supergiant ζ Puppis. *ApJ*, **494**(Feb.), 799–805.

Eyles, C. J., Simnett, G. M., Cooke, M. P., *et al.* 2003. The Solar Mass Ejection Imager (Smei). *Sol. Phys.*, **217**(Nov.), 319–347.

Feldmeier, A. 1995. Time-dependent structure and energy transfer in hot star winds. *A&A*, **299**(July), 523.

Ferraz-Mello, S. 1981. Estimation of Periods from Unequally Spaced Observations. *AJ*, **86**(Apr.), 619.

Fitch, W. S. 1981. L O,1,2, and 3 Pulsation Constants for Evolutionary Models of Delta-Scuti Stars. *ApJ*, **249**(Oct.), 218.

Fletcher, L., Dennis, B. R., Hudson, H. S., *et al.* 2011. An Observational Overview of Solar Flares. *Space Sci. Rev.*, **159**(Sept.), 19–106.

Foukal, P. V. 2004. *Solar Astrophysics, 2nd, Revised Edition.*

Fullerton, A. W., Gies, D. R., & Bolton, C. T. 1992. Propagating absorption enhancements in the wind of the extreme Of supergiant HD 151804. *ApJ*, **390**(May), 650–660.

Fullerton, A. W., Gies, D. R., & Bolton, C. T. 1996. Absorption Line Profile Variations among the O Stars. I. The Incidence of Variability. *ApJS*, **103**(Apr.), 475.

Fullerton, A. W., Massa, D. L., & Prinja, R. K. 2006. The Discordance of Mass-Loss Estimates for Galactic O-Type Stars. *ApJ*, **637**(Feb.), 1025–1039.

Gaia Collaboration. 2018. VizieR Online Data Catalog: Gaia DR2 (Gaia Collaboration, 2018). *VizieR Online Data Catalog*, **1345**.

Gal-Yam, A., & Leonard, D. C. 2009. A massive hypergiant star as the progenitor of the supernova SN 2005gl. *Nature*, **458**(Apr.), 865–867.

Gautschy, A., & Saio, H. 1993. On non-radial oscillations of B-type stars. *MNRAS*, **262**(May), 213–219.

Giannone, P. 1967. Sequences of Inhomogeneous Models for Helium-Burning Stars. *ZAP*, **65**, 226.

Gies, D. R., Williams, S. J., Matson, R. A., *et al.* 2012. A Search for Hierarchical Triples using Kepler Eclipse Timing. *AJ*, **143**(June), 137.

Glatzel, W. 2009. Nonlinear strange-mode pulsations. *Communications in Asteroseismology*, **158**(July), 252.

Glatzel, W., & Kiriakidis, M. 1993. Stability of Massive Stars and the Humphreys / Davidson Limit. *MNRAS*, **263**(July), 375.

Gnevyshev, M. N. 1938. On the Nature of Solar Activity. *Mitteilungen der Nikolai-Hauptsternwarte zu Pulkowo*, **16**, B36–B45.

Goldreich, P., & Keeley, D. A. 1977. Solar seismology. II - The stochastic excitation of the solar p-modes by turbulent convection. *ApJ*, **212**(Feb.), 243–251.

Gonczi, G., & Roddier, F. 1971. A Model of the Solar Photospheric Velocity Field. *A&A*, **11**(Mar.), 28.

Gontcharov, G. A. 2006. Pulkovo Compilation of Radial Velocities for 35 495 Hipparcos stars in a common system. *Astronomy Letters*, **32**(Nov.), 759–771.

Goodricke, J. 1786. A Series of Observations on, and a Discovery of, the Period of the Variation of the Light of the Star Marked δ by Bayer, Near the Head of Cepheus. In a Letter from John Goodricke, Esq. to Nevil Maskelyne, D. D. F. R. S. and Astronomer Royal. *Philosophical Transactions of the Royal Society of London Series I*, **76**, 48–61.

Gosling, J. T., & Pizzo, V. J. 1999. Formation and Evolution of Corotating Interaction Regions and their Three Dimensional Structure. *Space Sci. Rev.*, **89**(July), 21–52.

Grady, C. A., Snow, Jr., T. P., & Timothy, J. G. 1983. Observations of Of-star wind variability. *ApJ*, **271**(Aug.), 691–701.

Gray, D. F. 2005. *The Observation and Analysis of Stellar Photospheres*.

Hackman, T., Jetsu, L., & Tuominen, I. 2001. Surface imaging of <ASTROBJ>HD 199178</ASTROBJ> (<ASTROBJ>V1794 Cygni</ASTROBJ>). *A&A*, **374**(July), 171–181.

Hamann, W.-R., & Gräfener, G. 2003. A temperature correction method for expanding atmospheres. *A&A*, **410**(Nov.), 993–1000.

Hamann, W.-R., & Gräfener, G. 2004. Grids of model spectra for WN stars, ready for use. *A&A*, **427**(Nov.), 697–704.

Handler, G., Arentoft, T., Shobbrook, R. R., *et al.* 2000. Delta Scuti Network observations of XX Pyx: detection of 22 pulsation modes and of short-term amplitude and frequency variations. *MNRAS*, **318**(Oct.), 511–525.

Handler, G., Matthews, J. M., Eaton, J. A., *et al.* 2009. Asteroseismology of Hybrid Pulsators Made Possible: Simultaneous MOST Space Photometry and Ground-Based Spectroscopy of γ Peg. *ApJL*, **698**(June), L56–L59.

Harmon, R. O., & Crews, L. J. 2000. Imaging Stellar Surfaces via Matrix Light-Curve Inversion. *AJ*, **120**(Dec.), 3274–3294.

Harutyunyan, G., Strassmeier, K. G., Künstler, A., Carroll, T. A., & Weber, M. 2016. Anti-solar differential rotation on the active sub-giant HU Virginis. *A&A*, **592**(Aug.), A117.

Heger, A., Fryer, C. L., Woosley, S. E., Langer, N., & Hartmann, D. H. 2003. How Massive Single Stars End Their Life. *ApJ*, **591**(July), 288–300.

Henrichs, H. F. 1999. Pulsations in O stars. *Page 304 of:* Wolf, B., Stahl, O., & Fullerton, A. W. (eds), *IAU Colloq. 169: Variable and Non-spherical Stellar Winds in Luminous Hot Stars*. Lecture Notes in Physics, Berlin Springer Verlag, vol. 523.

Henrichs, H. F. 2012. Magnetism in Massive Stars. *Publications de l'Observatoire Astronomique de Beograd*, **91**(Dec.), 13–20.

Henrichs, H. F., Kaper, L., & Nichols, J. S. 1994. The extent of variability in the stellar wind of the O7.5 giant ξ Persei. *A&A*, **285**(May), 565–572.

Henrichs, H. F., de Jong, J. A., Verdugo, E., *et al.* 2013. Discovery of the magnetic field in the pulsating B star β Cephei. *A&A*, **555**(July), A46.

Henwood, R., Chapman, S. C., & Willis, D. M. 2010. Increasing Lifetime of Recurrent Sunspot Groups Within the Greenwich Photoheliographic Results. *Sol. Phys.*, **262**(Apr.), 299–313.

Hertzsprung, E. 1911. Ueber die Verwendung photographischer effektiver Wellenlaengen zur Bestimmung von Farbenaequivalenten. *Publikationen des Astrophysikalischen Observatoriums zu Potsdam*, **63**.

Hervé, A., Rauw, G., & Nazé, Y. 2013. A detailed X-ray investigation of ζ Puppis. III. Spectral analysis of the whole RGS spectrum. *A&A*, **551**(Mar.), A83.

Hillier, D. J., Bouret, J.-C., Lanz, T., & Busche, J. R. 2012. The influence of rotation on optical emission profiles of O stars. *MNRAS*, **426**(Oct.), 1043–1049.

Houdek, G. 2006 (Oct.). Stochastic excitation and damping of solar-like oscillations. *Page 28 of: Proceedings of SOHO 18/GONG 2006/HELAS I, Beyond the spherical Sun*. ESA Special Publication, vol. 624.

Howarth, I. D. 1992a. Discrete absorption components in O-type stars. *Page 131 of:* Heber, U., & Jeffery, C. S. (eds), *The Atmospheres of Early-Type Stars*. Lecture Notes in Physics, Berlin Springer Verlag, vol. 401.

Howarth, I. D. 1992b. Intrinsic Stellar-Wind Variability (Invited Paper). *Page 155 of:* Drissen, L., Leitherer, C., & Nota, A. (eds), *Nonisotropic and Variable Outflows from Stars*. Astronomical Society of the Pacific Conference Series, vol. 22.

Howarth, I. D., & Prinja, R. K. 1989. The stellar winds of 203 Galactic O stars - A quantitative ultraviolet survey. *ApJS*, **69**(Mar.), 527–592.

Howarth, I. D., & Stevens, I. R. 2014. Time-series photometry of the O4 I(n)fp star ζ Puppis. *MNRAS*, **445**(Dec.), 2878–2883.

Howarth, I. D., Prinja, R. K., & Massa, D. 1995. The IUE MEGA Campaign: The Rotationally Modulated Wind of zeta Puppis. *ApJ*, **452**(Oct.), L65.

Howarth, I. D., Siebert, K. W., Hussain, G. A. J., & Prinja, R. K. 1997. Cross-correlation characteristics of OB stars from IUE spectroscopy. *MNRAS*, **284**(Jan.), 265–285.

Howarth, I. D., Goss, K. J. F., Stevens, I. R., Chaplin, W. J., & Elsworth, Y. 2014. Amplitude variability in satellite photometry of the non-radially pulsating O9.5 V star ζ Oph. *MNRAS*, **440**(May), 1674–1679.

Howell, S. B., Sobeck, C., Haas, M., *et al.* 2014. The K2 Mission: Characterization and Early Results. *PASP*, **126**(Apr.), 398.

Hubrig, S., Kholtygin, A., Ilyin, I., Schöller, M., & Oskinova, L. M. 2016. The First Spectropolarimetric Monitoring of the Peculiar O4 Ief Supergiant ζ Puppis. *ApJ*, **822**(May), 104.

Humphreys, R. M. 1978. Studies of luminous stars in nearby galaxies. I. Supergiants and O stars in the Milky Way. *ApJS*, **38**(Dec.), 309–350.

Humphreys, R. M., & Davidson, K. 1979. Studies of luminous stars in nearby galaxies. III - Comments on the evolution of the most massive stars in the Milky Way and the Large Magellanic Cloud. *ApJ*, **232**(Sept.), 409–420.

Hundhausen, A. J. 1972. Interplanetary Shock Waves and the Structure of Solar Wind Disturbances. *NASA Special Publication*, **308**, 393.

Iglesias, C. A., Rogers, F. J., & Wilson, B. G. 1992. Spin-orbit interaction effects on the Rosseland mean opacity. *ApJ*, **397**(Oct.), 717–728.

Ignace, R., & Gayley, K. G. 2003. The Zeeman effect in the Sobolev approximation: applications to spherical stellar winds. *MNRAS*, **341**(May), 179–191.

Ignace, R., & Hendry, M. A. 2000. Analytic Inversion of Emission Lines of Arbitrary Optical Depth for the Structure of Supernova Ejecta. *ApJ*, **537**(July), L131–L134.

Ignace, R., Hubrig, S., & Schöller, M. 2009. Spectropolarimetric Variability and Corotating Structure in HD 92207. *AJ*, **137**(Feb.), 3339–3344.

Ignace, R., St-Louis, N., & Proulx-Giraldeau, F. 2015. Polarimetric modeling of corotating interaction regions threading massive-star winds. *A&A*, **575**(Mar.), A129.

Israelian, G., & de Groot, M. 1999. P Cygni: An Extraordinary Luminous Blue Variable. *SSR*, **90**(Oct.), 493–522.

Israelian, G., Rebolo, R., Basri, G., Casares, J., & Martín, E. L. 1999. Evidence of a supernova origin for the black hole in the system GRO J1655 - 40. *Nature*, **401**(Sept.), 142–144.

Kallinger, T., Weiss, W. W., Barban, C., *et al.* 2010. Oscillating red giants in the CoRoT exofield: asteroseismic mass and radius determination. *A&A*, **509**(Jan.), A77.

Kaper, L., & Henrichs, H. F. 1994. Wind variability in O-type stars: On the behavior and origin of DACs. *Ap&SS*, **221**(Nov.), 115–133.

Kaper, L., Henrichs, H. F., Nichols, J. S., *et al.* 1996. Long- and short-term variability in O-star winds. I. Time series of UV spectra for 10 bright O stars. *A&AS*, **116**(Apr.), 257–287.

Kaper, L., Henrichs, H. F., Nichols, J. S., & Telting, J. H. 1999. Long- and short-term variability in O-star winds. II. Quantitative analysis of DAC behaviour. *A&A*, **344**(Apr.), 231–262.

Kasen, D., Metzger, B., Barnes, J., Quataert, E., & Ramirez-Ruiz, E. 2017. Origin of the heavy elements in binary neutron-star mergers from a gravitational-wave event. *Nature*, **551**(Nov.), 80–84.

Kippenhahn, R., & Weigert, A. 1990. *Stellar Structure and Evolution*.

Kipping, D. M. 2012. An analytic model for rotational modulations in the photometry of spotted stars. *MNRAS*, **427**(Dec.), 2487–2511.

Kiriakidis, M., Fricke, K. J., & Glatzel, W. 1993. The Stability of Massive Stars and its Dependence on Metallicity and Opacity. *MNRAS*, **264**(Sept.), 50.

Kjeldsen, H., & Bedding, T. R. 1995. Amplitudes of stellar oscillations: the implications for asteroseismology. *A&A*, **293**(Jan.), 87–106.

Kochanek, C. S., Szczygieł, D. M., & Stanek, K. Z. 2012. Unmasking the Supernova Impostors. *ApJ*, **758**(Oct.), 142.

Kochukhov, O., & Sudnik, N. 2013. Detectability of small-scale magnetic fields in early-type stars. *A&A*, **554**(June), A93.

Kolbin, A. I., & Shimansky, V. V. 2014. Spotted star light curve numerical modeling technique and its application to HII 1883 surface imaging. *Astrophysical Bulletin*, **69**(Apr.), 179–190.

Kolbin, A. I., Shimansky, V. V., & Sakhibullin, N. A. 2013. On the reconstruction of the surface structure of the spotted stars. *Astronomy Reports*, **57**(July), 548–561.

Kolbin, A. I., Sakhibullin, N. A., & Gabdeev, M. M. 2015. Multipassband photometric mapping of three fast rotating stars: HII 1883, AP 86 and AP 226. *Advances in Space Research*, **55**(Feb.), 808–816.

Kovári, Z., Strassmeier, K. G., Granzer, T., *et al.* 2004. Doppler imaging of stellar surface structure. XXII. Time-series mapping of the young rapid rotator LQ Hydrae. *A&A*, **417**(Apr.), 1047–1054.

Kramer, Mark A. 1991. Nonlinear principal component analysis using autoassociative neural networks. *AIChE Journal*, **37**(2), 233–243.

Kroupa, P. 2001. On the variation of the initial mass function. *MNRAS*, **322**(Apr.), 231–246.

Krtička, J., Mikulášek, Z., Zverko, J., & Žižňovský, J. 2007. The light variability of the helium strong star HD 37776 as a result of its inhomogeneous elemental surface distribution. *A&A*, **470**(Aug.), 1089–1098.

Kumar, P., Talon, S., & Zahn, J.-P. 1999. Angular Momentum Redistribution by Waves in the Sun. *ApJ*, **520**(Aug.), 859–870.

Kuschnig, R., Weiss, W. W., Gruber, R., Bely, P. Y., & Jenkner, H. 1997. Microvariability survey with the Hubble Space Telescope Fine Guidance Sensors. Exploring the instrumental properties. *A&A*, **328**(Dec.), 544–550.

Lamb, H. 1909. On the theory of waves propagated vertically in the atmosphere. *Proc. London Math. Soc.*, **7**(Jan.), 122–141.

Lamers, H. J. G. L. M. 1997. The Atmospheres of LBVs near the Eddington Limit. *Page 76 of:* Nota, A., & Lamers, H. (eds), *Luminous Blue Variables: Massive Stars in Transition*. Astronomical Society of the Pacific Conference Series, vol. 120.

Lamers, H. J. G. L. M., & Cassinelli, J. P. 1999. *Introduction to Stellar Winds*.

Lamers, H. J. G. L. M., & Fitzpatrick, E. L. 1988. The relationship between the Eddington limit, the observed upper luminosity limit for massive stars, and the luminous blue variables. *ApJ*, **324**(Jan.), 279–287.

Lamers, H. J. G. L. M., Cerruti-Sola, M., & Perinotto, M. 1987. The 'SEI' method for accurate and efficient calculations of line profiles in spherically symmetric stellar winds. *ApJ*, **314**(Mar.), 726–738.

Lamers, H. J. G. L. M., Maeder, A., Schmutz, W., & Cassinelli, J. P. 1991. Wolf-Rayet stars as starting points or as endpoints of the evolution of massive stars? *ApJ*, **368**(Feb.), 538–544.

Lamers, H. J. G. L. M., Bastiaanse, M. V., Aerts, C., & Spoon, H. W. W. 1998. Periods, period changes and the nature of the microvariations of Luminous Blue Variables. *A&A*, **335**(July), 605–621.

Langer, N., García-Segura, G., & Mac Low, M.-M. 1999. Giant Outbursts of Luminous Blue Variables and the Formation of the Homunculus Nebula around eta Carinae. *ApJL*, **520**(July), L49–L53.

Lanza, A. F., Rodonò, M., Pagano, I., Barge, P., & Llebaria, A. 2003. Modelling the rotational modulation of the Sun as a star. *A&A*, **403**(June), 1135–1149.

Ledoux, P. 1951. The Nonradial Oscillations of Gaseous Stars and the Problem of Beta Canis Majoris. *ApJ*, **114**(Nov.), 373.

Leighton, R. B. 1964. Transport of Magnetic Fields on the Sun. *ApJ*, **140**(Nov.), 1547.

Lenz, P., & Breger, M. 2005. Period04 User Guide. *Communications in Asteroseismology*, **146**(June), 53–136.

Lepine, S. 1994. Wavelet analysis of Wolf-Rayet emission line variability: Evidence for clumping. *Ap&SS*, **221**(Nov.), 371–382.

Lépine, S., & Moffat, A. F. J. 1999. Wind Inhomogeneities in Wolf-Rayet Stars. II. Investigation of Emission-Line Profile Variations. *ApJ*, **514**(Apr.), 909–931.

Lépine, S., & Moffat, A. F. J. 2008. Direct Spectroscopic Observations of Clumping in O-Star Winds. *AJ*, **136**(Aug.), 548–553.

Lépine, S., Moffat, A. F. J., & Henriksen, R. N. 1996. Wind Inhomogeneities in Wolf-Rayet Stars. I. Search for Scaling Laws Using Wavelet Transforms. *ApJ*, **466**(July), 392.

Lesh, J. R., & Aizenman, M. L. 1974. The pulsation properties of the beta Cephei stars. *A&A*, **34**(Aug.), 203–210.

Lindegren, L., Lammers, U., Hobbs, D., *et al.* 2012. The astrometric core solution for the Gaia mission. Overview of models, algorithms, and software implementation. *A&A*, **538**(Feb.), A78.

Lobel, A., Dupree, A. K., Stefanik, R. P., *et al.* 2003. High-Resolution Spectroscopy of the Yellow Hypergiant ρ Cassiopeiae from 1993 through the Outburst of 2000-2001. *ApJ*, **583**(Feb.), 923–954.

Loumos, G. L., & Deeming, T. J. 1978. Spurious results from Fourier analysis of data with closely spaced frequencies. *Ap&SS*, **56**(July), 285–291.

Lucy, L. B., & Solomon, P. M. 1970. Mass Loss by Hot Stars. *ApJ*, **159**(Mar.), 879.

Lucy, L. B., & White, R. L. 1980. X-ray emission from the winds of hot stars. *ApJ*, **241**(Oct.), 300–305.

Lüftinger, T., Fröhlich, H.-E., Weiss, W. W., *et al.* 2010. Surface structure of the CoRoT CP2 target star HD 50773. *A&A*, **509**(Jan.), A43.

MacGregor, K. B., Hartmann, L., & Raymond, J. C. 1979. Radiative amplification of sound waves in the winds of O and B stars. *ApJ*, **231**(July), 514–523.

Maeder, A., & Meynet, G. 1987. Grids of evolutionary models of massive stars with mass loss and overshooting - Properties of Wolf-Rayet stars sensitive to overshooting. *A&A*, **182**(Aug.), 243–263.

Mahy, L., Gosset, E., Baudin, F., *et al.* 2011. Plaskett's star: analysis of the CoRoT photometric data. *A&A*, **525**(Jan.), A101.

Maíz-Apellániz, J., Walborn, N. R., Galué, H. Á., & Wei, L. H. 2004. A Galactic O Star Catalog. *ApJS*, **151**(Mar.), 103–148.

Markova, N., & Puls, J. 2008. Bright OB stars in the Galaxy. IV. Stellar and wind parameters of early to late B supergiants. *A&A*, **478**(Feb.), 823–842.

Martín-Fleitas, J., Sahlmann, J., Mora, A., *et al.* 2014 (Aug.). Enabling Gaia observations of naked-eye stars. *Page 91430Y of: Space Telescopes and Instrumentation 2014: Optical, Infrared, and Millimeter Wave.* Proc. SPIE, vol. 9143.

Martins, F., Schaerer, D., & Hillier, D. J. 2005. A new calibration of stellar parameters of Galactic O stars. *A&A*, **436**(June), 1049–1065.

Massa, D., Fullerton, A. W., Nichols, J. S., *et al.* 1995a. The IUE MEGA Campaign: Wind Variability and Rotation in Early-Type Stars. *ApJ*, **452**(Oct.), L53.

Massa, D., Prinja, R. K., & Fullerton, A. W. 1995b. Wind Variability of B Supergiants. I. The Rapid Rotator HD 64760 (B0.5 Ib). *ApJ*, **452**(Oct.), 842.

Matthews, J. M., Kuschnig, R., Guenther, D. B., *et al.* 2004. No stellar p-mode oscillations in space-based photometry of Procyon. *Nature*, **430**(July), 51–53.

Mauerhan, J. C., Smith, N., Filippenko, A. V., *et al.* 2013. The unprecedented 2012 outburst of SN 2009ip: a luminous blue variable star becomes a true supernova. *MNRAS*, **430**(Apr.), 1801–1810.

Mazzali, P. A. 1990. The effect of stellar rotation on the properties of a radiatively driven stellar wind. *A&A*, **238**(Nov.), 191–206.

McComas, D. J., Barraclough, B. L., Funsten, H. O., *et al.* 2000. Solar wind observations over Ulysses' first full polar orbit. *J. Geophys. Res.*, **105**(May), 10419–10434.

McErlean, N. D., Lennon, D. J., & Dufton, P. L. 1998. Helium enhancements in luminous OB-type stars: the effect of microturbulence. *A&A*, **329**(Jan.), 613–623.

McQuillan, A., Aigrain, S., & Mazeh, T. 2013. Measuring the rotation period distribution of field M dwarfs with Kepler. *MNRAS*, **432**(June), 1203–1216.

Moffat, A. F. J. 1994. Turbulence in Outflows from Hot Stars. *Pages 51–72 of:* Klare, G. (ed), *Reviews in Modern Astronomy*. Reviews in Modern Astronomy, vol. 7.

Moffat, A. F. J., & Michaud, G. 1981. Zeta Puppis - an O-type oblique rotator. *ApJ*, **251**(Dec.), 133–138.

Moffat, A. F. J., & Robert, C. 1994. Clumping and mass loss in hot star winds. *ApJ*, **421**(Jan.), 310–313.

Moffat, A. F. J., Drissen, L., Lamontagne, R., & Robert, C. 1988. Spectroscopic evidence for rapid blob ejection in Wolf-Rayet stars. *ApJ*, **334**(Nov.), 1038–1043.

Moffat, A. F. J., Lepine, S., Henriksen, R. N., & Robert, C. 1994. First wavelet analysis of emission line variations in Wolf-Rayet stars. *Ap&SS*, **216**(June), 55–65.

Moffat, A. F. J., Marchenko, S. V., Seggewiss, W., *et al.* 1998. Wolf-Rayet stars and O-star runaways with HIPPARCOS. I. Kinematics. *A&A*, **331**(Mar.), 949–958.

Montgomery, M. H., & Odonoghue, D. 1999. A derivation of the errors for least squares fitting to time series data. *Delta Scuti Star Newsletter*, **13**(July), 28.

Moreno-Insertis, F., & Vazquez, M. 1988. A statistical study of the decay phase of sunspot groups from 1874 to 1939. *A&A*, **205**(Oct.), 289–296.

Morton, D. C. 1976. P Cygni profiles in zeta Ophiuchi and zeta Puppis. *ApJ*, **203**(Jan.), 386–398.

Moskalik, P., & Buchler, J. R. 1990. Resonances and period doubling in the pulsations of stellar models. *ApJ*, **355**(June), 590–601.

Moss, D. 1990. Time-dependent models for magnetic CP stars. V - The oblique rotator. *MNRAS*, **244**(May), 272–280.

Mullan, D. J. 1986. Displaced narrow absorption components in the spectra of mass-losing OB stars - Indications of corotating interaction regions? *A&A*, **165**(Sept.), 157–162.

Natale, G., Marconi, M., & Bono, G. 2008. Theoretical Fits of the δ Cephei Light, Radius, and Radial Velocity Curves. *ApJ*, **674**(Feb.), L93.

Nazé, Y., Oskinova, L. M., & Gosset, E. 2013. A Detailed X-Ray Investigation of ζ Puppis. II. The Variability on Short and Long Timescales. *ApJ*, **763**(Feb.), 143.

Oskinova, L. M., Todt, H., Ignace, R., *et al.* 2011. Early magnetic B-type stars: X-ray emission and wind properties. *MNRAS*, **416**(Sept.), 1456–1474.

Oudmaijer, R. D., Davies, B., de Wit, W.-J., & Patel, M. 2009 (Sept.). Post-Red Supergiants. *Page 17 of:* Luttermoser, D. G., Smith, B. J., & Stencel, R. E. (eds), *The Biggest, Baddest, Coolest Stars*. Astronomical Society of the Pacific Conference Series, vol. 412.

Owocki, S. P., & Rybicki, G. B. 1984. Instabilities in line-driven stellar winds. I - Dependence on perturbation wavelength. *ApJ*, **284**(Sept.), 337–350.

Owocki, S. P., Castor, J. I., & Rybicki, G. B. 1988. Time-dependent models of radiatively driven stellar winds. I - Nonlinear evolution of instabilities for a pure absorption model. *ApJ*, **335**(Dec.), 914–930.

Pablo, H., Richardson, N. D., Moffat, A. F. J., *et al.* 2015. A Coordinated X-Ray and Optical Campaign of the Nearest Massive Eclipsing Binary, δ Orionis Aa. III. Analysis of Optical Photometric (MOST) and Spectroscopic (Ground-based) Variations. *ApJ*, **809**(Aug.), 134.

Pablo, H., Whittaker, G. N., Popowicz, A., *et al.* 2016. The BRITE Constellation Nanosatellite Mission: Testing, Commissioning, and Operations. *PASP*, **128**(12), 125001.

Pablo, H., Richardson, N. D., Fuller, J., *et al.* 2017. The most massive heartbeat: an in-depth analysis of ι Orionis. *MNRAS*, **467**(May), 2494–2503.

Pamyatnykh, A. A. 1999. Pulsational Instability Domains in the Upper Main Sequence. *Acta Astron.*, **49**(June), 119–148.

Pauldrach, A. W. A., Vanbeveren, D., & Hoffmann, T. L. 2012. Radiation-driven winds of hot luminous stars XVI. Expanding atmospheres of massive and very massive stars and the evolution of dense stellar clusters. *A&A*, **538**(Feb.), A75.

Penny, L. R. 1996. Projected Rotational Velocities of O-Type Stars. *ApJ*, **463**(June), 737.

Petit, P., Donati, J.-F., Oliveira, J. M., *et al.* 2004. Photospheric magnetic field and surface differential rotation of the FK Com star HD 199178. *MNRAS*, **351**(July), 826–844.

Petrenz, P., & Puls, J. 1996. Hα line formation in hot star winds: the influence of rotation. *A&A*, **312**(Aug.), 195–220.

Petrovay, K., & van Driel-Gesztelyi, L. 1997. Making Sense of Sunspot Decay. I. Parabolic Decay Law and Gnevyshev-Waldmeier Relation. *Sol. Phys.*, **176**(Dec.), 249–266.

Pigott, E. 1785. Observations of a New Variable Star. In a Letter from Edward Pigott, Esq. to Sir H. C. Englefield, Bart. F. R. S. and A. S. *Philosophical Transactions of the Royal Society of London Series I*, **75**, 127–136.

Pigulski, A., & Pojmański, G. 2008. β Cephei stars in the ASAS-3 data. II. 103 new β Cephei stars and a discussion of low-frequency modes. *A&A*, **477**(Jan.), 917–929.

Pigulski, A., Cugier, H., Popowicz, A., *et al.* 2016. Massive pulsating stars observed by BRITE-Constellation. I. The triple system β Centauri (Agena). *A&A*, **588**(Apr.), A55.

Pizzo, V. 1978. A three-dimensional model of corotating streams in the solar wind. I - Theoretical foundations. *J. Geophys. Res.*, **83**(Dec.), 5563–5572.

Pollard, K. R., Cottrell, P. L., Kilmartin, P. M., & Gilmore, A. C. 1996. RV Tauri stars. I. A long-term photometric survey. *MNRAS*, **279**(Apr.), 949–977.

Popowicz, A. 2016 (July). Image processing in the BRITE nano-satellite mission. *Page 99041R of: Space Telescopes and Instrumentation 2016: Optical, Infrared, and Millimeter Wave*. Proc. SPIE, vol. 9904.

Popowicz, A., Pigulski, A., Bernacki, K., *et al.* 2017. BRITE Constellation: data processing and photometry. *A&A*, **605**(Sept.), A26.

Press, William H., Teukolsky, Saul A., Vetterling, William T., & Flannery, Brian P. 2007. *Numerical Recipes 3rd Edition: The Art of Scientific Computing*. 3 edn. New York, NY, USA: Cambridge University Press.

Prinja, R. K. 1988. Evidence for rotationally modulated variability in O star winds. *MNRAS*, **231**(Mar.), 21P–24P.

Prinja, R. K., Howarth, I. D., & Henrichs, H. F. 1987. Ultraviolet observations of extensive variability in the stellar wind of XI Persei. *ApJ*, **317**(June), 389–411.

Prinja, R. K., Barlow, M. J., & Howarth, I. D. 1990. Terminal velocities for a large sample of O stars, B supergiants, and Wolf-Rayet stars. *ApJ*, **361**(Oct.), 607–620.

Prinja, R. K., Balona, L. A., Bolton, C. T., *et al.* 1992. Time series observations of O stars. I - IUE observations of variability in the stellar wind of Zeta Puppis. *ApJ*, **390**(May), 266–272.

Prinja, R. K., Massa, D., & Fullerton, A. W. 1995. The IUE MEGA Campaign: Modulated Structure in the Wind of HD 64760 (B0.5 Ib). *ApJ*, **452**(Oct.), L61.

Prinja, R. K., Fullerton, A. W., & Crowther, P. A. 1996. Variability in the optical wind lines of HD 151804 (O8 Iaf). *A&A*, **311**(July), 264–272.

Puls, J., Markova, N., Scuderi, S., *et al.* 2006. Bright OB stars in the Galaxy. III. Constraints on the radial stratification of the clumping factor in hot star winds from a combined $H_?$, IR and radio analysis. *A&A*, **454**(Aug.), 625–651.

Puls, J., Vink, J. S., & Najarro, F. 2008. Mass loss from hot massive stars. *A&ARv*, **16**(Dec.), 209–325.

Ramiaramanantsoa, T., Moffat, A. F. J., Chené, A.-N., *et al.* 2014. MOST detects corotating bright spots on the mid-O-type giant ξ Persei. *MNRAS*, **441**(June), 910–917.

Ramiaramanantsoa, T., Moffat, A. F. J., Harmon, R., *et al.* 2018. BRITE-Constellation high-precision time-dependent photometry of the early O-type supergiant ζ Puppis unveils the photospheric drivers of its small- and large-scale wind structures. *MNRAS*, **473**(Feb.), 5532–5569.

Rauw, G., De Becker, M., van Winckel, H., *et al.* 2008. Spectroscopic and photometric variability of the O9.5 Vp star HD 93521. *A&A*, **487**(Aug.), 659–670.

Reegen, P., Kallinger, T., Frast, D., *et al.* 2006. Reduction of time-resolved space-based CCD photometry developed for MOST Fabry Imaging data*. *MNRAS*, **367**(Apr.), 1417–1431.

Reeve, D. C., & Howarth, I. D. 2016. Limb-darkening coefficients from line-blanketed non-LTE hot-star model atmospheres. *MNRAS*, **456**(Feb.), 1294–1298.

Reid, A. H. N., & Howarth, I. D. 1996. Optical time-series spectroscopy of the O4 supergiant ζ Puppis. *A&A*, **311**(July), 616–630.

Repolust, T., Puls, J., & Herrero, A. 2004. Stellar and wind parameters of Galactic O-stars. The influence of line-blocking/blanketing. *A&A*, **415**(Feb.), 349–376.

Richardson, N. D., Pablo, H., Sterken, C., *et al.* 2018. BRITE-Constellation reveals evidence for pulsations in the enigmatic binary η Carinae. *MNRAS*, **475**(Apr.), 5417–5423.

Ringnes, T. S. 1964. On the lifetime of sunspot groups. *Astrophysica Norvegica*, **9**, 95.

Rivinius, T., Baade, D., & Štefl, S. 2003. Non-radially pulsating Be stars. *A&A*, **411**(Nov.), 229–247.

Roberts, D. H., Lehar, J., & Dreher, J. W. 1987. Time Series Analysis with Clean - Part One - Derivation of a Spectrum. *AJ*, **93**(Apr.), 968.

Roettenbacher, R. M., Harmon, R. O., Vutisalchavakul, N., & Henry, G. W. 2011. A Study of Differential Rotation on II Pegasi via Photometric Starspot Imaging. *AJ*, **141**(Apr.), 138.

Roettenbacher, R. M., Monnier, J. D., Harmon, R. O., Barclay, T., & Still, M. 2013. Imaging Starspot Evolution on Kepler Target KIC 5110407 Using Light-Curve Inversion. *ApJ*, **767**(Apr.), 60.

Roettenbacher, R. M., Kane, S. R., Monnier, J. D., & Harmon, R. O. 2016. KOI-1003: A New Spotted, Eclipsing RS CVn Binary in the Kepler Field. *ApJ*, **832**(Dec.), 207.

Rogers, T. M., & MacGregor, K. B. 2011. On the interaction of internal gravity waves with a magnetic field - II. Convective forcing. *MNRAS*, **410**(Jan.), 946–962.

Rogers, T. M., Lin, D. N. C., McElwaine, J. N., & Lau, H. H. B. 2013. Internal Gravity Waves in Massive Stars: Angular Momentum Transport. *ApJ*, **772**(July), 21.

Russell, H. N. 1913. "Giant" and "dwarf" stars. *The Observatory*, **36**(Aug.), 324–329.

Rybicki, G. B., & Hummer, D. G. 1983. The specific luminosity of a three-dimensional medium in terms of the escape probability. *ApJ*, **274**(Nov.), 380–398.

Saio, H. 2009. Strange modes. *Communications in Asteroseismology*, **158**(July), 245.

Saio, H. 2011. Linear analyses for the stability of radial and non-radial oscillations of massive stars. *MNRAS*, **412**(Apr.), 1814–1822.

Saio, H., Kambe, E., & Lee, U. 2000. Nonradial Pulsations in ϵ Persei. *ApJ*, **543**(Nov.), 359–367.

Saio, H., Kuschnig, R., Gautschy, A., *et al.* 2006. MOST Detects g- and p-Modes in the B Supergiant HD 163899 (B2 Ib/II). *ApJ*, **650**(Oct.), 1111–1118.

Saio, H., Georgy, C., & Meynet, G. 2013 (Dec.). Strange-Mode Instability for Micro-Variations in Luminous Blue Variables. *Page 47 of:* Shibahashi, H., & Lynas-Gray, A. E. (eds), *Progress in Physics of the Sun and Stars: A New Era in Helio- and Asteroseismology*. Astronomical Society of the Pacific Conference Series, vol. 479.

Salpeter, E. E. 1955. The Luminosity Function and Stellar Evolution. *ApJ*, **121**(Jan.), 161.

Sander, A., Shenar, T., Hainich, R., *et al.* 2015. On the consistent treatment of the quasi-hydrostatic layers in hot star atmospheres. *A&A*, **577**(May), A13.

Scholz, Matthias. 2012. Validation of Nonlinear PCA. *Neural Processing Letters*, **36**(1), 21–30.

Schumann, J. D., & Seggewiss, W. 1975. Variations of the C III 5696 A emission line in Wolf-Rayet stars. *Pages 299–302 of:* Sherwood, V. E., & Plaut, L. (eds), *Variable Stars and Stellar Evolution*. IAU Symposium, vol. 67.

Shenar, T., Oskinova, L., Hamann, W.-R., *et al.* 2015. A Coordinated X-Ray and Optical Campaign of the Nearest Massive Eclipsing Binary, δ Orionis Aa. IV. A Multiwavelength, Non-LTE Spectroscopic Analysis. *ApJ*, **809**(Aug.), 135.

Shibahashi, H., & Osaki, Y. 1981. Nonradial Oscillations for Stars on the Left-Hand Side of the Cepheid Instability Strip. *PASJ*, **33**, 427.

Shiode, J. H., Quataert, E., Cantiello, M., & Bildsten, L. 2013. The observational signatures of convectively excited gravity modes in main-sequence stars. *MNRAS*, **430**(Apr.), 1736–1745.

Shore, S. N. 1987. Stellar winds and magnetic fields in the helium peculiar stars. *AJ*, **94**(Sept.), 731–736.

Smith, H. A. 2004. *RR Lyrae Stars*.

Snow, Jr., T. P. 1977. Long-term changes in ultraviolet P Cygni profiles observed with Copernicus. *ApJ*, **217**(Nov.), 760–770.

Snow, Jr., T. P., & Morton, D. C. 1976. Copernicus ultraviolet observations of mass-loss effects in O and B stars. *ApJS*, **32**(Nov.), 429–465.

Solanki, S. K. 2003. Sunspots: An overview. *A&ARv*, **11**, 153–286.

Sota, A., Maíz Apellániz, J., Morrell, N. I., *et al.* 2014. The Galactic O-Star Spectroscopic Survey (GOSSS). II. Bright Southern Stars. *ApJS*, **211**(Mar.), 10.

Sprague, Thomas Bradford. 1990. *Shape-preserving Piecewise Cubic Interpolation.* Ph.D. thesis, Kalamazoo, MI, USA. AAI9121894.

St-Louis, N., Tremblay, P., & Ignace, R. 2018. Polarization light curve modelling of corotating interaction regions in the wind of the Wolf-Rayet star WR 6. *MNRAS*, **474**(Feb.), 1886–1899.

Stankov, A., & Handler, G. 2005. Catalog of Galactic β Cephei Stars. *ApJS*, **158**(June), 193–216.

Stein, R. F. 1968. Waves in the Solar Atmosphere. I. The Acoustic Energy Flux. *ApJ*, **154**(Oct.), 297.

Stibbs, D. W. N. 1950. A study of the spectrum and magnetic variable star HD 125248. *MNRAS*, **110**, 395.

Stothers, R. B., & Chin, C.-W. 1993. Dynamical instability as the cause of the massive outbursts in Eta Carinae and other luminous blue variables. *ApJL*, **408**(May), L85–L88.

Stothers, R. B., & Chin, C.-w. 2001. Yellow Hypergiants as Dynamically Unstable Post-Red Supergiant Stars. *ApJ*, **560**(Oct.), 934–936.

Strassmeier, K. G., Kratzwald, L., & Weber, M. 2003. Doppler imaging of stellar surface structure. XX. The rapidly-rotating single K2-giant HD 31993 = V1192 Orionis. *A&A*, **408**(Sept.), 1103–1113.

Struve, O., & Elvey, C. T. 1934. The Intensities of Stellar Absorption Lines. *ApJ*, **79**(May), 409.

Sudnik, N., & Henrichs, H. F. 2018. Multiple, short-lived "stellar prominences" on the O giant ξ Persei: a magnetic star? *Contributions of the Astronomical Observatory Skalnate Pleso*, **48**(Jan.), 305–306.

Sudnik, N. P., & Henrichs, H. F. 2016. Multiple short-lived stellar prominences on O stars: The O6.5I(n)fp star λ Cephei. *A&A*, **594**(Oct.), A56.

Sundqvist, J. O., & Owocki, S. P. 2013. Clumping in the inner winds of hot, massive stars from hydrodynamical line-driven instability simulations. *MNRAS*, **428**(Jan.), 1837–1844.

Szabó, R., Kolláth, Z., Molnár, L., *et al.* 2010. Does Kepler unveil the mystery of the Blazhko effect? First detection of period doubling in Kepler Blazhko RR Lyrae stars. *MNRAS*, **409**(Dec.), 1244–1252.

Tassoul, M. 1980. Asymptotic approximations for stellar nonradial pulsations. *ApJS*, **43**(Aug.), 469–490.

Tassoul, M. 1990. Second-order asymptotic approximations for stellar nonradial acoustic modes. *ApJ*, **358**(July), 313–327.

Thompson, M. J., Christensen-Dalsgaard, J., Miesch, M. S., & Toomre, J. 2003. The Internal Rotation of the Sun. *ARA&A*, **41**, 599–643.

Thoul, A., Aerts, C., Dupret, M. A., *et al.* 2003. Seismic modelling of the beta Cep star EN (16) Lacertae. *A&A*, **406**(July), 287–292.

Todt, H., Sander, A., Hainich, R., *et al.* 2015. Potsdam Wolf-Rayet model atmosphere grids for WN stars. *A&A*, **579**(July), A75.

Tody, D. 1986 (Jan.). The IRAF Data Reduction and Analysis System. *Page 733 of:* Crawford, D. L. (ed), *Instrumentation in astronomy VI.* Proc. SPIE, vol. 627.

Tody, D. 1993 (Jan.). IRAF in the Nineties. *Page 173 of:* Hanisch, R. J., Brissenden, R. J. V., & Barnes, J. (eds), *Astronomical Data Analysis Software and Systems II.* Astronomical Society of the Pacific Conference Series, vol. 52.

Tokovinin, A., Fischer, D. A., Bonati, M., *et al.* 2013. CHIRON–A Fiber Fed Spectrometer for Precise Radial Velocities. *PASP*, **125**(Nov.), 1336.

Touhami, Y., Richardson, N. D., Gies, D. R., *et al.* 2010. Spectral Energy Distributions of Be and Other Massive Stars. *PASP*, **122**(Apr.), 379.

Townsend, R. H. D., Owocki, S. P., & Howarth, I. D. 2004. Be-star rotation: how close to critical? *MNRAS*, **350**(May), 189–195.

Twomey, S. 2013. *Introduction to the Mathematics of Inversion in Remote Sensing and Indirect Measurements.* Developments in Geomathematics. Elsevier Science.

ud-Doula, A., & Owocki, S. P. 2002. Dynamical Simulations of Magnetically Channeled Line-driven Stellar Winds. I. Isothermal, Nonrotating, Radially Driven Flow. *ApJ*, **576**(Sept.), 413–428.

Ud-Doula, A., Owocki, S. P., & Townsend, R. H. D. 2008. Dynamical simulations of magnetically channelled line-driven stellar winds - II. The effects of field-aligned rotation. *MNRAS*, **385**(Mar.), 97–108.

Uuh-Sonda, J. M., Rauw, G., Eenens, P., *et al.* 2014. Epoch-dependent absorption line profile variability in lambda Cep. *Rev. Mex. Astron. Astrofis.*, **50**(Apr.), 67–76.

van Genderen, A. M. 2001. S Doradus variables in the Galaxy and the Magellanic Clouds. *A&A*, **366**(Feb.), 508–531.

van Genderen, A. M., Bovenschen, H., Engelsman, E. C., *et al.* 1989. Light variations of massive stars (Alpha Cygni variables). IX. *A&AS*, **79**(Aug.), 263–282.

van Leeuwen, F. (ed). 2007. *Hipparcos, the New Reduction of the Raw Data*. Astrophysics and Space Science Library, vol. 350.

Vanbeveren, D. 2012 (Dec.). ζ Pup: The Merger of at Least Two Massive Stars? *Page 342 of:* Drissen, L., Robert, C., St-Louis, N., & Moffat, A. F. J. (eds), *Proceedings of a Scientific Meeting in Honor of Anthony F. J. Moffat*. Astronomical Society of the Pacific Conference Series, vol. 465.

Vanbeveren, D., De Loore, C., & Van Rensbergen, W. 1998a. Massive stars. *A&ARv*, **9**, 63–152.

Vanbeveren, D., van Rensbergen, W., & De Loore, C. (eds). 1998b. *The brightest binaries.* Astrophysics and Space Science Library, vol. 232.

Vanbeveren, D., Belkus, H., van Bever, J., & Mennekens, N. 2009. Stellar dynamics in young clusters: the formation of massive runaways and very massive runaway mergers. *Ap&SS*, **324**(Dec.), 271–276.

Villamariz, M. R., & Herrero, A. 2000. Fundamental parameters of Galactic luminous OB stars. V. The effect of microturbulence. *A&A*, **357**(May), 597–607.

Vink, J. S., de Koter, A., & Lamers, H. J. G. L. M. 2001. Mass-loss predictions for O and B stars as a function of metallicity. *A&A*, **369**(Apr.), 574–588.

Wade, G. A., & Collaboration MiMeS. 2015 (Apr.). Review: Magnetic Fields of O-Type Stars. *Page 30 of:* Balega, Y. Y., Romanyuk, I. I., & Kudryavtsev, D. O. (eds), *Physics and Evolution of Magnetic and Related Stars*. Astronomical Society of the Pacific Conference Series, vol. 494.

Wade, G. A., Howarth, I. D., Townsend, R. H. D., *et al.* 2011a. Confirmation of the magnetic oblique rotator model for the Of?p star HD 191612. *MNRAS*, **416**(Oct.), 3160–3169.

Wade, G. A., Alecian, E., Bohlender, D. A., *et al.* 2011b (July). The MiMeS project: overview and current status. *Pages 118–123 of:* Neiner, C., Wade, G., Meynet, G., & Peters, G. (eds), *Active OB Stars: Structure, Evolution, Mass Loss, and Critical Limits*. IAU Symposium, vol. 272.

Wade, G. A., Grunhut, J. H., & MiMeS Collaboration. 2012 (Dec.). The MiMeS Survey of Magnetism in Massive Stars. *Page 405 of:* Carciofi, A. C., & Rivinius, T. (eds), *Circumstellar Dynamics at High Resolution*. Astronomical Society of the Pacific Conference Series, vol. 464.

Waldmeier, M. 1955. *Ergebnisse und Probleme der Sonnenforschung.*

Walker, G., Matthews, J., Kuschnig, R., *et al.* 2003. The MOST Asteroseismology Mission: Ultraprecise Photometry from Space. *PASP*, **115**(Sept.), 1023–1035.

Walker, G. A. H., Kuschnig, R., Matthews, J. M., *et al.* 2005. Pulsations of the Oe Star ζ Ophiuchi from MOST Satellite Photometry and Ground-based Spectroscopy. *ApJ*, **623**(Apr.), L145–L148.

Weiss, W. W., Rucinski, S. M., Moffat, A. F. J., *et al.* 2014. BRITE-Constellation: Nanosatellites for Precision Photometry of Bright Stars. *PASP*, **126**(June), 573.

Weiss, W. W., Fröhlich, H.-E., Pigulski, A., *et al.* 2016. The roAp star α Circinus as seen by BRITE-Constellation. *A&A*, **588**(Apr.), A54.

Wild, W. J. 1989. Matrix formalism for inferring planetary surface albedo distributions from light-curve measurements. *PASP*, **101**(Sept.), 844–848.

Wild, W. J. 1991. Light-curve inversion formalism. *ApJ*, **368**(Feb.), 622–625.

Wolf, B. 1989. Empirical amplitude-luminosity relation of S Doradus variables and extragalactic distances. *A&A*, **217**(June), 87–91.